The Dissertation Committee for Sandy Kurniawan Suhardja Certifies that this is the approved version of the following dissertation:

Mapping the Rivera and Cocos Subduction Zone

Committee:

Steve Grand, Supervisor

Mark Cloos

Jay Pulliam

Mrinal Sen

Fenglin Niu

James Ni

Mapping the Rivera and Cocos Subduction Zone

by

Sandy Kurniawan Suhardja, B. S.; M. E.

Dissertation

Presented to the Faculty of the Graduate School of

The University of Texas at Austin

in Partial Fulfillment

of the Requirements

for the Degree of

Doctor of Philosophy

The University of Texas at Austin

December, 2013

Acknowledgement

I would like to thank Prof. Dr. Steve Grand for giving me a chance to study at the Jackson School of Geoscience, the University of Texas at Austin. I am grateful to have the opportunity to study one of the most complex and challenging geological area at the southern western Mexico. His continue support has allowed me to study a lot of aspects in geoscience. My study was fully supported through NSF funding from Dr. Grand's research and industry scholarships.

I would also like to thank Prof Dr Luca Ferrari at the Centro de Geosciencias, UNAM for detail information on the geological setting and valuable discussion.

I also would like to thank Dr. Nick Rawlinson from Australian National University for giving accommodation during my visit there and also his guidance on seismic tomography inversion scheme using 3-D ray tracing.

I am also grateful to my committees especially Prof. Dr. Mark Cloos for his professional revision and input on the dissertation.

I would like to thank my wife for his companion and patience during my study. She has been very supportive and working hard raising our kids.

Lastly, I would like to thank everyone that are not mentioned here but have been greatly contributed in finishing this study.

Mapping the Rivera and Cocos Subduction Zone

Sandy Kurniawan Suhardja, Ph.D.

The University of Texas at Austin, 2013

Supervisor: Stephen Grand

The crust and upper mantle seismic structure beneath southwestern Mexico was investigated using several techniques including teleseismic tomography using 3D raytracing, a joint tomographic inversion of teleseismic and regional data that included relocation of regional seismicity, and a P to S converted wave study. The data used in these studies came from a broadband seismic deployment called MARS. The seismic deployment lasted 1.5 years from January 2006 to June 2007 and the stations covered much of Jalisco and Colima states as well as the western part of Michoacan states.

At depth less than 50 km, P-wave receiver function images show a clear dipping slow velocity anomaly above a fast velocity layer. The slow anomaly convertor seen in receiver functions is directly above a fast dipping seismic anomaly seen in regional tomography results. The slow velocity with high Vp/Vs ratio is interpreted as a high pore fluid pressure zone within the upper layer of subducting oceanic crust. Regional seismicity was located using the double difference technique and then relocated in a tomography inversion. The seismicity is located very close to the slow dipping boundary to depths of 30-35 km and thus along the plate interface between the subducted and overlying plate. Deeper events are below the slow layer and thus are intraplate. Receiver function results also show a weaker continental Moho signal above the dipping slab that I

interpret as a region of mantle serpentinization in the mantle wedge. Inland of the subduction zone, a clear Moho is observed with a maximum thickness of near 42 km although it thins to near 36 km depth towards the north approaching the Tepic-Zacoalco Rift. Using H-K analysis to examine Vp/Vs ratios in the crust, I find a band of very high Vp/Vs along the Jalisco Volcanic lineament as well as beneath the Michoacan-Guanajuato volcanic field. These observations suggest the continental crust is warm and possibly partially molten over broad areas associated with these two magmatic regions and not just locally beneath the volcanoes. I also found seismicity associated with the Jalisco Volcanic Lineament but it was trenchward of the volcanoes. This may indicate extension in this region is part of the explanation for this magmatic activity.

At depths below 100 km, the tomography results show clear fast anomalies, about 0.3 km/s faster than the reference model, dipping to the northeast that I interpret as the subducting Rivera and Cocos plates. Tomography models show that the Rivera slab is dipping much steeper than the Cocos plate at depth. Below 150 km depth, the Rivera plate shows an almost vertical dip supporting the interpretation that the slab has steepened through time beneath Jalisco leading to a coastward migration of young volcanism with mixed geochemical signatures. The location of the young volcanism of the Jalisco Volcanic Lineament is just at the edge of the steeply dipping slab seen in the tomography. The magmatism is thus likely a nascent arc. The models also display evidence of a gap between the Rivera and Cocos plates that increases in width with depth marking the boundary between the two plates. The gap lies just to the west of Colima graben and allows asthenosphere to rise above the plates feeding Colima volcano. Another interesting finding from this study is a possibility of a slab tear along the western

edge of the Cocos plate at a depth of about 50 km extending 60 km horizontally. The tear is coincident with a lack of seismicity in this region although there are events below and above the tear.

TABLE OF CONTENTS

List of Figures

Chapter 1: Introduction

The current tectonic configuration of the Mexican subduction zone results from successive fragmentation events that affected the ancient Farallon plate as various segments of the East Pacific rise approached the paleo-trench off western North America as shown on Figure 1.1. When a spreading center encounters a subduction zone, a major change in stress and plate boundaries occurs. The change in stress affects the tectonics of the overriding plate which may include unusual volcanism, fragmentation of the overriding plate, and micro- plate capture (Stock and Lee, 1994). However, the details of how this occurs and the controlling dynamics are still poorly understood.

One place on Earth where micro plate fragmentation and capture is presently occurring is in the Rivera subduction zone of south western Mexico. In this area, the Rivera plate detached from the Cocos plate some 5-10 Ma and is presently subducting beneath the Jalisco block. Figure 1.2 shows the current plate ages of the Rivera and Cocos plates at the Mexican coast as well as projected beneath Mexico. At the present time, the Rivera plate is about 10 Ma, at the trench, and the Cocos plate 13 Ma (Lawver, L. A. et al., 2013). Due to a triple junction just off shore Manzanillo, Colima (Fig. 1.3), the ocean crust subducting in the gap between the Cocos and Rivera plates is much younger than to the east or west. We estimate roughly 4 Ma crust is being subducted in this region. The estimation of the oceanic crust age at depth is calculated using crustal ages from the last 10 Ma (Lawver, L. A. et, 2013), the angle of slab dip from this study and convergence rates through time from Demets and Wilson (1997). Concurrently, the Jalisco block may be separating from the North American plate along the Colima graben

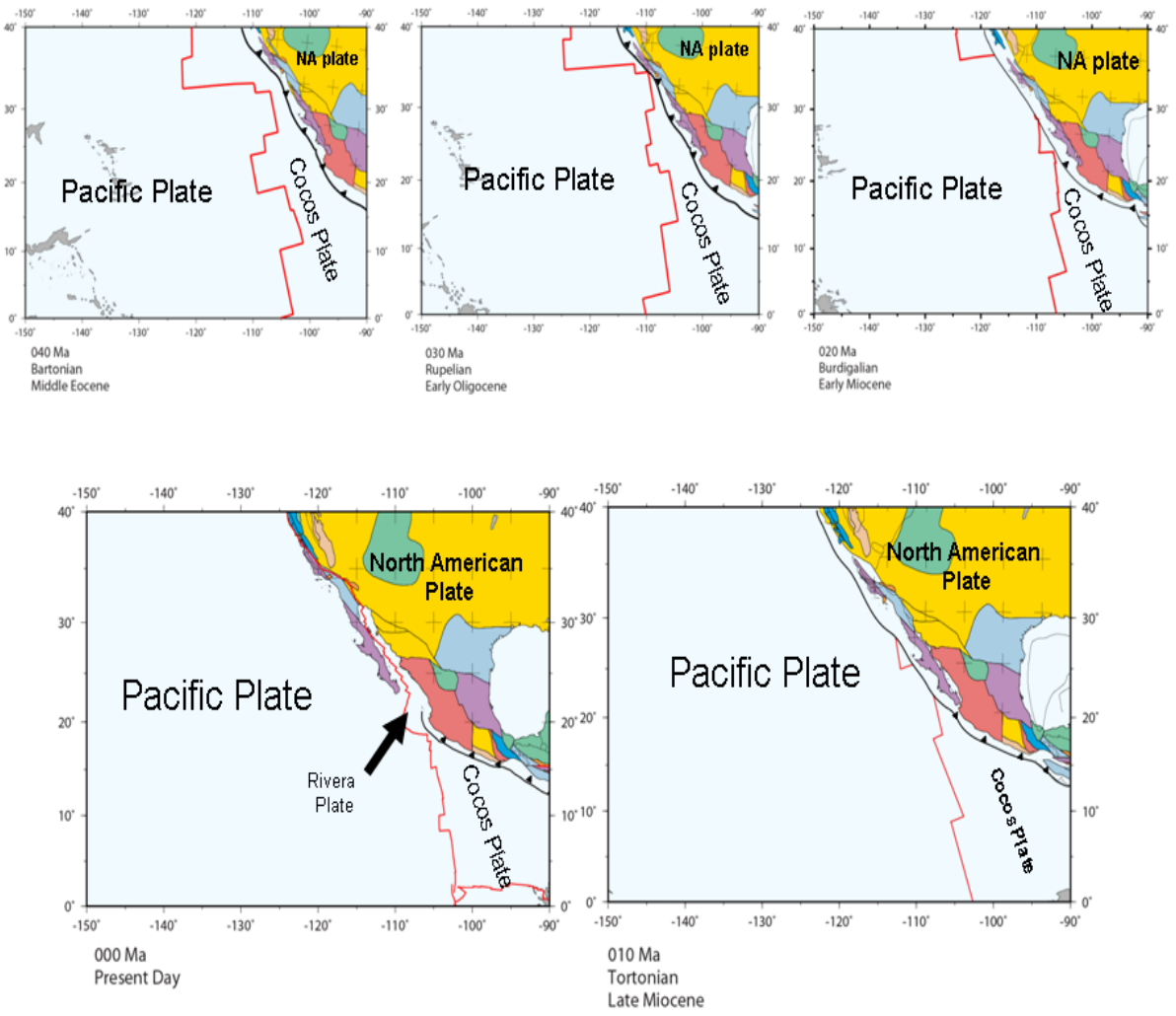

Figure 1.1. Plate evolution along the western boundary of North America. The East Pacific Rise began converging with the Western North America subduction zone ~30 Ma. The converging process is occurring today in Cascadia and Southwestern Mexico. Data taken from Lawver, L. A. et, (2013).

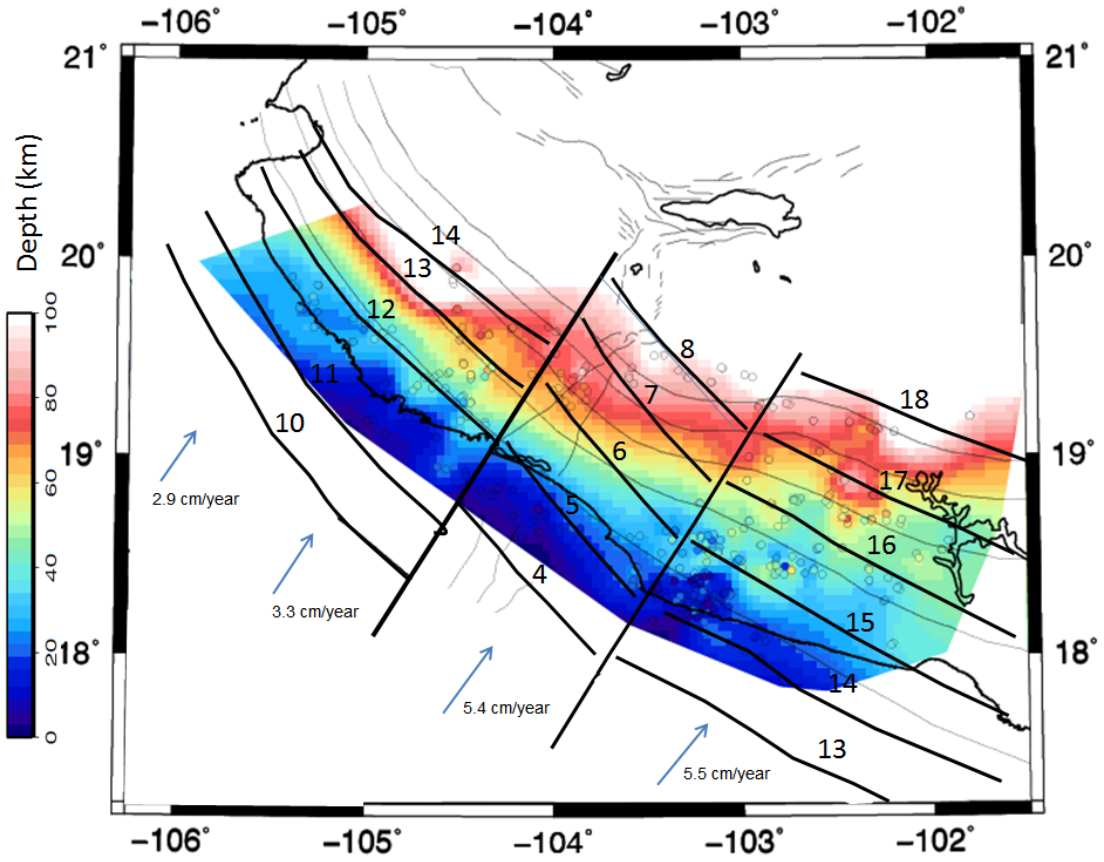

Figure 1.2. The age of the Rivera and Cocos crust. The pole rotation between Rivera plate and North American plate is located at latitude 21.4^{o} and longitude -108.2^{o} with angular velocity 4.2 deg/Myear. The pole rotation between Cocos plate and North American plate is located at latitude 29.4^{o} and longitude -125.1^{o} with angular velocity 1.24 deg/Myear. The data are taken from Demets and Wilson (1997). The age of the crust on the trench from present time to the last 10 Ma is taken from Lawver, L. A. et al ,(2013). The number above the contour line is the age of the crust and the color in the background color is depth of the slab.

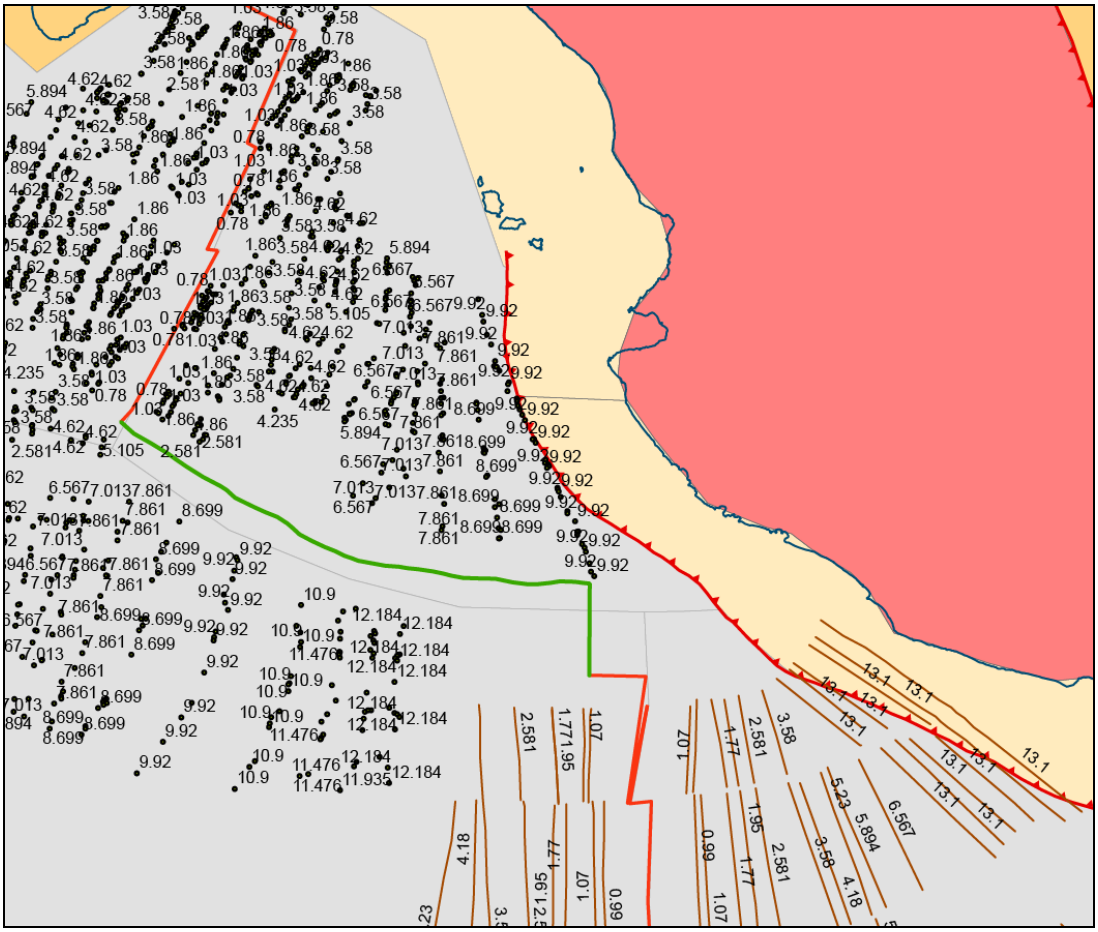

Figure 1.3. Present time crustal age on the Rivera and Cocos plate. The data were originally from magnetic lineament measurement (Lawver, L. A. et al, 2013) that has been converted to time using Gee, J.S. and Kent, D.V., (2007).

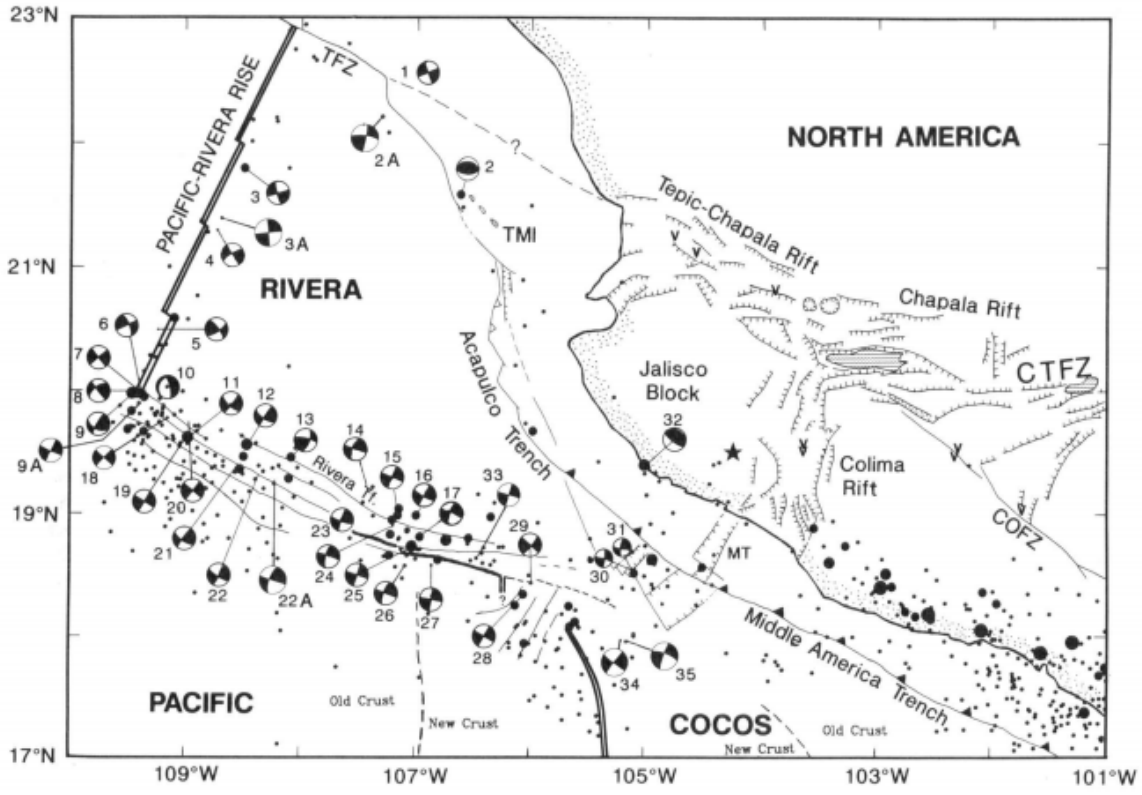

Figure 1.4. Neotectonics of the Rivera plate region (image taken from DeMets and Stein, 1990). Small circles show all earthquakes between January 1967 and December 1986. Medium and large solid circles show all 1964-1976 earthquakes with magnitude larger than 4.8 M that were relocated by Eissler and McNally (1984). The star shows the location of the 1932 Jalisco earthquake (Eissler and McNally, 1984). Abbreviations are MT, Manzanillo trough; COFZ, Chapala-Oaxaca fault zone; CTFZ, Chapala-Tula fault zone; TMI, Tres Marias island; TFZ, Tamayo fracture zone.

to the east and the Tepic-Zacoalco graben to the north, and may actually be a microplate in its own right (Figure 1.4).

Jalisco block magmatism is located at the western part of the Trans-Mexican Volcanic Belt (TMVB), a 1000 km continental magmatic arc containing nearly 8000 volcanic structures and a few intrusive bodies, that extends from San Blás, Nayarit, and Banderas Bay, Jalisco on the Mexican Pacific coast to Palma Sola, Veracruz on the coast of the Gulf of Mexico (Demant, 1978).

The Jalisco block shows unusual magmatic activity in terms of age and composition. Geochemical analyses of some lavas indicate both an ocean island basalt component and an arc signature. Ferrari (2001) shows that magmatism is younger towards the trench (Figure 1.5 and 1.6). In addition to that, Colima Volcano, a large active stratovolcano, is offset trenchward from other volcanoes along the Mexican Volcanic Belt.

The complexity and uniqueness of the Jalisco region is related to the presence of two independent subducting oceanic plates, the Rivera and Cocos plates, with different ages, compositions, convergence velocities and subduction dip angles. Each sector of the arc is also controlled by a different stress fields and deformation history that includes extensional and strike-slip faulting concurrent with magmatism. In addition, the convergent margin and the magmatic arc have not remained static throughout their histories, but instead have undergone notable modifications in terms of geometry and composition.

Although a great deal of geodetic, petrologic, structural, and paleomagnetic work has been done in the region, yet no detailed seismic study of the region were carried out.

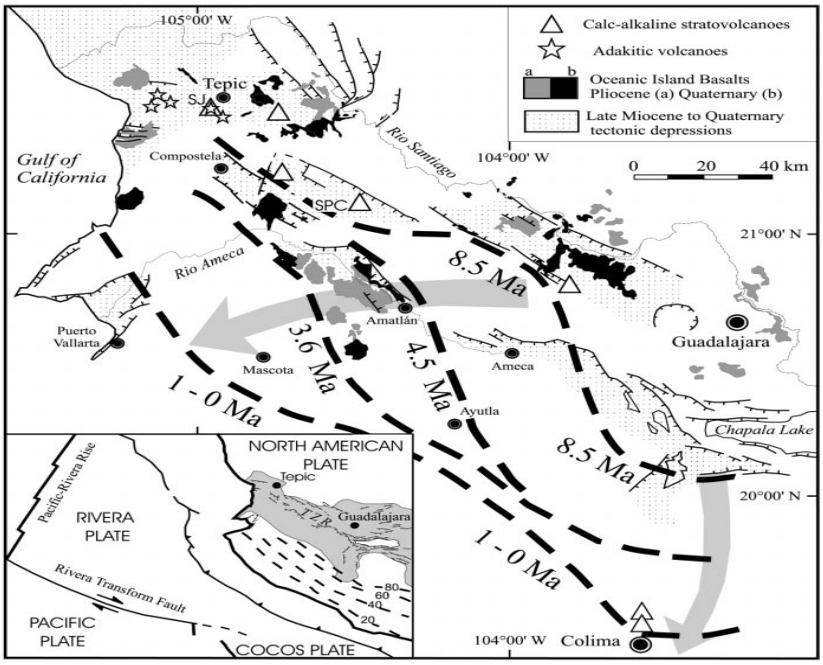

Figure 1.5. Age of magmatism on the Jalisco block (image taken from Ferrari et al., 2001). The dashed line shows a trend of magmatism age from 8.5 Ma to the north trending to 1.0 Ma in the south. The trend shows younger magmatism closer to the trench. The youngest magmatism along a line at places like Mascota and Ayutla and is popularly known as the Jalisco Volcanic Lineament. SJ is San Juan volcano and SPC is San Pedro Ceboruco volcano.

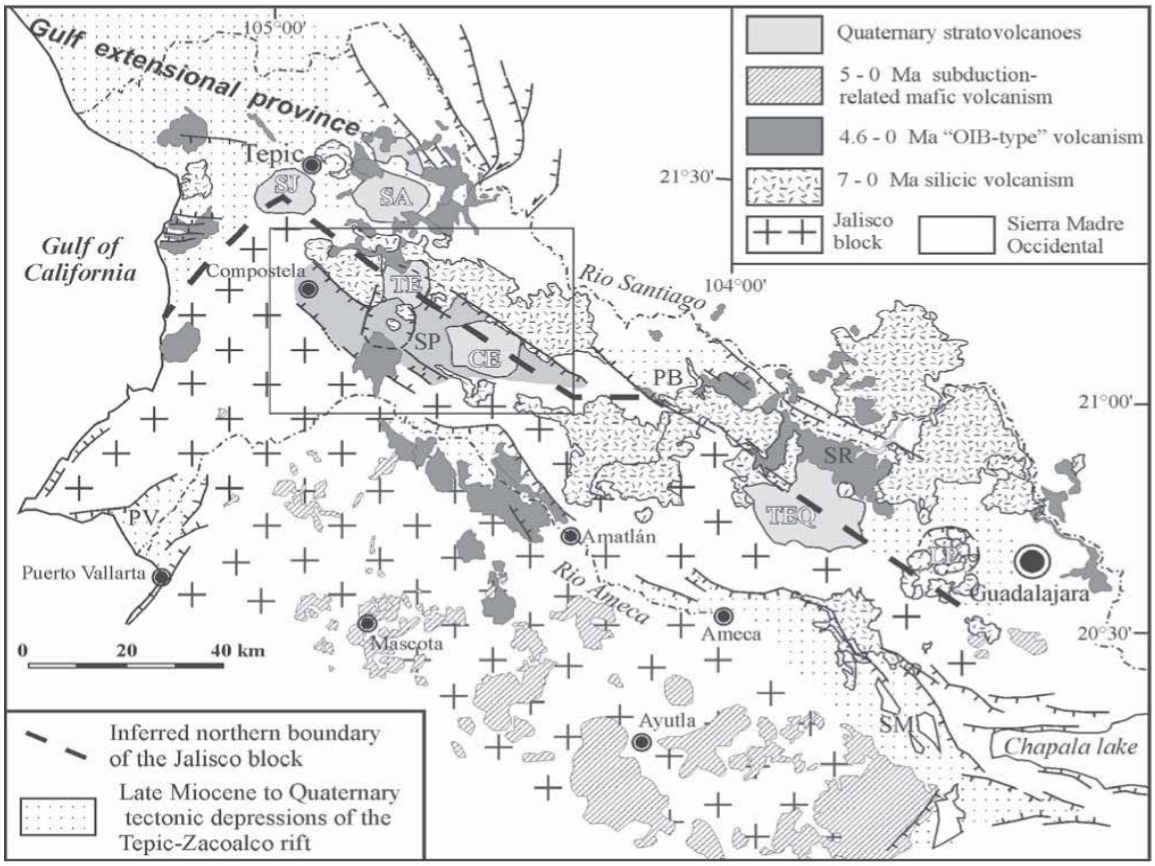

Figure 1.6. Geochemical and petrologic character of magmatism in the northwest of the Jalisco block (image taken from Ferrari, 2001). The magmatic pattern is complex with subduction related mafic magmatism and OIB type volcanism relatively close in distance and time. The figure also shows a belt of younger magmatism closer to trench.

Previous seismicity studies Pardo and Suarez (1993, 1995) in this region have used few stations with limited aperture. The data used in their study consisted of 5 temporary stations deployed for one month in 1989, 20 teleseismic events that were relocated using joint hypocenter determination and 5 additional events with magnitude greater than 5 determined by a long period body wave inversion scheme. In this study, I use data collected from a passive deployment of 50 seismometers through the Mexican states of Jalisco, Colima, and Michoacan. The seismic data from this study are used to image the top of the subducting Rivera and Cocos plates as well as image the crust and shallow mantle beneath the fore arc region. The main goal of my work is to provide constraints on the kinematic connection between the subducting Rivera plate and the deformation and magmatism of the overriding Jalisco plate.

The second chapter of this dissertation is an introduction to the tectonic setting of the region. A history of subduction and the tectonics of the overriding plate is reviewed to introduce the complexity of the area. Previous geophysical studies will also be reviewed to provide background for my work. The second chapter will end with an evaluation of some hypotheses concerning the tectonic evolution of the region and the goals of this study.

The third chapter is a study of the crustal structure of southwestern Mexico using a P to S converted wave method known as the receiver function technique. I derive a model of crustal thickness as well as P to S velocity ratios for Southwestern Mexico. The top slab interface is also imaged in this study. The crustal variations can be used to help constrain the tectonic history of the region.

The fourth chapter is a comparison of teleseismic tomography methods which are

used to obtain subsurface seismic velocity variations in the crust and mantle. A previous study of southwestern Mexico has used a finite frequency seismic tomography method using 1-D ray tracing (Yang et al, 2009). I compare those results to results derived from a different technique using 3-D ray tracing and discuss the strengths and weaknesses of the two approaches.

In chapter five, I combine regional and teleseismic data in a tomography inversion to produce a 3-D P wave velocity model for Southwestern Mexico. Regional earthquake locations are included as variables in the inversion and I also present a relocated seismicity map for the region in this chapter. The velocity model and seismicity will be discussed to determine the relationship between slab interface properties and seismicity as well as the source of magmas in the Jalisco block.

Chapter 6 reviews the results from the previous chapters and discusses the implications for understanding the evolution of plate boundaries when ridges and subduction zones impinge including the generation of unusual magmatism. A suggestion of future work is also included.

Chapter 2: Tectonic Setting

The nature of the boundary between the Rivera and Cocos plates was still uncertain (Bandy et al, 1995). Based on a detailed analysis of sea floor magnetic lineation, Demets and Traylen (2000) have proposed a complicated history of convergence between the Rivera and North American plates during the past 10 Ma. The convergence rate decreased gradually from 10 to 3.6 Ma, followed by a rapid decrease after 3.6 Ma, and then a rapid increase after 1 Ma. At present, the relative motion of the Rivera plate with respect to the North American plate is almost perpendicular to the trench near Colima but becomes progressively more oblique to the northwest. The 1932 Jalisco earthquake, the largest subduction event in Mexico's recorded history (Eissler and McNally, 1984), is clear evidence of convergence in this region (Figure 2.1). Offshore recorded seismicity clearly shows the boundaries of the Rivera plate to the west and south. The focal mechanisms show transform motion along the Rivera-Pacific Boundary with the northern boundary between the Pacific and Rivera plate marked by the East Pacific Rise. The Rivera-Cocos plate boundary is unclear and may be a diffuse zone. It is bounded by two triple junctions. Note that the triple junction Rivera-Pacific-North America plate is Ridge-Trench-Tranform (RTF) and Rivera-Pacific-Cocos triple junction is Trench-Trench-Transform (TTF) system. The Rivera-Cocos boundary intersects the North America plate near the Colima Rift. The north-south Colima rift intersects the east-west trending Tepic-Zacoalco Rift, marking the boundary of the Jalisco block. Luhr et al (1985) and Allan et al (1991) proposed that the intersection between the north-south rift and the east-west rift reflects initiation of a major continental rifting event, which

ultimately will lead to transfer of the Rivera plate and the Jalisco Block (at the present, currently part of the North American plate) to the Pacific plate. Luhr (1985) has argued that this rifting is related to the Pacific-Rivera spreading ridge jumping to the site of the Colima Rift. Four similar eastward ridge-jumps have progressed northward in sequence along the East Pacific Rise during the last 12 Ma (Van Andel et al. 1975, Mammerickx & Klitgord 1982), and the proposed on-going ridge-jump would be a continuation of this series and the first event to intersect continental crust. Various investigators have emphasized that the on-going continental rifting event in western Mexico provides an excellent analog for the initial rifting of Baja California at about 14 Ma (Luhr et al., 1985, Allan et al. 1991., Lyle and Ness 1991)

The Jalisco block exhibits two distinct surface lithologic zones. Southwest of Sierra Cacoma, in the coastal region, the lithology is predominantly Cretaceous granitoids (Schaaf et al., 1994, 1995) as shown in Figure 2.2. Northeast of Sierra Cacoma, is dominantly Cretaceous to early Cenozoic silicic ash flows that are disrupted by several extensional structures, including the Mascota and Talpa de Allende grabens, which contain Plio-Quaternary basalts (Luhr et al., 1989; Righter and Carmichael, 1992). The Jalisco Block also stands high relative to the terrane north of the Tepic-Zacoalco Rift at about 2000 m elevation, apparently as a result of Neogene uplift (Ferrari 1995, Righter et al., 1995). The Tepic-Zacoalco rift, the northern boundary of the Jalisco block can be divided into two zones (Jose´ Rosas-Elguera et al., 1996): a northern branch, located at the boundary between the Jalisco block and the Sierra Madre Occidental, is a 70-km long and 20-km-wide depression with about 550 m of vertical displacement, mainly attained during the Pliocene and a southern branch that is located inside the Jalisco block.

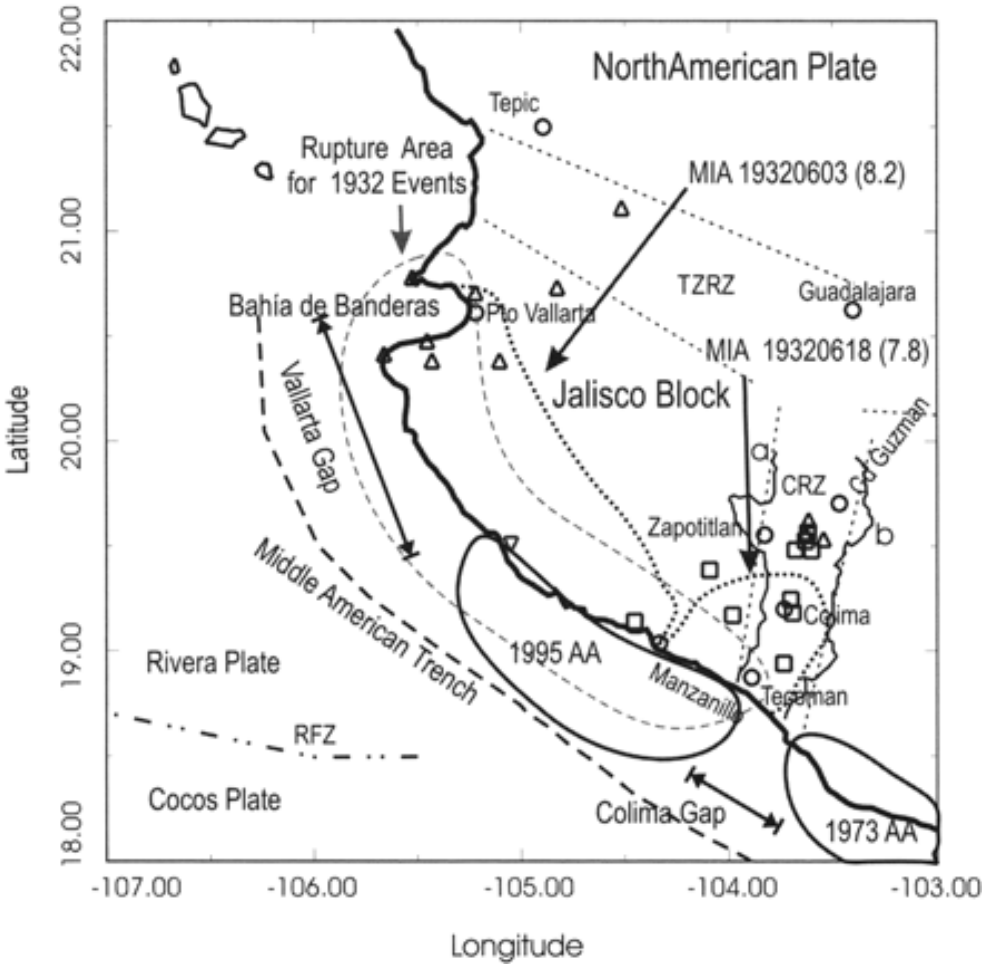

Figure 2.1. Major earthquake location and its rupture area (image taken from Eissler and McNally, 1984). Dotted line shows the maximum intensity areas (MIA) of shaking and the dashed lines show the inferred rupture areas for the 1932 events. The circled AA areas enclose the aftershock locations for earthquakes in 1995 and 1973. RFZ: Rivera Fault zone; CRZ: Colima rift zone; TZRZ: Tepic-Zacoalco rift zone; a: Armería River; b Cohuayana River; Seismic stations in the region: squares: RESCO stations; triangles RESJAL stations; inverted triangle: Chamela station (CJIG). Circles: major cities.

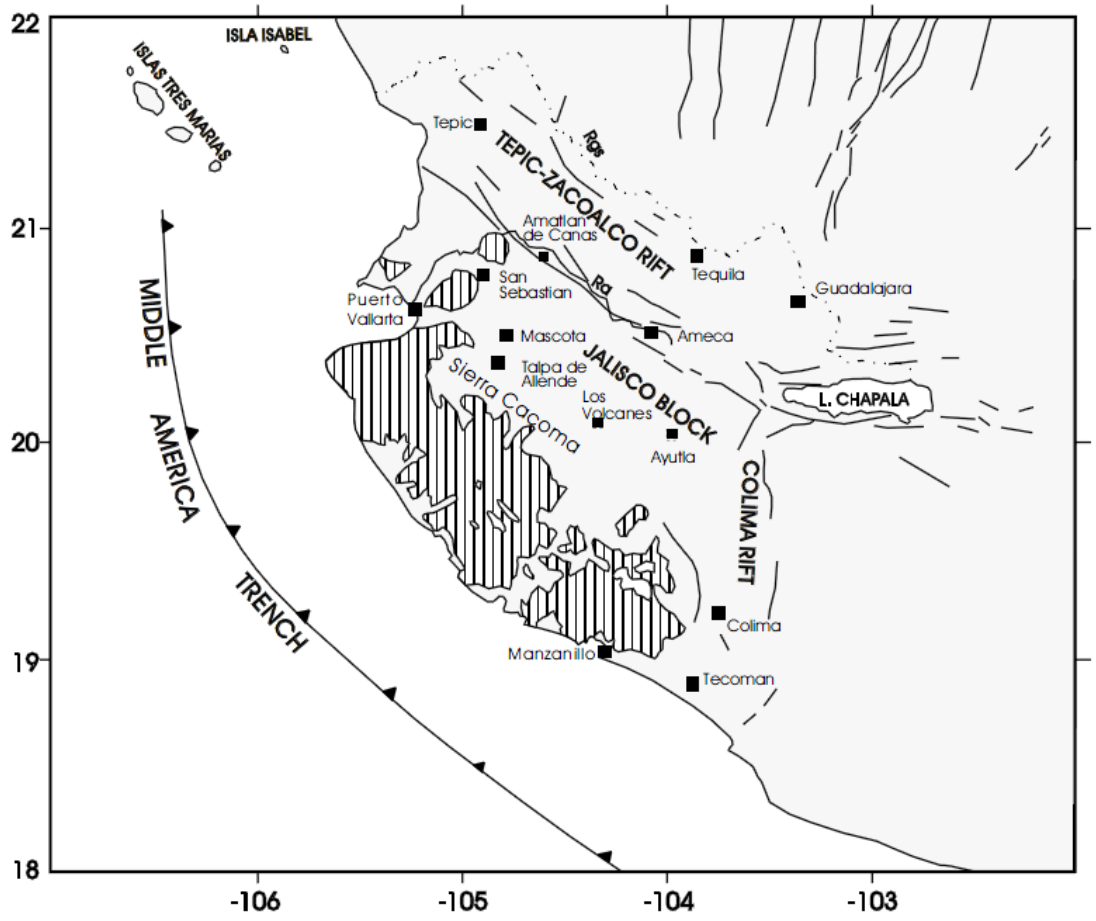

Figure 2.2. Location of Sierra Cacoma and the surface lithology of the region (image taken from Mailol, J. M., 1996) To the southwest (hatched line) of Sierra Cacoma, the lithology is predominantly Cretaceous granitoids and to the Northeast of Sierra Cacoma it is dominated by Cretaceous to early Cenozoic silicic ash flows.

block and parallel to the northern branch of the Tepic-Zacoalco rift. The easternmost depression, the Zacoalco half graben, is formed by a south- to southwest-dipping detachment fault with a minimum of 1400 m of vertical displacement with most of the extension occurring during the Pliocene.

The eastern boundary of the Jalisco block, the Colima rift, can also be divided into two parts. To the north, gravimetric modeling indicates a vertical offset of about 2500 m (Allan et al., 1991) with extension in the northern Colima rift starting at the beginning of the Pliocene. Compared to the northern rift, the southern Colima Rift is a wider topographic depression and shows almost no seismicity.

The Oceanic Plates (History, Geometry and the Composition of the Subducting Oceanic Plates)

Geophysical studies clearly indicate that the Cocos and Rivera oceanic plates are currently being subducted under the continent in the direction of the Trans-Mexican Volcanic Belt (Urrutia-Fucugauchi and Del Castillo, 1977; Urrutia-Fucugauchi and Böhnel, 1987; Pardo and Suárez, 1993, 1995). For this reason, most researchers consider that magma genesis in the Trans-Mexican Volcanic Belt and the belt's oblique orientation to the trench must be related in some way to the subduction process. However, due to petrologic peculiarities of the arc, the unusual presence of an extensional tectonic regime accompanying primitive magmas, and the poorly defined Wadati-Benioff zone beneath most of the arc, some researchers question whether a subducting slab is causing the magmatism (Márquez et al., 1999; Verma, 1999, Sheth et al., 2000, Verma, 2000, 2002).

Verna and co-workers have suggested instead that magmatism in the Trans Mexican Volcanic Belt is the product of active continental rifting that is occurring in central Mexico, which is expressed by the presence of normal faults along the arc. Then, the primitive magmas found there are related to partial melting of the mantle during adiabatic decompression and have compositional similarities to magmas observed in intraplate settings without any slab-derived chemical agents.

The tectonic history of the oceanic plates has been explored through magnetic studies (Atwater, 1970; Menard, 1978; Londsdale, 1991). In general, the Rivera plate is relatively younger and has a slower convergence rate than the Cocos plate (Nixon, 1982; Pardo and Suárez, 1993; DeMets et al., 1994; Kostoglodov and Bandy, 1995; Pardo and Suárez, 1995). The Rivera plate is between ca. 9 and ca. 13 Ma old at the trench off Puerto Vallarta and Manzanillo, respectively, and currently converges with the North American plate at a rate that varies between 1.7 and 2.2 cm/yr (DeMets et al., 1994) or between 4 and 4.9 cm/yr (Kostoglodov and Bandy, 1995), depending on the model used. The age of the Cocos plate ranges between 12.7 and 16 Ma along the trench, and is older to the east. The convergence velocity also increases toward the east from ~4.7 to ~6.7 cm/yr (Pardo and Suárez, 1995)

The thickness and compositional variations of the subducted oceanic crust and its sedimentary cover are still poorly known. The Deep Sea Drilling Project Igneous Petrogenesis of the Trans-Mexican Volcanic Belt 141 (DSDP) was the first study to reveal the oceanic crust composition. Another geophysical study that investigated the oceanic crust was a gravity study across the trench by Manea et al. (2003). The gravity study of Manea et al. (2003) suggested that the thickness of the sedimentary column over

the Rivera plate probably does not exceed ~20 m, and that it gradually increases eastward along the trench. On the other hand, the DSDP carried out several seismic profiles and drillings along the Middle America Trench revealing that the sedimentary column at this site is composed of ~100 m of Quaternary hemipelagic sediments which overlay ~70 m of late Miocene to Pliocene pelagic sediments. The oceanic crust at this site should be ca. 13 Ma old according to the magnetic anomaly patterns.

The Continental Plate

Information on the crustal structure along the TMVB has been mostly derived from gravimetric studies (Molina-Garza and Urrutia-Fucugauchi, 1993; Urrutia-Fucugauchi and Flores-Ruiz, 1996; García-Perez and Urrutia-Fucugauchi, 1997; Campos- Enríquez and Sánchez-Zamora, 2000) and seismic studies (Urrutia-Fucugauchi, 1986; Nava et al., 1988; Geolimex-Group, 1994; Campillo et al., 1996). Additional information comes from aeromagnetic studies (Campos-Enríquez et al., 1990) and magneto-telluric profiles (Jording et al., 2000), and although their coverage is very broad, they generally agree with seismic and gravimetric data.

The pattern of gravimetric anomalies along the arc defines a relatively simple structure consistent with a gradual increase in crustal thickness from the coast to the continental interior. The crustal thickness structure estimated for the TMVB is consistent with the data obtained from the seismic profiles in southern México, where thickness increases inland from the Pacific Coast and reaches ~47 km beneath the Oaxacan complex (Urrutia-Fucugauchi, 1986; Valdés et al., 1986).

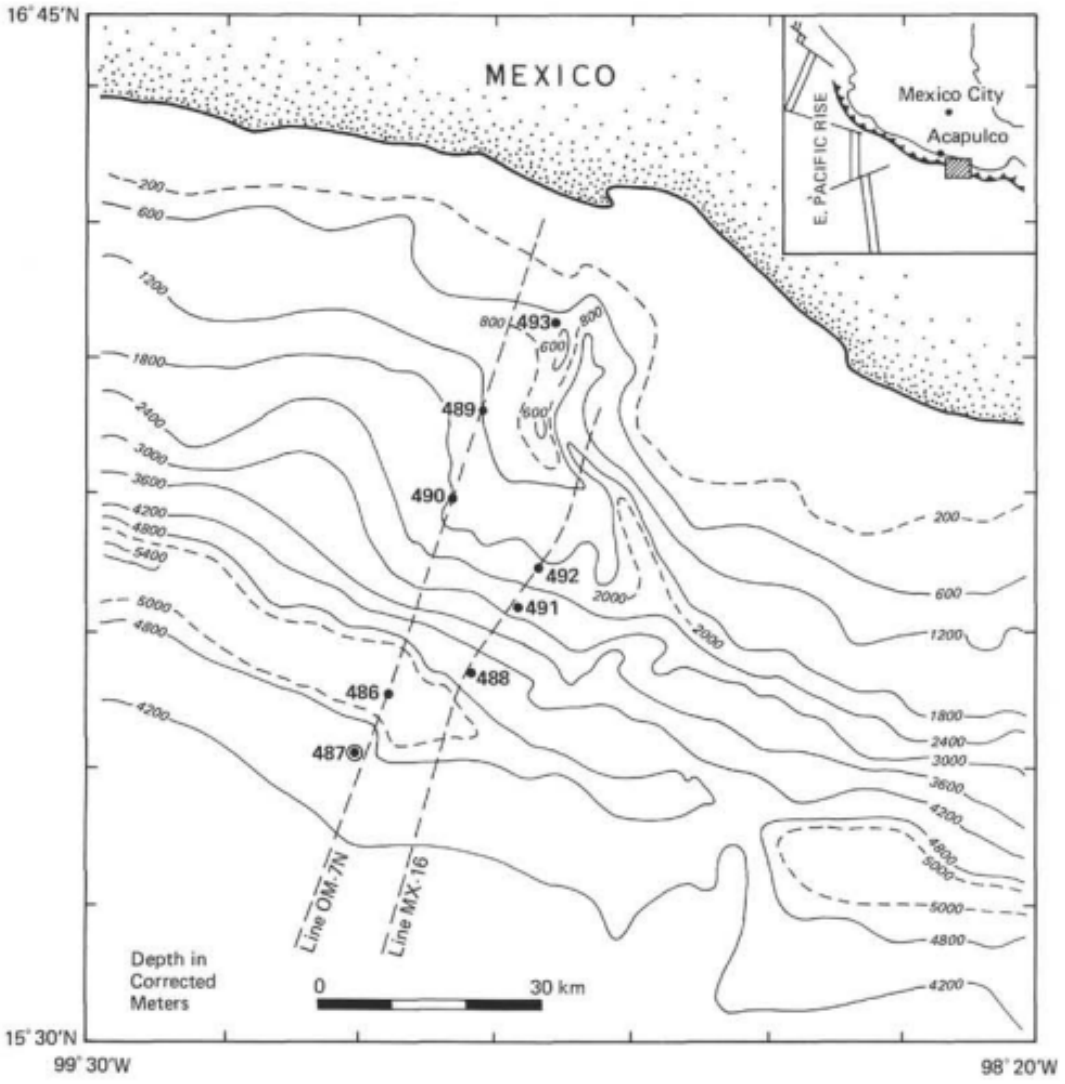

Figure 2.3. Map of Deep Sea Drilling Project Igneous Petrogenesis of the Trans-Mexican Volcanic Belt 141 (DSDP) location. Site 487 show an estimate 170 m sediment thickness. Image taken from http://www.deepseadrilling.org/66/volume/dsdp66_03.pdf

The present topography of the Trans-Mexican Volcanic Belt generally correlates with gravimetric data and crustal thickness. In a general way, elevations tend to increase from the coast to the continental interior, where the maximum elevations (>3,500 m) correspond to the large active stratovolcanoes of the eastern sector. A general correlation can also be observed between the concentration of the stratovolcanoes and the regions of higher crustal thickness. Elevations also tend to decrease gradually toward the north of the volcanic front (Figure 2.3).

Previous Seismic studies

Seismicity data show occasional large-thrust earthquakes within the Rivera plate: the 1932 Jalisco event with 8.2 M, the magnitude-8.0 Colima-Jalisco earthquake in 1995 (Hutton et al., 2001), and the January, 2003 7.6 M Colima earthquake. However, in general there is very little teleseismically observed earthquake activity in the region. This behavior may be similar to the Juan de Fuca subduction zone that has been postulated to have infrequent large earthquakes but has shown almost no seismicity during recorded history (Heaton and Hartzell, 1987).

Pardo and Suarez (1993, 1995) have located microseismic events near the Colima rift at the eastern edge of the Jalisco block (Figure 2.4). Their study revealed that the Rivera plate dips at an angle of ~50° beneath the continent and that earthquakes extend to a depth of ~120 km. In contrast, the subduction angle of the Cocos plate is more variable and the hypocenters do not exceed ~80 km in depth. In fact, the dip angle of the Cocos plate progressively decreases from its boundary with the Rivera plate to approximately

101°W longitude, after which it becomes almost horizontal southward in the western half of the eastern sector of the TMVB. The temporary array used by Pardo and Suarez (1993) had a very small aperture and most of the deeper events they located were outside the array, so that the detailed geometry of the subducting Rivera plate and the location and nature of the boundary between the Rivera and Cocos plates is still quite uncertain.

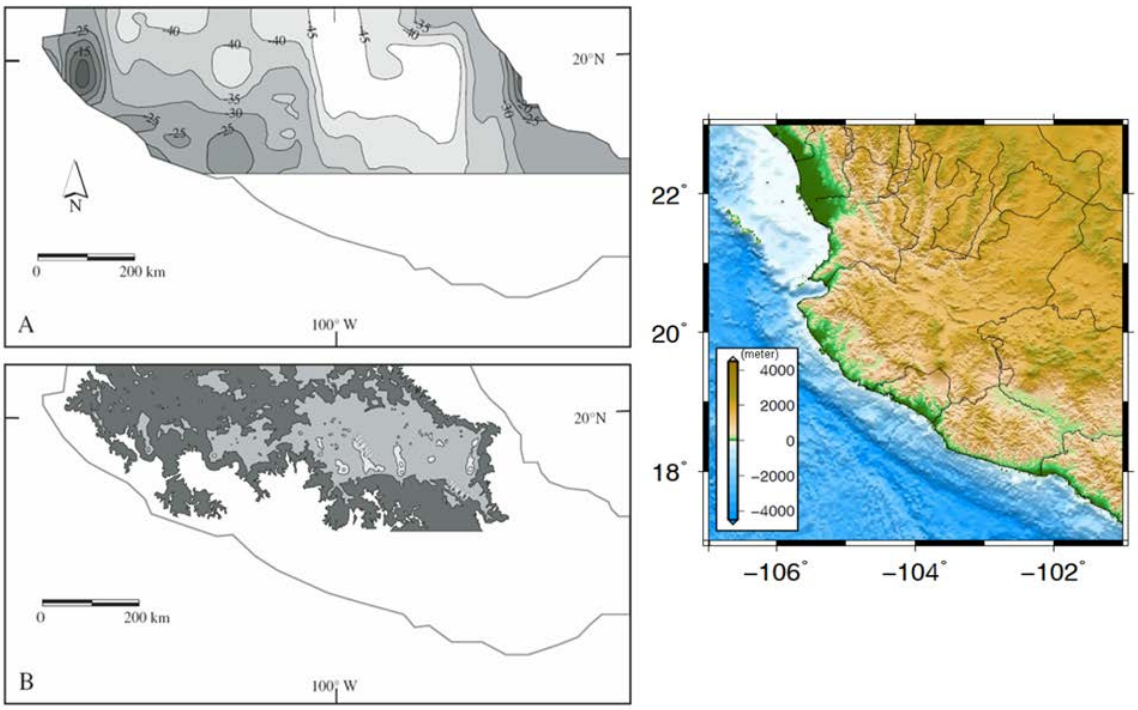

Figure 2.4. Top left, a crustal thickness map derived from gravity data. The contour lines are crust thickness. Bottom left is the corresponding regional topography (image taken from Urrutia-Fucugauchi and Florez-Ruiz, 1996). Lighter color represent higher topography. To the right is a more detailed topography map for the Jalisco block (topography data taken from www.noaa.gov). In general, along the coast the crustal maps show 15-25 km depths which is likely the depth to subducting oceanic crust that deepens inland. Continental crust shows an average of 40 km depth and thicker continental crust correlates with higher topography.

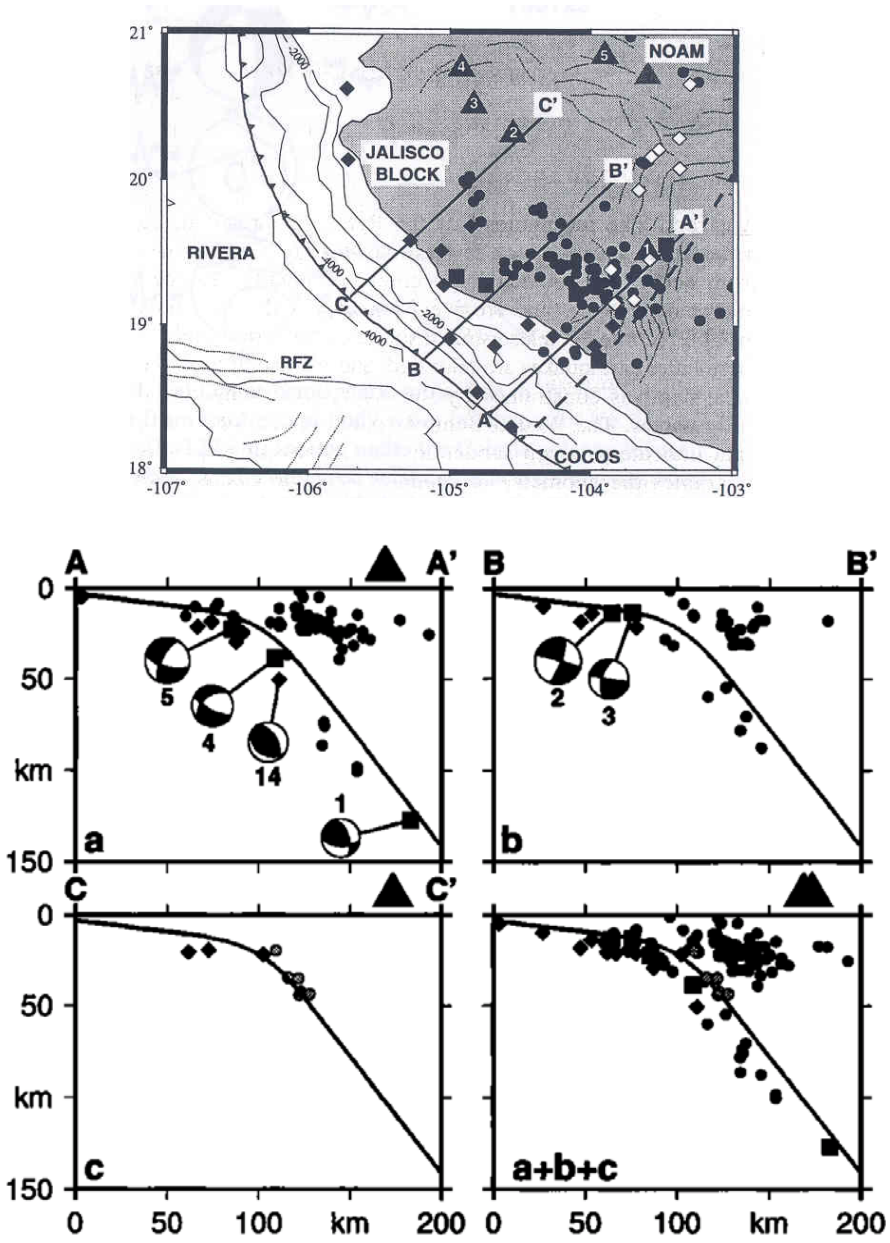

Figure 2.5. Hypocenters of earthquakes related to the subduction of the Rivera plate (image taken from Pardo and Suarez, 1993). The temporary stations used in this analysis are shown as open diamonds with the southern stations operating one year and the other stations only three weeks. All but one of the intermediate earthquakes were microearthquakes (shown as circles) located by the temporary array and most of these events were largely outside the aperture of the array and thus poorly located. Solid diamonds and squares represent hypocenters located from teleseismic observations from 1964 to 1983. Triangles represent volcanoes.

Magmatism

Cenozoic volcanism in Mexico is divided into two magmatic provinces, the mid-Tertiary Sierra Madre Occidental and the Miocene-Quaternary Trans-Mexican Belt. Volcanism in both provinces has been linked directly with the tectonic evolution of western Mexico and adjacent oceanic plates. The TMVB which started to form around 15 Ma, has a peculiar oblique orientation with respect to the trench (Figure 2.5). Several active volcanoes lie on the front of the TMVB: Popocatepetl, Colima and Pico de Orizaba.

In general, the compositional diversity of a continental magmatic arc depends on various components and processes that are often difficult to distinguish. The current petrologic evidence indicates that arc volcanics could represent mixtures of a great number of geologic materials: (1) magmas derived from the partial melting of the asthenospheric or lithospheric mantle that are intrinsically heterogeneous at all scales; sediments, and underlying serpentinized mantle; (2) melts generated by partial melting of the subducted materials; and (3) melts derived from a compositionally diverse continental crust. If most of the magmatism is related to subduction, other parameters may play a significant role, such as the age of the subducted slab, the convergence rate, the subduction dip angle, continental crustal thickness, and the state of stress that operates on the upper plate.

The Jalisco block is a part of the southwestern edge of the Trans-Mexican Volcanic Belt, a broad band of volcanic activity that strikes east-west across Mexico.

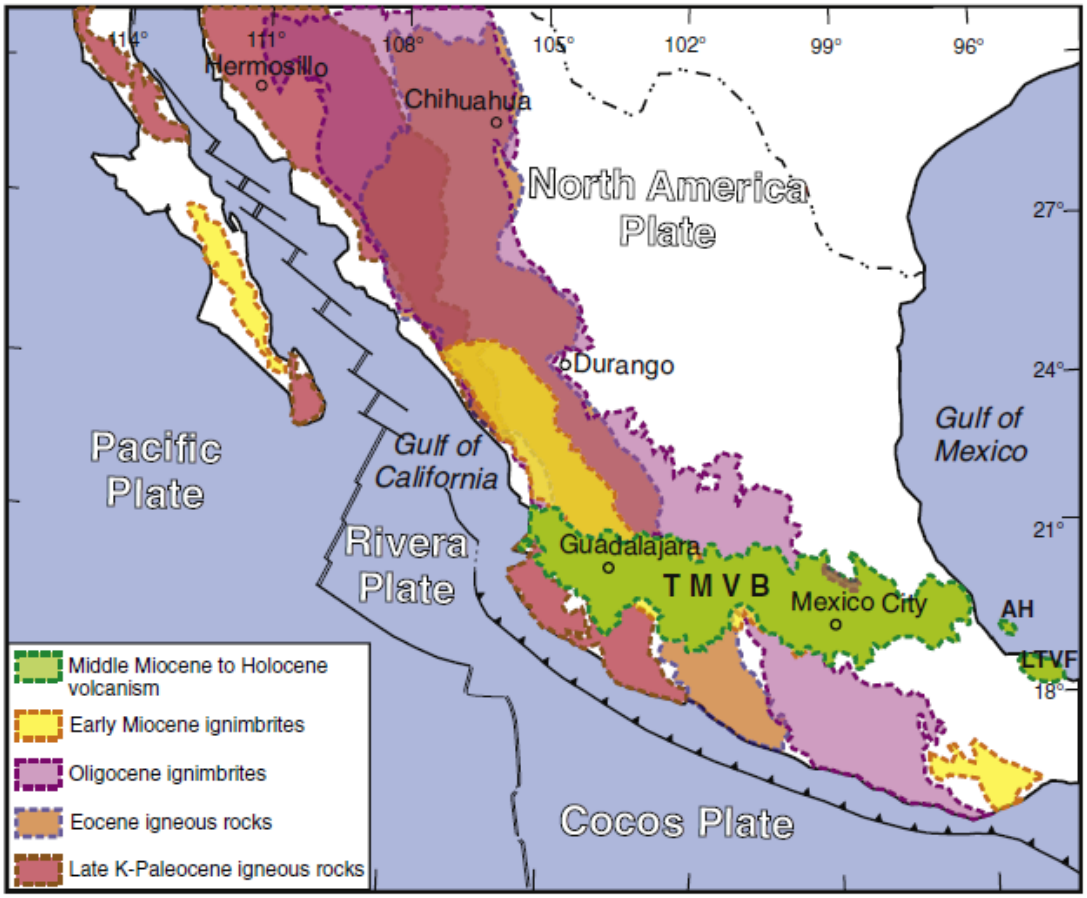

Figure 2.6. Geodynamic setting and main continental magmatic provinces (image taken from Ferrari, 2012) AH : Anegada high; LTVF : Los Tuxtlas volcanic TMVB : Trans-Mexican Volcanic Belt)

Through intensive work using a large geochemical data set that incorporates over 1000 ages and 2700 geochemical measurements, Gomez-Tuena et al. (2007) has developed the first digital geologic information system of the whole TMVB (Figure 2.6). In general, the magmatism in the Jalisco block shows a complex age and composition distribution. Important observations are:

- A current trend of younger magmatism towards the trench.
- The Colima Volcano is closer to the trench than the trend of the TMVB.
- The occurrence of calc-alkaline volcanoes close to intraplate type alkaline basalts similar to ocean island basalt (Luhr, 1997; Ferrari et al., 2003)
- Recent magmatism trending in the northwest direction popular as the Jalisco Volcanic Lineament (Bandy et al, 2001)

The geochemical, structural, thermal, and seismic data has led to different models to explain the complex geology in the region. Ferrari et al (2001) proposed a tear between the Cocos and Rivera plate provides a way for asthenosphere mantle to flow into the mantle wedge of the Rivera plate and eventually cause slab steepening. This model is also able to explain the location of Colima Volcano closer to the trench, a trend of younger magmatism toward the trench due to the slab steepening and the finding of calc-alkaline volcanoes close to intraplate type alkaline basalts. In a later study, Ferrari (2004) proposed that lateral propagation of a slab detachment that was initiated in the southern Gulf of California (Figure 2.7) crossed the entire TMVB beginning about 12 Ma. The model was based on an observation that an eastward migrating pulse of mafic magmatism has crossed Mexico from west to east for the past 12 to 6 Ma. The tearing of the slab that

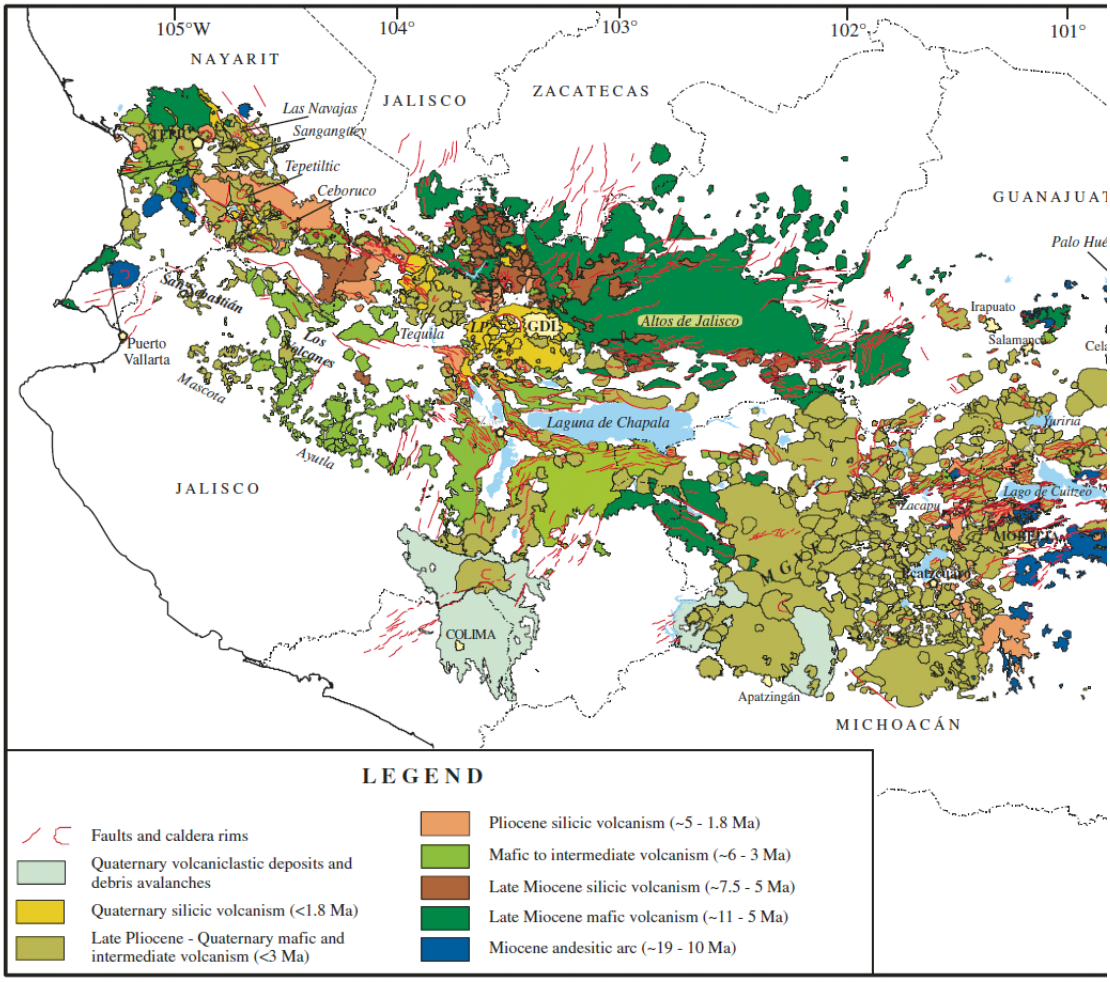

Figure 2.7. Simplified geologic map showing magmatic activity of the Trans-Mexican Volcanic (image taken from Gomez-Tuena et al., 2007) GDL—Guadalajara; Zac—Zacoalco; MGVF—Michoacán-Guanajuato volcanic fi eld; NT—Nevado de Toluca; LP—La Primavera; Izta—Iztaccíhuatl; Popo—Popocatépetl ; Pico—Pico de Orizaba; Cu—Las Cumbres; Cofre—Cofre de Perote.

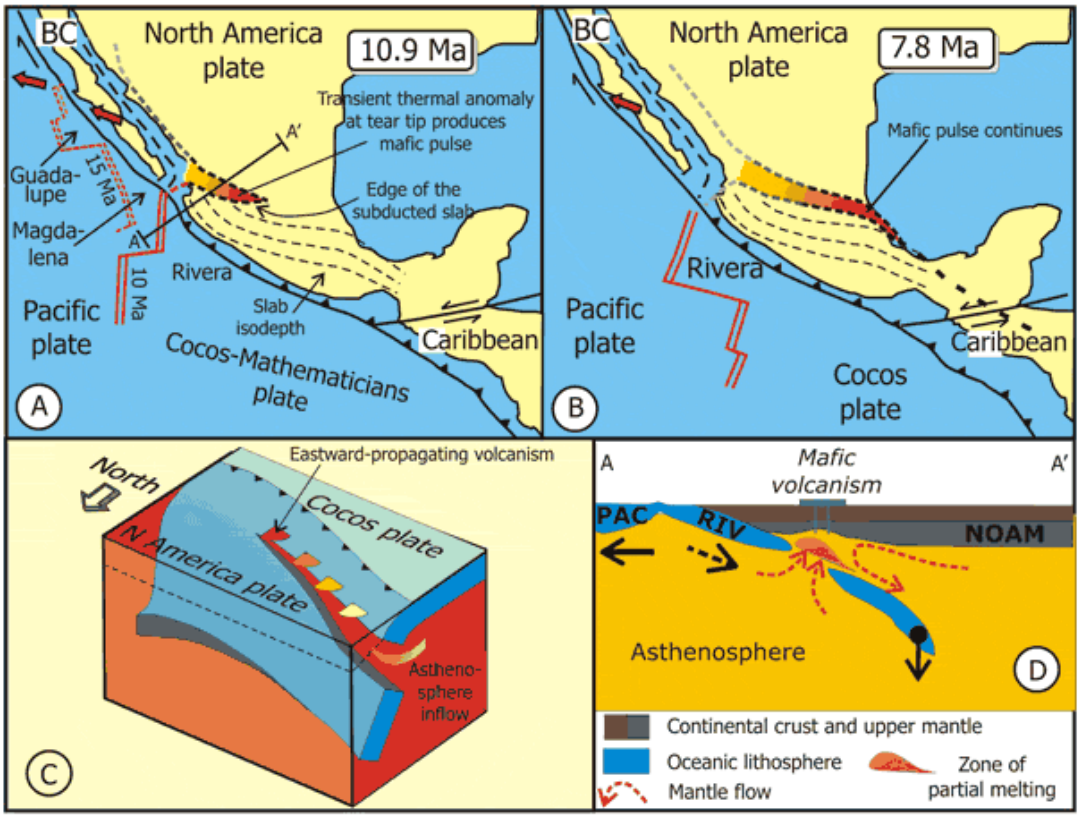

Figure 2.8. Late Miocene tectonic setting of the Mexican subduction zone at 10.9 and 7.8 Ma with proposed location of a slab detachment after Ferrari (2004). Line AA' in A indicates location of cross section in D. Figure 2.7C shows a three-dimensional block diagram showing the proposed lateral propagation of a detachment and resulting migrating volcanism induced by upwelling, hot, sub-slab asthenosphere (modified after Worrel & Spakman, 2000). Figure 2.7D shows a schematic cross section of following slab detachment and the consequences in western Mexico. Mafic volcanism on the North American plate (NOAM) resulted from thermal melting of the mantle wedge previously modified by subduction. RIV=Rivera plate; PAC=Pacific plate.

maybe related to the end of convergence of the Magdalena plate, then caused roll the slab to steepen with an influx of deep mantle in the mantle wedge. The model can explain the complex magmatic pattern by variations in the mode of subduction of the Rivera and Cocos plates.

Several other ideas have been proposed to explain the tectonic and magmatic evolution of the region from the late Miocene to the present. One of them is proposed by Moore et al (1994) and later expanded by Marquez et al (1999). The unusual tectonics and volcanism in the region were proposed to be mainly caused by the interaction of a mantle plume with the overriding plate. Marquez (1999) proposed that the mantle plume broke the existed subduction plate from the bottom, however, the plate at a later time dominated and pushed the plume. Both Moore and Marquez models used geochemistry data only and have difficulty explaining the geology and tectonics of the TMVB well, such as : there is no regional uplift usually observed when a plume arrives beneath the litshophere, and neither the rifting nor the OIBs present the age progression required by the plume model (Ferrari and Rosas, 1999).

Using petrologic and geochemical data and supported by the observation of less seismicity beneath the arc, Verma (2002) argued that the complex magmatism in the TMVB is not caused by subduction at all but is related to continental rifting. They proposed that the source of complex magmatism in the TMVB may be generated by partial melting during the ongoing rifting.

Luhr et al (1985) proposed that the Jalisco block is being transferred from North America to the Pacific plate as Baja California did in the past. According to this model, the Colima rift would therefore represent an extension of the East Pacific Rise under the

continent. This model also explains the presence of volcanism as a result of crustal extension within the forearc region (Wallace et al., 1992; Righter et al, 1995) and might be related to a separation of the Jalisco block from the rest of the North American plate.

Beyond the controversies associated with broad tectonic models of Southwestern Mexico, there are also specific questions related to the region that need to be answered. For example, it is not known exactly where the boundary between the Rivera-Cocos plates is and what the relationship is between the Colima rift and Colima Volcano to this boundary. Another question is why is Colima Volcano located closer to the trench compared to others volcanoes along the Trans Mexican Volcanic belt? Previous studies of gravity, seismicity and sea floor morphology of the Rivera-Cocos plate suggest that the subducted part of this boundary lies directly beneath and is oriented parallel to the Southern Colima rift. Thus, the Southern Colima rift likely formed in response to divergence between the subducting Rivera-Cocos plates due to direct coupling between these two plates and the overriding North American plate. Surface exposures of Cretaceous granitoids and associated thermal springs and shallow- focus earthquakes are characteristics that can be explained by thermal convection induced in the upper mantle by divergence of the subducting Rivera and Cocos plates. To test this idea it is necessary to have a good image of the geometry of the Rivera and Cocos plates at depth but currently images of the subsurface are not accurate enough to know the plate locations. The complex magmatism in space, time, and chemical composition has been explained by different models, as discussed above, but in many cases these models can only be tested by examining seismic images of the subsurface that are still not available.

Seismic experiment

To attempt to answer the questions posed above as well as to provide constraints on some of the broad tectonic models of the Rivera Subduction zone and Jalisco Block, 50 broadband seismometers were deployed in the states of Jalisco, Michoacan and Colima for a year and a half beginning in January, 2006. The stations consisted of STS2, 3T and ESP broadband sensors with new PASSCAL data acquisition systems equipped with GPS clocks and external links. The Mapping the Rivera Subduction zone (MARS) array spans most of the Jalisco block and the western Michoacán block to the east. Figure 2.8 shows the locations of the stations. The array had 35-50 km spacing between stations which provides good data coverage for micro earthquake studies and seismic tomography. Each station has one data stream that continuously recorded 24-bit data at 40 samples per second. Eighteen months of data gave good azimuthal coverage of teleseismic and regional events for our imaging studies (Figure 2.9).

The MARS experiment involved two U.S. institutions, the University of Texas at Austin and New Mexico State University, and was in collaboration with Mexican colleagues at the Centro de Geociencias, UNAM and the Volcanic Observatory at the Universidad de Colima. In addition, data collected by the CODEX (Colima Volcano Deep Seismic Experiment) experiment [Gardine et al., 2007], a seismic deployment of short period seismometers focused on Colima volcano, were also used in my studies. The two arrays overlapped in time for five months. In this thesis, I use data from the MARS and CODEX seismic deployments to accomplish the following objectives.

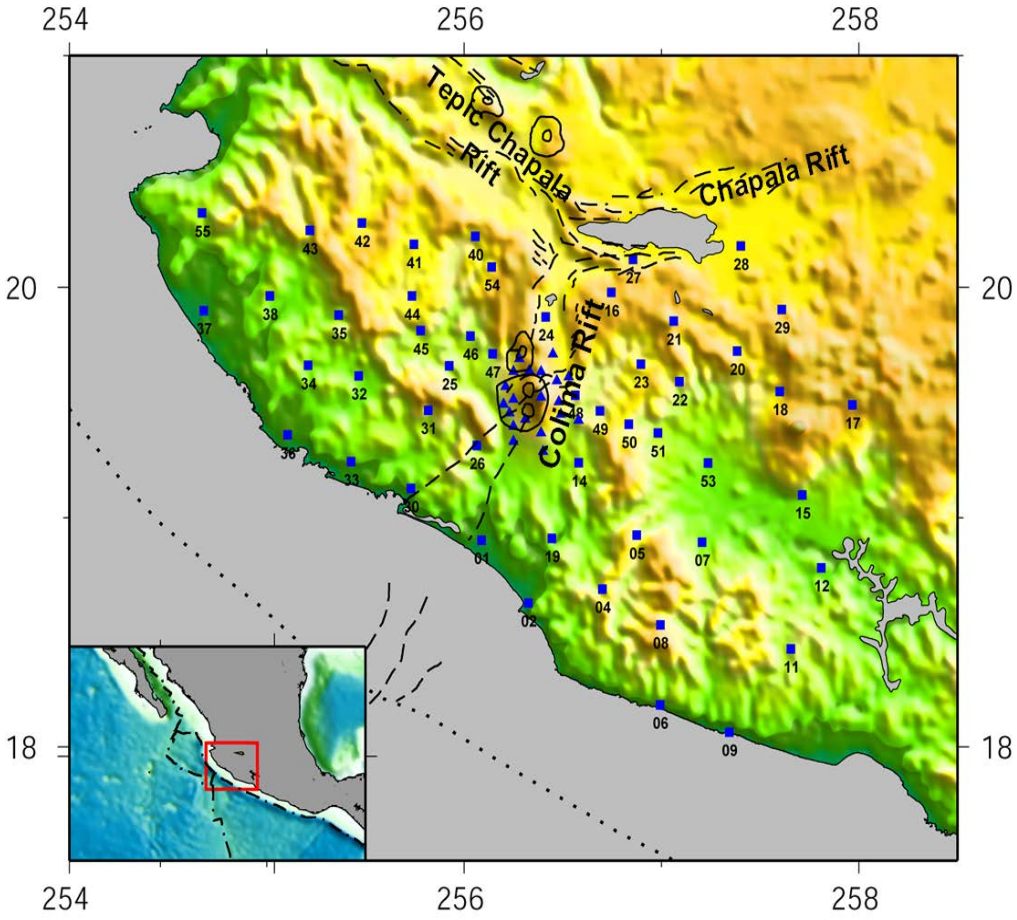

Figure 2.9. Seismic stations deployed in the MARS experiment. Rectangles show MARS broadband stations and triangles show short period seismometers installed by collaborators from the University of Alaska (CODEX) at the same time as the MARS deployment.

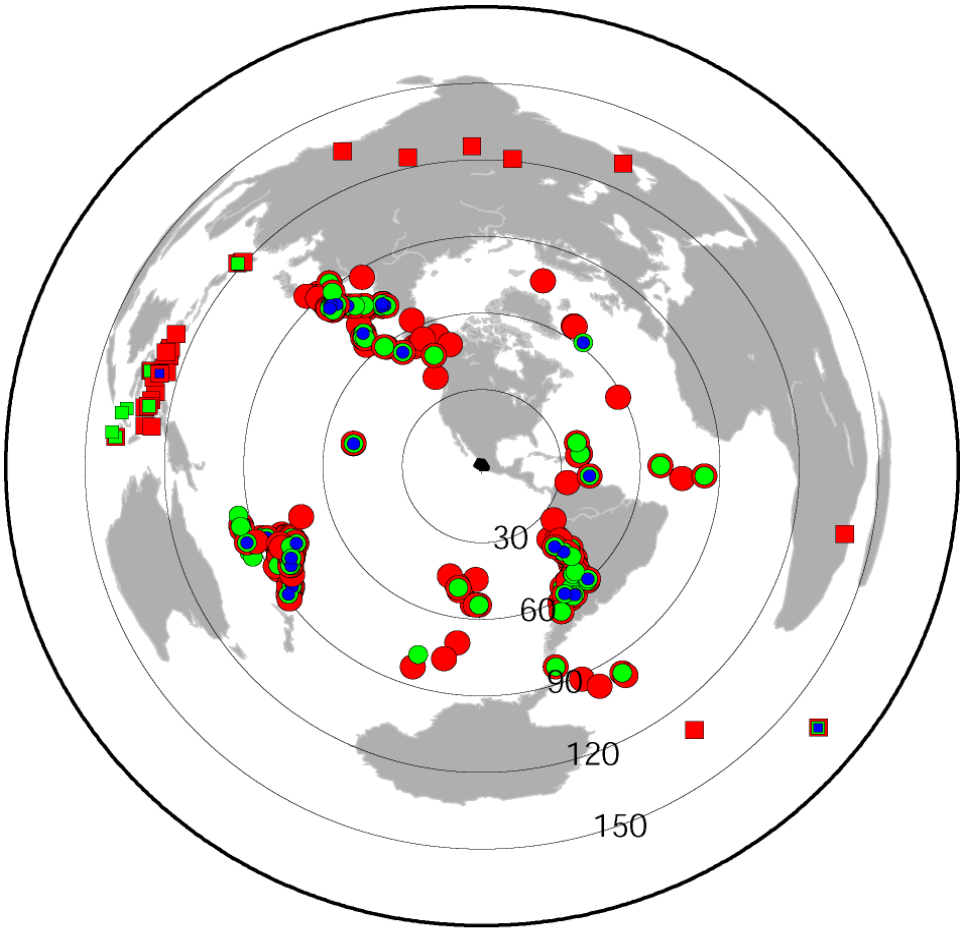

Figure 2.10. Seismicity with earthquake magnitudes larger than 5.4 that occurred during the deployment of the MARS array. The map is centered on the Jalisco region.

1. Accurately locating microseisms in the Wadati-Benioff zone during the deployment, that better defines the geometry of the subducting Rivera and Cocos slabs.

2. Using seismic tomography, I developed a seismic image of the subducting Rivera plate, the western edge of the Cocos plate and the surrounding mantle and crust. A previous tomography study used a finite frequency method limited to teleseismic data (Yang et al, 2009). Here I used three dimensional raytracing in tomography that allowed use of regional waves. The results provide a more detailed image of mantle wedge velocities as well as the geometry of the subducting Rivera and Cocos plates.

3. Using converted Ps waves, I investigated the crustal structure of Southwestern Mexico. Near the coast, this study provided constraints on the subducting plate interface. Inland, I have mapped crustal thickness with more detail than previous studies have provided.

Chapter 3: Lithosphere structure of Southwestern Mexico

Introduction

Southwestern Mexico is a tectonically complicated region, with a subduction zone on the southwestern boundary, volcanism in the overriding plate, and three extensional rifts including the Colima rift with a large volcano. As discussed in the previous chapter, there have been few studies of the crustal structure or detailed studies of the subduction zone. Knowledge of the lithosphere structure is important for understanding the tectonics of the region. Crustal thickness determination in extensional zones will place some constraints on the amount of extension that has occurred. Knowing the crustal structure in a region can also shed light on mantle properties by comparing predicted topography for a given crust thickness compared to observed topography. In a subduction zone, detailed seismic images can help constrain physical properties of the descending slab that can have important consequences for earthquake potential. Finally, a detailed crustal and mantle lithosphere seismic velocity model will improve earthquake locations which in turn are our primary tool for determining the geometry of the subducting plate.

In this chapter I use receiver functions to develop a velocity model of southwestern Mexico using MARS data as well as 3 stations of the Mexican national network. The results of the modeling show the overriding plate Moho and the subducting slab interface. I am also able to estimate the Poisson ratio of crust using receiver functions. Crustal structure can be obtained using several methods. In seismic studies, detailed velocity versus depth can be determined using controlled source seismic refraction/wide angle reflection methods. However, this approach is expensive and

usually limited in spatial coverage. Alternatively, the Receiver Function method (RF method) uses passive seismic recording to determine crustal structure. Using temporarily deployed broadband stations and teleseismic earthquakes, the crustal structure can be determined over a broad region at a reasonable cost. The method is based upon identifying P waves that have been converted to S waves at interfaces beneath a seismic station (Figure 3.1). In principle, a crustal model can be determined using a single passive seismometer and when arrays of stations are available, migration techniques can be employed to produce a true 3D structure. Bostock (2006) used the RF technique to image a dipping subducting slab as well as the continental Moho beneath Oregon in the Cascadia subduction zone, a region with many similarities to Southwestern Mexico.

The early work on the Receiver Function method had an ambiguity in determining the depth of interfaces due to the dependence on velocity in the crust. Very often the velocity is estimated using other methods such as seismic tomography, well log data, or surface waves. In this study, the ambiguity of crustal depth estimates is addressed by using the times of multiple reflected waves. The final products of this study are depth to the Moho, the Vp/Vs ratio of the crust which is sensitive to the chemical composition of the crust as well as the melt content, and reflectivity within the crust and lithosphere. I compare our results with previous crustal studies from gravity and seismicity which have been discussed in the previous chapter.

The aim of this study is to reveal the crustal structure for both continental and oceanic crust of the Rivera and Cocos plates. A detailed knowledge of crustal structure can help us understand the dynamic link between the tectonics of the over-riding plate and the evolution of the down-going Rivera slab. Bandy (1999) suggests that the density

of the upper part of the subducting lithosphere increases at a depth of ~30 km, perhaps reflecting a phase transition of basalt to eclogite. In this study, I hope to find evidence of the basalt to eclogite transition and its relationship with the oceanic crust subduction process and continental crust.

Method

The teleseismic receiver function represents the reflectivity of crust and mantle beneath a seismic station. In particular, it shows the location in either time or depth of any strong, sharp shear velocity contrasts in the subsurface such as the Moho discontinuity, close to a recording station The technique is based on the fact that when a P wave encounters a boundary separating layers of rock with different S wave velocities, an S wave is created at the boundary (Figure 3.1). The S wave created at the boundary arrives at a seismic station following the P wave since shear velocity is always less than P velocity in a given rock. It should also be noted that if the boundary is such that if the Vs velocity is higher below the boundary a positive pulse is produced but a negative pulse is produced by a decrease in S velocity with depth. If one can separate the S waves following the P wave then one has information on the subsurface boundaries that created the S waves. To separate S waves from the P energy, one uses the fact that the S waves largely cause motion in the horizontal direction whereas the P waves primarily cause motion in the vertical direction (Figure 3.1). Thus the “receiver function” is calculated by removing or deconvolving the recorded vertical motion on a seismogram from the radial motion ideally resulting in a series of pulses that are converted wave arrivals. Details on the computation can be found in Langston (1977) and Owen et al. (1984).

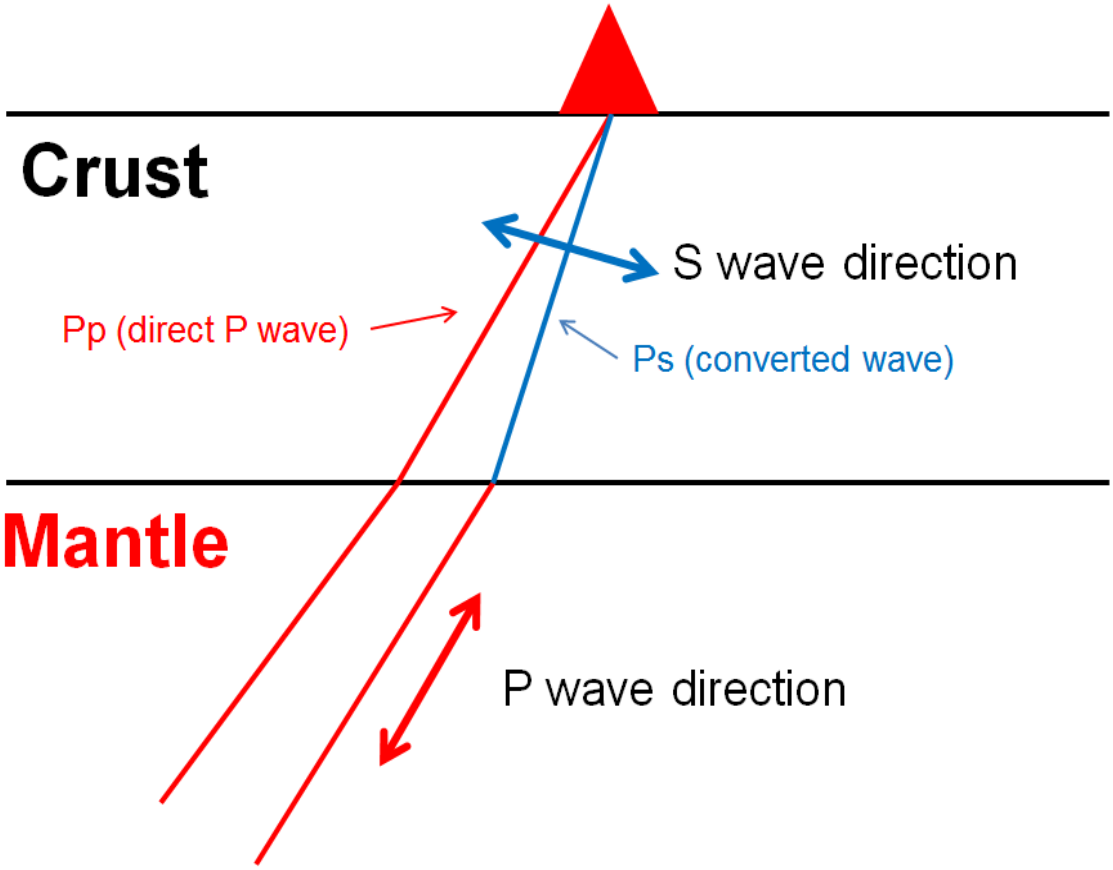

Figure 3.1. A simple illustration of the ray paths of a P wave and converted S wave from the Moho boundary arriving at a seismic station. The red line represents a P wave phase that refracts through the Moho boundary. The red line that transforms into the blue line represents the same P wave that partially changed into an S wave at the Moho. Note that the direction of P wave motion is largely vertical but the S wave has motion primarily in the horizontal direction at the surface.

Due to the sharp velocity contrast at the crust-mantle boundary, first order information about crustal structure under a station can be obtained by assuming the largest signal following the direct P wave in a receiver function comes from the Moho. The time difference between Ps converted waves and the P wave depends on the depth of the interface and also on the P and S wave velocities in the medium above the conversion depth. Thus, if a converted S wave is identified, the depth to the subsurface boundary can only be determined if one knows the P and S velocities of the crust and mantle beneath the station. Usually knowledge of the velocities is limited but approaches have been developed to overcome the tradeoffs between seismic velocities and depths. Two approaches were used to image the subsurface layering as discussed below.

Data Processing

The first step in Receiver Function data processing is to obtain a data catalog for earthquake sources that occurred during our station deployment. For this study, data from 100 earthquakes with magnitudes greater than 5.7 and epicentral distances between 30 to 100 degrees were collected. The locations of the hypocenters and the station locations are shown in Figure 3.2. Most of the good quality data come from Tonga, South America and the Aleutian islands. Next, I cut the seismic traces 20 seconds before the incoming P wave and 100 seconds after the P wave for the time window to be analyzed to ensure all converted phases to a depth of 100 km are included.

Next, the data was rotated into radial and tangential directions where the radial direction is parallel to the great circle from the event to the station. The vertical and radial

motion of the ground should record P-SV waves, respectively, for a radial symmetric Earth. Ideally receiver functions consist solely of converted SV energy to increase the converted wave signal amplitude, a rotation in the vertical plane can be made that transforms vertical and horizontal components into P-SV components that result in P motion on one component and S motion on the second component. A rotation into P-SV components theoretically will increase the amplitude of the Ps wave on the SV component. However, it depends on knowledge of the incidence angle which in turn depends on the near surface velocities. This procedure should also minimize the direct P wave amplitude on the SV component. The P-SV rotation did increase the amplitude of converted waves on the SV component, but there is still significant direct P energy on the SV component.

A signal to noise ratio check was done by comparing the power in the seismic traces 20 sec before and after the arrival time of the P wave. Only data with a signal to noise ratio higher than 2 for both the P and SV component data were used to ensure high quality data before deconvolution. Overall, the signal to noise ratio criteria removed about 35% of all collected traces. For example, at station MA35, Among 120 seismograms only 44 traces have signal to noise ratio lower than 2 and were removed.

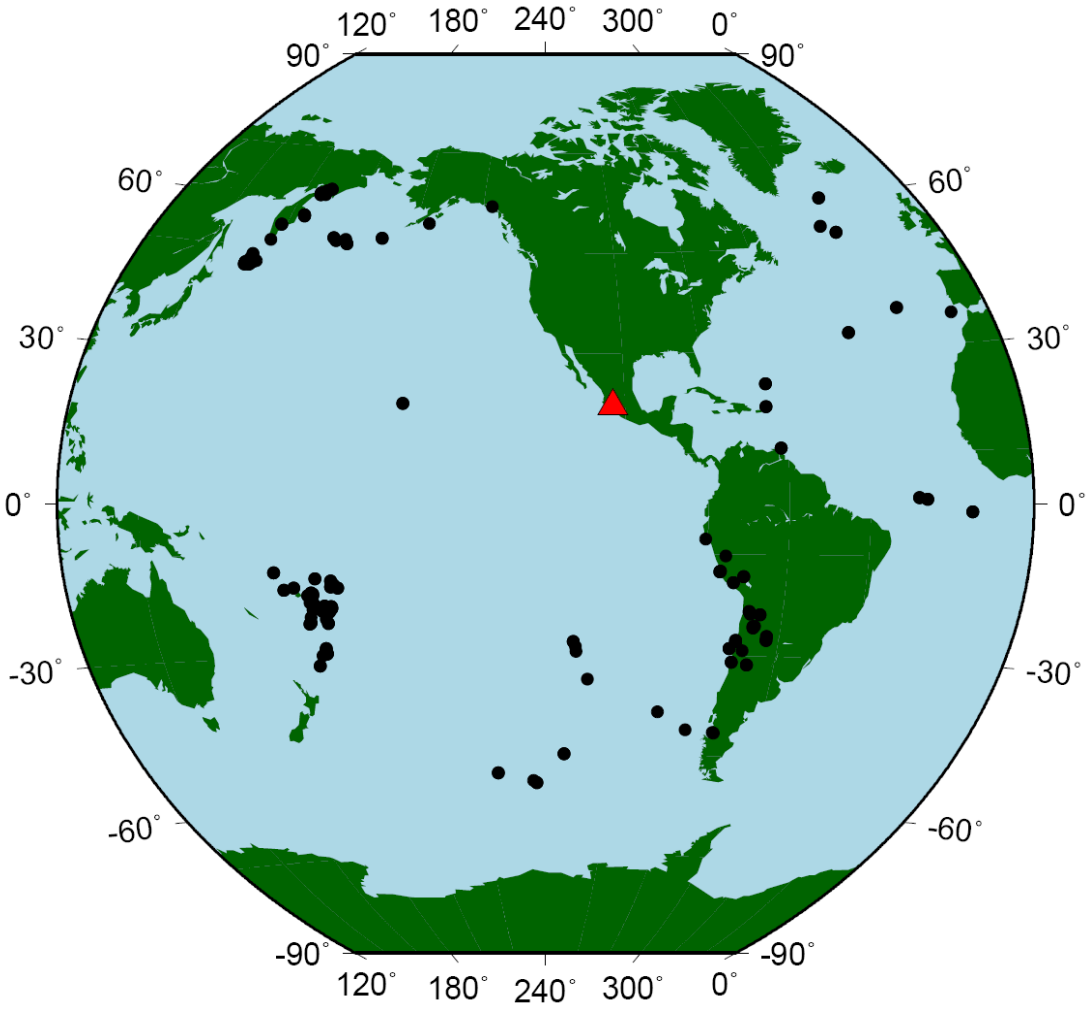

Figure 3.2. Distribution of earthquakes used for the teleseismic Receiver Function study. Red triangle show station locations. Black circles show earthquake epicenters.

An incoming P wave can have a very complicated shape due to the source time function of the source, near surface reverberations at the source, multipathing along the propagation path as well as the P wave multiples near the receiver. Each Ps converted wave should also have the same complicated shape as the incoming P wave. Thus, to isolate the Ps waves and convert them to simple pulses, the P component is deconvolved from the SV component.

The deconvolution was done in the frequency domain by using the water-level stabilization method and a low-pass Gaussian filter to remove high frequency noise (Langston, 1979). The RF equation in the frequency domain can be seen to be a simple division of the radial component by the vertical component (or the P and SV components respectively). The receiver function H(ω) is calculated as:

$$H(\omega) = \frac{R(\omega)Z^*(\omega)}{\max\{Z(\omega)Z^*(\omega), c\max\{Z(\omega)Z^*\}\}} G(\omega) \qquad \text{(eq. 3.1)}$$

$$G(\omega) = \exp\left(\frac{-\omega^2}{4\alpha^2}\right) \text{ ……(eq. 3.2)}$$

where, ω is angular frequency, Z(ω) is the fourier transform of the P-component waveform, R(ω) is the transform of the SV component, and Z*(ω) is the complex conjugate of Z(ω). G(ω) is a Guassian filter that has zero phase distortion and a lack of side-lobes [Langston, 1979]. It is added to eliminate high frequency noise in the RF. The frequency content of the Gaussian filter is controlled by the parameter α. Finally, the denominator of equation 3.1 is either $Z(\omega)Z^*(\omega)$ or a constant $c*\max\{Z(\omega)Z*(\omega)\}$ depending on which value is larger. This is necessary to account for holes in the spectra

of $Z(\omega)$ and therefore division by a small number which is inherently unstable. The constant c is called the "water level" and serves to stabilize the deconvolution. The values of α and c were chosen by trial and error where I tried to make the receiver function as "spiky" as possible with minimal noise.

All receiver functions were computed using equation 3.1 using a water-level parameter c of 0.001 and a Gaussian smoothing parameter α of 3.5. A final visual check was performed by examining all receiver functions. Good receiver functions are identified by having a sharp P wave signal with little energy arriving earlier. Low quality RF's tend to have anomalously high amplitude signals at later times or very wide side lobes. These data were eliminated before further analysis.

An example of receiver functions for station MA18, plotted as a function of epicentral distance, is shown in Figure 3.3. Many events are concentrated between epicentral distance 50^0 to 65^0 followed by events between epicentral distances between 80^0 and 90^0. Most receiver functions have similar signals with a peak at 0 second (the P wave) followed by negative side lobes, some of them show double negative side lobes and almost all RFs show a strong positive pulse at about 5 seconds. After 5 seconds, there is variability in the RFs but still some similarity is observable. Station MA18 is located far from the coast where a relatively flat Moho is expected. At this station, 35 clean RFs were collected and the clear arrival at about 5 sec is interpreted as the P- to S-wave conversion from the Moho. To improve our result for station MA18 a stack of all receiver functions in the depth domain was performed. Starting with a 1-D velocity model and horizontal slowness information, each RF can be interpolated into the depth domain to correct for move out and then stacked. This simple stacking procedure can reduce noise

and eliminates variations caused by 3-D structure, so that the summed response reflects the average structure. On the right side of Figure 3.3, a stacked RF in the depth domain shows high amplitude at 0 second followed by a strong positive amplitude at 39 km depth interpreted as an arrival from the Moho. Strong multiple signals are also clear at 150 km (at 16.3 s in time domain) and 180 km (at 22 s in time domain) which are likely PpPs and PsPs/PpSs multiples from the Moho but which could also be due to conversions from deeper discontinuities.

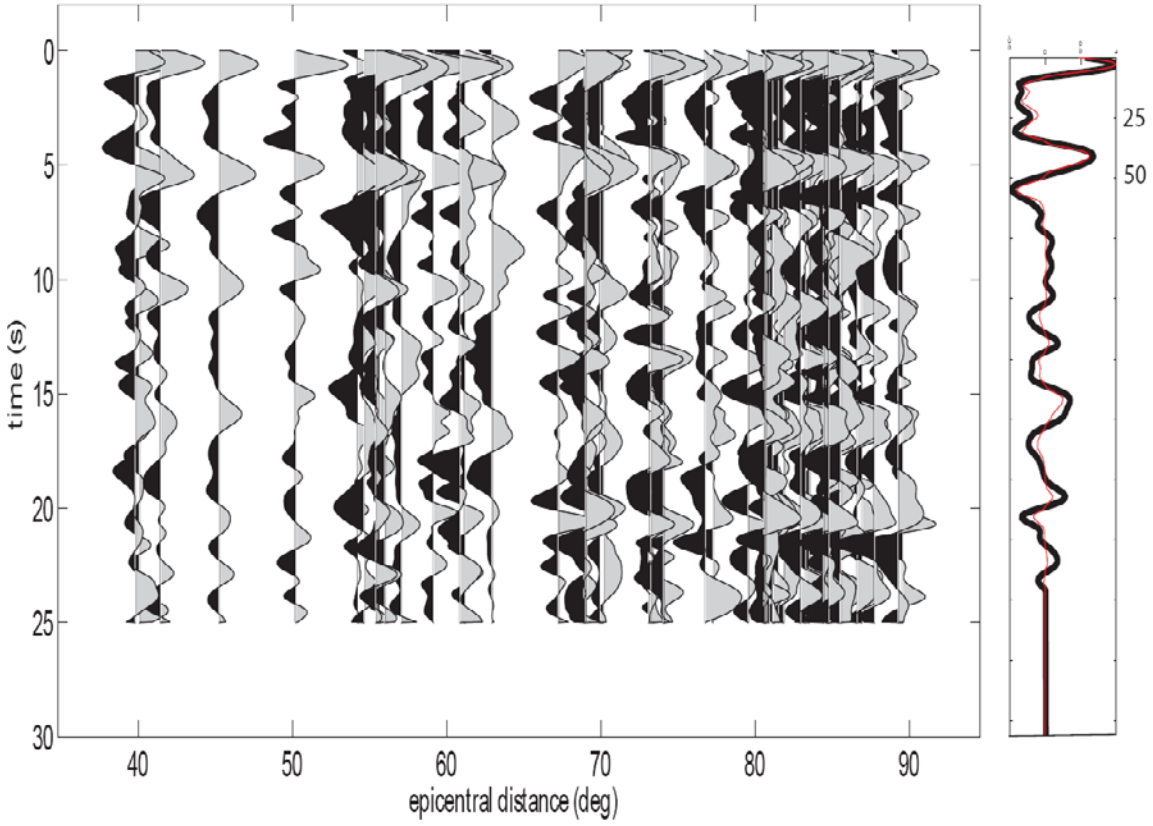

Figure 3.3. Receiver functions for station MA18 with time on the vertical axis and epicentral distance on the horizontal axis. On the right is a linear stack of the receiver functions in the depth domain using a 1-D velocity model to adjust for timing variations due to different incidence angles.

Receiver Function Imaging

Ideally receiver functions show pulses as a function of time that are due to converted P to S waves from interfaces in the subsurface beneath a seismic station. To convert those pulses to depths to interfaces beneath the station requires knowledge of the P and S velocities in the rocks above the interface. Without knowing the P and S speeds there is a tradeoff between depth and velocity in the interpretation of receiver functions. Zhu and Kanamori (2000) introduced a method (the H-K method) that can minimize the ambiguity due to the trade-off between depth and velocity. The idea of this method is that the time difference between the converted wave and direct P wave depends on the angle of incidence of the incoming P wave, the subsurface P and S velocities and the depth of the interface. The angle of incidence depends on the distance of the earthquake from the station. The timing of multiple reflected waves from the conversion depth also depends on incidence angle but differ in their dependence on depth of converter and velocity (Fig3.4). Assuming a flat layer and a uniform velocity model, the estimated arrival time for the Ps wave (Tps) can be derived as

$$T_{ps} = H\left(V_{s1}^{-2} - p^2\right)^{1/2} - H\left(V_{p1}^{-2} - p^2\right)^{1/2} \text{ ……..(eq. 3.3)}$$

and the arrival times of the multiples as

$$T_{PpPs} = H(V_{s1}^{-2} - p^2)^{1/2} + H\left(V_{p1}^{-2} - p^2\right)^{1/2} \text{ …….(eq. 3.4)}$$

$$T_{PpSs} = 2 * H\left(V_{s1}^{-2} - p^2\right)^{1/2} \text{ …….(eq. 3.5)}$$

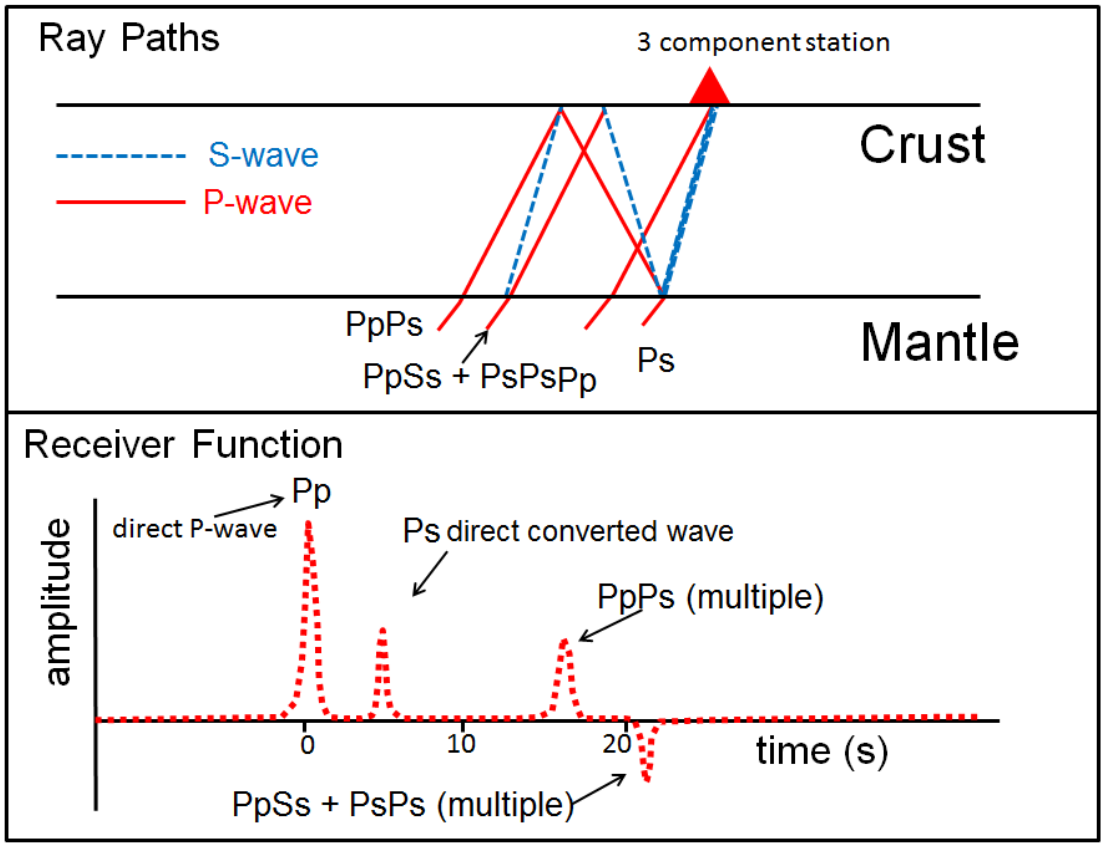

Figure 3.4. Upper figure is an illustration of ray paths for a converted P to S wave from an interface as well as multiple reflections within the layer. Pp is the direct P wave, Ps is a P wave that converted into an S wave, PpPs is a P wave that reflected from the surface and then converted into a reflected S wave when encountering the Moho. PpSs is a P wave that reflected from the surface as an S wave and reflected up as an S wave. Finally, PsPs is a P wave that transforms into an S wave at the interface, transforms back to P wave at the surface and reflects up as an S wave. For flat structure, PpSs and PsPs arrive at the same time and both have negative polarity relative to other phases. The lower figure shows an idealized receiver function for this case. The direct P wave comes at zero time with the highest amplitude followed by the Ps wave with much lower amplitude. The PpPs multiple comes later followed by the PpSs+PsPs waves with negative polarity. As an example, a 38 km crust thickness with Vp/Vs ratio 1.81 will have a Ps wave at about 5 seconds, followed by PpPs wave at about 15 seconds and PpSs + PsPs at about 20 seconds.

where Tps is the arrival time of the Ps wave, TPpPs and TPpSs are the arrival times for multiples (see Figure 3.4 for an illustration of the raypaths), H is the crustal thickness, Vs is the crustal S wave velocity, Vp is the crustal P wave velocity, and p is the ray parameter.

The arrival times of the multiples differ in their dependence on velocity and interface depth from the direct converted wave. The H-K method adds the receiver function amplitudes from multiple distances and azimuths (therefore different p values) recorded by a common receiver at the times predicted for a given Moho depth and Vp/Vs velocity ratio at the appropriate ray parameter using the formulas 3.3-3.5. When the correct depths and velocities are used, the summation should be large as one would be summing receiver function peaks associated with the converted direct arrival and its multiples. If the wrong model parameters are used, some peaks of arrivals will be missed and the summation will be smaller. Figure 3.5 illustrates the different moveouts of the multiples relative to the primary Ps arrival as a function of distance or incidence angle. Thus the summation with the largest overall amplitude (summed over time for the primary and multiple waves) should correspond to the correct Moho depth and Vp/Vs ratio. Essentially the method is a grid search of all possible combinations of crustal thickness and Vp/Vs ratio.

The H-K method stacks all receiver function amplitudes at one station including the Ps converted wave and its two multiples (Figure 3.4). The direct Ps converted wave has the largest amplitude and is the least sensitive to dips in the crust-mantle boundary thus the Ps converted wave is often given heavier weight in the stacking process. The stacking can be written as:

$$S(H,K) = \sum w_1 r(t_1) + w_2 r(t_2) - w_3 r(t_3) \quad \text{.....(eq. 3.6)}$$

where, H is crustal thickness, K is Vp/Vs ratio, $r_i(t)$ is the i^{th} receiver function at times t_1, t_2, and t_3 which are the predicted times for T_{Ps}, T_{PpPs} and $T_{PsSs+PsPs}$. During the stacking process, the weighting w_i was adjusted to be 0.5, 0.3, and 0.2. for w_1, w_2, and w_3 respectively. Note that higher weighting is put on the Ps mode that has the largest signal and less weight is put on the multiples. Originally, Zhu and Kanamori (2000) used 0.7, 0.2 and 0.1 for the weighting in their method. I tried several weighting schemes and found a slightly better result with the weights given above. However, overall, a significant change in results was not detected if using different weighting schemes.

The H-K method has several benefits such as fast computation time and the fact that it is unnecessary to pick arrival times. However this method also has a disadvantage in that the theoretical arrival times for the converted waves assumes a single flat layer. For a dipping layer, such as might be expected in a subduction zone, the arrival times of the converted phases will come a little bit later or earlier than for a flat layer depending on the ray direction and thus this method will fail. Another possible problem is that if there are multiple layers above the Moho, such as a layer of sediment that has a large impedance contrast with the basement, then its multiple reflections may interfere with the Moho signal. In this study, the use of the H-K method was limited to stations inland far from the trench since the stations located close to the trench show evidence for a dipping layer that is likely the subducting oceanic crust.

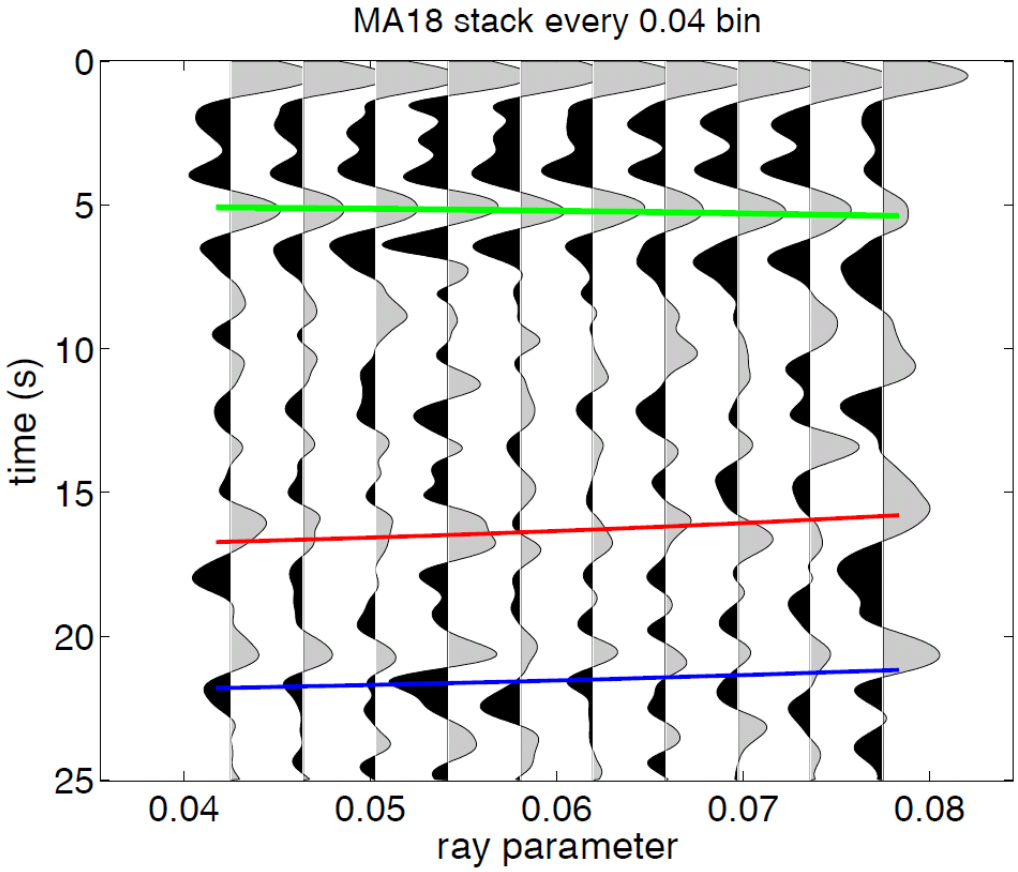

Figure 3.5. Receiver function traces that have been binned with respect to ray parameter on the horizontal axis at station MA18. The Ps, PpPs, and PpSs arrivals are represented with green, red and blue color line respectively. Note the change in relative times of the three arrivals as a function of ray parameter. The green line is the predicted Ps time assuming a crustal thickness of 39.2 km and a Vp/Vs ratio of 1.82 using eq 3.3. Similarly, the red line is predicted time for PpPs and the blue line is predicted PpSs using equations 3.4 and 3.5 respectively.

Crustal thickness and Vp/Vs ratio of the crust beneath Southwestern Mexico were analyzed using the H-K stacking method described above. The boundary for the grid search was set at 20 to 45 km for Moho depth and 1.65 to 1.90 for Vp/Vs ratio. Figure 3.6, illustrates the results for station MA18, which had 35 high quality receiver functions. I contoured the value of the stacked receiver functions as a function of Moho depth and Vp/Vs ratio with the highest value being the likely true parameters. The contour plot shows a clear maximum with a realistic crustal thickness (39.2 km) and crustal Vp/Vs ratio of 1.82. The predicted Moho Ps arrival times, which are obtained by plugging the estimated crustal thickness and Vp/Vs ratio into equation 3.3, agree with the receiver function signal showing a strong positive converted wave at 5 s. Predicted times for the multiples are also plotted (shown on Figure 3.5). The contour of amplitude summation, enable one to calculate uncertainties by measuring the flatness at the maximum point. I take the 0.95 contour as an estimate for uncertainties. For station MA18, a plus or minus 0.7 km is obtained for Moho depth and a plus or minus 0.02 for the Vp/Vs ratio.

Most stations in this study, especially the inland stations, have clear peaks in the stack contour plots indicating well resolved crustal thicknesses and Vp/Vs ratios. However, some stations show unrealistic results such as incoherent crustal thickness results with neighboring stations, no clear peaks in the contour plot, a very shallow crustal thickness or a very high/low Vp/Vs ratio. Two reasons can be identified for the weakness of the H-K method. A significant layer of sediments that create multiples and interferes with Moho signals and its multiple or a dipping crustal horizon that changes the arrival time for the Ps wave and its multiples as a function of azimuth are examples of problems associated with the H-K method.

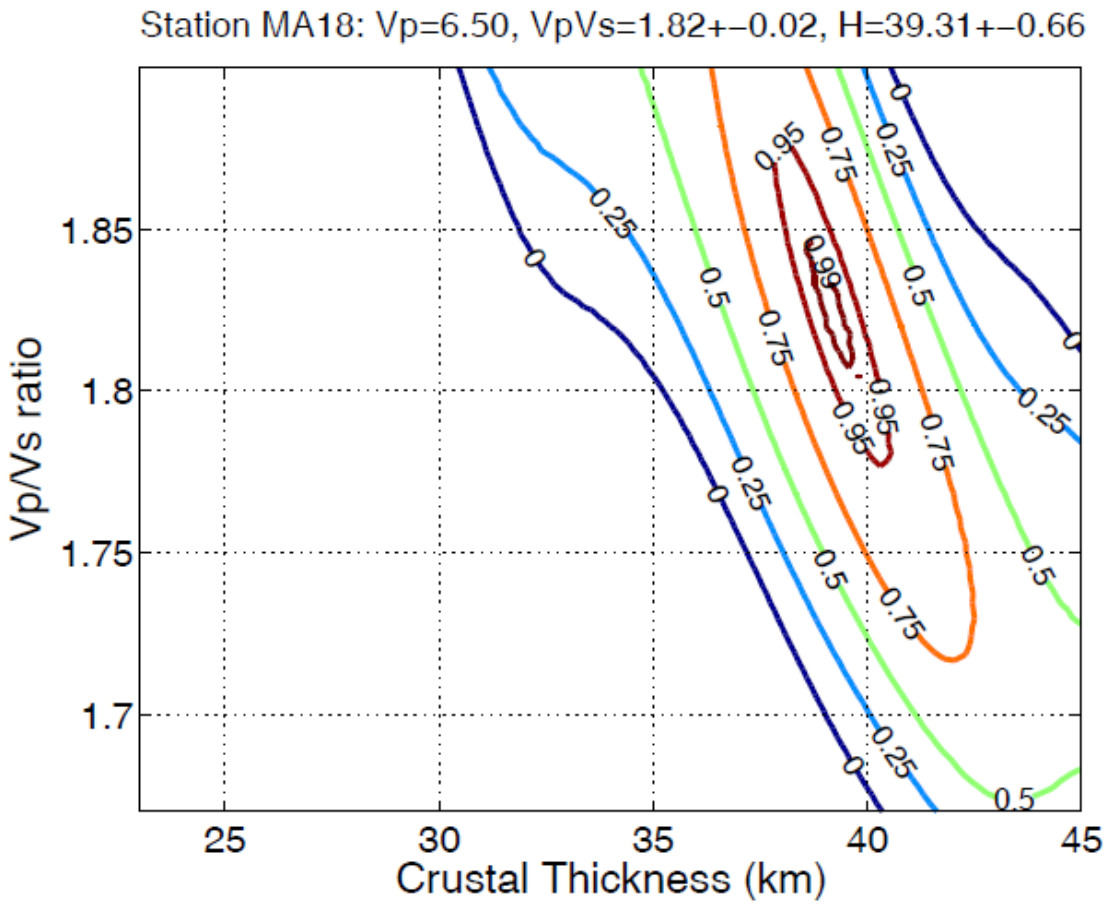

Figure 3.6. Contour of stack amplitudes for station MA18 as a function of crustal thickness H and Vp/Vs ratio. The grid search calculates a stack amplitude of receiver functions for the ranges of possible crustal thickness (20-50 km) and Vp/Vs ratio (1.65-2.). The final result is taken by choosing the highest amplitude from the contour and uncertainty is calculated by measuring the flatness of the contour peak

Results

The H-K method was applied to all data collected by the MARS array as well as three stations from the Mexican National Network. The receiver functions for each station as well as the H-K grid search contours are shown in Appendix A. Altogether, 24 reliable Vp/Vs ratio measurements and 47 reliable crustal thickness measurements were obtained. The contour plots using the H-K method show strong peaks and thus good resolution for most inland stations far from the coast but poorer results for stations closer to the coast. This is not surprising as it is likely there are strongly dipping structures near the coast where the subducting plate is near the surface. For the coastal stations the peaks in the H-K contour plots are not sharp and just taking the maximum value from the plots results in unrealistic values for Moho depth and Vp/Vs ratio. For the coastal stations where the H-K method failed I used a velocity model with a Vp/Vs ratio of 1.78, the global crustal average according to Chevrot and van der Hilst (2000), to stack receiver functions in the depth domain. The peak in the stacks was then measured to give an estimate of crustal thickness. Near the coast the first peak in the receiver functions is usually a negative pulse indicating a drop in velocity with depth. This has been observed in other subduction zones and has been interpreted as over pressured oceanic basalt crust. Thus, I picked these negative peaks as the Moho. This is discussed further below.

The results of the receiver function analysis are shown in Figure 3.7 and 3.8. In Figure 3.7, point measurements of crustal thickness are interpolated and plotted in map view.

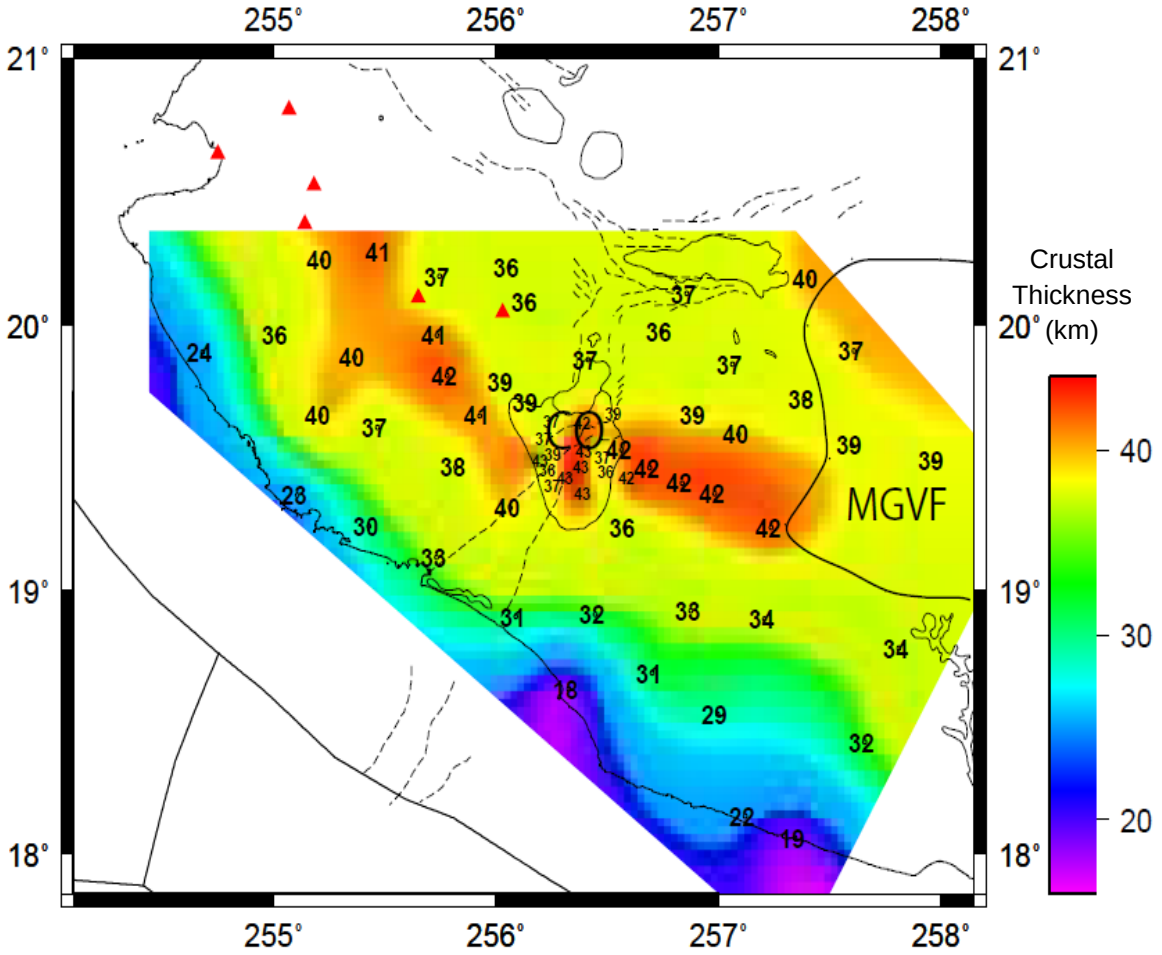

Figure 3.7. An interpolation of crustal thickness measurements using the H-K method. The measured crustal thickness beneath individual stations is also given with units of kms. Crustal thickness varies between 18~ km on the coast and 43 km in land. CO is Colima Volcano and MGVF is an active volcano field known as Michoacán-Guanajuato Volcanic Field

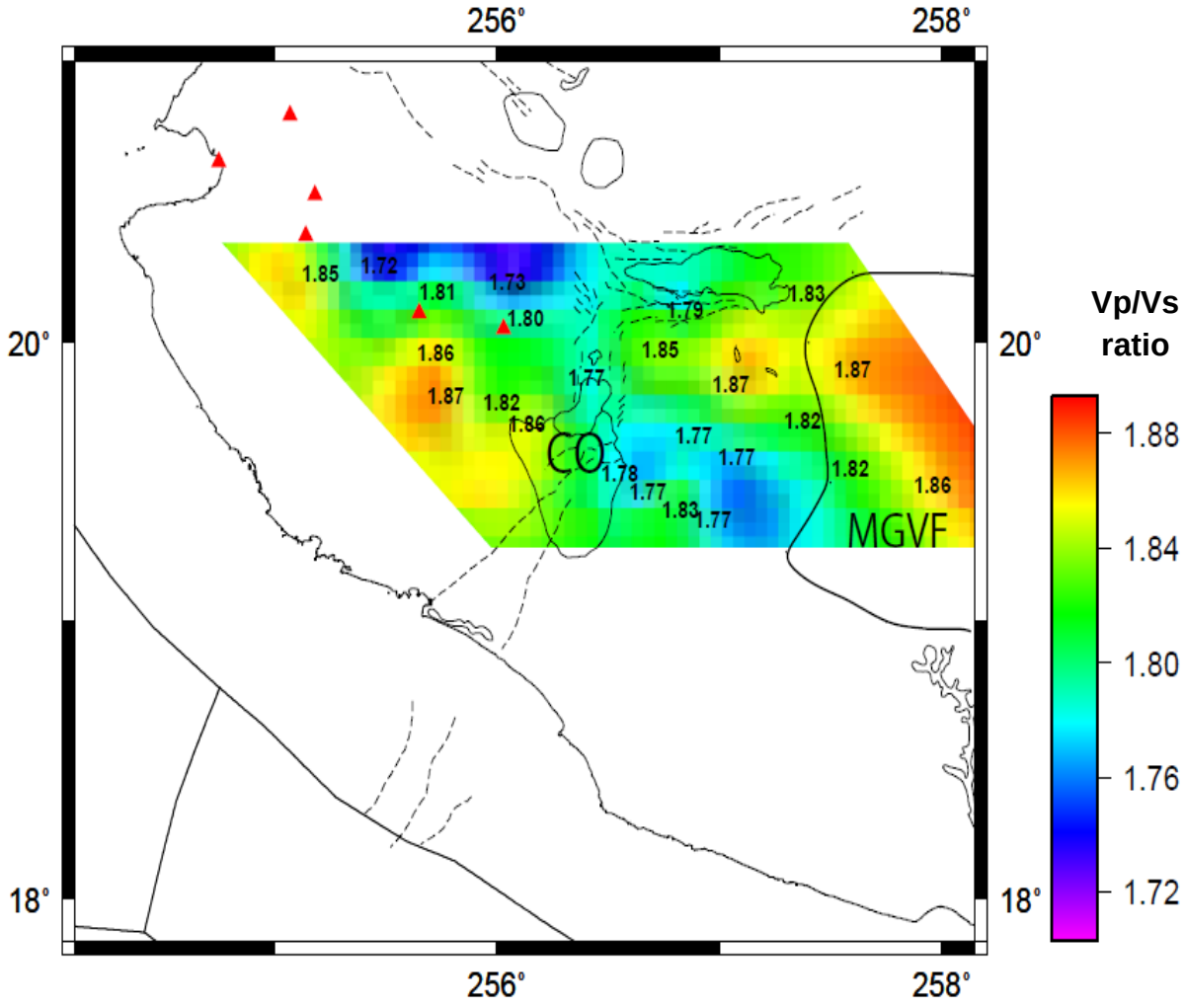

Figure 3.8. An interpolated map of Vp/Vs ratio of the crust as well as the individual measurements. The Colima and Tepic-Zacoalco Rifts are shown as dashed lines. Young volcanoes along the Jalisco Volcanic Lineament are shown as red triangles. CO is Colima Volcano and MGVF is an active volcano field known as Michoacán-Guanajuato volcanic Field.

Figure 3.8 shows the interpolated Vp/Vs ratio in the region where I was able to make reliable measurements. Crustal thickness varies from 20 km along the coast to a maximum of 42 km inland. There is a difference in crustal structure between the Jalisco block to the northwest and Michoacan to the southeast. Beneath the Jalisco block, which is underthrust by the Rivera plate, the crust is 25-30 km thick along the coast and increases to 40 km thick 50 km from the coast. To the southeast of the Colima Rift, however, the crustal thickness along the coast is 20-25 km thick and gradually thickens inland reaching 40 km more than 100 km from the coast. In Figure. 3.9, I plot the crustal thickness estimates at each station on a map of topography. Note that there is not a good correlation between crustal thickness and topography (Figure. 3.10 shows the correlation). While the thickest crust is roughly in the middle of the study region, perpendicular to the strike of the subduction zone, the topography is subdued there. Further inland, the topography increases to near 2 km yet the crust actually thins to 37-39 km thick. This indicates the high topography is due to buoyant mantle which agrees with a model of slab rollback and perhaps tearing as proposed by Ferrari (2004) and Yang et al. (2009). In this model hot asthenospheric mantle fills the space previously occupied by slab to relatively shallow depths providing a source of buoyancy in the mantle beneath the high topography. If this interpretation is correct then the high topography would be relatively recent i.e. at the time of the roll back estimated to be during the last 5 Ma (Ferrari, 2004).

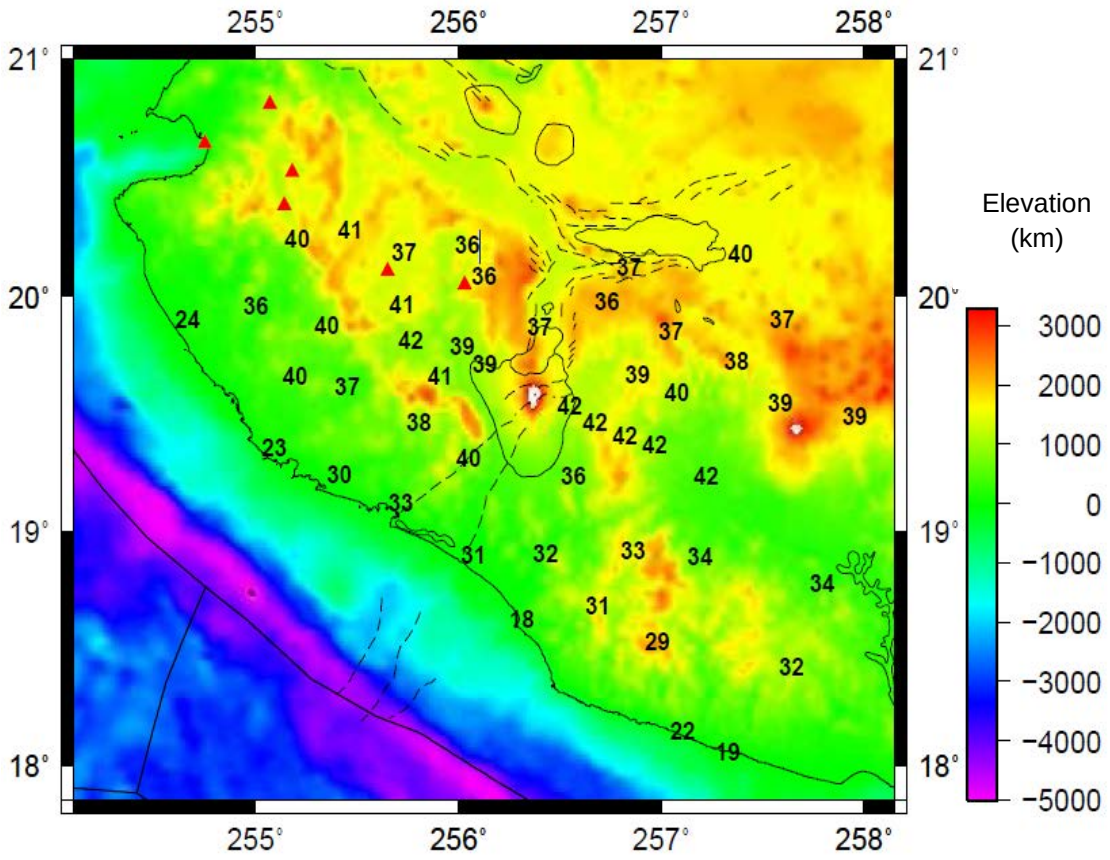

Figure 3.9. Crustal thickness measurement and topography background. Topography data were taken from National Oceanic and Atmospheric Administration website (www.noaa.gov).

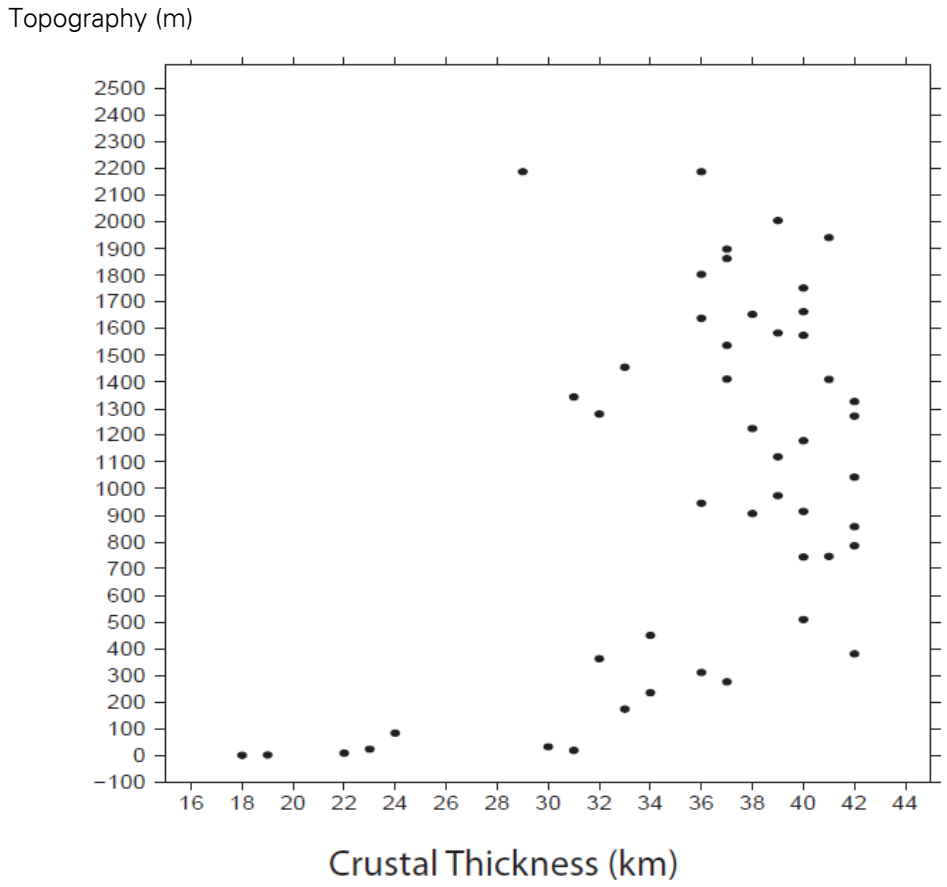

Figure 3.10. Plot of crustal thickness, calculated from receiver function technique on the horizontal axis versus topography, measured at every station on the vertical axis.

Another interesting aspect of the crustal thickness map is the lack of crustal thinning in the Colima Rift (Figure. 3.7). The station density at the Rift is sparse but stations close to the Rift such as MA26 and MA24 do not show thinner crust than stations outside the Rift. I conclude that there has been very little extension in the Rift. This agrees with the conclusion of Rosas-Elguera (1996) that the southern Colima Rift is actually a broad slowly extending (< 1mm/yr) zone that has been active only since the late Pliocene. I do see a trend to the north of thinning crust from 40-42 km thick to 36-37 km thick but our deployment did not reach the surface manifestation of the Tepic-Zoacala Rift so it is difficult to place constraints on the overall extension across that Rift.

The average Vp/Vs ratio of the crust in this study is 1.81 (Figure 3.7) which is slightly higher than the global average of 1.78 (Christensen, 1996; Chevrot and van der Hilst, 2000). However, there is a large range in values, from 1.72 to 1.87. Two regions have abnormally high crustal Vp/Vs ratios. The first region is located in the central part of the Jalisco block, close to the volcanoes shown as red triangles in Figure. 3.8. Four stations located at the southwestern edge of the region where I have data have Vp/Vs rations of 1.85 or greater. To the north of these stations, the Vp/Vs ratio is closer to normal. The second region, located to the northeast of Colima Volcano, shows a band of high Vp/Vs ratios ranging from 1.85 to 1.87. The eastern part of this band is within the Michoacan-Guanajuato Volcanic Field (MGVF), a wide region of volcanic activity that began about 2.8 Ma and continues today (Gomez-Tuena et al., 2007). The band of high Vp/Vs crust extends further west than the MGVF, towards the northern Colima Rift. Bandy et al. (1995) located the Rivera-Cocos boundary at depth beneath this region based on the occurrence of thermal springs and shallow seismicity.

Average crustal Vp/Vs can be used to constrain the petrology and physical state of the crust. Christensen (1996) showed from laboratory experiments that Vp/Vs ratio does not vary much with changes in temperature and pressure for pressures greater than 100-200 Mpa. The factors that controls the Vp/Vs ratio in the crust is the presence of melting or fluids and the mineralogy. The relative abundance of quartz and plagioclase feldspar has a dominant effect on Vp/Vs (Christensen, 1996): for felsic quartz-rich rocks such as granite, Vp/Vs is 1.71; intermediate rocks have a Vp/Vs ratio of near 1.78 and mafic plagioclase-rich rocks such as gabbro have a Vp/Vs ratio near 1.87. The average composition for continental crust is close to andesite or diorite (Anderson, 1989) and laboratory measurements by Carmichael (1982) confirmed that Vp/Vs for diorite at crustal pressures ranges from 1.75 to 1.79. I found the region just to the east of Colima volcano and the northern part of the Jalisco block have "normal" continental crust Vp/Vs ratios (Fig. 3.7). The high Vp/Vs ratio regions could indicate a very mafic crust or that the crust has high pore pressure fluids or partial melt. The surface geology of the region is largely granitic or siliceous volcanic rock with no indication of a particularly mafic crustal composition. Thus I conclude that the high Vp/Vs ratios I observe along two bands in our study area are due to partial melt or high fluid content within the crust although some mafic underplating of the crust could also contribute.

There is high Vp/Vs ratio in the Jalisco block seaward of a trend of young volcanoes (red triangles in Figure. 3.7) known as the Central Jalisco Volcanic Lineament (CJVL). Bandy et al. (2001) performed K-Ar age dating of rocks along this line finding ages from 3 Ma to Quaternary. There is also a trend of decreasing age to the northwest along the line. It has been known for some time that there has been an overall trenchward

migration of magmatism in Jalisco for the past 10 Ma (Ferrari et al., 2001). The CJVL forms the front of this migrating magmatism. Ferrari (2004) and Ting et al. (2009) proposed that this migration was due to slab steepening of the Rivera plate allowing asthenosphere to warm the lithosphere progressively trenchward. Arc magmas could also be rising from the deepening slab. The highest Vp/Vs ratios in the Jalisco block are just trenchward of the CJVL volcanoes and are not collocated with any volcanoes. This indicates, perhaps, the crust is being broadly heated with possible partial melt developing trenchward of the recent volcanism. This would support a model with a continuing roll back and steepening of the Rivera plate and would predict a continuation of trenchward migrating magmatism. A denser array of seismic stations is needed to confirm the nature of the anomalous Vp/Vs ratio trend.

The second region with anomalously high crustal Vp/Vs is located to the north east of the study area partly within the Michoacan-Guanajuato volcanic field. This region also has late Pliocene – quaternary mafic and intermediate volcanism less than 3 Ma (Gomez-Tuena et al., 2007). It is a 40,000 km^2 area with more than 1000 Quaternary eruptive centers and thus a crust with distributed partial melt is not surprising (Gomez-Tuena et al., 2007). High crustal Vp/Vs ratios to the west of the MGVF are found as well forming a swath of crust that I interpret as containing widely distributed partial melt. The cause of the melting over this region could also be related to partial slab steepening and roll back of the Cocos plate.

Seismic Cross sections

To further extract information from the receiver functions, linear profiles were plotted relative to an estimate of depth to the subducting Rivera and Cocos plates. I divide the data into two groups (Figure. 3.11) corresponding to the Jalisco Block with the Rivera plate subducting beneath it and stations to the east which is the subducting Cocos plate. This division was made because of the apparent difference in crustal structure discussed above as well as the difference in subduction slab dip claimed by Pardo and Suarez (1995) between the two regions. I use estimates of slab interface depth from Pardo and Suarez (1995), who based their estimates on rather poorly constrained seismicity. For each of our stations, I plotted the stacked receiver function as a function of depth to slab (Figure 3.12 and 3.13). The stacking was done assuming the Vp/Vs ratio found by H-K analysis. For stations that had a null result from the H-K analysis, a Vp/Vs ratio of 1.78 was assumed. The idea of plotting our data this way is to examine the waveforms of the receiver functions in relation to the subduction process. In addition, by plotting RF's as a function of depth to the slab, the slab contour model of Pardo and Suarez can be tested. An estimated depth from H-K analysis is also placed on Figure 3.12. Overall, the stacked RF's show good agreement with the H-K analysis results although there are slight differences that may be due to a more complex crustal velocity structure than the simple homogenous layer assumed in H-K analysis.

The simple linear stack that I performed above is just an arithmetic mean of the individual observations. Unfortunately, seismic data can have a non-Gaussian noise distribution and unusual noise data spikes can show up in simple stacks. Muirhead (1968)

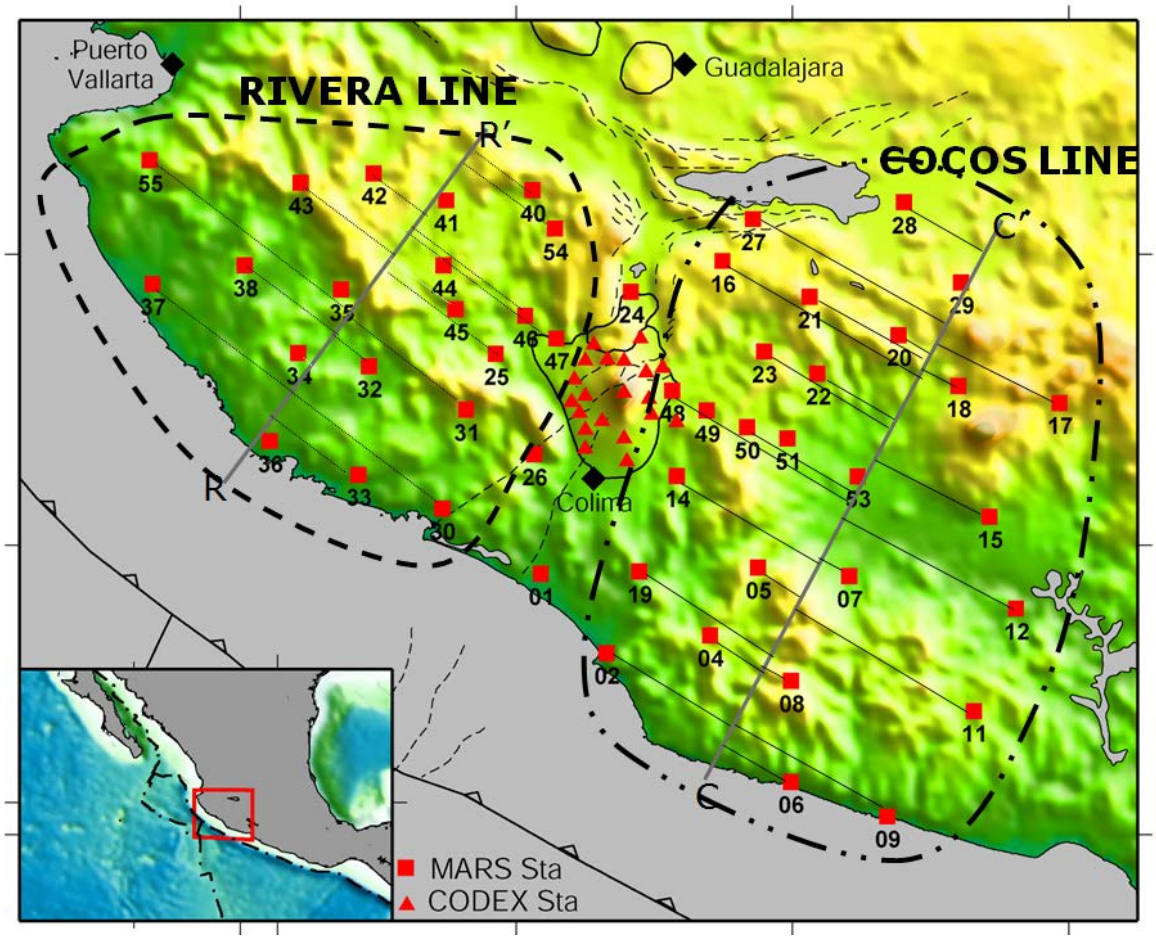

Figure 3.11. The groups of stations used for the Rivera and Cocos Line RF plots. R-R' is the line used for CCP imaging of the Rivera plate and C-C' is used for CCP imaging of the Cocos plate.

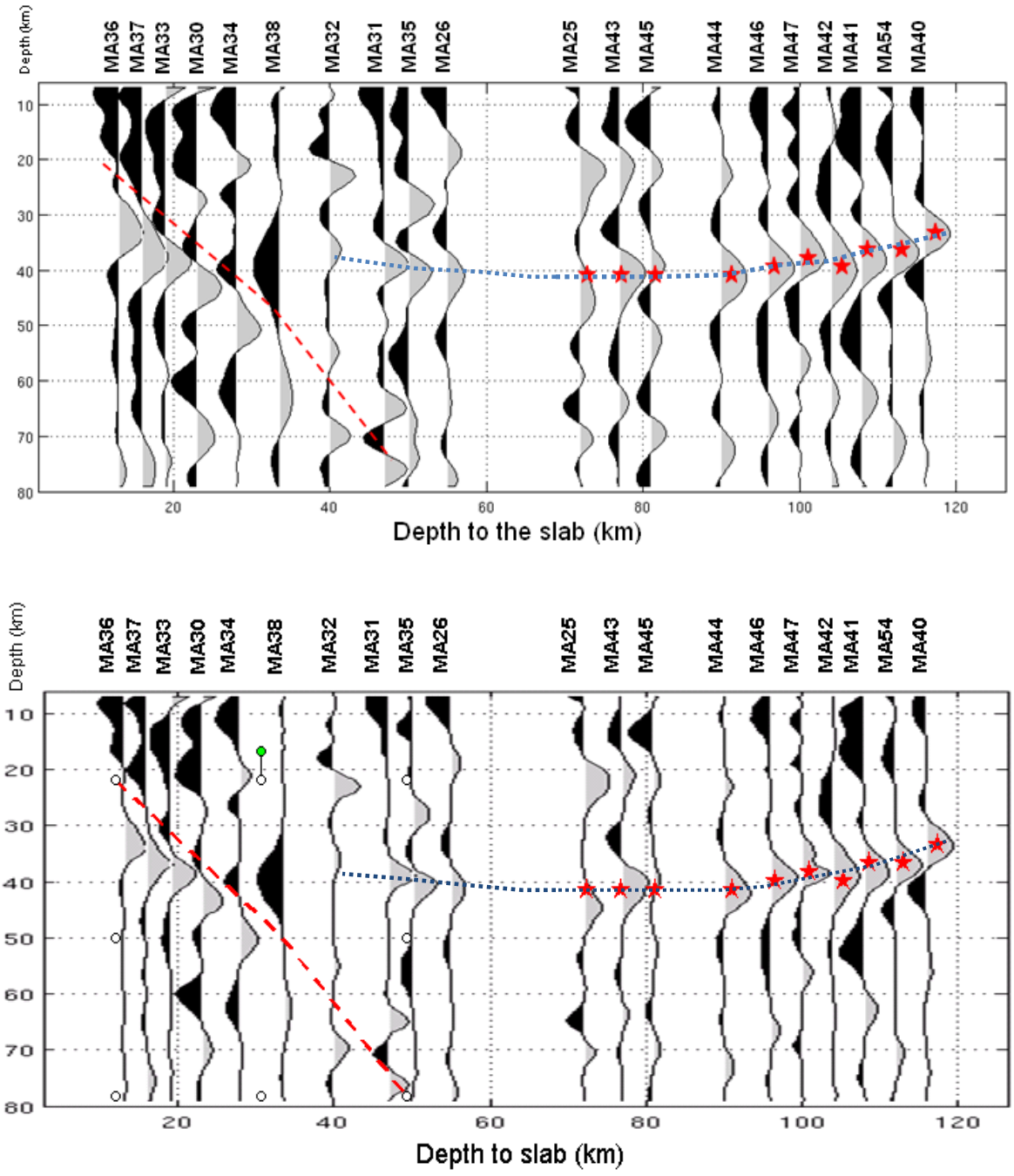

Figure 3.12. Plot of stacked RF's with respect to depth to the slab for the Rivera Line. The lower figure is the 2nd order root stack RF. The vertical axis is depth and horizontal axis is the depth to top the slab taken from Pardo and Suarez (1995). The dashed red line is our interpretation of the top oceanic crust. The red stars are the estimates of continental crust Moho depth using the H-K method.

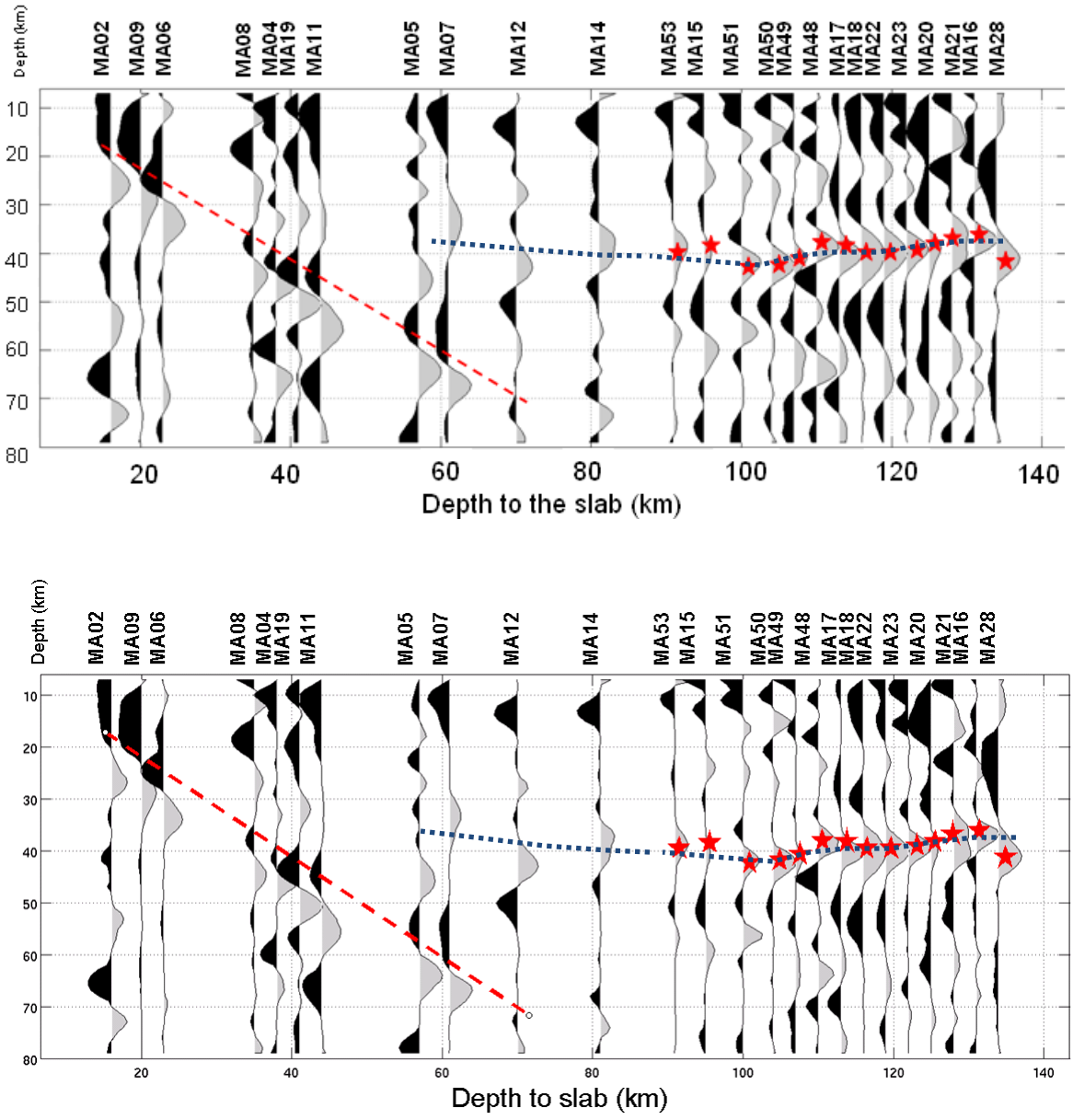

Figure 3.13. Plot of stacked RF's with respect to depth to the slab for the Cocos Line. The lower figure is the 2nd order root stack. The vertical axis is depth and the horizontal axis is the depth to top the slab taken from Pardo and Suarez (1995). The dashed red line is our interpretation of the dipping oceanic crust. The red stars are the estimates of continental crust Moho depth using the H-K method.

introduced the Nth-root stack as a means of eliminating false alarms caused by noisy data during the automatic detection of seismic events using seismic arrays. The Nth-root stack equation can be written as

$$R_N = \left[\frac{1}{m} \sum_{i=1}^{m} \sqrt[N]{t_i} \right]^N$$

Where m is the number of RF data and N is the root of the stack.

I performed an Nth-root stack, with N equal to 2, of all our RF data and compare it with our simple stacks in Figure. 3.12 and 3.13. In general the Nth root and linear stacks show similar signal, however, the Nth-root stack has a slightly spikier positive signal and removes some of the noise, especially at a later times.

It is clear in Figure. 3.12 and 3.13 that there is a dipping structure to the southwest that is visible to near 60 km depth whereas in the northeast there is a relatively simple Moho near 40 km depth with no visible dipping structures. I plot the receiver functions to 80 km depth because at deeper depths crustal multiples are visible and make any interpretation problematic. The dipping structures to the southeast clearly mark the subducting Rivera (Figure. 3.12) and subducting Cocos (Figure. 3.13) plates, respectively. I will discuss these features further below and show that the negative pulses shown in Figure. 3.12 and 3.13 mark the top of the descending oceanic crust in their respective subduction zones. Note that for the subducting Cocos plate, Figure 3.13, the top of the descending plate agrees with the results of Pardo and Suarez (1995) but I find the Rivera plate to be about 10 km systematically deeper (Figure 3.12) than Pardo and Suarez (1995) claim. This discrepancy is not surprising in that seismicity is sparse in the

Jalisco subduction zone and instrumentation was lacking in the past such that earthquake locations in Pardo and Suarez (1995) likely have large uncertainties. An accurate model of the slab interface is critical for understanding GPS measurements in subduction zones.

The techniques used above, H-K analysis and stacking of receiver functions, work well for flat lying structures but are problematic for dipping structures. The reason for this is simple, waves arriving from the down dip direction will encounter a boundary at a deeper depth than waves arriving from the up dip direction. My analyses to this point have assumed all the arrivals from a given boundary at a single station are produced at the same depth. To account for the different location of conversion points corresponding to different back azimuths to a station I have also processed our receiver functions using the Common Conversion Point (CCP) stacking method. The idea of this method is to back project individual receiver functions along the raypath corresponding to the receiver function. The back projected amplitudes are stacked in lateral and vertical bins resulting in a 3D image of convertors in the sub surface. This approach has been used in numerous studies [e.g. Dueker and Sheehan (1997), Eagar et al (2010), Schulte-Pelkum et al (2005), Perarnau et al (2012)] but requires a high density of stations with numerous receiver functions such that each bin is sampled by numerous traces from different directions. The MARS array is relatively sparse so I collapsed the images onto 2-D lines to better compare the results with Figures 3.12 and 3.13. I divided the data into the same two groups as before (Figure. 3.11) and back projected the receiver functions onto lines RR' and CC' respectively. This was done by projecting each convergence point to its correct location and then projecting that location onto the respective lines along a perpendicular to the lines.

Figures 3.14 and 3.15 show the results of our CCP stacking along the two lines, RR' and CC'. I used a bin size of 12 km for the CC' line and 14 km for RR' in the lateral direction that increases with depth. The results can be compared to Figures. 3.12 and 3.13 although it should be noted that I use distance on the horizontal axis here but depth to slab was used in the previous figures. The red color in Figures 3.14 and 3.15 correspond to a positive pulse in the receiver functions and thus to a jump in shear velocity with increasing depth. The blue color corresponds to a decrease in shear velocity with depth. The CCP results are similar to the stacking results shown in Figures 3.12 and 3.13 in that a clear dipping structure is seen in the southwest and a sharp relatively flat continental Moho is seen in the northeast for both profiles. The dipping slab structure is detected to about 50 km depth and then disappears. The other thing to note is the lack of any clear discontinuities in the middle of the model along either profile.

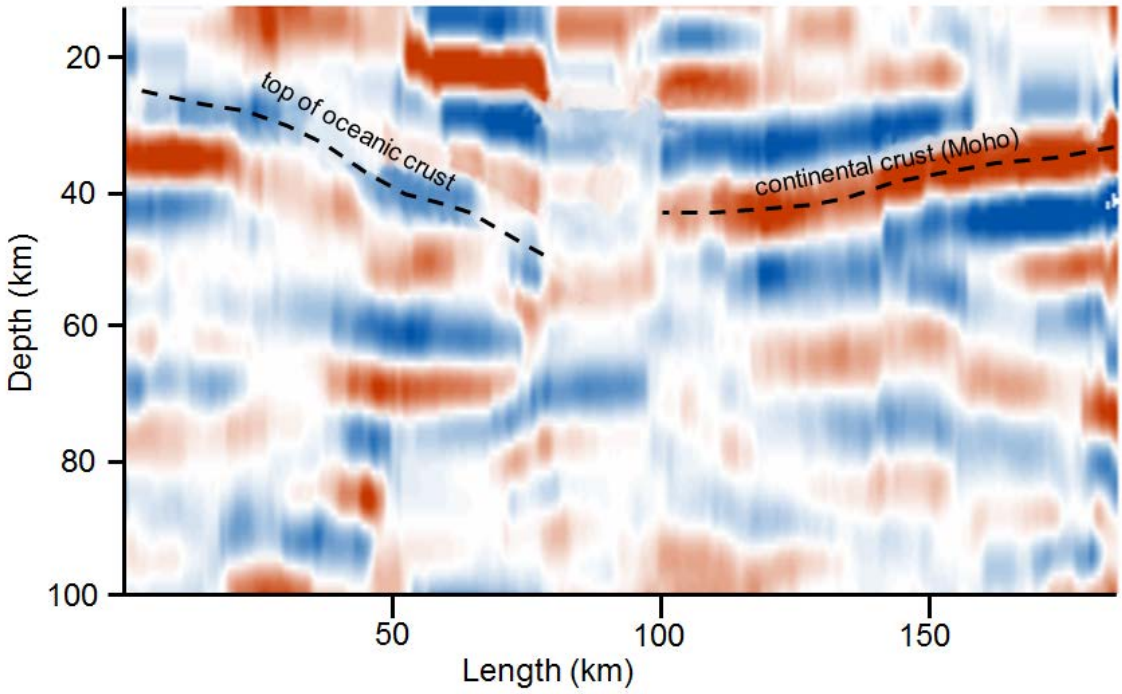

Figure 3.14. The final CCP image result above the Rivera plate line (line R-R' on Figure 3.11). The vertical axis is depth in km and the horizontal axis is the distance calculated along the line. Note the starting point is close to the coast. Blue colors show negative receiver function pulses and red positive.

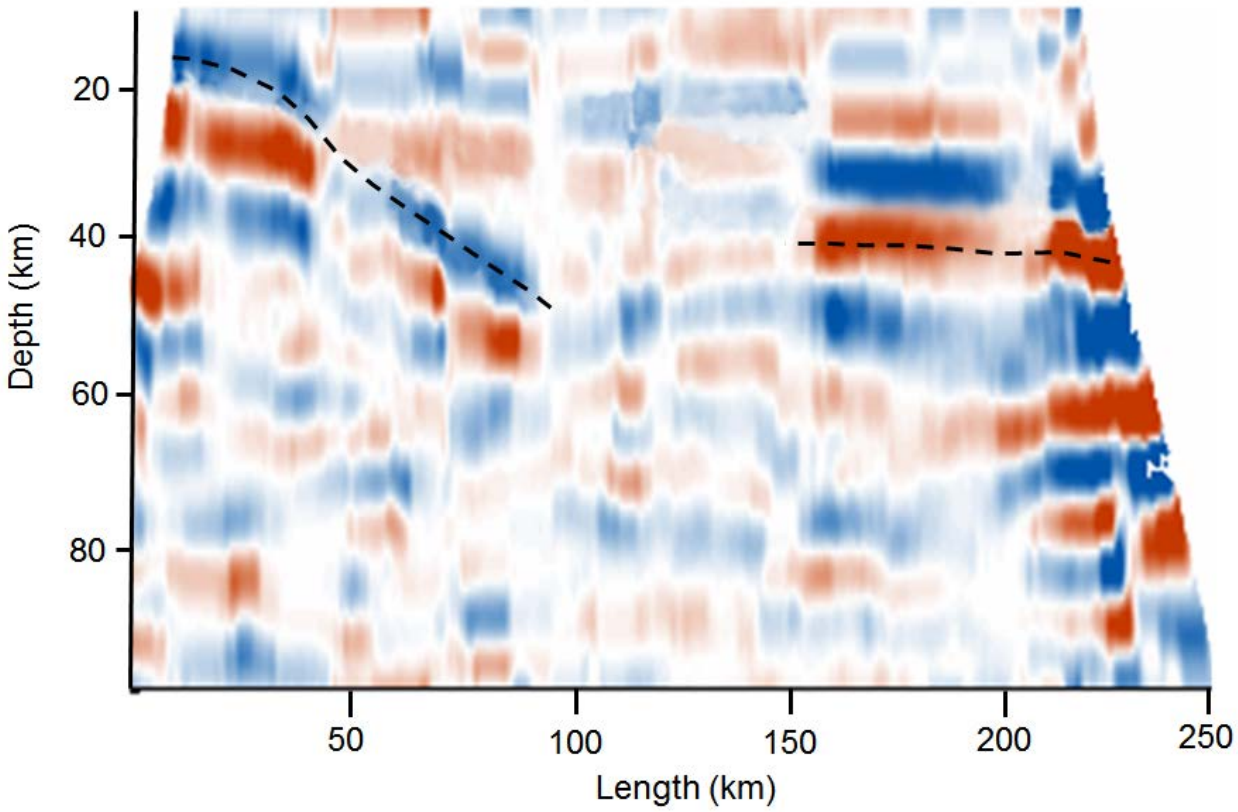

Figure 3.15. The final CCP image above the Cocos plate (line C-C' on figure 3.11). The vertical axis is depth in km and the horizontal axis is the distance calculated along the line. Note the starting point is close to the coast. Blue colors show negative receiver function pulses and red positive.

Slab Structure

The cross sections shown in Figure 3.12, 3.13, 3.14 and 3.15 show several interesting features. First, the dipping structure in the southwest is marked by a negative pulse over a positive pulse (blue over red in Figure. 3.14 and 3.15 –dashed line in Figure. 3.12 and 3.13). This indicates that there is a shear velocity drop with depth associated with the subducting slabs underlain by a sharp jump in velocity. Figure 3.16 shows the raypaths and velocity model for this situation as well as an example receiver function response. In this example I assume the dipping crustal layer has a low velocity layer underlain by a jump in velocity to normal crustal velocity and then finally another jump in velocity representing the oceanic Moho. The converted wave going from low velocity up into high velocity has a negative polarity. The converted waves from the deeper layers go from higher velocity at depth to lower velocity above and thus have positive polarities. There are also multiple reflections and conversions within the layers. All these waves arrive closely in time resulting in a two sided pulse in the receiver function similar to what I observe in the coastal data.

One might interpret the slow shear velocity layer to be subducting sediment however, the gravity study of Manea et al. (2003) suggests that the thickness of the sedimentary column over the Rivera plate probably does not exceed ~20 m, and that it gradually increases eastward along the trench. Moreover, the Deep Sea Drilling Project at a drill hole at site 487, located ~11 km offshore of Guerrero State (lat 15°51.210′ N and long 99°10.518′ W) reveals that the sedimentary column at this site is composed of

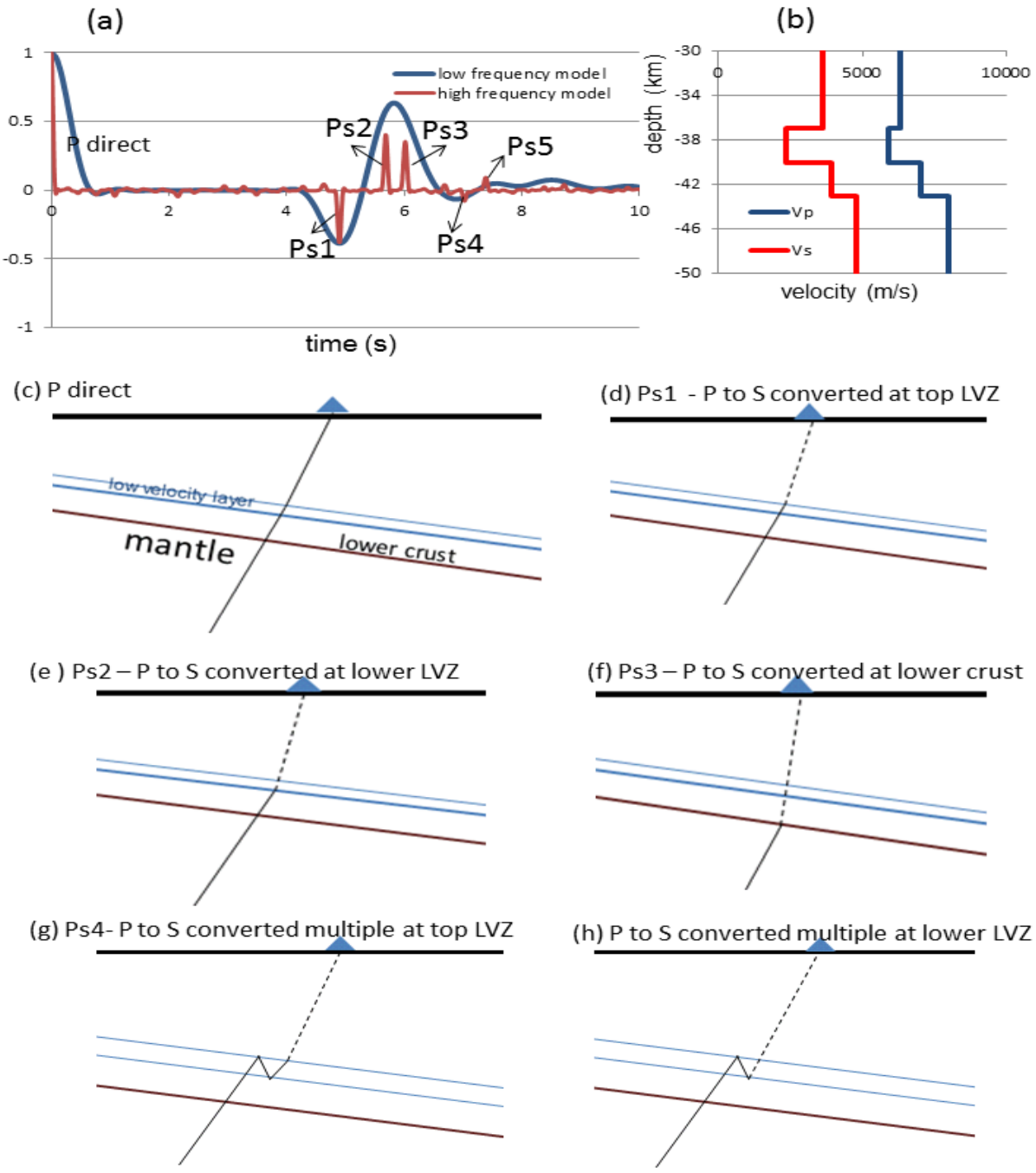

Figure 3.16. (a) Synthetic seismogram response for the 4 layer velocity model shown in (b). The red line in (a) shows impulsive spikes corresponding to different converted arrivals while the blue line shows the corresponding receiver function at the longer periods used in this study.(c)-(h) show the raypaths for various converted and reflected waves with labels corresponding to the arrivals in (a).

~100 m of Quaternary hemipelagic sediments which overlay ~70 m of late Miocene to Pliocene pelagic. For the slow layer to be visible in our long period receiver functions it must be several kms thick – roughly the distance from the peak low velocity to the peak high velocity. A slow layer of 170 m thick would simply be averaged out in my analysis.

A slow velocity layer associated with subducting oceanic lithosphere has been observed in several other regions. Bostock (2002) used a scattered wave inversion technique on seismic data recorded over the Juan de Fuca plate in central Oregon. Their images show a layer of slow velocity that is associated with the subducting plate to a depth near 45 km. His results are shown in Figure 3.17 though it should be noted that the results shown are velocity and not shear velocity jumps as in our work. It should also be noted that the Oregon experiment consisted of a linear array of stations with a nominal spacing of about 5 km and thus the image is clearer than our work with 50 km spaced stations that were not placed on a line. Still, I find the comparison between our image and the Oregon image striking. In both regions, a layer of slow velocity 5-10 km thick, is seen descending to about 45 km depth in the subduction zone. Bostock et al. interprets the slow anomaly as the basaltic oceanic crust subducting beneath continental forearc. In Figure 3.12 and 3.13 it can be seen that the receiver function peak corresponding to the top of slow velocity occurs at the depth predicted for the subducting plate by Pardo and Suarez (1995) in Figure 3.13 and even deeper in Figure 3.12. Pardo and Suarez (1995) identify as the depth to the subducting plate. Thus, I interpret the drop in velocity found in the receiver functions to mark the top of the subducting oceanic crust in accord with Bostock et al. (2002).

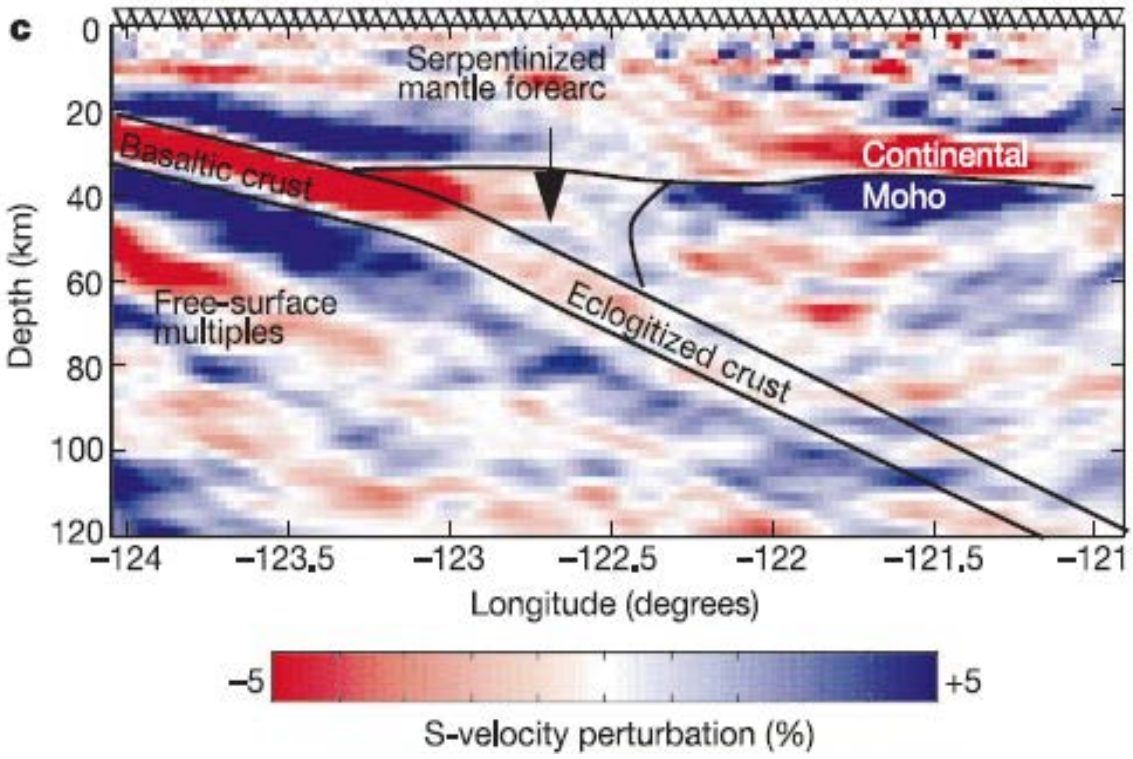

Figure 3.17. S wave velocity perturbation below an array deployed across central Oregon, recovered from the inversion of scattered waves in the P-wave coda of 31 teleseismic events. Image is taken from Bostock et al, (2002). The interpretation model show a dipping basaltic crust that changes into eclogitized crust at about 40 km depth. Note that the region where the velocity contrast corresponding to depths expected for the continental Moho seems to disappear is interpreted as where the mantle forearc is serpentinized.

The estimate of thickness of the low velocity layer depends on the Vp/Vs ratio of P and S waves within the slow layer. Using normal values of Vp/Vs ratio the thickness of the layer in Bostock et al. (2002) corresponds to a layer roughly 8 km thick and thus he associates the layer with the entire oceanic basalt crust. However, Audet et al. (2009), using multiple reflections within the slow layer for data collected above Cascadia, found that the Vp/Vs ratio is abnormally high within the low velocity layer, 2.4 to 2.8, and thus the low velocity layer is thinner than previously thought and is on the order of 3 to 5 km thick. Recently, Kim et al. (2010) and Song et al. (2009) examined data from a dense linear profile across central Mexico. They also found a thin 2-4 km thick layer of anomalously slow S velocity with anomalously high Vp/Vs ratio dipping beneath the continent. Audet et al. (2009) as well as Kim et al. (2010) and Song et al. (2009) identify the slow layer as the top half of the subducting oceanic crust.

To better constrain the structure producing my receiver functions I calculated synthetic receiver functions for various models using a reflectivity code (Levin and Park, 1998). The three parameters I investigated are the drop in shear velocity at the basalt interface, the Vp/Vs ratio within the slow layer, and the thickness of the slow layer. The velocity model I used has 4 layers, a continental crust, a low velocity layer identified with the subducting oceanic crust, a lower oceanic crust, and the mantle. I constrain the continental crust, lower oceanic crust and mantle to have a Vp/Vs ratio of 1.78 and vary the thickness, shear velocity, and Vp/Vs ratio of the low velocity layer to match our data. The velocity of the lower oceanic crust and mantle are taken as normal, 6.8 km/sec Vp and 3.8 km/sec Vs for deep ocean crust and 8.0 km/sec Vp and 4.5 km/sec Vs for the mantle. My receiver functions along the coast vary considerably with different amounts

of noise such that no single model will fit all the data. For the purposes of waveform modeling I chose receiver function data from station MA19 because that station shows a clear negative amplitude followed by positive amplitude (Figure 3.13) but shows little indication of other arrivals indicating there is little noise or complicated structure associated with the MA19 receiver function. I took filtered RFs for MA19 that have back-azimuth near 300 degree and stacked them using a 2nd order root stack to compare to synthetics.

Figure 3.18 shows the results of our simulations with varying thicknesses of the low velocity layer compared to the stacked receiver function from station MA19. I adjusted the S velocity and P velocity in the low velocity layer to best match the data. For thick layers, 5 to 6 km, the width of the two sided waveform is greater than observed even with relatively low Vp/Vs ratios. For thin layers 1 to 2 km thick, the synthetics have a broad tail which is due to strong multiples within the thin layer. A low velocity layer 3 to 4 km thick gives an optimal fit to station MA19. Figure 3.19 shows further synthetic modeling for a low velocity layer 3 km thick. Here I modified the shear velocity drop in the low velocity layer as well as the Vp/Vs ratio. My optimal model is a 3 km thick layer with a drop in shear velocity of 35% and a Vp/Vs ratio within the low velocity layer of 2.4-2.6, well above the range for normal rocks at this depth. This is similar to the results of Audet et al. (2009) although I clearly do not have tight constraints on the slow velocity layer's properties due to variable receiver functions in our profile as well as the fact that multiple variables affect the results.

Basalt is usually considered a high velocity component of crust, particularly within continental crust, therefore it is a surprise that it is showing up as a slow velocity

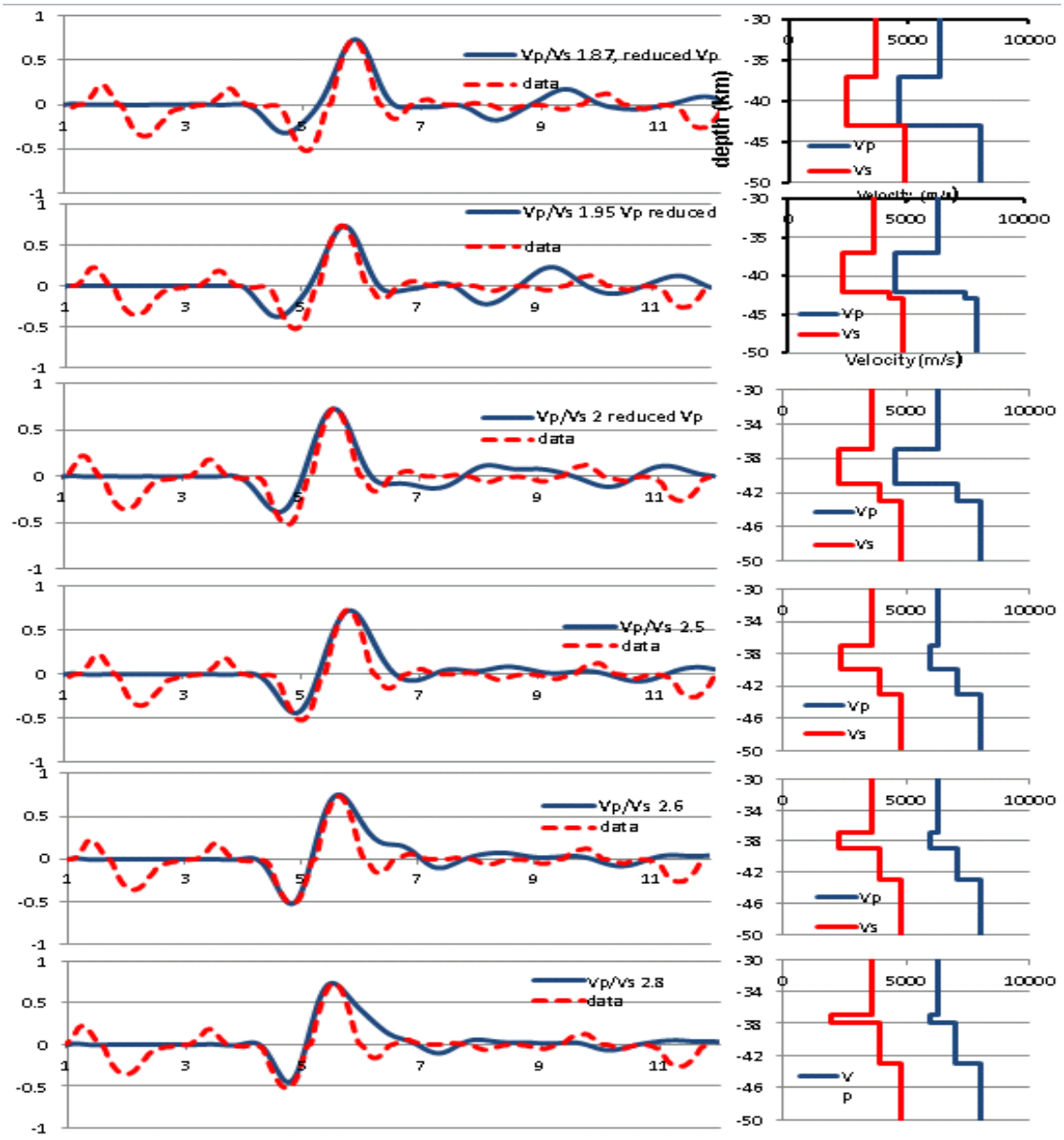

Figure 3.18 Synthetic to data comparison for a range of low velocity layer thickness with an optimized velocity model. The crust is set at 6 km thickness. From top to bottom are 6 km crustal thickness, 5 km LVZ, 4 km LVZ, 3 km LVZ, 2 km LVZ and 1 km LVZ with the velocity model on the right Models that have a thicker than 4 km low velocity layer produce broader waveforms than observed for reasonable Vp/Vs ratios. Models with a very thin 1-2 km thick layer produce strong multiples that also broaden the synthetics and do not match the data.

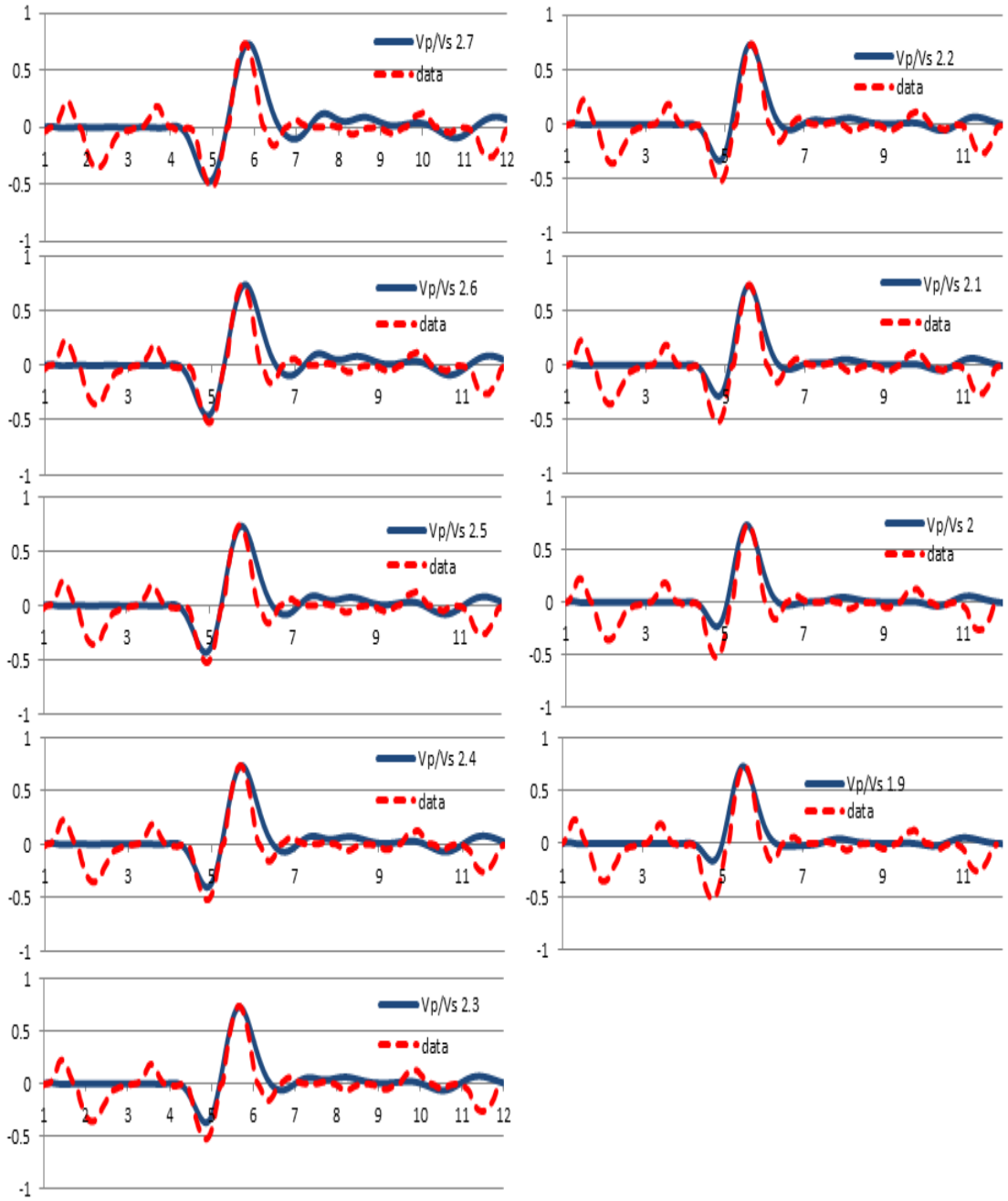

Figure 3.19. Synthetic to data match for a constant P velocity in the lower velocity layer but varying shear velocity drops resulting in a range of Vp/Vs ratios. The low velocity layer is held at 3 km thick. Our optimal model has a shear velocity drop of 35% resulting in a Vp/Vs ratio from 2.5 to 2.6.

anomaly in our study as well as in the work of Bostock et al. (2002). Audet et al. (2009) studied this issue and concluded that the basalt would have the observed low velocities if it had pervasive water present that was overpressured i.e. at lithostatic pressure. They propose that the top of the oceanic crust formed of pillow basalts and sheeted dikes of gabbro, contains significant water as well as hydrated minerals. As the plate subducts some of the minerals dehydrate creating high pore fluid pressures that cause the dramatic drop in shear velocity observed. This would imply the boundary between the subducting oceanic crust and the overriding continental material is impermeable as well as the deeper crust. Kim et al (2010) and Song et. al. (2009) propose a similar interpretation for their images in central Mexico although Kim et al. (2010) also suggest hydrous minerals such as talc may be an important contributor to the velocity drop.

At deeper depths, I observe the disappearance of the slow dipping converted phase at about 45 km (Figure. 3.14 and 3.15). I interpret this to be the depth where the basalt begins to transform to eclogite. When this occurs there is a relatively large volume change that may make the subducting crust and its boundary more permeable and thus allow it to lose water to the overlying mantle wedge. If the slow velocity layer is due to high pore pressure fluids then its disappearance may show the depth at which the water can escape to the mantle wedge. Eclogite also has high seismic velocity and thus its contrast with the surrounding mantle will be less than the contrast of the slow basalt with mantle causing the disappearance of the positive converted wave at the oceanic Moho. The slow layer in the results of Bostock et al. (2002) also disappears at a similar depth (Figure. 3.16).

The similarity of subduction zone structure between Cascadia and southwestern Mexico is striking but both regions have young ocean (5Ma – 15Ma) subducting beneath continent so perhaps this is not surprising. One difference between the regions is the thickness of sedimentary cover in the subduction zone. Off shore southwestern Mexico estimates of the sedimentary thickness range from 20 to 170 m as mentioned above. However, the subduction zone offshore Cascadia has a thick sedimentary prism and far more flux of sediment in the subduction zone (Rea and Ruff, 1996). The similarity of the two regions shows sediment flux is not a significant factor in the permeability of the oceanic crust interface nor the temperature structure of the slab as the eclogite phase transition seems to occur at similar depths as well. It also supports the model for the slow velocity layer being basalt crust and not a layer of subducting sediment.

A second unusual feature of the CCP images of Southwestern Mexico (Figure. 3.20) is the lack of any strong Moho signal in the middle of the images, both for the Rivera plate system and the Cocos plate system. A clear continental Moho is visible to the east and clear dipping convertors are seen to the west but in the middle there are no clear signals corresponding to the Moho. Above the Rivera slab, I measure a 20 km width of weak Moho signal and above the Cocos slab I measure about a 50 km width without a clear Moho. Again, this is similar to what is observed beneath Oregon (Figure 3.16). Bostock et al. (2002) explained this observation by postulating that the mantle wedge at this location is serpentinized due to the water release from the subducting slab. Serpentine has very low shear velocity and in fact has slower shear velocity than typical lower crustal mineral assemblages (Christensen,1996). Bostock et al. (2002) show that a peridotite with 50% serpentization will have shear velocity similar to lower crustal rocks.

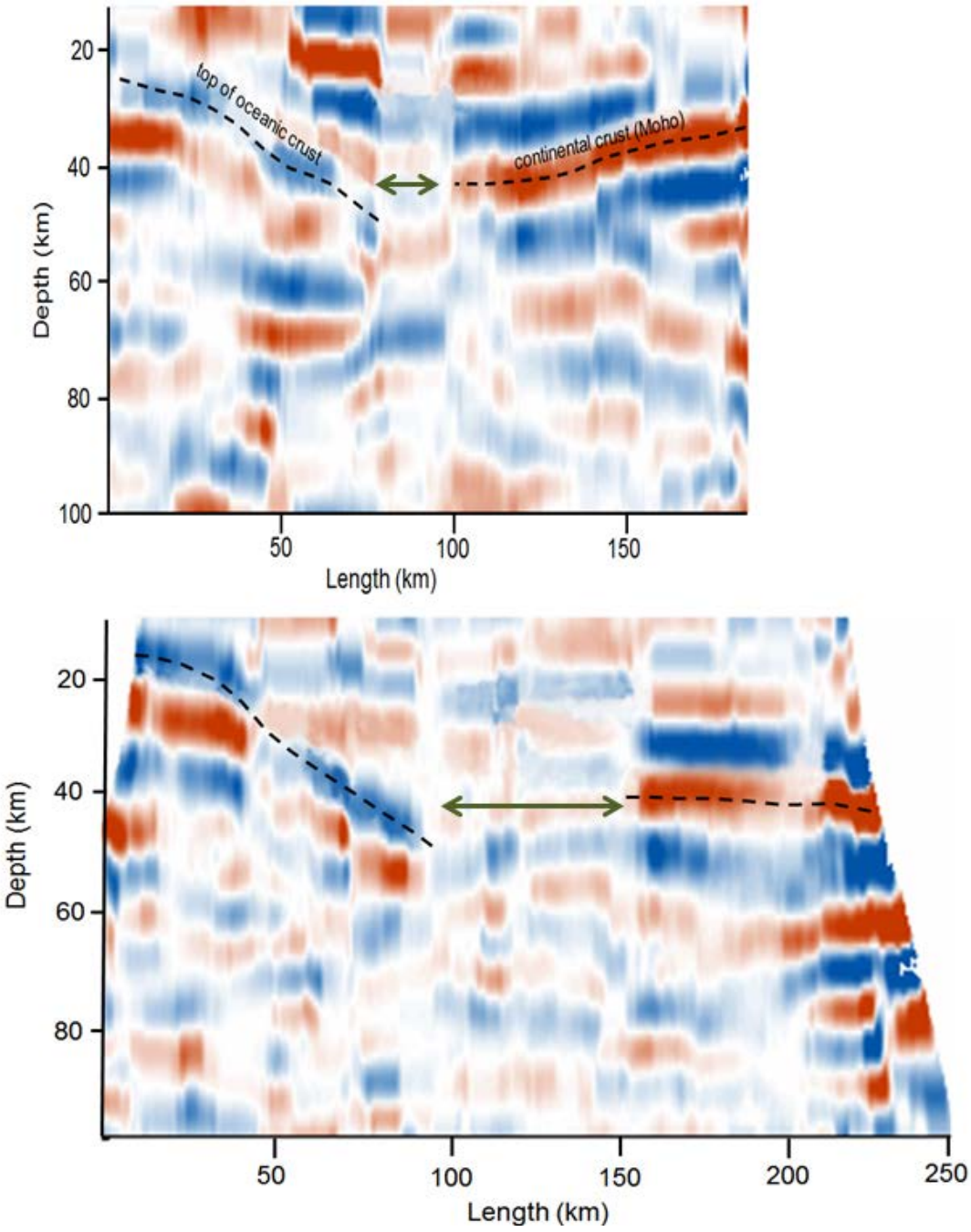

Figure 3.20 The CCP RFs corresponding to the Rivera (top) subduction zone and the Cocos (bottom) subduction zone. The arrows show regions where there are no clear signals from a Moho.

With no shear velocity contrast between crust and mantle no converted P to S wave will be created at the Moho. The implication is that this mantle does not participate in the mantle flow associated with the subducting slab and is hydrated by released water from the subducting crust. I support this interpretation. It is interesting that the width of the zone with weak Moho is quite different between the Rivera and Cocos subduction zones. The Rivera plate has a steeper subduction angle than the Cocos plate thus creating a thicker mantle wedge as a function of distance inland. A thicker mantle wedge can be entrained in the downward flow easier than a thin wedge and perhaps this is the reason for the difference. These observations may provide constraints on viscosity of the mantle wedge. Figure 3.21 summarizes our results for the dipping slab structure beneath Southwestern Mexico overlaid with the receiver functions used in the interpretation.

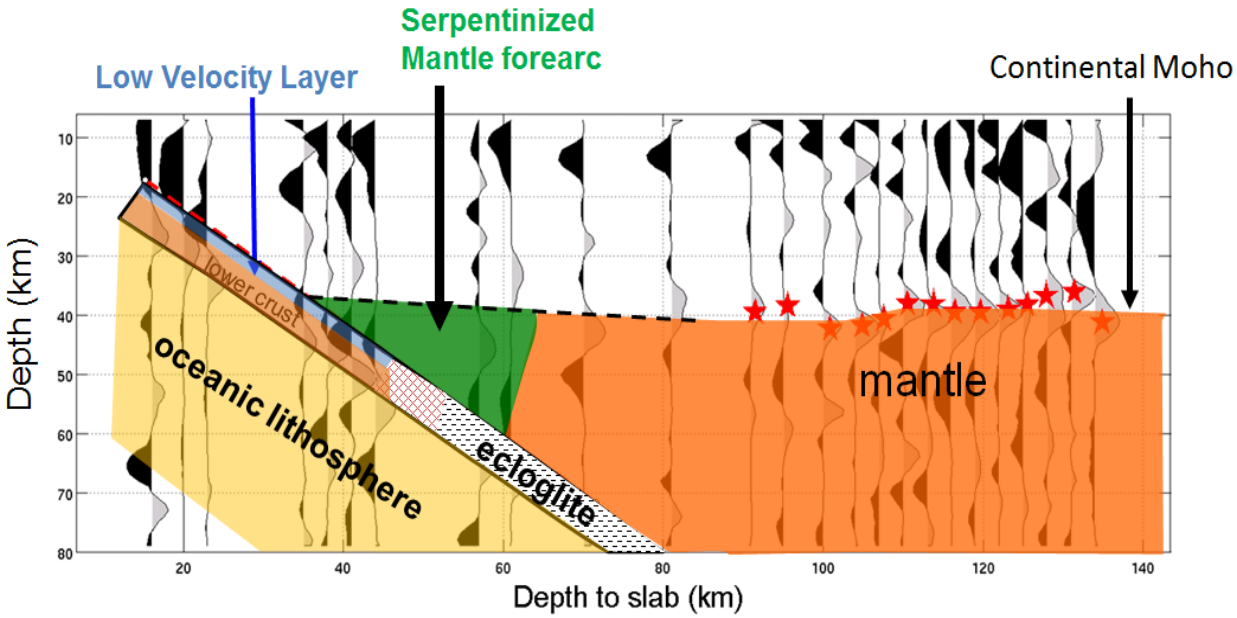

Figure 3.21 Cartoon illustrating our interpretation of the receiver functions above the Cocos slab. The receiver functions are overlaid on the interpretation

Conclusions

In this chapter I analyzed the lithospheric structure beneath Southwestern Mexico using the receiver function technique. Along the coast receiver functions show the dipping Rivera and Cocos plates subducting beneath Mexico. I find the Rivera plate along the coast is about 10 km deeper than previously estimated by Pardo and Suarez (1994). The receiver functions also show that the subducting slabs have a 3-4 km thick extremely slow shear velocity layer that is similar to what has been found in Cascadia. The thickness of the layer leads me to conclude this is part of the subducting oceanic crust that is under high pore fluid pressure and not a layer of sediment. Further detailed modeling of this feature would require a dense profile of seismic stations that could perhaps be carried out in the future. The contrast of a better imaged profile in Mexico with Cascadia should shed light on the role of thick versus very thin accretionary prisms in the subduction process.

Inland receiver functions show a clear Moho across much of our study area as well as variations in the crustal Vp/Vs ratio. There is no correlation of topography with crustal thickness leading me to assume mantle buoyancy causes much of the high relief in Jalisco and Michoacan. The Vp/Vs ratios I found seem to correlate with regions of incipient or recent magmatism. If this finding holds up it means broad swaths of crust are heated perhaps caused by migrating arc magmatism as the Rivera and perhaps Cocos slabs roll back. Again, to confirm these observations higher density stations are needed

Station Name	longitude	latitude	Crustal Thickness	uncertainty	Vp/Vs	uncertainty
MA27	-103.1435	20.1206	**36.9**	**1.26**	**1.81**	**0.03**
MA18	-102.3997	19.5489	**39.3**	**0.66**	**1.82**	**0.02**
MA21	-102.938	19.854	**37.34**	**0.55**	**1.87**	**0.02**
MA29	-102.39	19.9038	**41.2**	**1.18**	**1.76**	**0.04**
MA23	-103.1034	19.6671	**39.07**	**0.61**	**1.77**	**0.02**
MA53	-102.7644	19.2382	**42.03**	**1.31**	**1.67**	**0.03**
MA51	-103.018	19.3679	**42.53**	**0.91**	**1.77**	**0.02**
MA47	-103.8553	19.7118	**38.33**	**1.15**	**1.86**	**0.03**
MA48	-103.4362	19.5324	**41.79**	**0.64**	**1.78**	**0.02**
MA49	-103.3109	19.4638	**42.03**	**0.81**	**1.78**	**0.02**
MA50	-103.1648	19.4062	**42.53**	**0.70**	**1.77**	**0.02**
MA46	-103.968	19.7891	**38.57**	**1.16**	**1.81**	**0.03**
MA44	-104.2644	19.9627	**41.54**	**0.74**	**1.85**	**0.02**
MA45	-104.2197	19.8121	**42**	**1**	**1.87**	**0.02**
MA41	-104.2539	20.1853	**36.84**	**0.91**	**1.81**	**0.02**
MA42	-104.5175	20.777	**38.21**	**0.89**	**1.81**	**0.03**
MA40	-103.942	20.2198	**36.10**	**1.12**	**1.73**	**0.03**
MA54	-103.8605	20.0884	**36.10**	**0.98**	**1.80**	**0.02**
MA43	-104.7815	20.2457	**39.56**	**1.34**	**1.83**	**0.04**
MA16	-103.254	19.9778	**36.60**	**0.61**	**1.84**	**0.02**
MA20	-102.616	19.7235	**37.83**	**1.28**	**1.82**	**0.03**
MA28	-102.597	20.1786	**40.55**	**1.70**	**1.82**	**0.04**
MA17	-102.033	19.4898	**39.07**	**0.80**	**1.86**	**0.03**
MA22	-102.909	19.59	**40.30**	**0.68**	**1.77**	**0.02**
MA24	-103.5858	19.8719	**37**	**1**	**1.77**	**0.04**

Table 3.1. Crustal thickness and Vp/Vs ratio from H-K Method

Station Name	longitude	latitude	Crustal Thickness
MA01	-103.9112	18.9014	**31**
MA02	-103.6734	18.6273	**18**
MA04	-103.299	18.6885	**31**
MA05	-103.125	18.9236	**33**
MA06	-102.8798	18.1461	**22**
MA07	-102.7943	18.8933	**33.5**
MA08	-103.0045	18.5318	**29**
MA09	-102.6567	18.0625	**18.5**
MA11	-102.344	18.4271	**32**
MA12	-102.1906	18.7812	**34**
MA14	-103.419	19.2385	**36**
MA19	-103.5555	18.9097	**31.5**
MA25	-104.0746	19.6592	**40.52**
MA26	-103.9354	19.3136	**40**
MA30	-104.2688	19.1269	**33**
MA31	-104.1818	19.467	**38**
MA32	-104.534	19.6162	**37**
MA33	-104.5723	19.2432	**30**
MA34	-104.7898	19.6616	**40**
MA35	-104.6349	19.8796	**40**
MA36	-104.8932	19.3594	**23**
MA37	-105.3185	19.899	**24**
MA38	-104.9836	19.9624	**36**

Table 3.2. Crustal Thickness from Stacked Receiver Functions

Chapter 4: Comparison of 3-D Raytracing and Finite Frequency Tomography

Introduction

Seismic tomography is a technique to image 3D seismic velocities in the Earth's subsurface by employing seismic waves generated by earthquakes and/or explosions. Some variations of tomography include: waveform tomography that works by determining a velocity model through synthetic waveform matching, reflection travel time tomography that is popular in industry and works by optimizing velocity and reflector depth to minimize travel time of reflected waves, finite frequency tomography and ray based travel time tomography. The last two methods have been used extensively in global seismology and will be the focus of this chapter.

Travel time tomography assumes the travel time of a wave depends on the rock velocities along the geometric raypath corresponding to the observed wave. Technically, this is true only at infinite frequency. The finite frequency tomography technique works on the hypothesis that the observed seismic waves are finite frequency signals. For finite frequency waves, travel times are sensitive to the velocities in a three-dimensional volume around the geometric raypath. Seismic waves passing through velocity heterogeneities with dimensions smaller than the width of the Fresnel zone undergo significant wave-front healing, which results in reduced travel-time shifts compared to the predictions of ray theory [Hung et al., 2001]. The 3-D Frechet travel-time sensitivity kernels [Marquering et al., 1999; Dahlen et al., 2000; Zhao et al., 2000] provide a way to account for wave-front healing and off-ray scattering. Therefore, finite frequency seismic

tomography based on 3-D Frechet sensitivity kernels is theoretically more accurate in imaging velocity anomalies [Hung et al., 2000; Baig et al., 2003]. This method has been applied to regional [e.g., Hung et al., 2004; Yang et al., 2006] and global tomographic studies [Montelli et al., 2004] with great success. However, the finite frequency Frechet kernels are generally only computed once in a given tomography experiment due to the computation cost and effort to do so. The kernels are usually computed for a velocity model that only varies with depth because, again, the kernel calculations are easier in this case than for a fully three dimensionally varying structure. Thus, although using finite frequency kernels is theoretically more accurate than using geometric rays to calculate the sensitivity of travel time anomalies to velocity perturbations in the subsurface, the kernels themselves are approximations to the true kernels due to the fact that they are sensitive to the velocity model itself.

Although ray theory is an approximation, it does have the advantage that one can calculate ray paths through fully three dimensional structures. Thus, when structures are complex with large seismic velocity variations, calculating the actual raypaths through a complicated 3D model may provide better tomography images than using finite frequency kernels computed using a simple 1D model. Subduction zones may be regions where the distortion of raypaths is severe due to the high amplitude velocity anomaly within slabs compared to surrounding mantle. Figure 4.1 shows an example of this. Here I show the raypaths from a distant earthquake to a line of stations computed for a velocity model that varies in depth only as well as the raypaths for a model that has a dipping 6% fast velocity anomaly that could represent a subducting slab. Note how the raypaths are focused into the slab in the 3D model. It should also be noted that if one uses regional

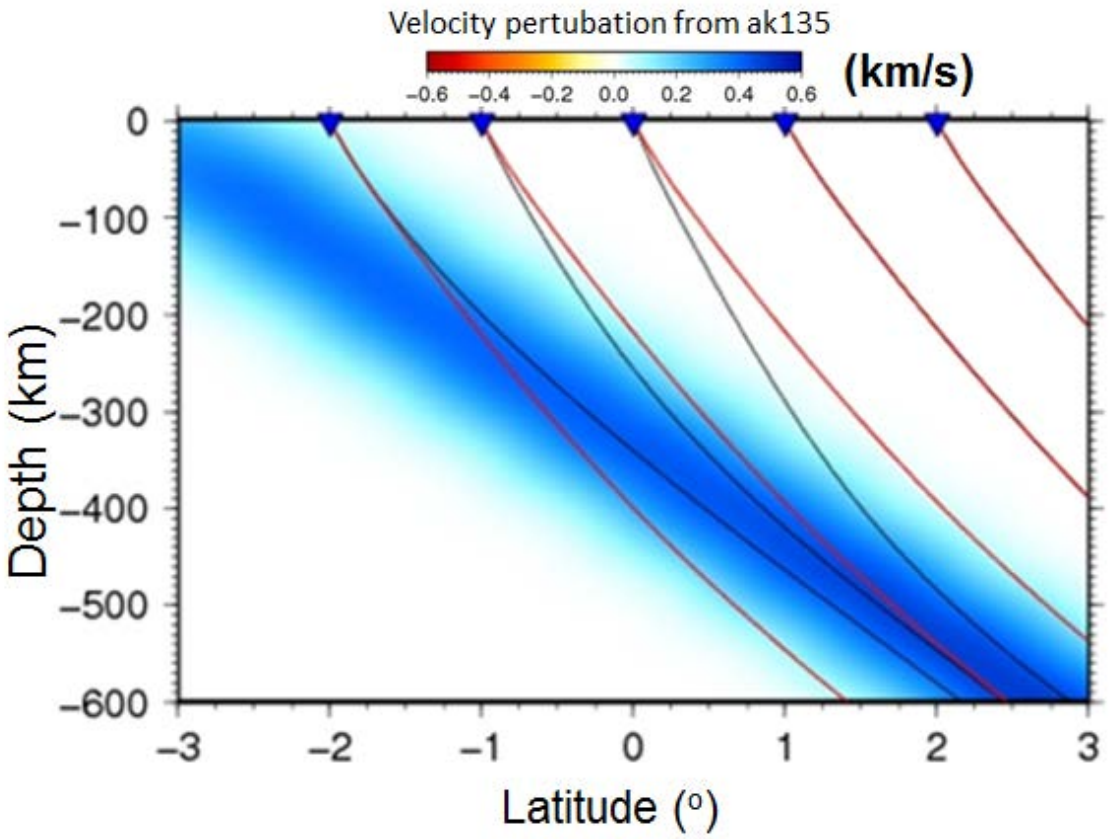

Figure 4.1. A 2-D synthetic subduction model that has dipping fast velocity 6% faster than the reference ak135 velocity model. The red line are raypaths associated with reference model, the black line are raypaths corresponds to 2-D dipping model that bend into the fast velocity nodes to travel on the shortest time.

waves that interact with the Moho and upper mantle discontinuities, 3D ray tracing is likely necessary to properly locate the paths through the Earth that such waves take.

Yang et al. (2009) presented a P wave finite frequency study of Southwestern Mexico using MARS and CODEX data. In this chapter, I use the same data measured by Yang et al. (2009) and perform teleseismic seismic tomography using 3-D ray tracing to investigate the difference in results between the finite frequency method and the 3-D ray theory method. Montelli et al (2004) performed a comparison between 3-D ray theoretical and finite-frequency travel time on global tomography. Their results show that depending on the depth and size of the anomaly, the amplitudes of the velocity perturbations in the finite-frequency tomography images can be up to 50 percent larger than in the corresponding ray-theory images. I will investigate this for a regional tomography experiment. I am also motivated to do this study because the MARS array recorded many regional earthquakes that can be incorporated into the ray tomography method but not the finite frequency method. Chapter 5 will discuss the combined tomographic inversion using regional and teleseismic data.

Method

I used a recently developed tomography inversion package called tomo3d [Rawlinson (2005)] to generate a 3-D velocity model of the crust and upper mantle beneath Southwestern Mexico. Parameterization is represented by 3-D velocity nodes defined in spherical coordinates that have continuous smooth velocity fields between the nodes that are interpolated with cubic B spline functions. The tomo3d method utilizes 3-

D ray tracing and a subspace inversion technique [Kennett et al, 1988] to solve the delay time tomography problem. The 3-D ray tracing is a grid-based eikonal-solver that uses a modified finite difference method that is known as the fast marching method. This method has been tested and shown to be computationally efficient and stable (Rawlinson and Sambridge, 2004). The method is discussed in more detail in Appendix B.

The last step in seismic tomography is to solve the inverse problem that can be seen as a way to adjust the value of model parameters (m) to satisfy the data (d_{obs}). Seismic tomography inverts the differences between measured and predicted travel times (travel time residuals) of seismic waves to obtain deviations in seismic velocity from the starting model used to make the travel time predictions. Two common approaches to solve the inversion problem are using the back projection and gradient based method. In the back projection method, the travel time can be seen as an integral quantity along a raypath that is estimated using ray tracing technique. Then, the relationship between travel time perturbation (d) and slowness perturbations (m) can be linearized as

$$d = Gm \quad \text{.....(eq 4.1)}$$

where G is a matrix of ray lengths corresponding to the distance traversed by each ray in each block. The new updated (m) is then solved by either using the algebraic reconstruction technique (ART) or simultaneous iterative reconstruction technique (SIRT). Once the new updated model (m) is calculated, new ray paths can be re-calculated and the back projection is repeated until satisfying some convergence criteria.

The second method used in this study is the gradient based method that uses the derivative of model predictions in order to produce a solution. Let the data d be a vector dependent on a model m that can be written as d=g(m). The difference/misfit between

observed travel time and calculated data from a model [dobs – g(m)] gives an indication of the accuracy of the model and can be quantified by constructing an objective function S(m) consisting of a weighted sum of data misfit and regularization terms. A typical objective S(m) function can be written as

$$S(m) = \overbrace{(g(m)-d_{obs})^T C_d^{-1}(g(m)-d_{obs})}^{1} + \overbrace{\varepsilon(m-m_o)^T C_m^{-1}(m-m_o)}^{2} + \overbrace{\eta m^T D^T Dm}^{3}$$

…… (eqn 4.2)

where m are the model parameters, d_{obs} the observed data residuals, g(m) the predicted residuals, C_d the a priori data covariance matrix, C_m the a priori model covariance matrix, ε is damping parameter, η is smoothing parameter and D is a second derivative smoothing operator. The first part of the objective function equation 4.2 that contains data covariance matrix C_d, is an operator that calculates the difference between observed and predicted data. The second part of the equation that contains damping parameter ε is a regularization term that provides additional constraints on the solution and reduces the non-uniqueness of the solution. The third term of the equation that contains the smoothing parameter η is additional regularization that attempts to find an acceptable trade-off between satisfying the data and finding a model with a minimum amount of structural variation (Constable et al. 1987).

In this study, I use an iterative nonlinear approach to minimize equation 4.2 as the solution to the inverse problem. Starting with an initial model [m], the objective function is then minimized by updating the initial model using a subspace inversion scheme (Kennett et al., 1998). Note that we use the ak135 velocity model (Kennett et al, 1995) as

the initial model. Once the new model is obtained ($m_{i+1} = m_i + \delta m$), new 3-D ray tracing is then performed to update ray path and travel time information. The looping continues until the misfit between observed data and calculated data becomes small and does not. The subspace inversion solution δm of equation 4.2 is derived as:

$$\delta m = -A\left[A^T\left(G^T C_d^{-1} G + \varepsilon C_m^{-1} + \eta D^T D\right)A\right]^{-1} A^T \hat{\gamma} \qquad \text{…….. (eqn 4.3)}$$

where $A = \left[a^j\right]$ is the M x N projection matrix (M is the number of unknowns and N is the subspace matrix dimension), G is the Frechet derivatives matrix and $\hat{\gamma}$ is the gradient vector. A full derivation of this equation can be found in Rawlinson and Sambridge [2003].

Inversion

In this study, I used the same data measured by Yang et al. (2009) in their tomographic study of southwestern Mexico. In the Yang et al. (2009) study, travel times were measured in three different frequency bands as finite frequency kernels are different depending on the frequency band used. Ray theory is an infinite frequency approximation so I only used the high frequency band measurements (.5-2 Hz) from their study. The travel times came from 269 earthquakes with body-wave magnitudes greater than 5.3 at epicentral distances from 30^0 to 90^0 for direct P phases. Additional PKPdf phases at epicentral distances greater than 158^0 were also used. The relative travel-time delays of waves recorded by MARS and CODEX stations were measured by a multi-channel cross-correlation (MCCC) method [VanDecar and Crosson, 1990] for each event with respect to the IASP91 seismic model [Kennett and Engdahl, 1991]. The resulting data set of

relative travel times is highly accurate as shown by the value of the MCCC standard deviations of 12ms. In total, 7890 high-quality P wave arrivals, including 774 PKPdf phase arrivals were collected. The azimuthal distribution of P earthquake sources is good as can be seen in Figure 4.2.

The tomo3D tomography technique uses absolute residual travel times, recorded across an array, as data. The residuals measured at a seismic network are due to seismic velocity variations throughout the Earth and are also susceptible to errors in the location and origin time of the source. Figure 4.3 shows the average residuals for each station. Negative residuals mean the observed data arrives faster than the reference model predicted and positive residuals indicate slower velocity rock beneath the station. The residuals shown in Figure 4.3 are relatively small ranging from -0.6 to 0.6 sec with faster stations through the middle of the array.

Figure 4.4 shows station residuals from four events with different back azimuths (northwest, northeast, southeast and southwest). In this figure large changes in residuals can be seen depending on the incoming direction of the waves. For events northeast of the array fast residuals are seen in the eastern part of the array at a latitude of about 19^0N and from the northwest fast residuals are measured for stations near Colima Volcano. These waves are likely passing through the deep Rivera and Cocos slabs. From the south, waves pass perpendicular through the slabs and do not result in strong variations in times across the array.

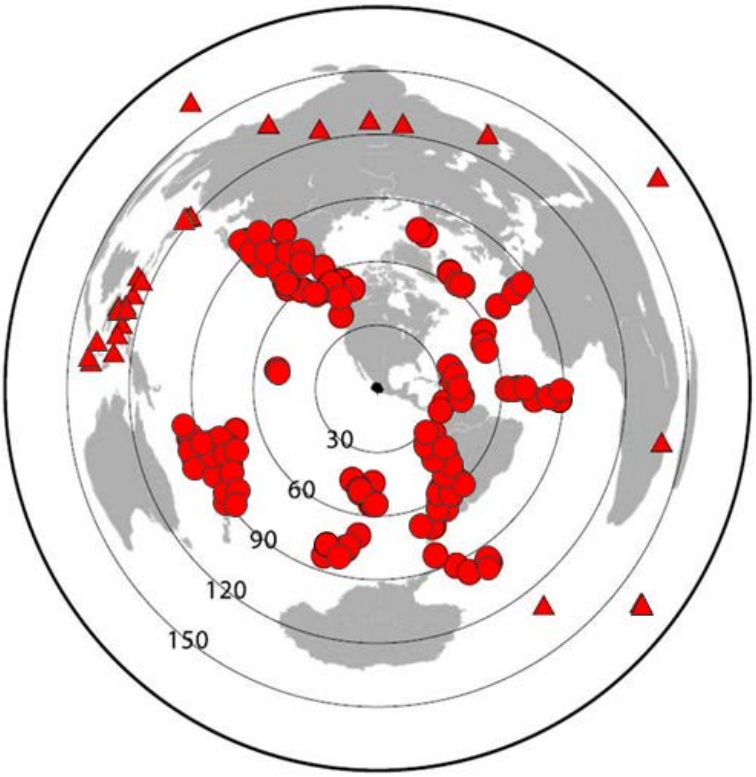

Figure 4.2 Source distribution map. The map is centered on Southwestern Mexico with the MARS seismic array shown as a black circle. Red circles are earthquakes for which P waves measured and red triangles are events that produced PKPdf arrival times.

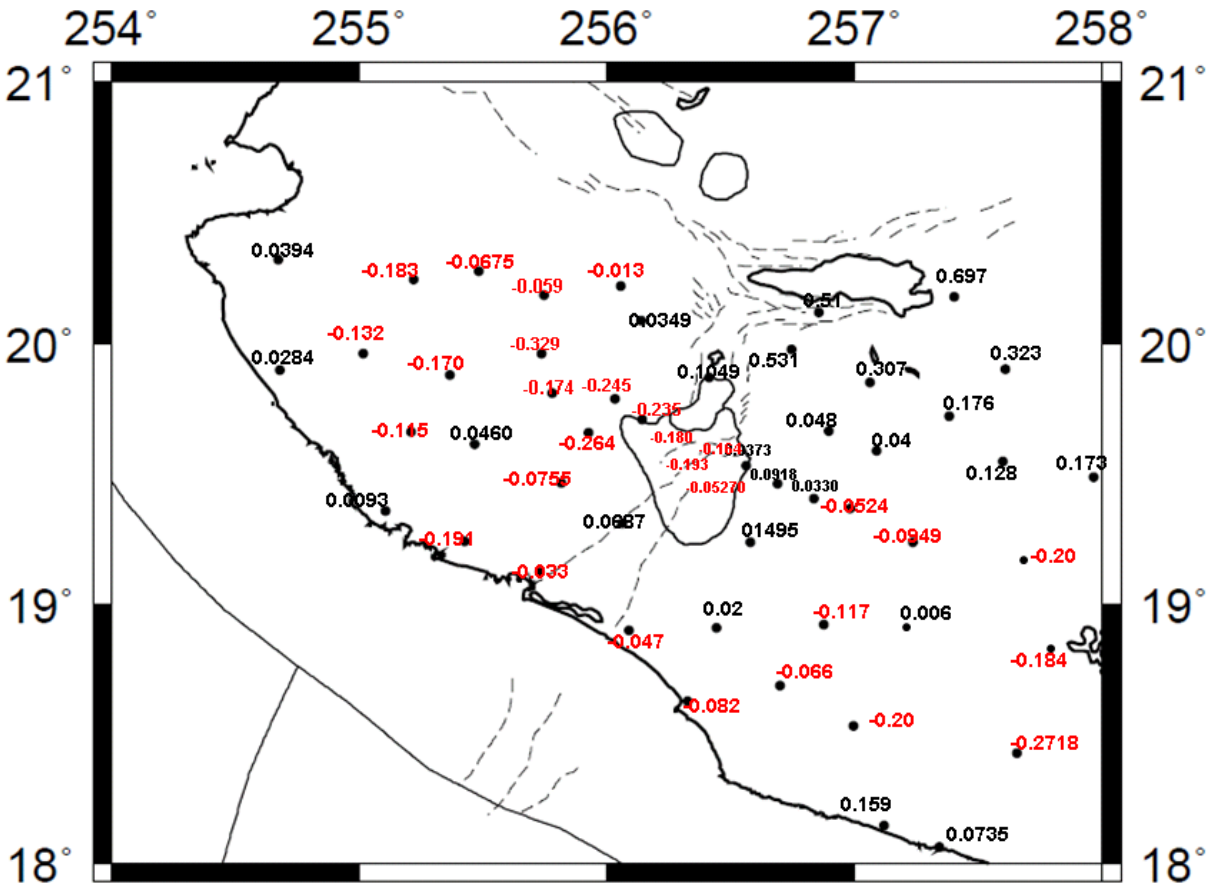

Figure 4.3 Map of average station residuals. The red numbers represent negative time residuals and black numbers are positive time residuals. All numbers are plotted in seconds.

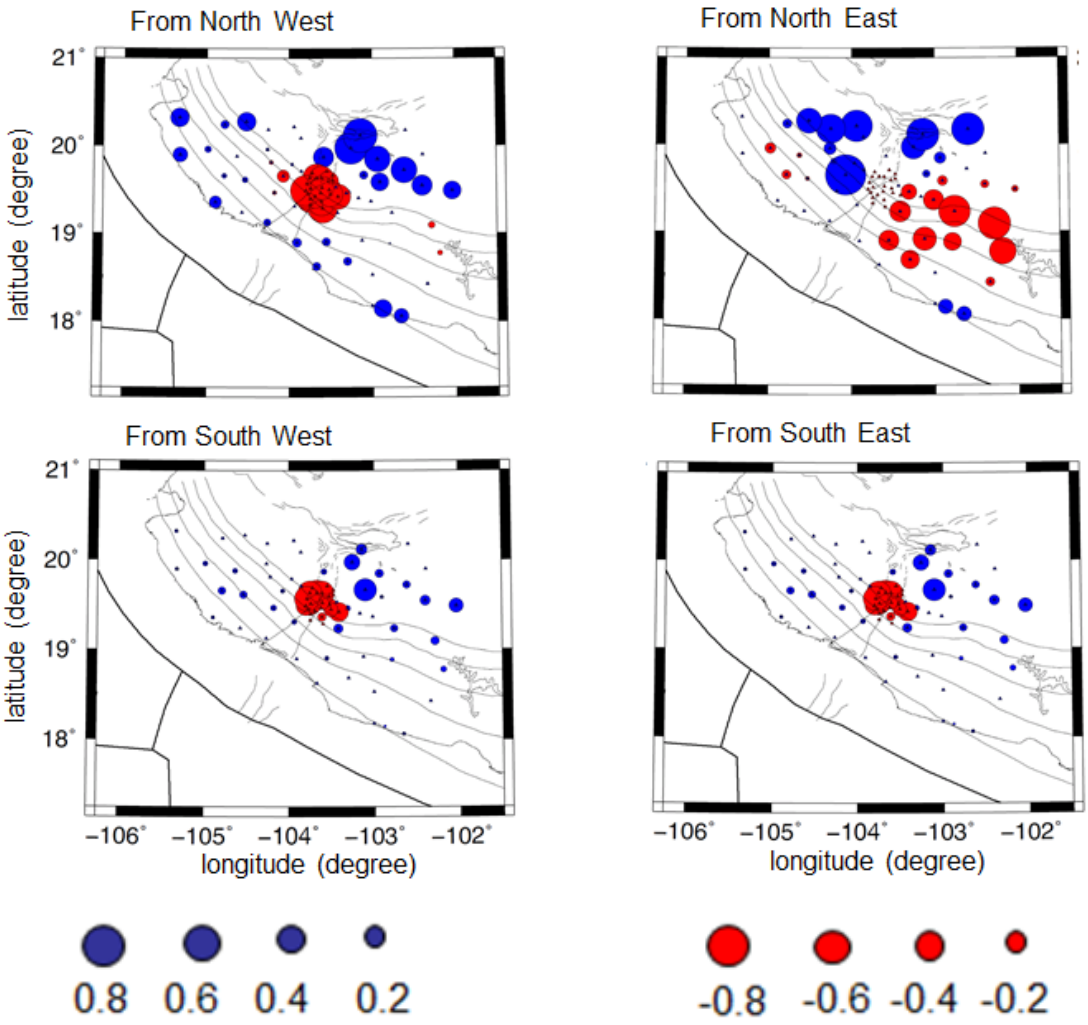

Figure 4.4. Circles show arrival time residuals (in seconds) from four different events from different back azimuths. Blue color represents positive relative time residuals (signal arrives slower than the reference model) and red color represents negative time residuals (signal arrives faster than the reference model).

The model volume consists of 61,380 velocity nodes spaced at approximately 20 km intervals in all three dimensions (latitude, longitude and depth) to represent velocity structure in the crust and upper mantle beneath Southwestern Mexico. The model spans 400 km in depth, 3.4^{o} in latitude and 5^{o} in longitude. Crustal thickness and velocity, obtained from the receiver function study discussed in chapter 3, were incorporated into the starting model. For the starting model below the crust I used the ak135 global reference model (Kennett et al, 1995). The travel time residuals were also corrected for elevation differences of the stations.

The inversion procedure was carried out in six iterations of a 20-D subspace inversion routine. The forward problem is solved at every iteration to obtain new travel times, ray paths, and Frechet derivatives. The difference between observed data and calculated data decreased significantly in the first 3 iterations but did not change much after the fifth iteration. For this reason the inversion was terminated after six iterations. A trade-off analysis of the model norm versus variance reduction [Menke, 1989] is performed to determine the damping factor and the smoothing weight. Figure 4.5 shows the steps to determine the number for damping and smoothing parameters. I initially start with damping parameter (ε) equal to 1 and vary the smoothing parameter from 300 to zero. The optimum smoothing parameter is chosen as the model with maximum smoothness that still fits the data to a high degree. Once the optimum number is selected, I repeated the same process by varying the damping parameter with the chosen smoothing parameter. The optimum number for the damping parameter is 5 and the optimum smoothing parameter is 10. These values are used for the final inversion.

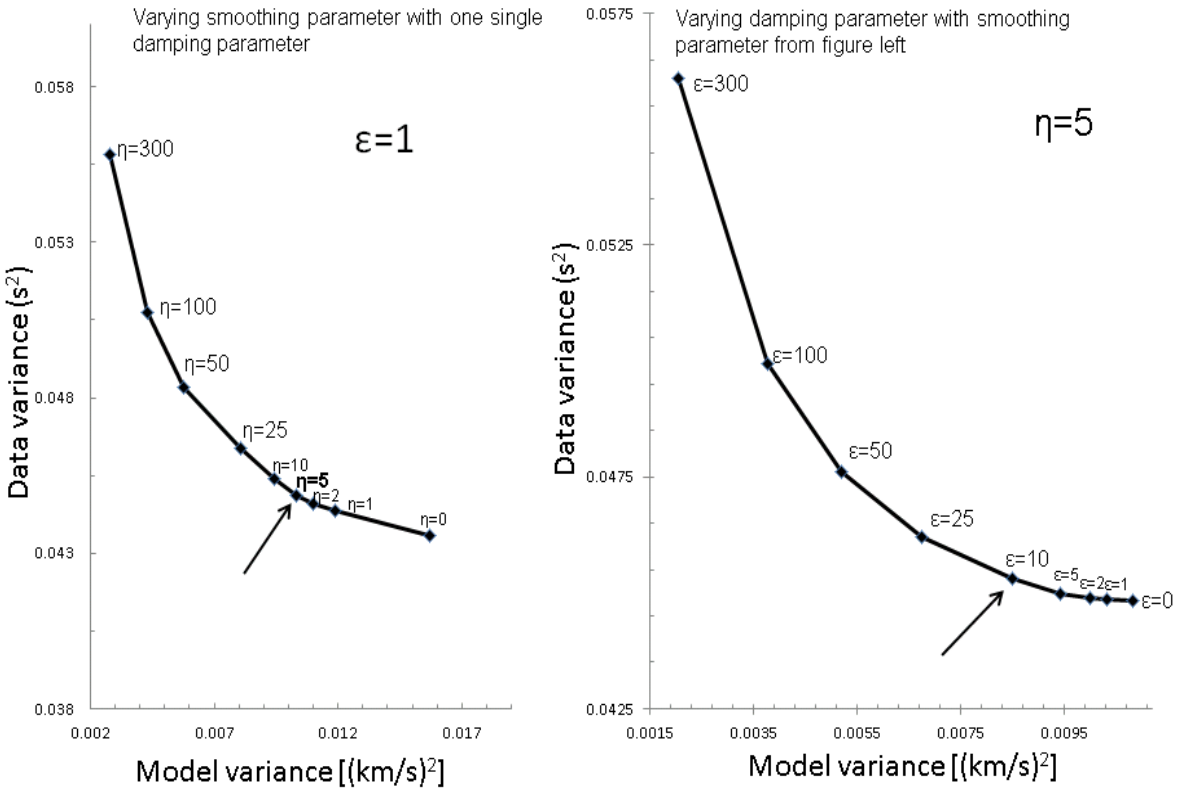

Figure 4.5 Steps to determine the damping and smoothing parameter for the inversion. Left, the model variance is plotted against the data variance while varying the smoothing parameter (η) between 300 and 0 with the damping parameter ε=1. Right, varying the damping parameter (ε) between 300 and 0 with a η=5. The final optimum number for the inversion (shown with the arrow symbol) are : smoothing parameter (η) =5 and damping parameter (ε)=10.

The final model reduces the data variance by 84% from 0.1423 s^2 to 0.0392 s^2, which corresponds to an RMS reduction from 377 ms to 199 ms. Histograms showing the distribution of time residuals using the initial and final models are shown in Figures 4.6. Before the inversion, most of the residual arrival times fall in a range -0.75 s to 0.75s with a relatively normal distribution and wide variance. After inversion most data now fall in a range of -0.3s to 0.3s.

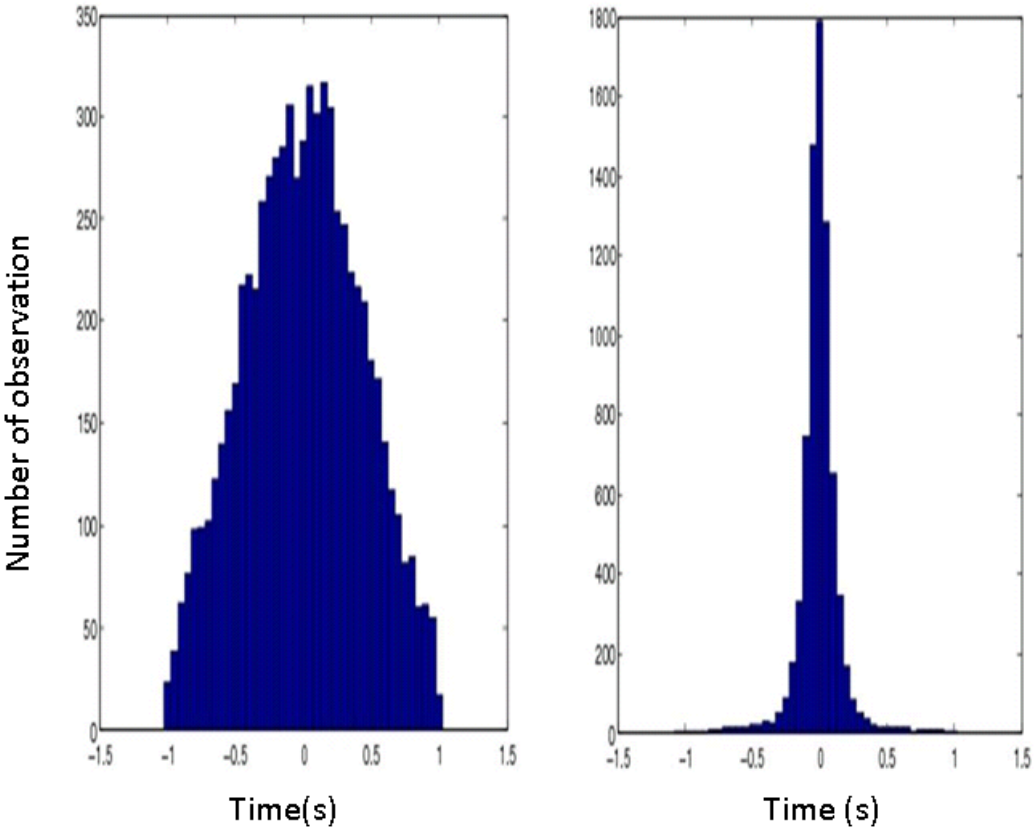

Figure 4.6. Residual histograms before (left) and after inversion (right).

Resolution Test

Resolution in most teleseismic tomography studies suffers to some extent due to most problems being under determined which happens when there is an un-balanced condition between unknown parameters and the available recorded data set that can lead to a non-unique solution in inversion. I performed a “checkerboard” synthetic experiment to test the robustness of the model. In the checkerboard test, the model is divided into alternating regions of high and low velocities. I divided the model into squares that have a maximum velocity of 0.1 km/s and a minimum velocity of -0.1 km/s relative to the ak135 velocity model. This corresponds to about 1.2-1.5% velocity differences (Figure 4.7). The highest amplitude of the anomaly is located at the center of the cube and decreases outward. The size of the cubes is about 160 km horizontally and vertically and spaces are located between cubes. A set of travel time residuals are calculated using identical sources, receivers and phase types as the observational data. The data are then inverted using the subspace inversion technique outlined above. Gaussian noise with a standard deviation of 10 ms is also added to the synthetic data sets to simulate the noise content of the observed data. The difference between the true model and the recovered structures indicate which regions of the model are well constrained by the data. Horizontal and vertical slices through the recovered models are shown in Figures 4.7 and 4.8.

The inverted synthetic models show good recovery in terms of the shape of the input anomalies down to 400-km-depth although the amplitude recovered in some cubes is lower than the input model. The quality of recovered images decreases on the sides

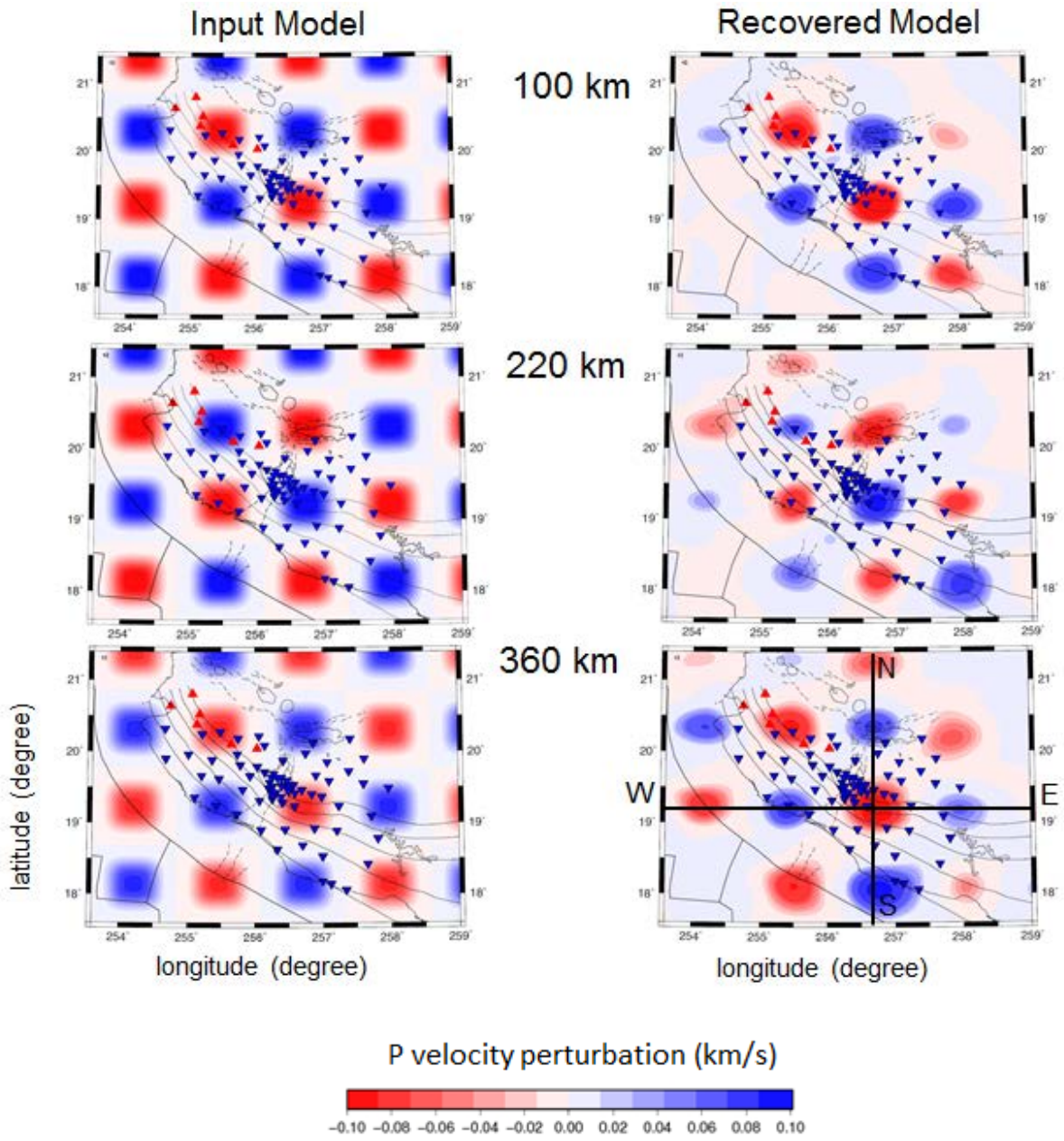

Figure 4.7. Inverted checker board model at different depths. Red color shows slow velocity anomalies and blue color shows fast velocity anomalies. The A-B and C-D lines are cross sections shown in figure 4.8.

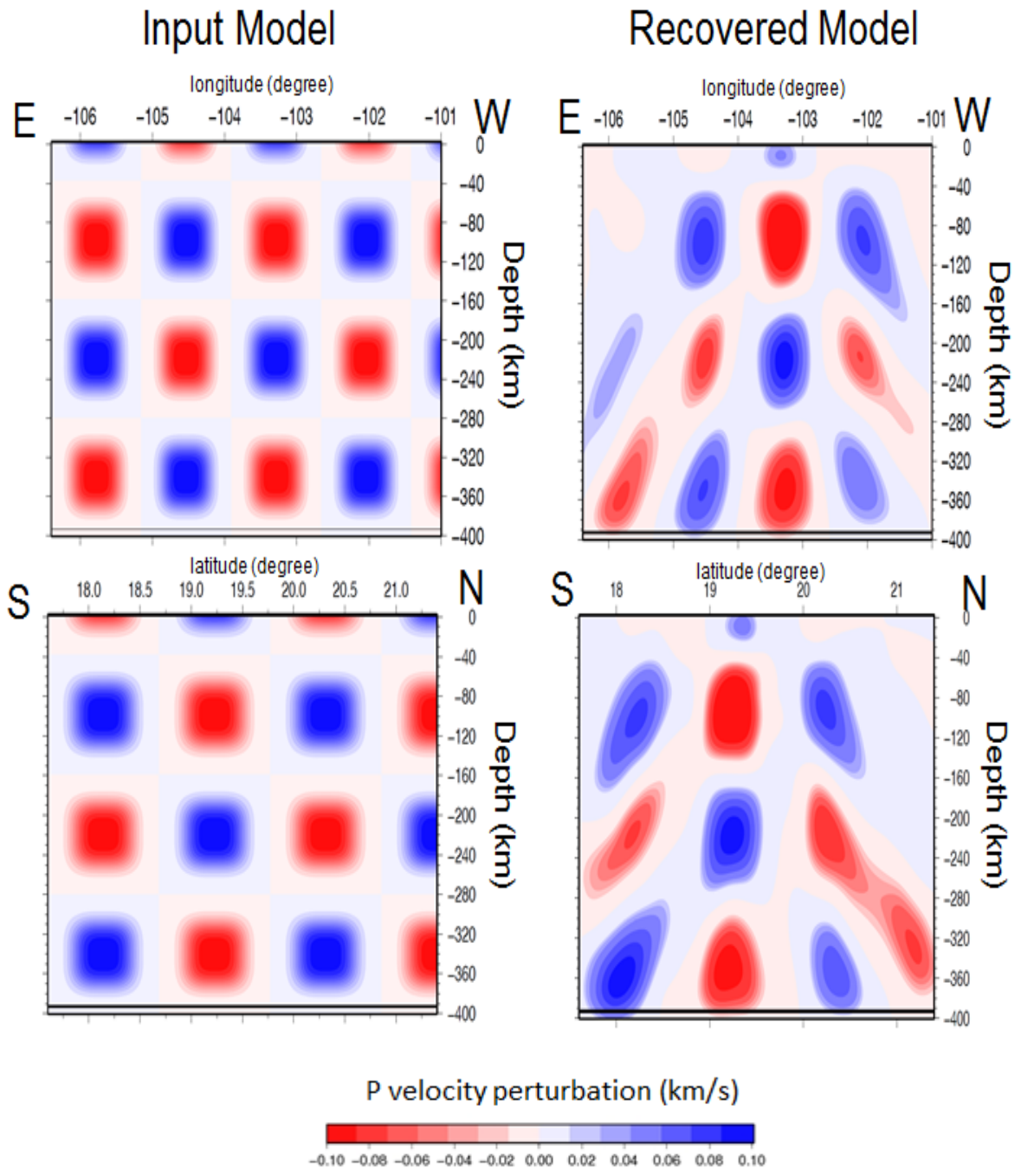

Figure 4.8. The right figures are the cross section recovered models and the left figures are the input models. Smearing is seen on the edges of the model especially for slow velocity anomalies. A-B and C-D map view can be seen on figure 4.7.

of the model as seen in figure 4.8. Vertical streaking is visible through most of the model but especially at the edges where there are no crossing paths. Still, the streaking does not extend more than about 50 km.

In classical tomography, where raypaths are fixed by the starting model, resolution tests such as discussed above do not depend on the amplitude of the anomaly i.e., one can scale the results above to larger or smaller amplitude anomalies. In this work, however, rays are traced through 3D structures. Even with a similar pattern, the raypaths will be different depending on the amplitude of lateral heterogeneities. To investigate this effect on resolution, I performed checker board tests with different amplitude anomalies keeping the spatial extent of anomalies the same. I ran inversions with the maximum input anomaly +- 0.2 km/s and +-0.9 km/s that corresponds to about 2.6-3% and 11-15% velocity differences respectively. Note that I use the same data input, noise level, and inversion parameters in the inversion process as before.

In general, the higher amplitude tests show worse results than the low amplitude study (Figure 4.9 and 4.10). The model with a 3% amplitude input shows similar results in pattern compared to the 1.5% amplitude model but has less amplitude recovery especially at deeper depths. The inversion result for an input model with 13% amplitude variations is far worse than the lower amplitude model results. The checkerboard pattern is not seen well and fast velocity anomalies dominate the slow velocity anomalies especially at shallow depths. This model also shows that slow anomalies in general are less well recovered compared to the lower amplitude results. The reason for this is that according to Fermat's principle, raypaths follow the path of least time. Thus in 3D structure the rays tend to follow the high velocity zones and avoid the slower regions and

thus the density of raypaths ends up higher in the fast anomalies. This effect, combined with the smoothing and damping in the inversion results in the strong fast anomalies showing up in the inversion and the relatively weak recovery of slow anomalies.

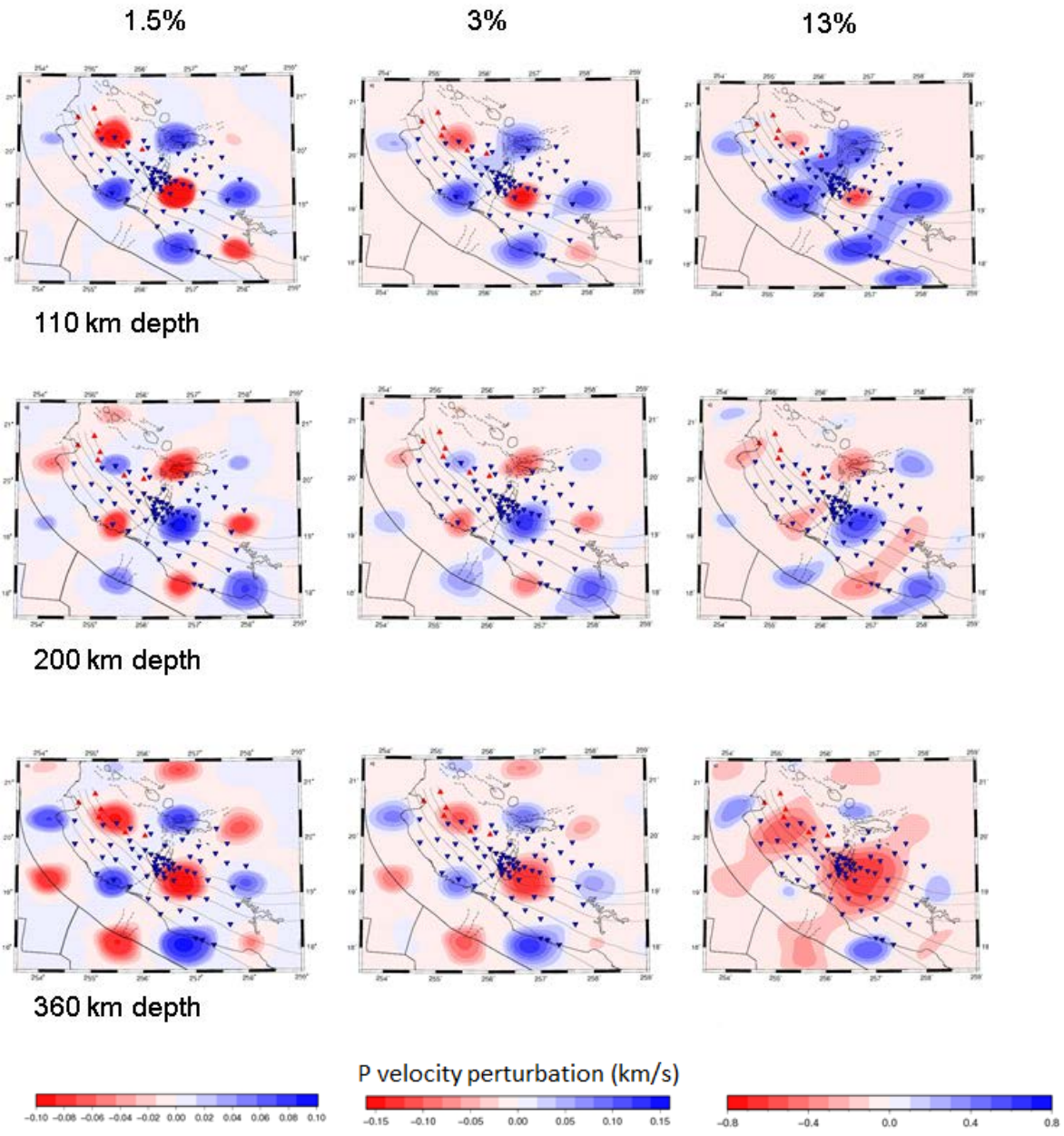

Figure 4.9. Recovered checker board tomography models at different anomaly input. Left is recovered model using a 1.5% anomaly input, the center is the recovered model using a 3% anomaly input. On the right is the recovered model using a 13% anomaly input with respect to the ak135 velocity model.

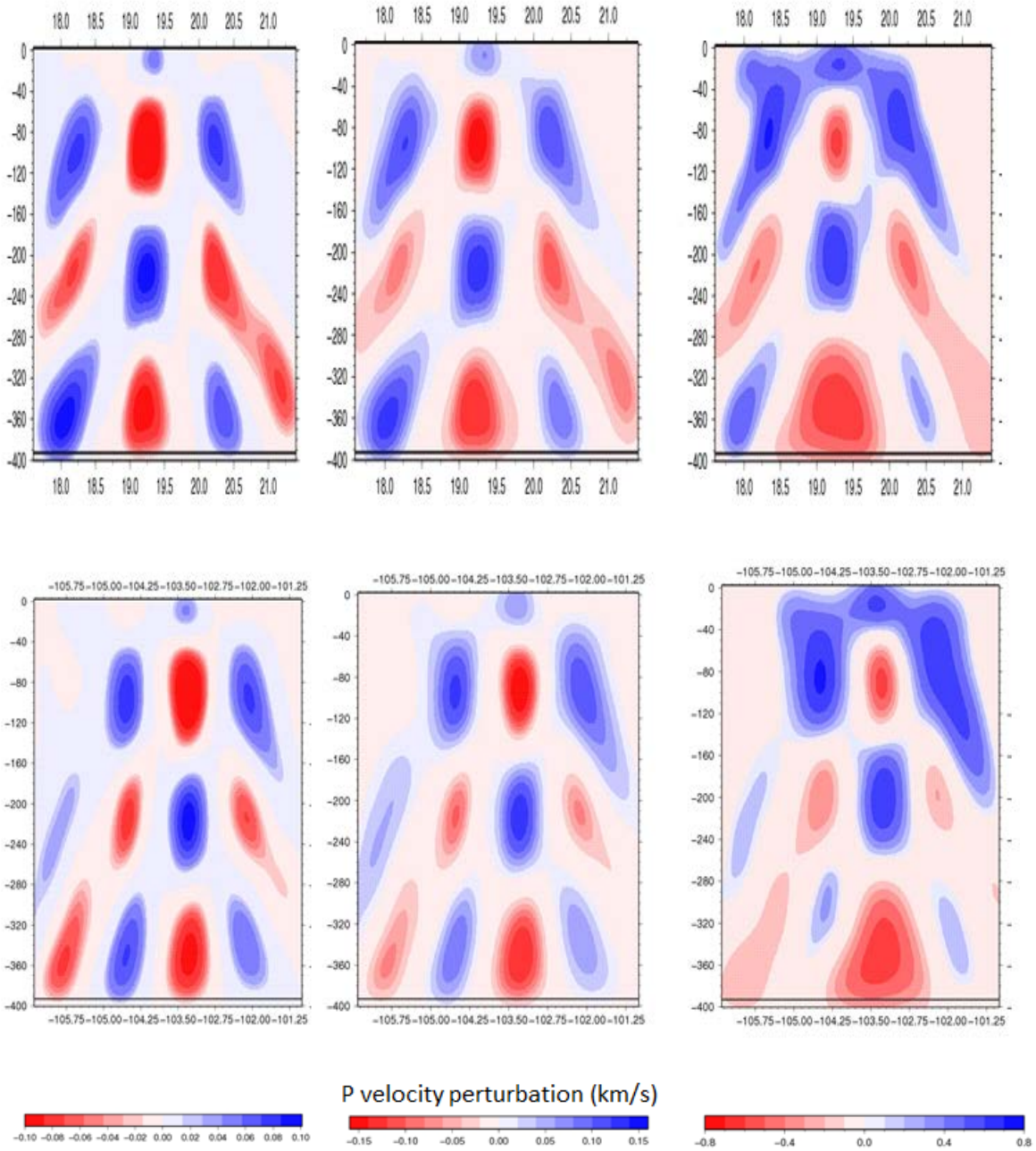

Figure 4.10. Cross sections along line A-B (top) and C-D (bottom) for different anomaly inputs. Left is using a 1.5% anomaly input, center is using a 3% and right is using a 13% anomaly input.

Tomographic Model

The final tomography model is shown and compared to the model of Yang et al. (2009) in Figures 4.11 and 4.12. It should be noted that the data used in both studies was similar but different approximations were used in the two studies. The two models show similar results with a few possibly important differences. Both models show a northwest-southeast band of high velocities that dips to the northeast. Yang et al. (2009) interpret this feature to be the subducting Rivera and Cocos slabs. A gap in the high velocity band has been interpreted as the boundary between the two subducting plates that diverge at depth thus allowing upwelling asthenosphere that feeds Colima Volcano. I find the gap to be a little deeper (~230 km) than the Yang et al. (2009) study but agree on the interpretation.

The main difference between the two studies is in the sharpness of the high velocity structures (slabs) and the amplitude of the slow velocity anomalies. These differences are seen more clearly in Figure 4.13 that shows a comparison of cross sections through the two models. The finite frequency results showed high velocity anomalies that broaden with depth and were interpreted as slabs. Due to the broadening it appeared that the slabs changed dip at depth. In contrast, the 3D raytracing results show slabs that maintain their thin width and dip with increasing depth (Fig. 4.13 sections A4-B4 and A1-B1). I feel the 3D raytracing result is more reliable because rays will tend to travel within the high velocity anomalies to obey Fermat's principle and can thus be concentrated into thin fast structures. The finite frequency results do not account for the perturbation of the raypaths and thus fast arrivals are backprojected over a broad region as predicted by 1D raytracing when in fact the raypaths have been perturbed into the

narrow slab. My result shows imaging and interpretation of subducting slabs require 3D raytracing to properly account for the width of the slab and its trajectory.

The second difference between the two approaches is in the amplitude of the slow anomalies. In the finite frequency results, figures 4.11 and 4.12 show very slow velocities in the north from shallow depths to 300 km depth. It should be noted that these slow anomalies are slower than the mantle to the south of the slab near the coast. Since the mantle beneath the slab to the south is presumably asthenosphere the implication of the slow velocities to the north is that this mantle is anomalous, perhaps with higher temperatures or with higher water content than normal asthenosphere. The 3D raytracing results also show anomalously slow mantle to the north down to a depth of 150 km or so but below 150 km depth, the velocity of the mantle in the north is similar to the mantle velocities to the south beneath the slab. As discussed above, ray theory tomography does a poor job of imaging slow anomalies whereas finite frequency tomography includes wavefront healing and thus does a better job of imaging slow anomalies. On the other hand, if the fast anomalies (slabs) are artificially widened in the finite frequency tomography, it may be that the extreme slow anomalies are just compensation for the misplaced deep fast anomalies and thus are not real features of the mantle beneath Southwestern Mexico. I note that the discrepancy in slow structure between the two inversion techniques occurs at the edge of the seismic array and thus is a region with relatively poor coverage. To determine which model is correct would likely require increasing data coverage to the north or perhaps attempting to model 3D regional or teleseismic waveforms that sample the northern part of our study area. With my current results, it is difficult to determine which inversion results are closer to the true structure.

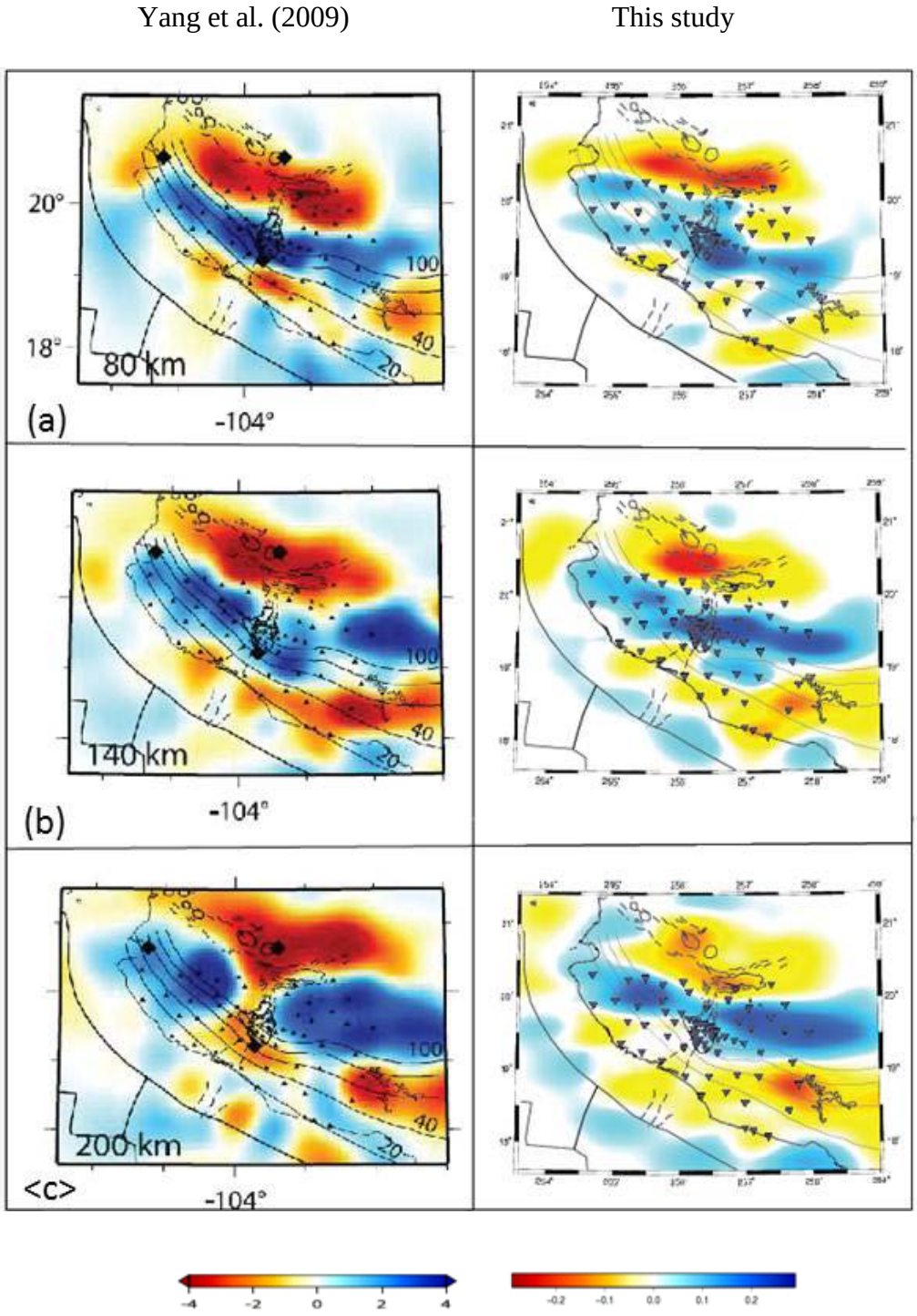

Figure 4.11 The final inverted model at depths of 80 km, 140 km and 200 km. The left side shows the results of a finite frequency inversion by Yang et al. (2009) and the right side is the final inversion from this study.

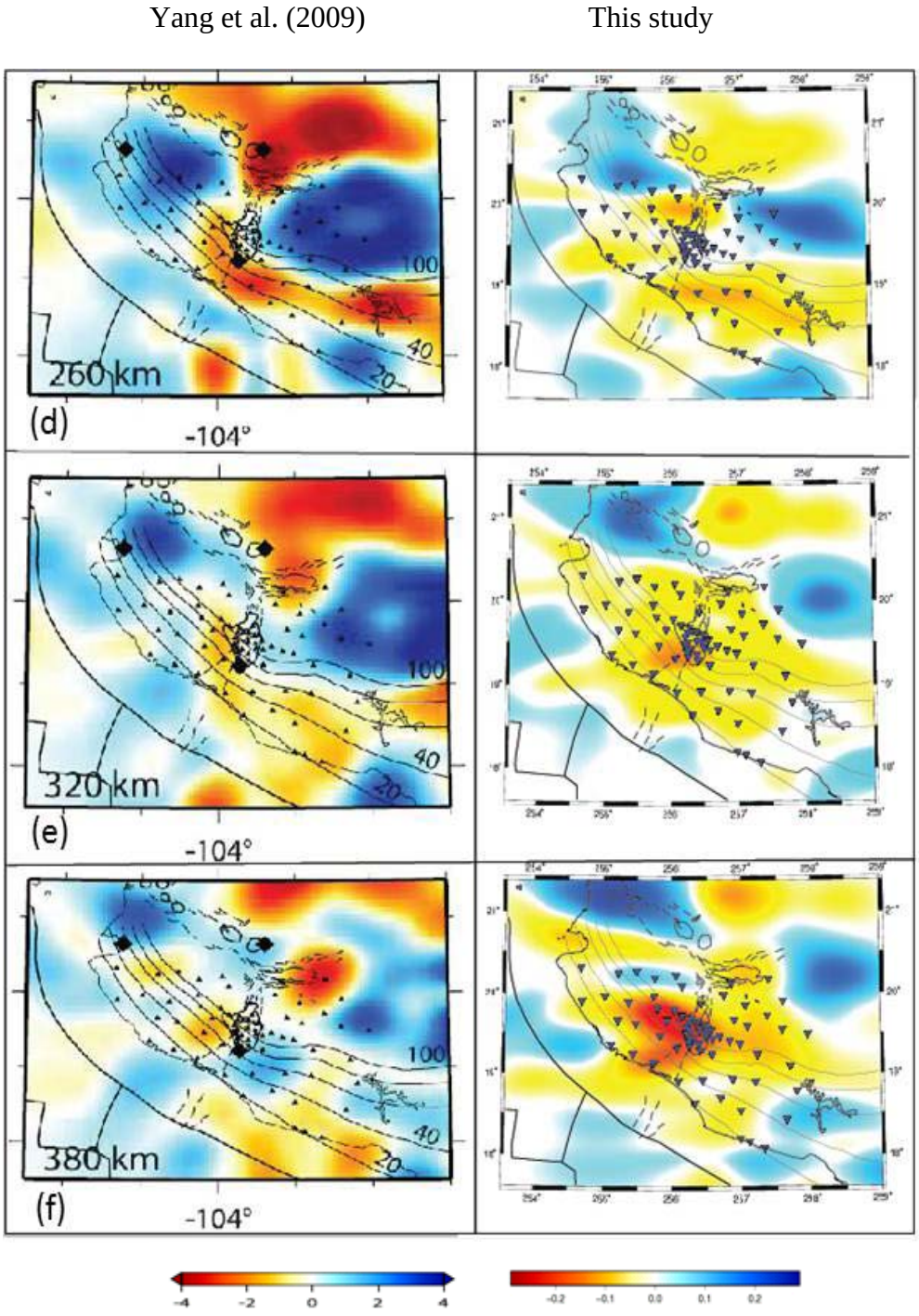

Figure 4.12 Tomography model at a depth of 260 km, 320 km and 380 km. The left side shows the result of previous finite frequency inversion from Yang et al. (2009) and the right side is the final inversion of this study.

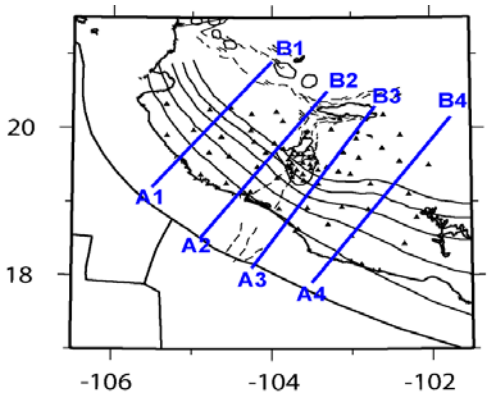

Finite frequency Tomography

3-D Ray Tomography

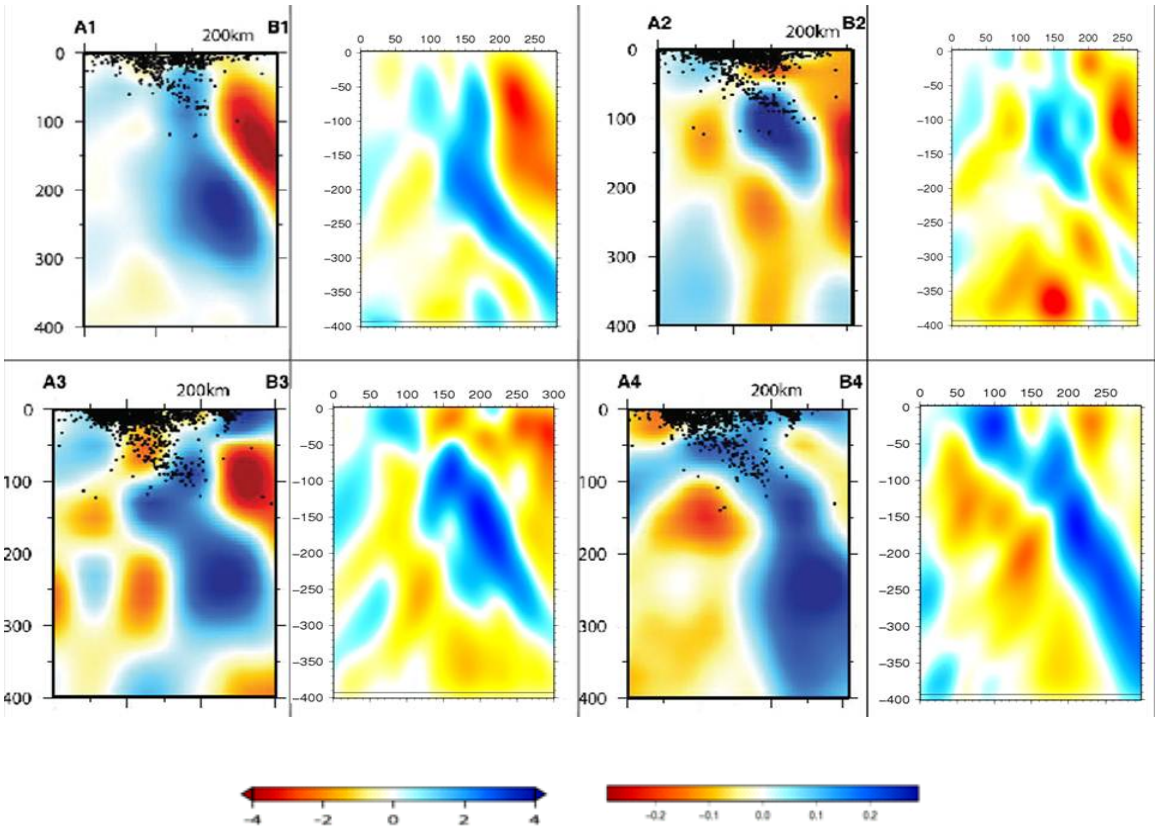

Figure 4.13. Comparison between finite frequency tomography results (left) and 3-D ray tracing tomography results (right) along cross sections located in the top.

Discussion

In this chapter I have compared two approaches to regional tomography applied to Southwestern Mexico. The two methods both involve approximations and show differences in the images produced. Using 3D raytracing but neglecting the finite sampling of structure by seismic waves produced sharper images of fast velocity structures in the mantle. In my work, the deeper slabs are more coherent and show less broadening with depth than inversions using 1D finite frequency kernels. This has implications for the amount of deformation in slabs as they descend through the upper mantle. I also find that deep slow anomalies that were found using finite frequency kernels are more subdued using the ray theory approach. This is to be expected as the finite frequency kernels take into account wavefront healing. Although the finite frequency and 3-D ray tracing models show some differences in amplitude and pattern, the overall agreement of the models supports the interpretation of Yang et al. (2009) that slab steepening is occurring in South Western Mexico leading to a coastward migration of volcanism. Our models support the idea of Ferrari et al (2001) who proposed that the dip of the Rivera slab increased when the convergence rate slowed between 8.5 Ma and 4.6 Ma resulting in slab roll back. This model can explain the trenchward migration of the volcanic front and the mixed geochemical signatures observed on the western TMBV. Both models also show a gap between the Cocos and Rivera slabs near 200 km depth and close to the location of Colima volcano.

One difference between the finite frequency and ray theory results that does contradict an interpretation from Yang et al. (2009) concerns the deep structure of the

Rivera slab. Ferrari (2004) analyzed the age of mafic volcanism and proposed a tear in the subducting slab that propagated from the Gulf of California to the Gulf of Mexico during the late Miocene. The location of the west to east tear is projected to be roughly beneath the northern part of the TMVB. The finite frequency models show that the Rivera slab is observable to a depth of about 300km but fades away at greater depths. Yang et al (2009) suggest that the Rivera slab tore at depth and the shallow part then steepened and rolled back. They also suggest that the Cocos slab may have also torn but the detachment is at a deeper depth. As can be seen in Fig. 4.11 cross section A1-B1, the finite frequency inversion shows an end to the subducting Rivera plate at about 300 km depth. Yang et al. (2009) interpreted this as the location of the end of the slab that tore and then rolled back. As can be seen in the same figure, the 3-D ray tracing model shows a clear fast velocity band down to a depth of 400km along A1-B1 and thus our model does not support a slab tear of the Rivera plate above 400 km depth. If a tear in the slab did occur, the slab end is deeper. Unfortunately, the resolving power of both our tomography inversions becomes weak at deeper depths, especially to the north.

Chapter 5: Joint inversion of teleseismic and local data for seismic structure and source location in Southwestern Mexico

Introduction

Seismic wave tomography is a reliable method for imaging subsurface velocity variations at a variety of scales; however, most applications only involve a single type of data set. On a regional scale, inversions that use teleseismic data have the capability to resolve structures down to a depth of about 400 km as discussed in the previous chapter. However, regional teleseismic inversions tend to have poor depth resolution at shallower depths due to the fact that teleseismic ray paths are near vertical. If an experiment is conducted in a region with abundant local seismicity, regional data that propagate at shallow depths can potentially provide better depth resolution in the crust and shallow mantle than teleseismic data alone. Although inversion of local data promises high resolution at shallow depth, a lack of events and the relatively small apertures of most regional arrays, limits the resolution that can be obtained at greater depth. Figure 5.1 shows an illustration of raypaths of teleseismic and regional raypaths. Note the different sampling that the regional waves provide.

A joint inversion using both regional waves and teleseismic waves should result in a better resolved model than a model using only one of the data sets. A number of studies have attempted joint inversions of complementary data; Thurber [1983] and Ankeny et al. [1986] combine data from explosive sources and local earthquakes in local refraction tomography studies; Parsons and Zoback [1997], Sato et al. [1996] and Zhao et

al. [1997] have simultaneously inverted local earthquake data and teleseismic data to image crust and upper mantle structure; and West et al. [2004] jointly invert surface and body wave data in an inversion for crust and mantle structure.

In this study, I simultaneously invert teleseismic and local event travel times to better define 3-D velocity variations and seismicity beneath southwestern Mexico. In this effort I also include source relocation of the regional events as unknowns in the inversion to obtain a more accurate hypocenter map that will better constrain the geometry of the subducting Cocos and Rivera slabs as well as more accurately locate shallow seismicity within the overriding plate.

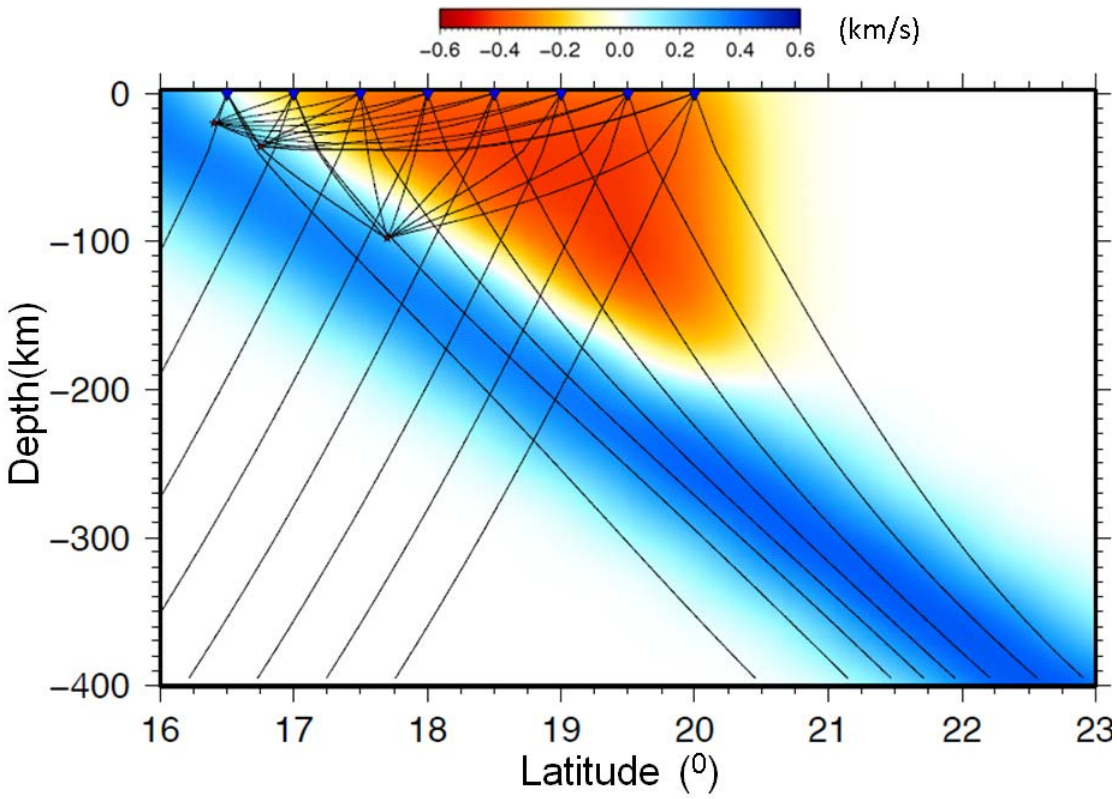

Figure 5.1 Illustration of regional and teleseismic raypaths. The velocity model has a dipping fast velocity anomaly (6% faster than the ak135 velocity model) representing the down-going slab and a region of slow velocity (-6% slower than the ak135 velocity model) above the dipping fast velocity. Rays from two teleseismic events at 60^0 distance and 30^0 distance, respectively, are shown. Rays from three local events associated with the subducting slab illustrate the coverage of seismicity and raypaths in this study.

Data

The same teleseismic data set as in chapter 4 (Yang et al., 2009) was used. Two different methods were used to collect regional data from local sources. First, I visually observed waveforms at every station and picked strong P and S phase arrival times using antelope software. I chose events that show strong P and S wave arrivals visible on most of the stations. However, since this method is time consuming, I only gathered two months of data using this manual approach. For the rest of the data, we used an arrival time catalog produced by a recently developed automatic picking algorithm (Gardine, 2008). The automatic picking algorithm process in antelope uses two algorithms, the dbdetect algorithm reads and processes seismograms (in my study a 1-10 Hz band-pass filter was applied to remove some of the high-frequency cultural noises) in two moving time windows, a short-time average window (SLA) and long-time average (LTA) window. Next, the ratio of the SLA and LTA is used to detect a potential event by flagging any times where the amplitude of the trace is significantly above background noise (Figure 5.2). An event is defined when at least six stations have detections with travel times within a reasonable time window. Once an event is identified, a potential candidate arrival time is picked for each recording station, more detailed information and explanation about the dbdetect algorithm can be found on http://www.brtt.com/w/index.php?title=Orbdetect(1).

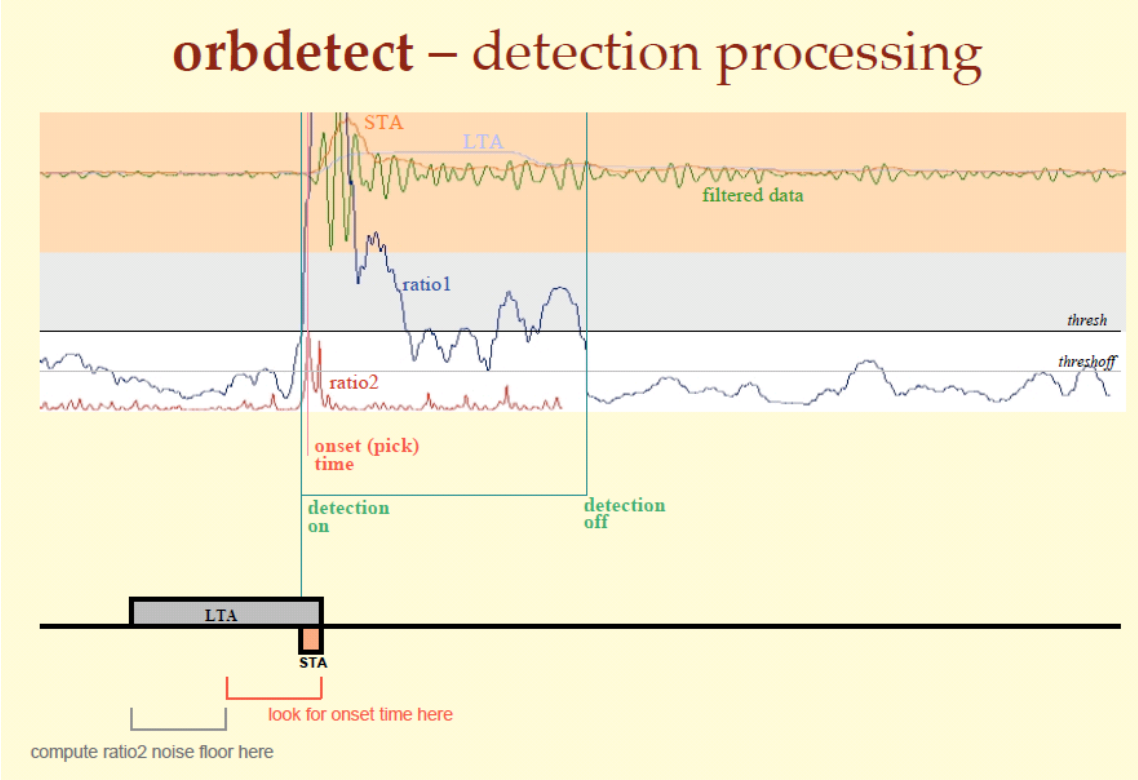

Figure 5.2 An example of the detection process done in Antelope. A short-time average window (STA) shown as a red line and a long-time average window (LTA) shown as a blue line are calculated from filtered data. Next, ratio1 (shown as a darker blue line) of STA to LTA is calculated. Once the ratio1 line passes the threshold line, dbdetect will pick the arrival time. Ratio2 which is the true signal to noise ratio based upon the ratio of time-abutting signal and noise windows is used when there is not enough data. The figure is taken from http://www.brtt.com/events/iris2002/pdf/danny.pdf

To locate events, code dbgrassoc reads candidate arrival detections from dbdetect and searches over a spatial grid for a hypocenter estimation. A potential hypocenter will create a theoretical moveout for each recorded station and the best estimation is taken that best matches all arrival observations. The dbgrassoc code outputs are hypocenter location (longitude, latitude, depth), origin time and all arrival information (phase and arrival time). More information about dbgrassoc can be found at http://www.brtt.com/w/index.php?title=Orbassoc(1). Gardine (2008) used the IASP91 global 1-D velocity model for the calculation. Figure 5.3 shows some example seismograms for an event that was detected using the automatic picking scheme for stations MA22 and MA50 on the vertical component (BHZ). I re-inspected and picked more arrivals at other stations for this event and all other events in the catalog that the automatic picking code missed. Figure 5.4 shows another event that was detected with the automatic picking scheme at 12 stations. Note that for the S wave first arrival picking, I rotated the North-South and East-West components for each station into radial and tangential components before re-inspecting and re-picking. In general, the arrival times from the automatic picking agree with visual picking with an estimated error under 10ms. In total, I found 1406 events with 16,478 high-quality regional P wave arrivals for the joint inversion. With the addition of teleseismic events, 25,080 P wave arrivals were gathered for this study. A set of regional first S wave arrivals (7499 arrivals) are also added for use in a double difference earthquake location scheme before performing a joint inversion. Figure 5.5 shows a map of the epicenters from the automatic picking catalog as well as all the events from automatic picking and manual picking. Cross sections are also shown. Dipping Benioff zones are obvious with shallower events near

the coast that get deeper further inland although some shallow events are also found further inland. Although a dipping Benioff zone is obvious, the seismicity is diffuse. Figure 5.6 shows a seismicity map showing the estimated magnitudes found from the antelope software code. Although there is no clear pattern, most of the large magnitude events are along the coast with the deeper events (>75 km) having smaller magnitudes.

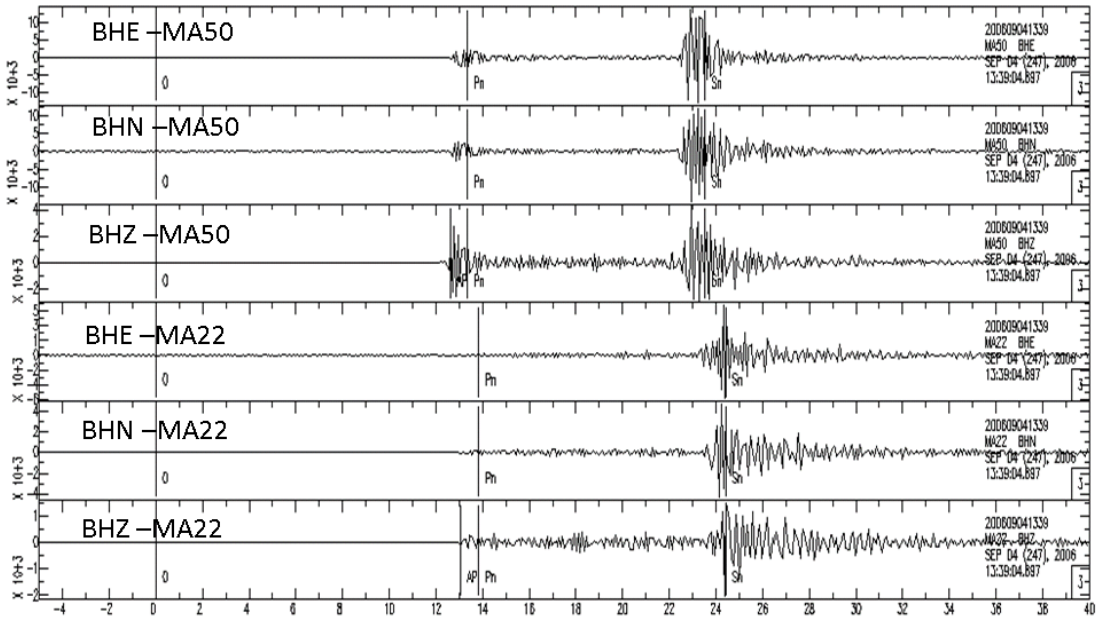

Figure 5.3 Examples of seismograms used for the automatic picking algorithm (Gardine, 2008) for two stations that have had the mean removed and were tapered and filtered. AP shows where the automatic picking chose the P wave arrival at station MA22. The event occurred on 9/4/2006 09:13 at 19.0553 latitude and -102.807 longitude at a depth of 77 km with 3.1 magnitude.

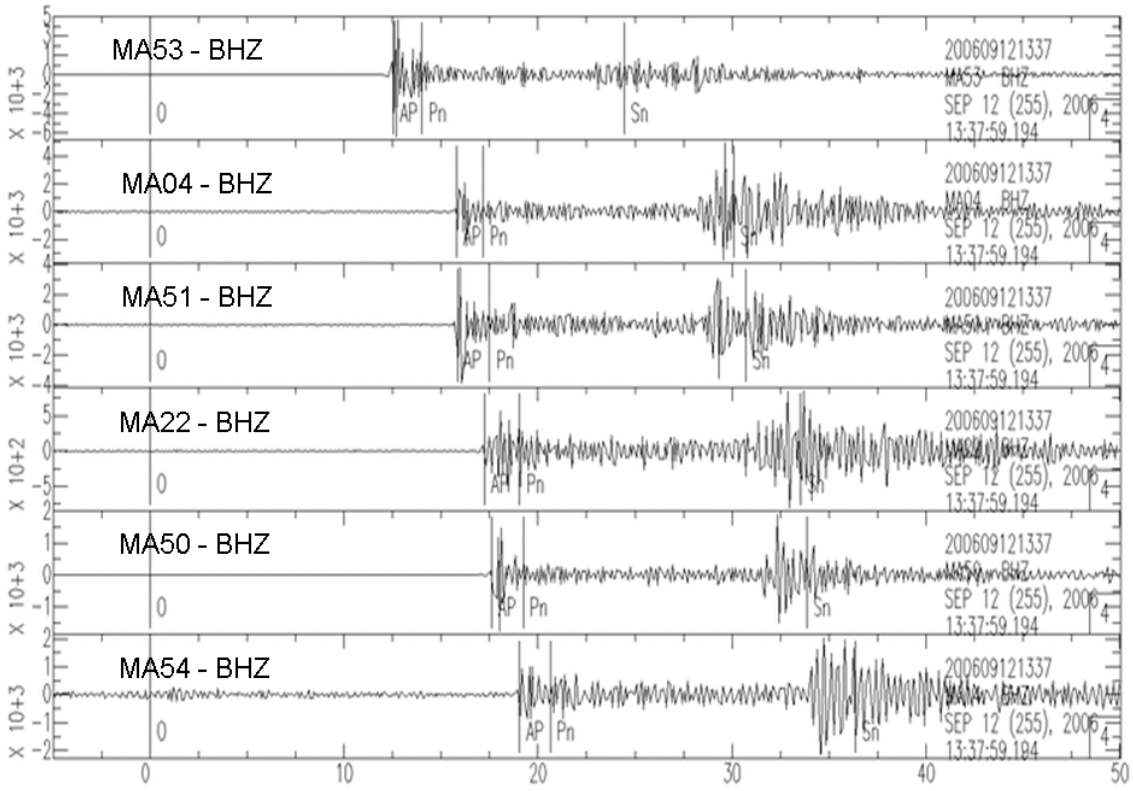

Figure 5.4 Another example of regional seismograms from an event that occurred on 12th September 2006 at 19:23 at 18.6774 latitude and -102.322 longitude at a depth of 28.8 km with a 3.3 magnitude. This event was detected by 12 stations and the seismograms show the first 6 arrivals.

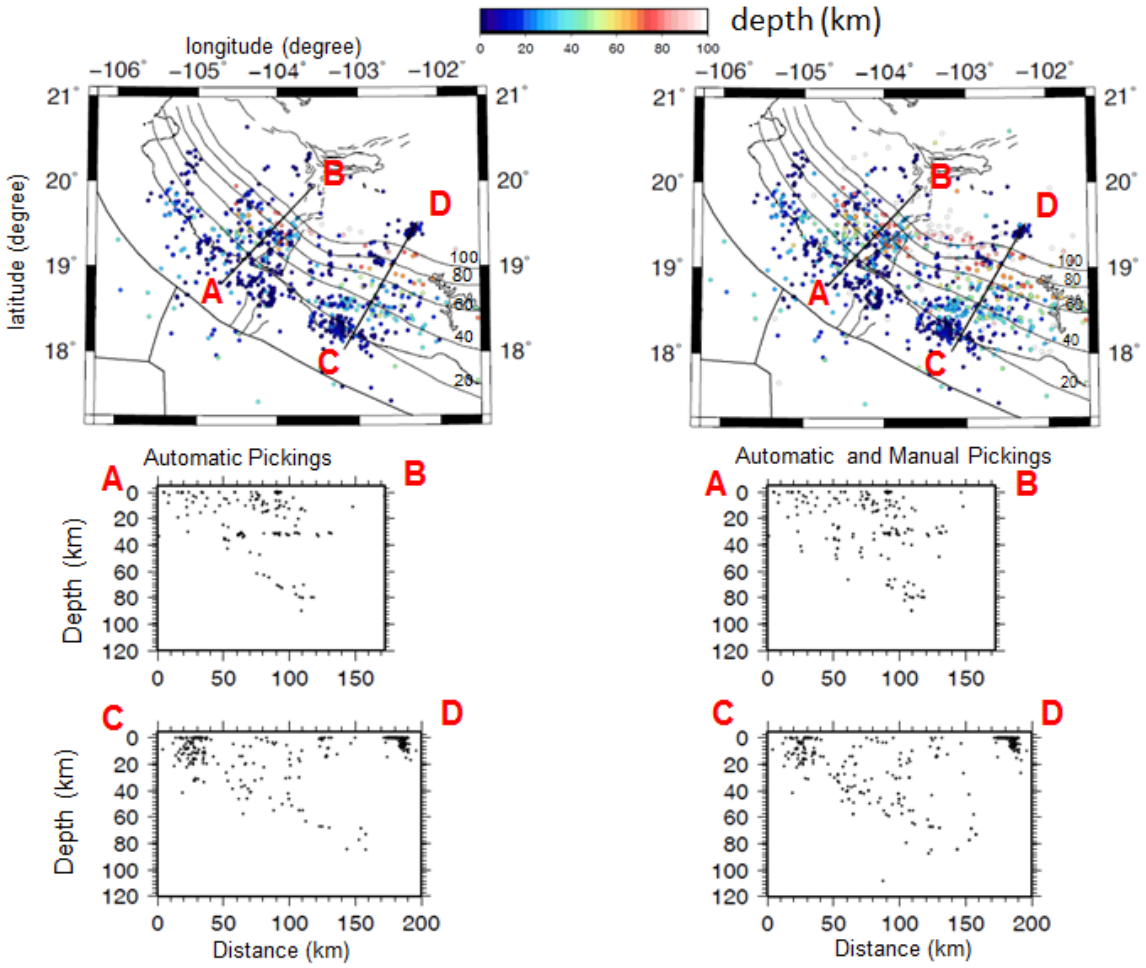

Figure 5.5 Top left is a map of epicenters found from the automatic picking algorithm. Top right shows all the epicenters combined from manual picking and automatic picking. The lower figures are associated cross sections. Hypocenters within 25 km orthogonal distance from the cross section lines are projected on to the sections.

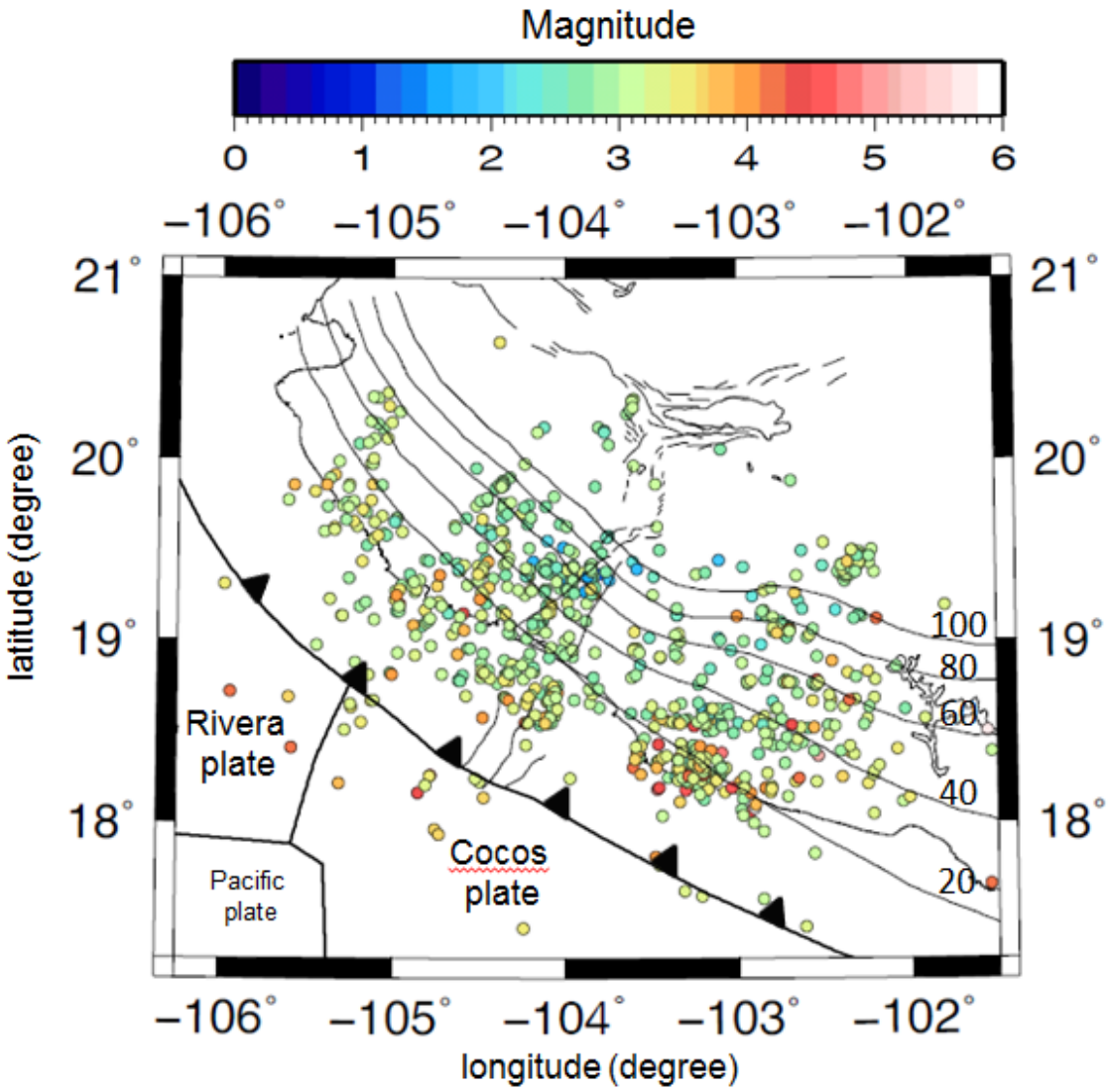

Figure 5.6 Magnitude map for all collected events (automatic picking catalog as well as manual picking).

Double Difference relocation method

Prior to performing a joint inversion, I relocated the local events using the double difference method (Waldhauser and Ellsworth, 2000) to obtain a more accurate catalogue of hypocenters. One reason for doing this is that the double difference method uses S waves as well as P waves but in the tomography inversion we only used P waves. The double difference method determines relative locations of earthquakes within a cluster of closely spaced events. The method assumes that raypaths from two close events recorded at a common station are relatively similar and thus the difference in their travel times can be attributed to the spatial offset between the events and does not depend on the velocity structure along the paths. The earthquake relocation in the double difference method is a two-step process. The first step involves the analysis of catalog phase data to derive travel time differences for pairs of earthquakes. The ph2dt code finds a network of links between events to build a cluster of connected events within a small distance. In this study, I set the maximum separation distance between hypocenters (MAXSEP) as 20 km and maximum neighboring events for each event as 8 (MAXNGH) . Events that have less than the minimum number of neighboring events (MINNGH=3) are still selected but have a lower weighting. The MAXOBS parameter (=50) is the maximum recorded arrival times per event and MINOBS parameter (=4) will discard linked events that have less than 4 arrival time observations. The full input parameter numbers and the results of the ph2dt process can be found on Appendix C

The next step after building the network of event pairs is the inversion scheme. For this step, I chose the least square inversion solver method with damping parameter equal to 40 and used the velocity model that is shown in Figure 5.7. The full inversion process

and output log at every iteration can be found in Appendix D. The inversion decreased the RMS of the relative residuals from 191 ms to 46 ms.

Figure 5.8 shows the difference between the original hypocenter locations and results from the double difference inversion. In general, the double difference method has removed some events that are located outside the station network. Note the new locations appear to show a narrower Benioff Zone for both the Rivera and Cocos slabs. Figure 5.9 shows the final hypocenter locations resulting from double difference relocation.

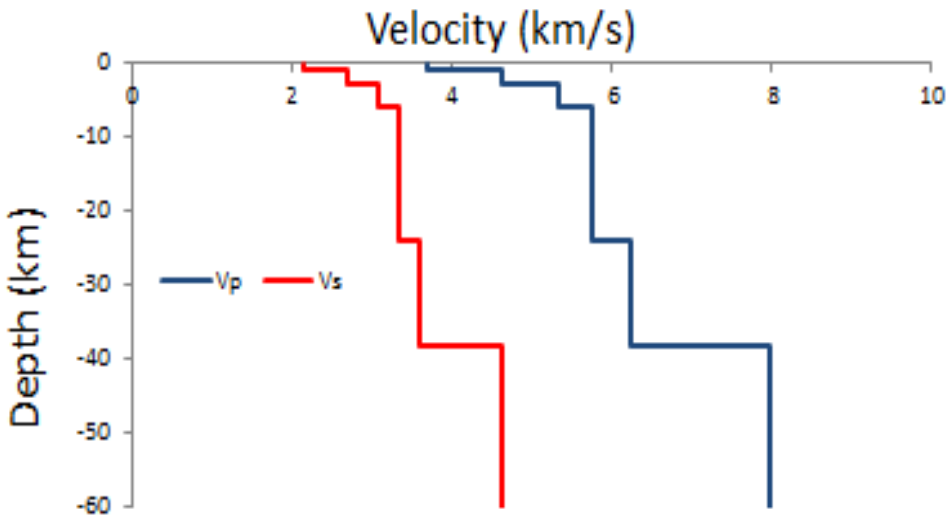

Figure 5.7. 1-D Velocity model used for the double difference inversion process.

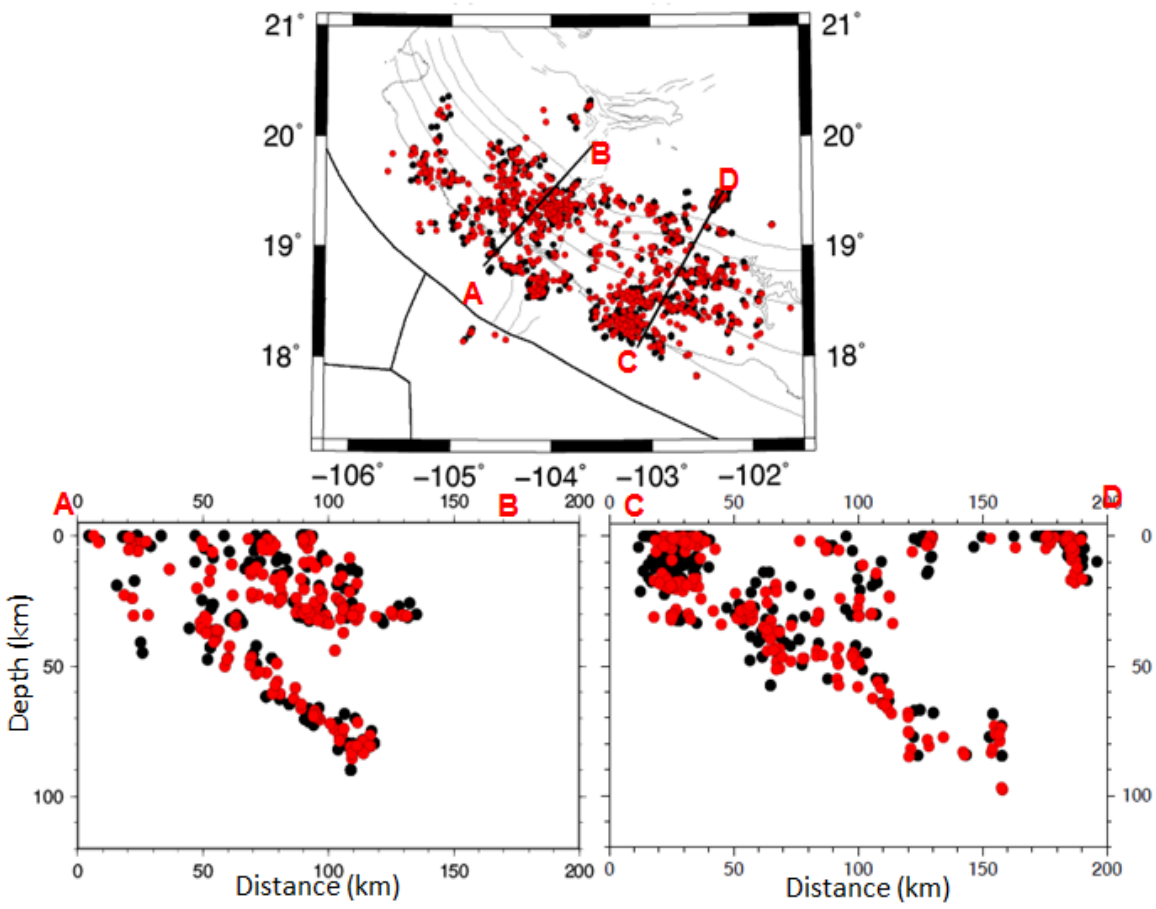

Figure 5.8 Cross Section comparison between original data and double difference results. Black circles are the original input locations from manual picking and automatic picking, The red circles are results from the double difference method. Hypocenters within 25 km orthogonal distance from the cross section line are projected onto the cross section lines. The maximum difference between relocated event and original event is 35 km.

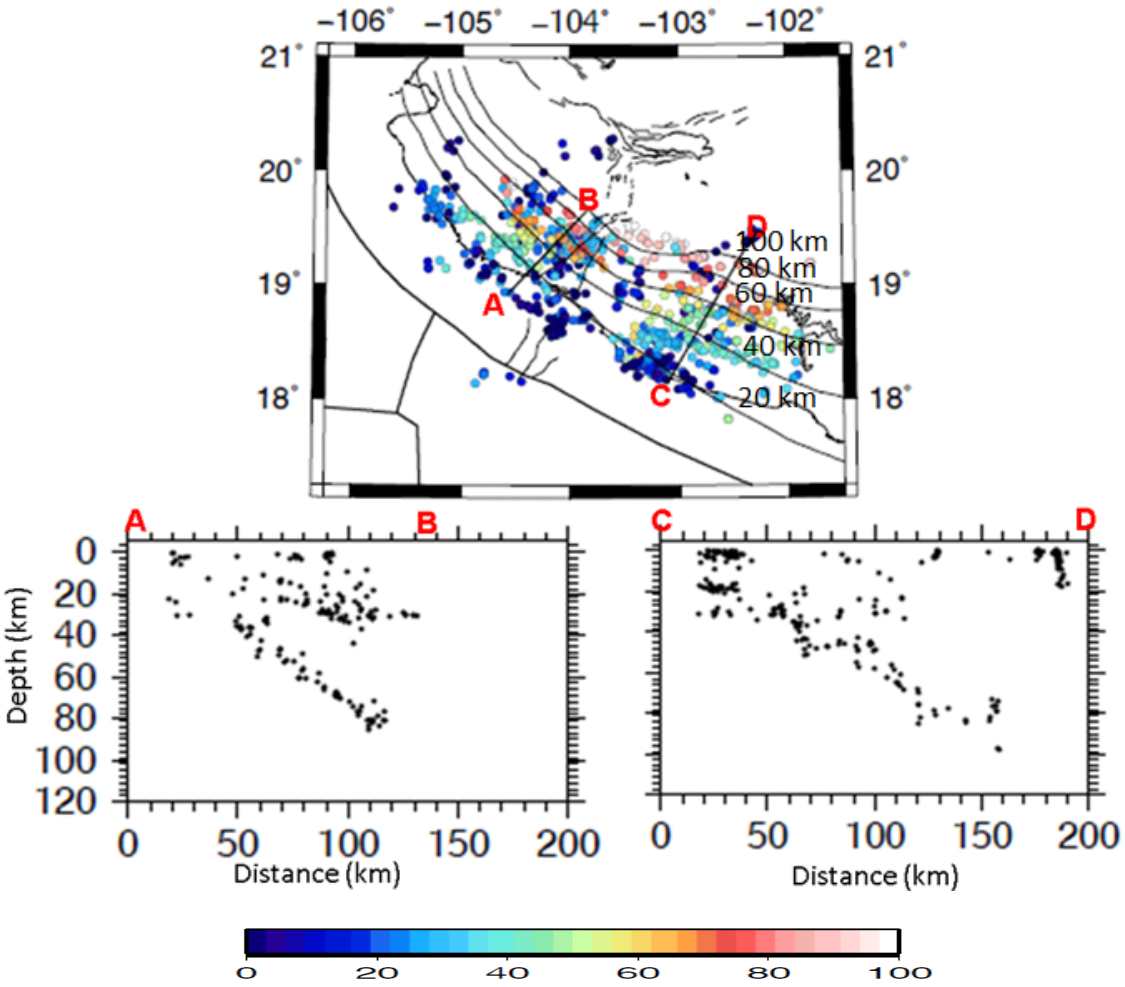

Figure 5.9 Final hypocenters using the double difference method. Below are cross section profiles.

Joint inversion method

A joint inversion in complex geology settings requires reliable 3-D ray tracing to estimate the ray paths and travel times between sources and receivers. I employed a 3-D finite difference ray tracing to estimate the ray path and travel times called the Fast Marching Method (Rawlinson, 2006), which has been previously discussed in chapter 4. I also use the same seismic inversion scheme including 3-D velocity nodes in a spherical coordinate parameterization and subspace inversion method (Kennett, 1988). A 3-D crustal model from the receiver function study discussed in Chapter 3 is used in the starting model. In the joint inversion, the data are the arrival time residuals of teleseismic events, the arrival times of local events, and local event locations. I invert a kernel matrix that contains the length of the ray on each node of teleseismic and local events in order to obtain an optimum velocity model and relocation vectors for the local events. I used an iterative non-linear inversion that allows velocity and source location parameters to be inverted. A non-linear approach means that the FMM ray tracing scheme and subspace inversion were applied iteratively to address the non-linear nature of the inverse problem.

Model resolution

I performed synthetic checker board tests to investigate the resolution of the joint teleseismic and local event inversion. The unbalanced distribution of locations of teleseismic and local events will contribute to making the problem under-determined and thus produce non-unique solutions. I created an input model consisting of high and low

velocity blocks between +1.5% and -1.5% of the ak135 model and computed synthetic residuals using the same source and station geometry as the actual data. I also shifted the initial regional earthquake sources 0.15 degree to the east, 0.15 degree to the north and 5 km deeper than the true locations to test the capability of joint inversion to retrieve the source locations. Note that I put the same amplitude and configuration in this synthetic test as we used in chapter 4. Next, we added random error with a standard deviation of 25ms and 50ms to the teleseismic arrival time residuals and the local event travel times, respectively, to simulate noise in the data. The starting velocity model is ak135. I simultaneously invert teleseismic arrival time data, local arrival time data and earthquake locations to obtain an optimized velocity model and new hypocenters.

Figure 5.10 shows the input model of checker board and Figure 5.11 shows a well recovered checkerboard after inversion at different depths. In general, the contribution from local events improves resolution at shallow depths from 50 km to the surface relative to using only teleseismic data. The northern part of the model shows lower amplitude recovery because fewer local events occurred in the northern part of the Jalisco block. The checkerboard models show good recovery in terms of shape and amplitude at each depth slice especially in areas that have abundant local sources.

Figure 5.12 shows West-East and South-North cross sections that can be used to investigate resolution in the vertical direction. At depths shallower than 100 km, due to the abundance of ray paths from teleseismic and local events, almost all regions show good recovered images. A smearing effect, that tends to spread velocity anomalies to neighboring grid points, is obvious on the edges of the model, outside our station

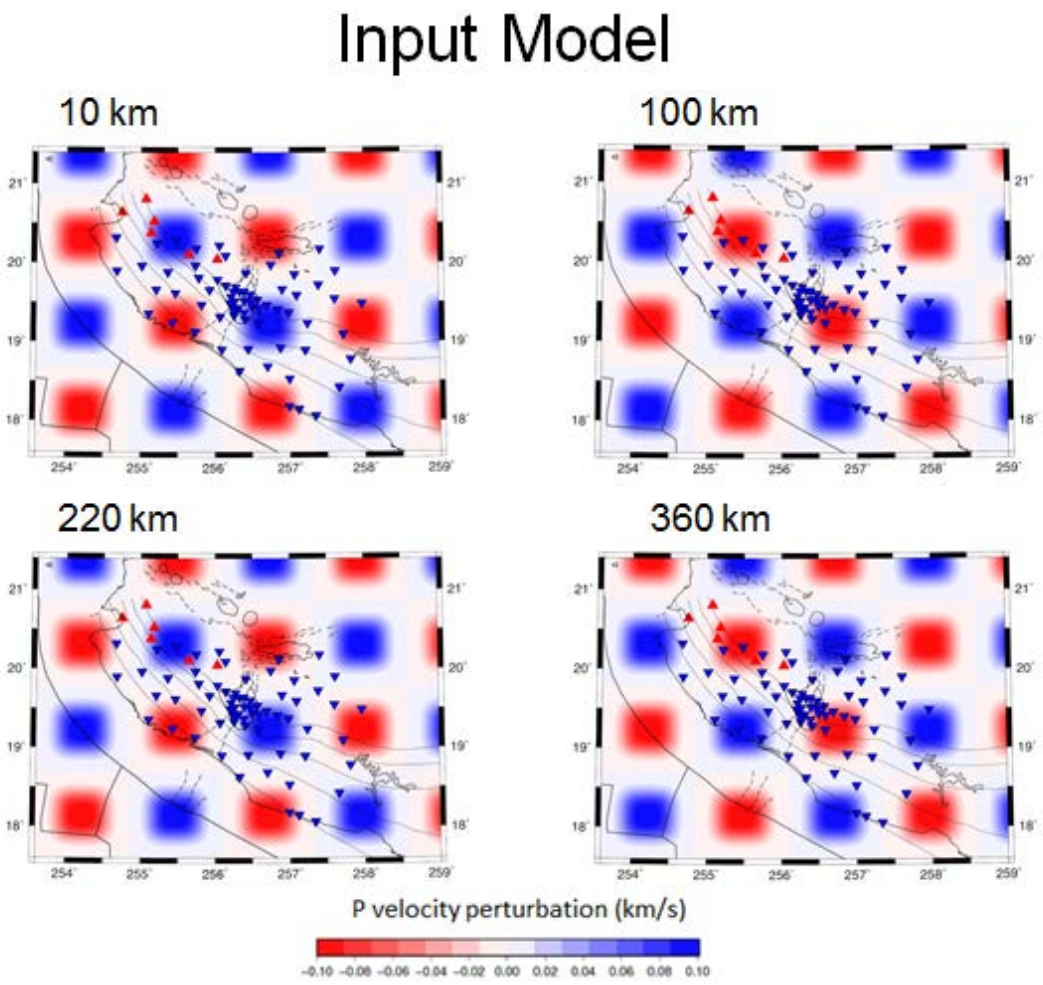

Figure 5.10. Input checker board model before inversion. Blue color shows faster velocity anomalies with a maximum of 1.5%, and red color shows slower velocity anomalies than the ak135 velocity reference

Recovered Checker Board

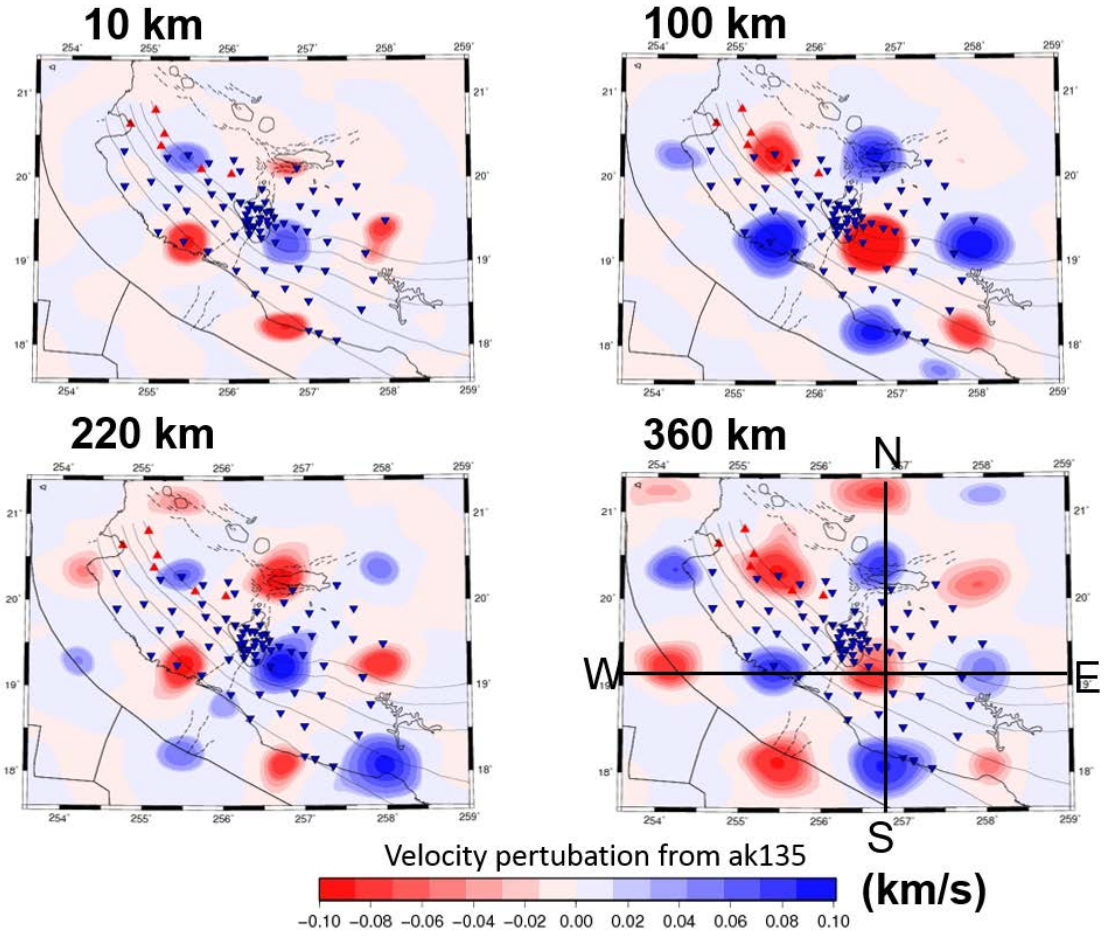

Figure 5.11. Checker board results after inversion. Blue color shows faster velocity anomalies with a maximum of 1.5%, and red color shows slower velocity anomalies than the ak135 velocity reference. Note that the velocity perturbation is plotted as the velocity difference with the ak135 velocity difference not as the percentage difference. The W-E and N-S lines plotted at a depth of 360 km are used for cross sections in the next figure.

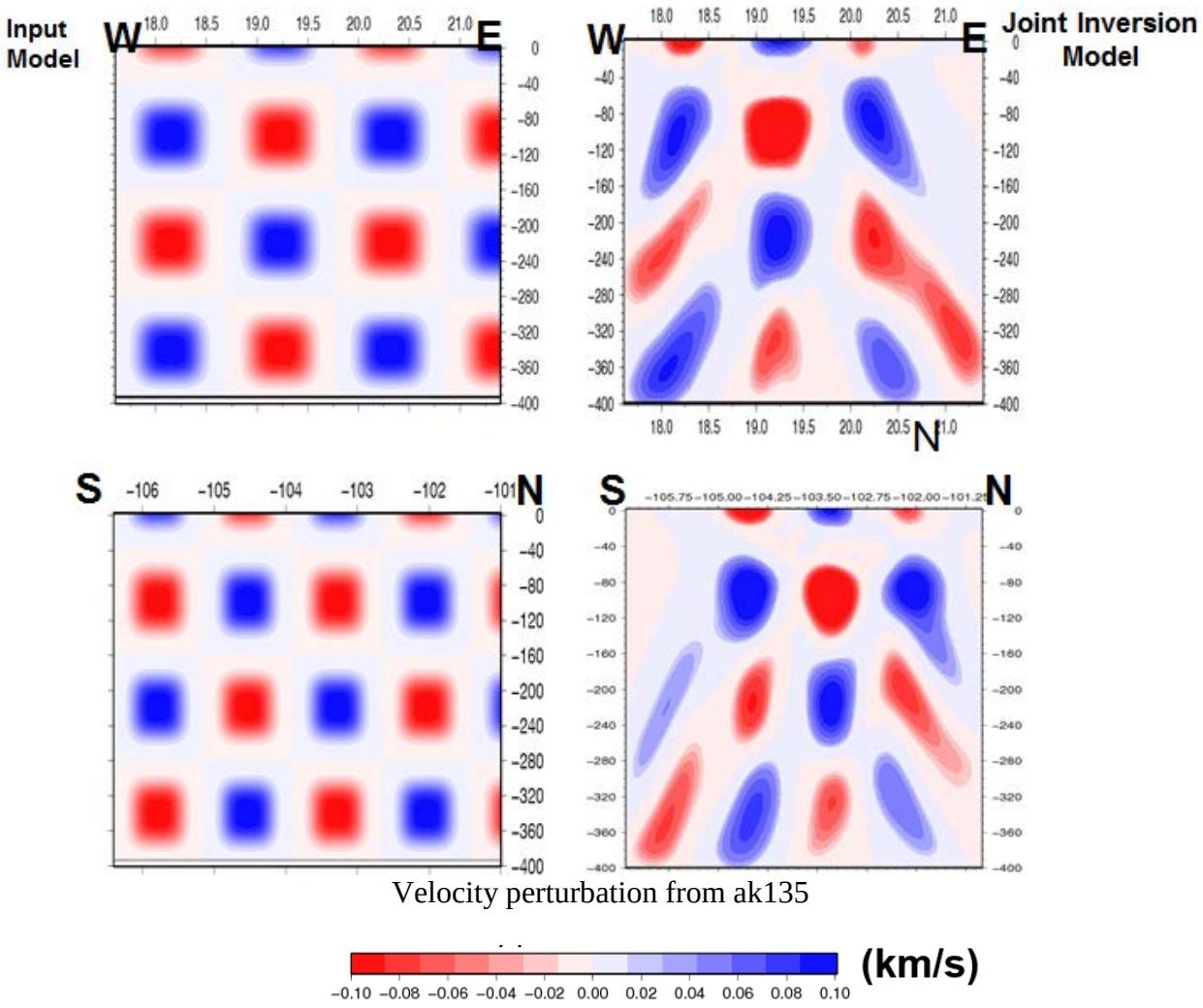

Figure 5.12. West- East and North – South (from figure 5.9) cross sections line showing the checker board inversion results. The left figure is the input model and the right is the model after inversion. Most anomalies are well reconstructed especially at shallow depths due the contribution from local events. A smearing effect can be seen in the deeper part of the model.

network. Cross section figures also suggest the extent of depth resolution of my model. In this case, the inversion is still able to resolve anomalies to a depth of 400 km without decreasing resolution at shallow depth.

I also investigated the source relocation resolution. Figure 5.13 shows a map view of the starting shifted input event locations, the relocated events after joint inversion and the true event locations. Most relocated events are successfully relocated back to their correct locations with only a few that are relocated far from the true locations. Figure 5.14 shows cross section profiles that show the difference between relocated event locations and the actual locations. Most relocated events in the Cocos plate (profile C-D) and the Rivera plate are almost exactly re-located to the true locations.

To further investigate the effect of adding local events in a joint inversion, I compare the checker board model tests using a joint inversion versus the teleseismic only inversion from the previous chapter. Adding local events into the inversion has resulted in stronger amplitude recovery in the shallow structure as seen in Figure 5.15. The results from the joint inversion show a stronger amplitude, better anomaly location recovery compared to the teleseismic only inversion at depths less than 100 km. At deeper depths the results are similar. In summary, the checker board test shows that seismic structure is adequately resolved by the combined datasets, particularly beneath regions of abundant ray coverage. However, similar to most tomography studies, less ray density and the application of damping and smoothing to regularize the inversion has generally resulted in the recovered models underestimating the true amplitudes of the velocity though adding local events significantly helps the amplitude recovery at shallow depths.

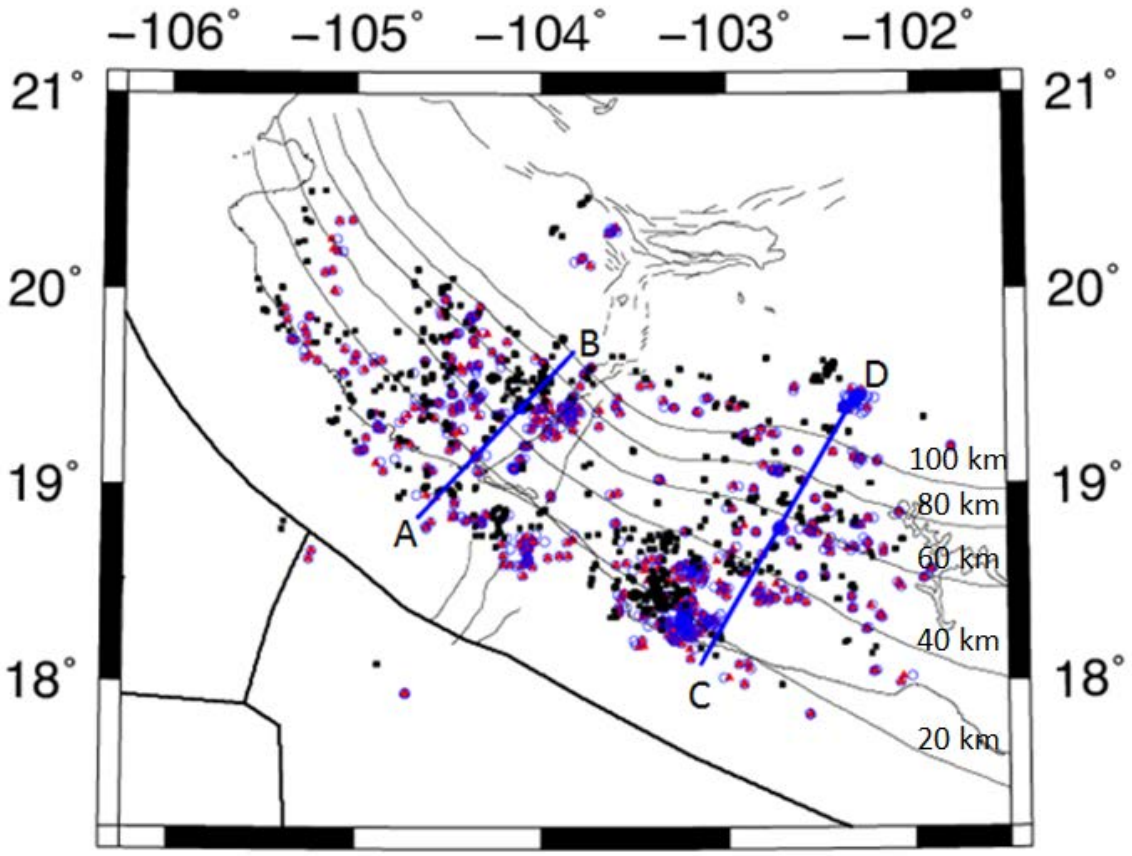

Figure 5.13 Map view of initial shifted event locations (black filled circles), actual event locations (red triangles), and relocated events (open blue cricles). The initial starting events are shifted 0.15 degree to the east, 0.15 degree to the north and 5 km deeper from the actual locations.

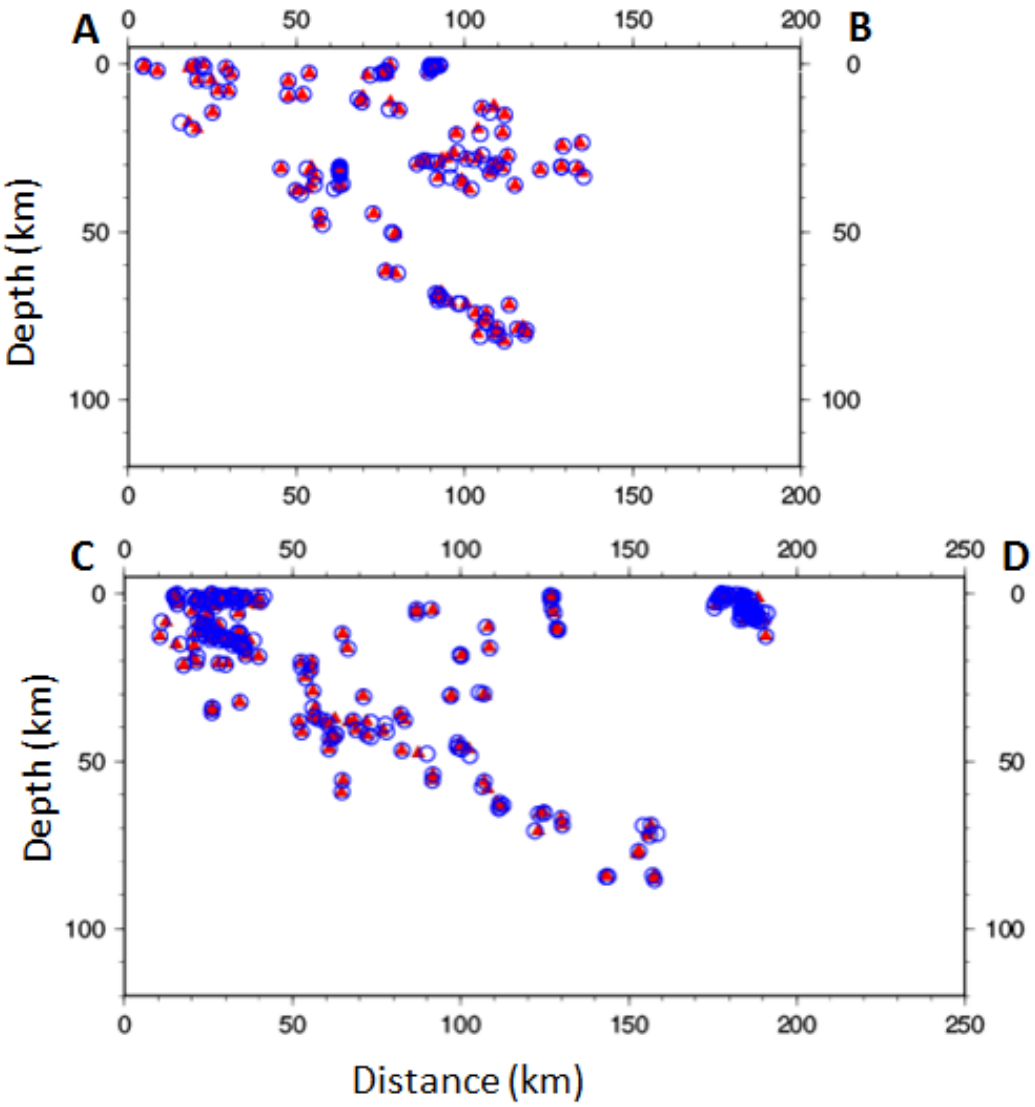

Figure 5.14. Cross section profiles (A-B and C-D) from figure 5.13. The red filled circles are the true initial locations and the open blue circles are the relocated events. Events within 25 km horizontal distance are projected onto the profile line.

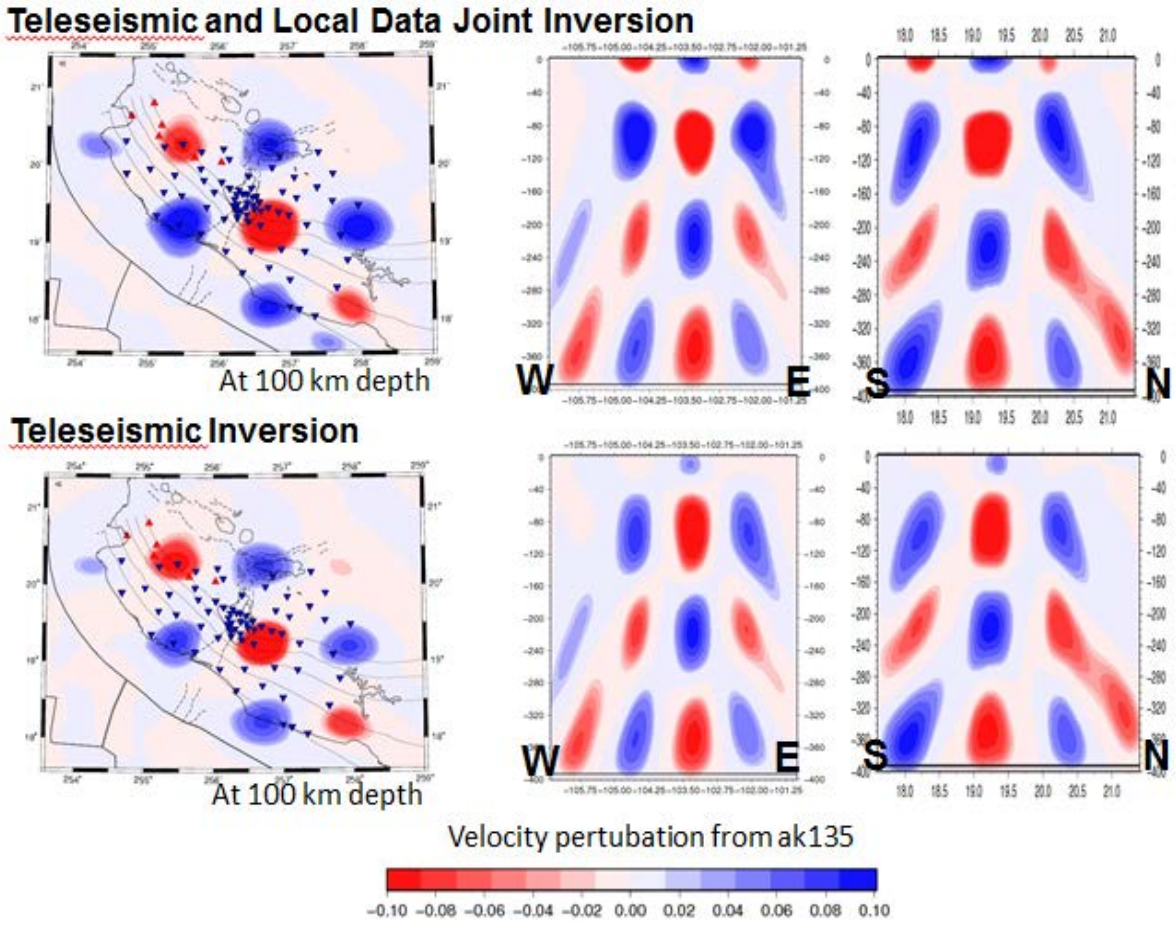

Figure 5.15 Comparison between checker board results for the joint inversion and the teleseismic only inversion. The input velocity anomaly model, teleseismic sources and receiver configuration and color bar are identical in the two inversions. Left is the model at a depth of 100 km, Middle is the S-N cross section. Right is the West-East cross section profile where the lines are taken from Figure 5.10.

Local source relocations from joint inversion

Figure 5.16 shows the relocated local hypocenters from joint inversion and a comparison with the double difference results. In general, the differences in hypocenters between the double difference input and the joint inversion relocations are relatively small. A few differences can be seen for some events on the coast line and shallow events in land although the changes are within 20km. Cross section profiles show that the overall geometry of both slabs is relatively similar between the two.

Figure 5.16 also shows that the far northwestern part of the region shows little seismicity similar to what a previous seismicity study (Pardo and Suarez, 1993, 1995) reported (Figure 5.21 shows the results from the previous seismicity study in cross section). We also observed a number of shallow events in land above the Rivera slab, in the vicinity of the Tepic-Zacoalco rift, and in the north of Michoacan that may be related to magmatic activity. In an area between the two slabs, in the vicinity of the Colima rift, a cluster of events are seen at the south end of the Colima rift and around Colima volcano that range from shallow to greater than 30 km depth. However, east of the Colima rift shows almost no seismicity.

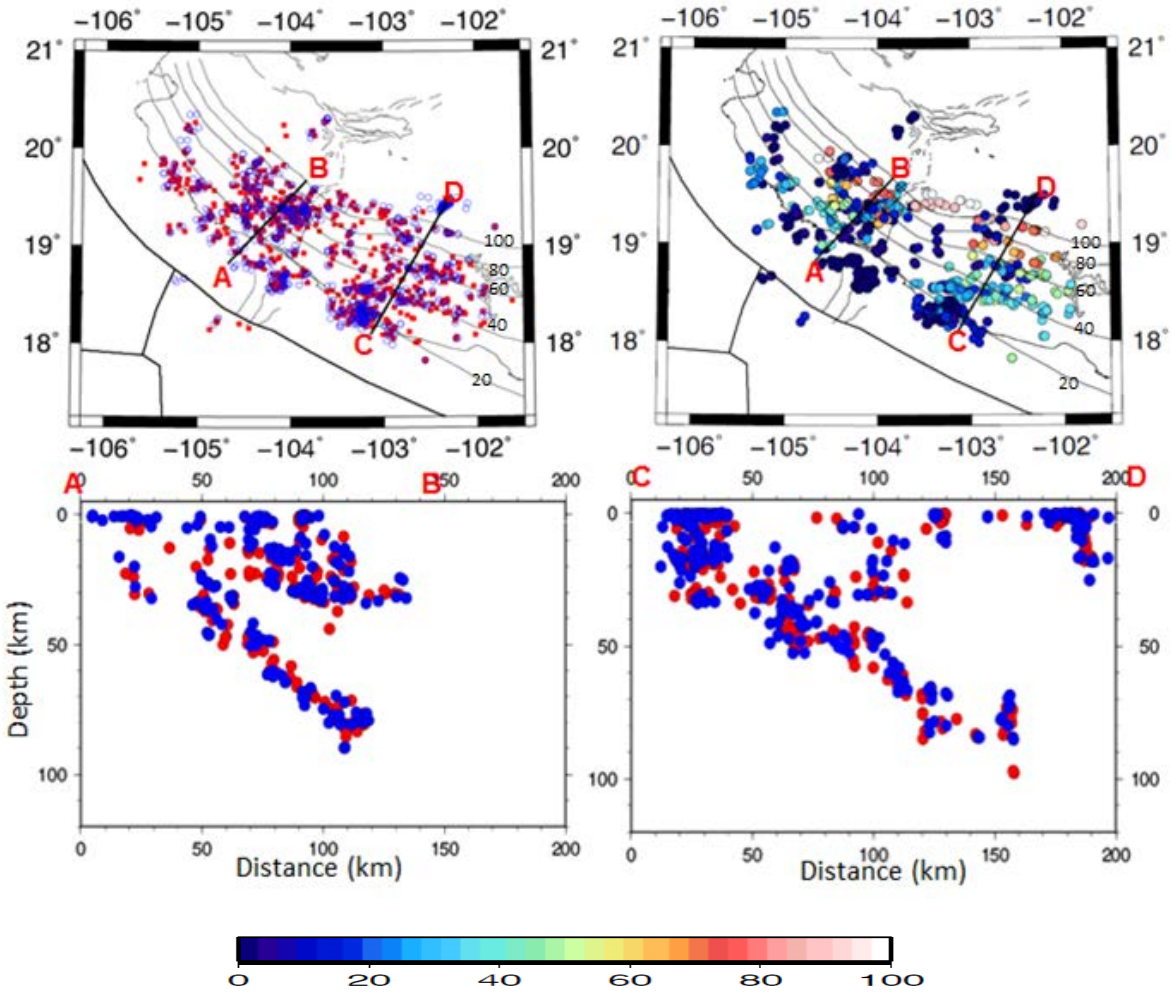

Figure 5.16. Top left is a comparison between the final joint inversion seismicity locations (blue circles) and the starting locations from the double difference inversion (filled red circles). The top right figure shows the joint inversion hypocenters. Contour lines are taken from the previous seismicity study by Pardo and Suarez (1995). The bottom figures are comparisons between double difference hypocenters (red circles) and joint inversion hypocenters (blue circles).

Tomography model

A series of constant depth slices through the final model from shallow to deep are presented in Figures 5.17 and 5.18. The faster velocity (blue color) most likely represents colder temperature subducting slab and slower velocity may be due to hotter temperatures, higher water content, or partial melt. Due to the combination of teleseismic and local sources, seismic images after joint inversion show strong amplitude anomalies at shallow depth. However, a lack of local events above the southwestern part of the Rivera plate does not improve the shallow image of the western side of the Jalisco block relative to the purely teleseismic image.

At 40 km depth (Figure 5.17), a significant fast velocity band is obvious to the south of 19^0 latitude although this could be due to errors in regional earthquake locations offshore. At 80 km depth, subducting slabs become noticeable with a distinct low velocity region in the north. The band of fast velocity moves further to the northeast direction with depth and follows the seismicity contours. At depths of 120 km and 160 km, a band of fast velocity is seen between slow velocity anomalies to the north and south with an average width of about 55 km. At these depths, the fast velocity corresponding to the Cocos slab is located to the north of the 100 km seismicity contour and the fast velocity Rivera slab is located to the south of the 100 km seismicity contour implying that the Rivera slab is steeper than Pardo and Suarez (1993) showed and the Cocos slab is less steep.

The seismic tomography images below 160 km show a decrease in amplitude especially with respect to the slow velocity zones. At a depth of 200 km, the band of fast

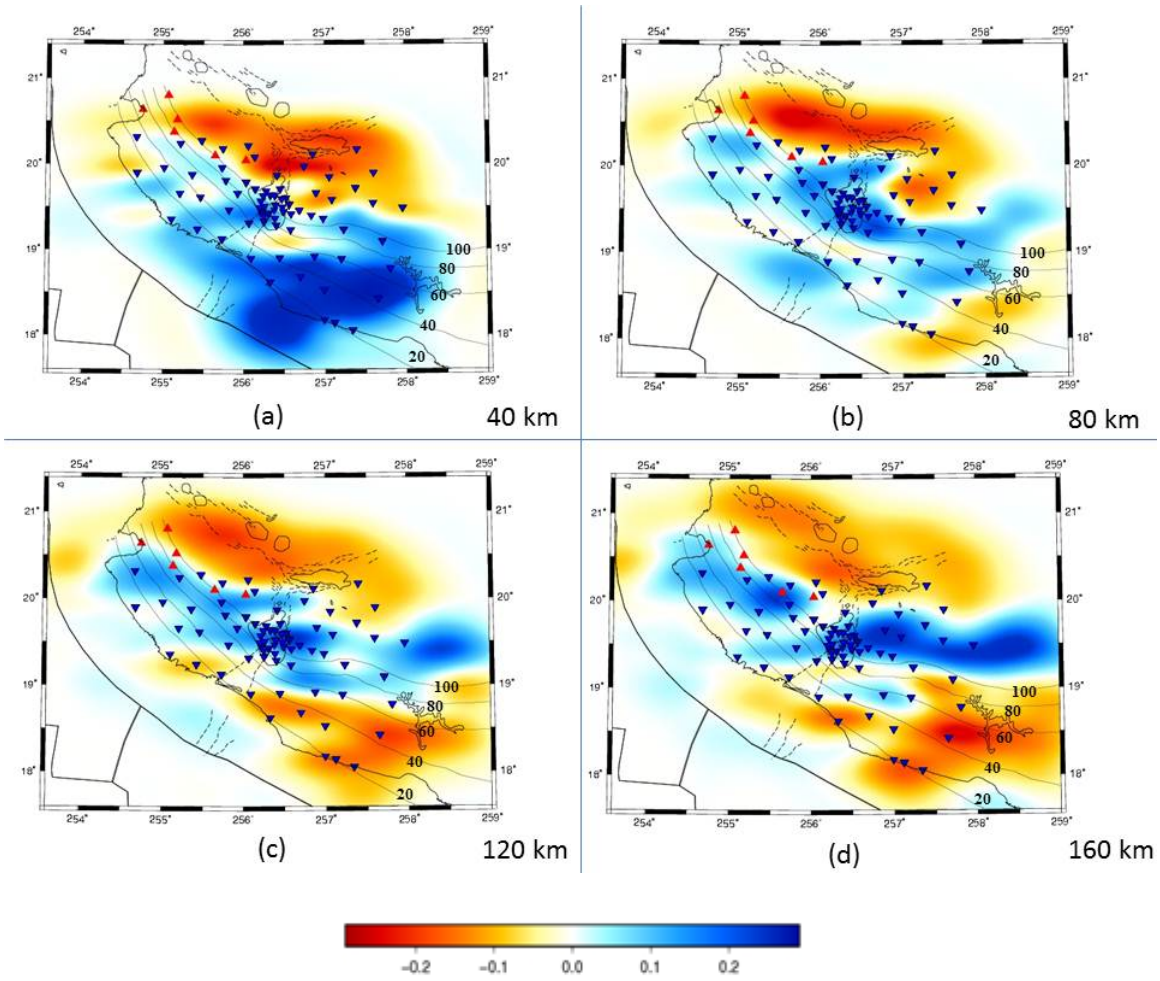

Figure 5.17. Joint inversion tomography velocity model at different depths. The maximum numbers on the scale correspond to roughly 4% velocity variations.

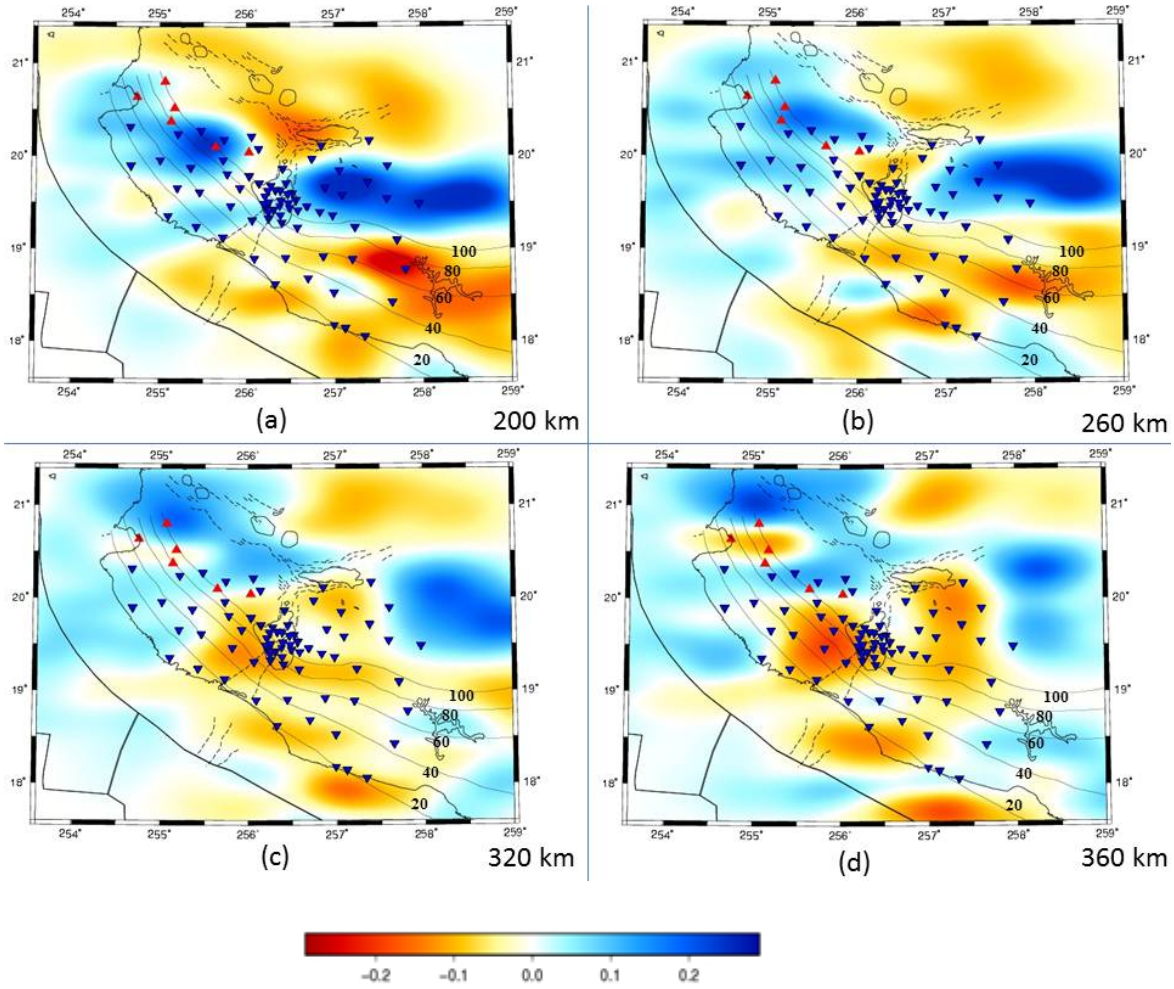

Figure 5.18. Joint Inversion tomography velocity model slices at depths of 200, 260, 320 and 360km respectively. Blue color represents faster velocity and red color represents slower velocity. All the inversion results are plotted with reference to the ak135 velocity model.

velocity is further north than at shallow depth. The Cocos slab seems to move farther to the north than the Rivera slab. A slow velocity anomaly between both slabs is obvious to the northwest of Colima Volcano and the gap between the slabs seems to expand at a depth of 260 km. At depths greater than 200km, all the seismic images reduce in amplitude and distinct slab shaped anomalies become less clear. However, in general, the band of fast velocity moves farther to the north with the gap between the Rivera slab and Cocos slab expanding.

The subducting Rivera and Cocos slabs can be seen in cross section in Figure 5.19. Overall, the dip of the slab changes from a steep Rivera slab to a less steep dip for the Cocos slab. Profile A1B1 shows a near vertical fast anomaly that becomes less steep below 200 km. On the right side of the slab, a region of strong slow velocity is obvious from a depth of 200 km to the surface. The surface location of the slow velocity region is coincident with the location of the Central Jalisco Volcanic Lineament. A plot of seismicity on this profile shows only a few shallow events from a depth of 20 km to 30 km, with no deep events.

Cross sections A2B2 and A3B3, located near the Colima rift, are similar to each other. The slab has a gradual dip down to a depth of 100 km but is truncated at deeper depths where the Cocos and Rivera plates diverge. The seismicity on both cross sections shows that local events occur close to the boundary of the fast velocity slab. Deeper than a depth of 40 km, most events occur inside the fast velocity slab. Cross section A3B3 shows that active seismicity is also seen above the Moho inside a slow velocity region. I also observed on both cross sections, the slow velocity zone can be tracked from a

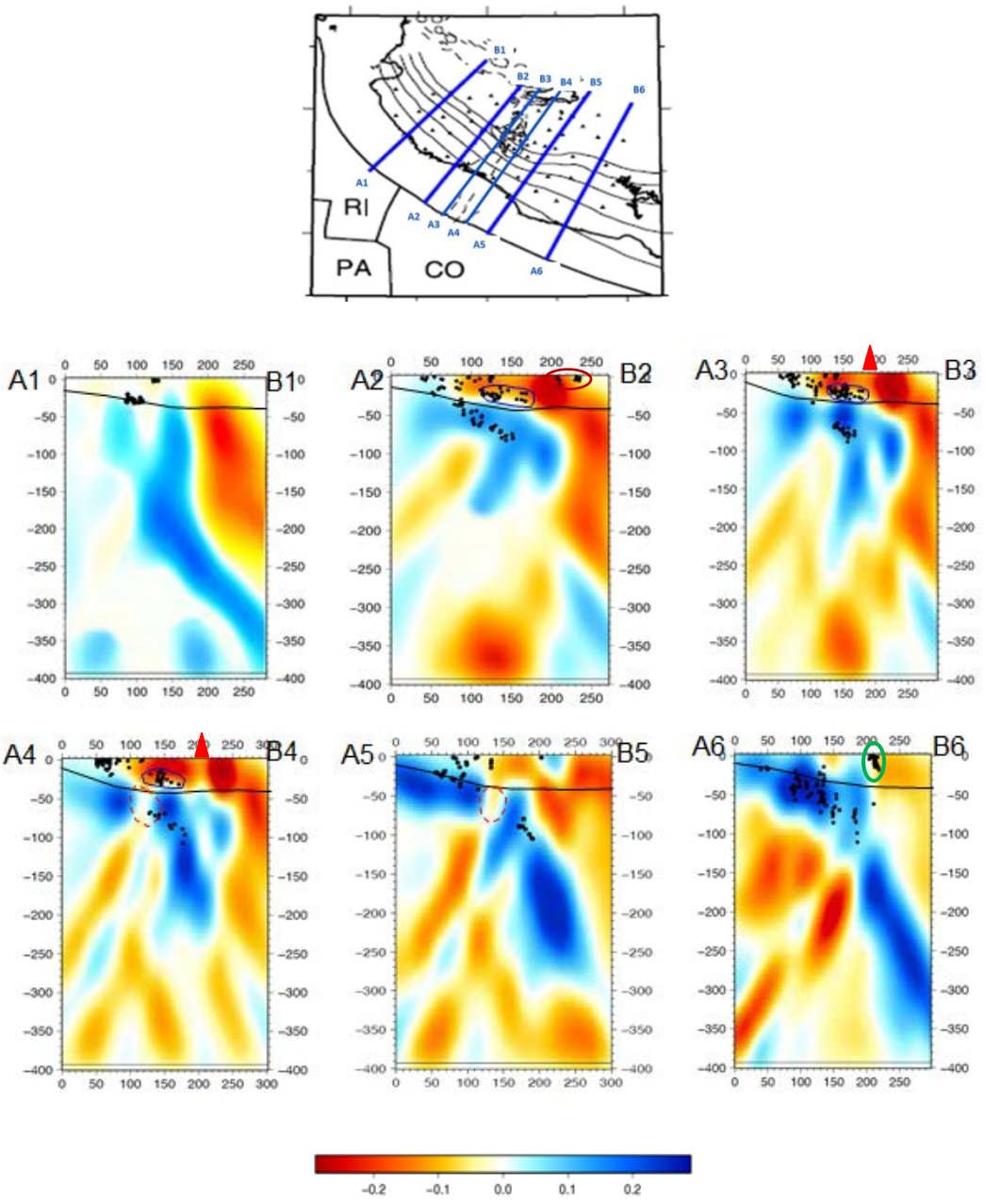

P Velocity Perturbation (km/s)

Figure 5.19. Joint inversion tomography cross sections. A red circle shows the location of a possible tear in the slab. Blue circles show shallow earthquakes that may be related to magmatic activity. The red triangle is the location of Colima Volcano and the green circled areas are clusters of shallow events located further inland. RI is Rivera plate, CO is Cocos plate and PA is Pacific plate.

depth of 300 km to the surface. The slowest velocity anomalies occur at a depth of 30 km in the vicinity of Colima volcano.

Cross sections A4B4 and A5B5 show the western most edge of the Cocos slab that subducts at a low angle and changes to a steeper dip at a depth of 80 km. The slab seems to terminate at a depth of 225 km where the Cocos and Rivera plates diverge (Yang et al. (2009). An interesting feature in these profiles is a gap in fast velocity within the Cocos slab at about 50 km depth (circled in red in Fig. 5.19). The circled region is also devoid of earthquakes. Finally, the amplitude of slow velocity anomalies near the surface along profile A5B5 are not as strong as along profiles A3B3 and A4B4. Furthermore, we do not observe deep crustal seismicity along profile A5B5 nor a strong deep slow anomaly relative to the two profiles to the west.

The last cross section, A6B6, shows the Cocos slab with a constant low angle dip that starts to change to a more steep dip below a depth of 100km. Here, we do not see any signs of slab break at shallow depth. The slab seems continuous down to a depth of 350km without any significant broadening. Abundant earthquakes between a depth of 40km and 90km that occur inside the slab are also observed. The crust is largely free of seismicity along this profile although there is an interesting cluster of seismicity at a strong lateral gradient in the crust circled in green.

Figure. 5.20 shows three cross sections discussed above with a comparison to the teleseismic only inversion results of chapter 4. Note the clearer shallow slab in the joint inversion relative to the inversion using only teleseismic data. Also note the sharp break in the slab with a gap in seismicity along profile A3B3. The change in seismicity along

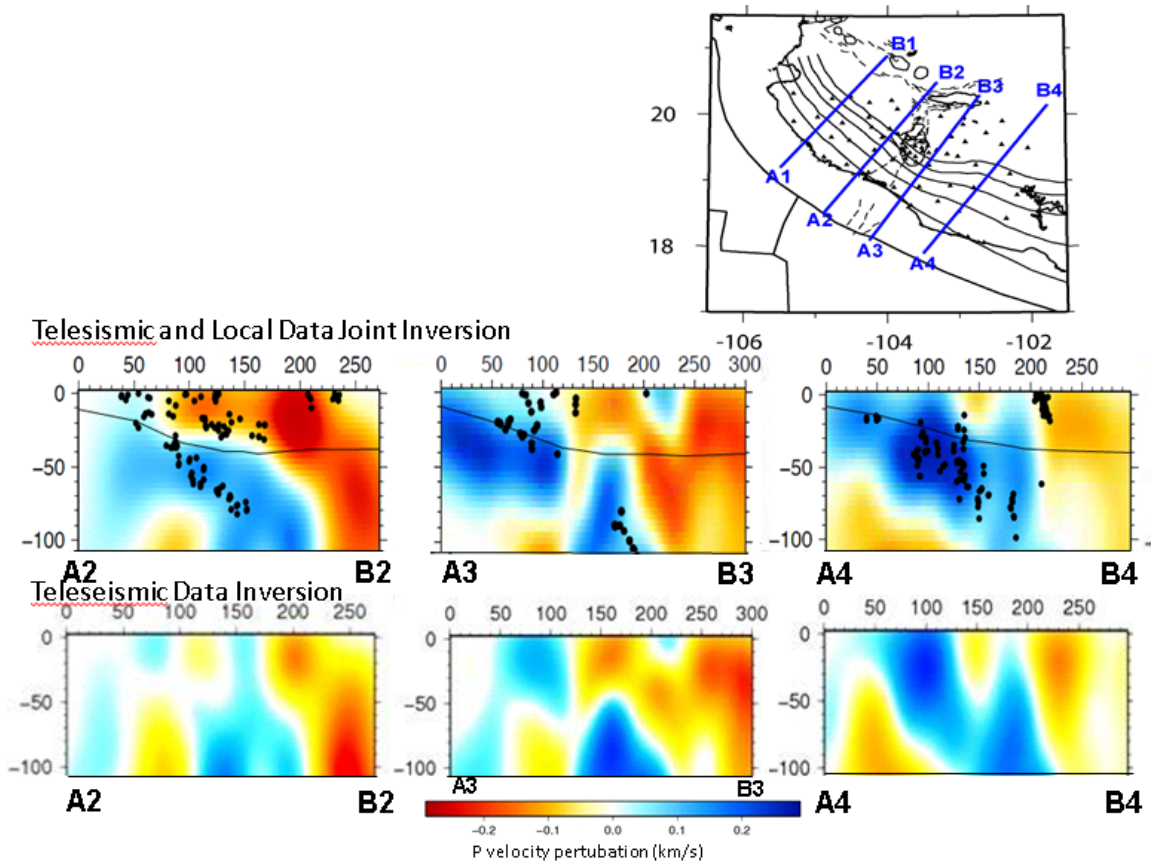

Figure 5.20. Comparison of cross sections for the joint inversion (top) and the inversion discussed in Chapter 4 using only teleseismic data (bottom).

the slab interface to within the slab is also clear. The change occurs at around 35 km depth.

Discussion

Seismicity and Geometry of the slab

Relocated seismicity from the joint inversion clearly shows the Benioff zones associated with the subduction of the Rivera and Cocos plates. The western side of the Rivera plate is largely aseismic (Profile A1B1 at Figure 5.19) but the eastern side, close to the Colima Rift, shows an abundance of seismicity (profile A2B2). Similarly, the western side of the Cocos plate shows less seismicity (profile A3B3) than the eastern side (profile A4B4).

Earthquakes that occur in subduction zones can be classified as two kinds. First are interplate thrust earthquakes that occur due to brittle fracture and frictional sliding at shallow depths down to about 65 km along the plate boundary between the descending plate and the continental margin. The second class is intraslab earthquakes that occur within the descending plate at depths below 35 km whose cause is less certain. One theory for intraslab earthquakes is that because of the increasing heat and pressure in subduction zones, metamorphic reactions occur in the descending oceanic crust that in many cases liberate water. This can increase the pore pressure that may reactivate pre-existing faults (Kirby, 1996; Kirby et al. 2000). Kirby et al. (2000) also proposed that in higher temperature subduction zones, the oceanic crust should liberate water at shallower depth and trigger shallower intraslab earthquakes and less volcanic activity than colder subduction zones. Note that the Rivera-Cocos subduction zone is similar to the Juan de Fuca plate in terms of young age (Wilson, 2002) and convergence rate (McCaffrey et al.,

2007) and can be categorized as one of the warmest subduction zones (Rondenay et al., 2008).

In Figure 5.20, a plot of seismicity on a background of the joint inversion velocity model shows interplate seismicity to a depth of about 35 km. Deeper than 35 km the seismicity seems to be located within the dipping fast velocity slab and are likely intraslab earthquakes.

Figure 5.21 shows the Common Conversion Point Receiver Function image from Chapter 3 with seismicity from the joint inversion along a line through the Cocos slab. I previously interpreted the dipping negative (blue) signal as a thin (3km) low velocity layer that has high Vp/Vs ratio that is the top of the ocean crust under high pore pressure (chapter 3). Also, recall that this image combines all receiver functions above the Cocos plate. Events from a depth of 10 km to about 30 km appear to be located on the plate interface. There appears to be a transition for seismicity from 30 to 40 km depth where some events may be on the interface but many are clearly intraslab events. Events deeper than 40 km are clearly located inside the positive signal (basaltic lower crust). Our seismicity results, combined with the tomography and receiver function analyses, show that the interplate earthquakes occur from 30 km to 35 km depth but below that depth events are occurring within the top part of the descending plate. These observations are consistent with the dehydration embrittlement model discussed in Kirby et al. (2000) for a warm slab. However, we note that the dipping low velocity layer that we associated with the descending overpressured basalt and sediments extends significantly deeper than 30 km so that the dehydration reactions causing the shallow

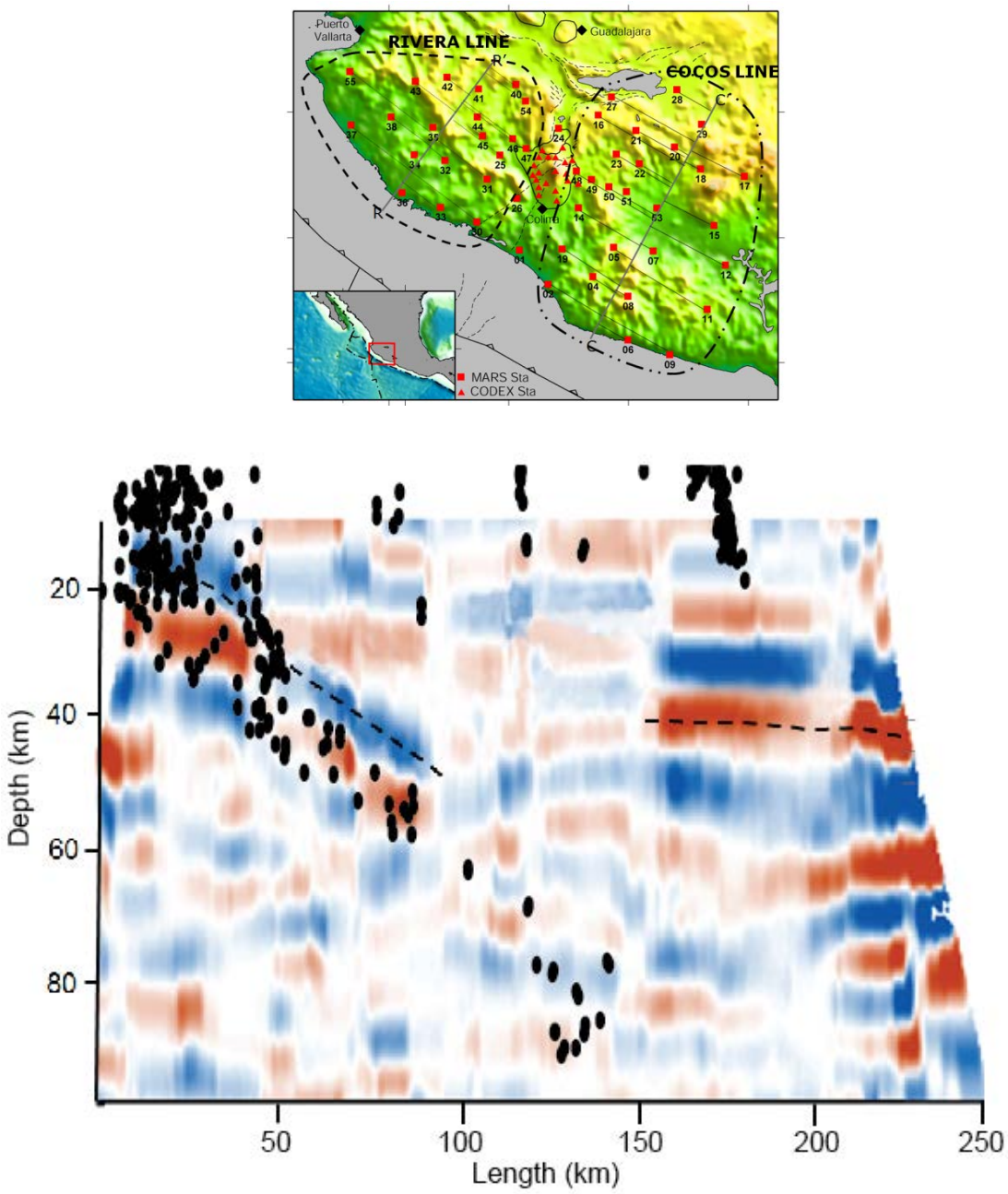

Figure 5.21. Plot of new seismicity from this study on Common Coversion Point Receiver Function image from chapter 3 at Cocos Line.

intraslab events are unlikely to be the phase transition of basalt to eclogite. My results are also significant for large earthquake hazard studies. It may be the interplate seismicity cutoff near 30 km depth marks the bottom of the locked zone. Pardo and Suarez (1993, 1995) located microseismic events in the region. Their study revealed that the Rivera plate dips at an angle of ~50° beneath the continent and that earthquakes extend to a depth of ~120 km. In contrast, the subduction angle of the Cocos plate is more variable and the hypocenters do not exceed ~80 km in depth. In fact, the dip angle of the Cocos plate progressively decreases from its boundary with the Rivera plate to approximately 101°W longitude, after which it becomes almost horizontal to the east. Figure 5.22 shows a comparison between our new hypocenters and the Pardo and Suarez results along the same lines they show located above the Rivera plate. Note that the Pardo and Suarez profile included teleseismic events that were recorded between 1964 and 1983. Profile C-C' represents the western part of the Rivera plate. A plot of our tomography model on this cross section shows a steep fast velocity structure from a depth of 20km down to a depth of 200 km. Our new seismicity locations show a cluster of events at a depth of 20-30 km. The Pardo and Suarez results show a cluster of teleseismically relocated events at this depth and a few more events at a depth of 40 km further inland. Cross section profiles B-B' and A-A' represent a structural change from the very steep profile along C-C' to a less steep structure. Cross section B-B' shows a dipping seismicity pattern from a depth of 30 km to 70 km inside the fast velocity structure and a cluster of events from a depth of 20-35 km at the plate boundary. Pardo and Suarez show a much steeper dip of downgoing events. Both studies show a cluster of events about 30

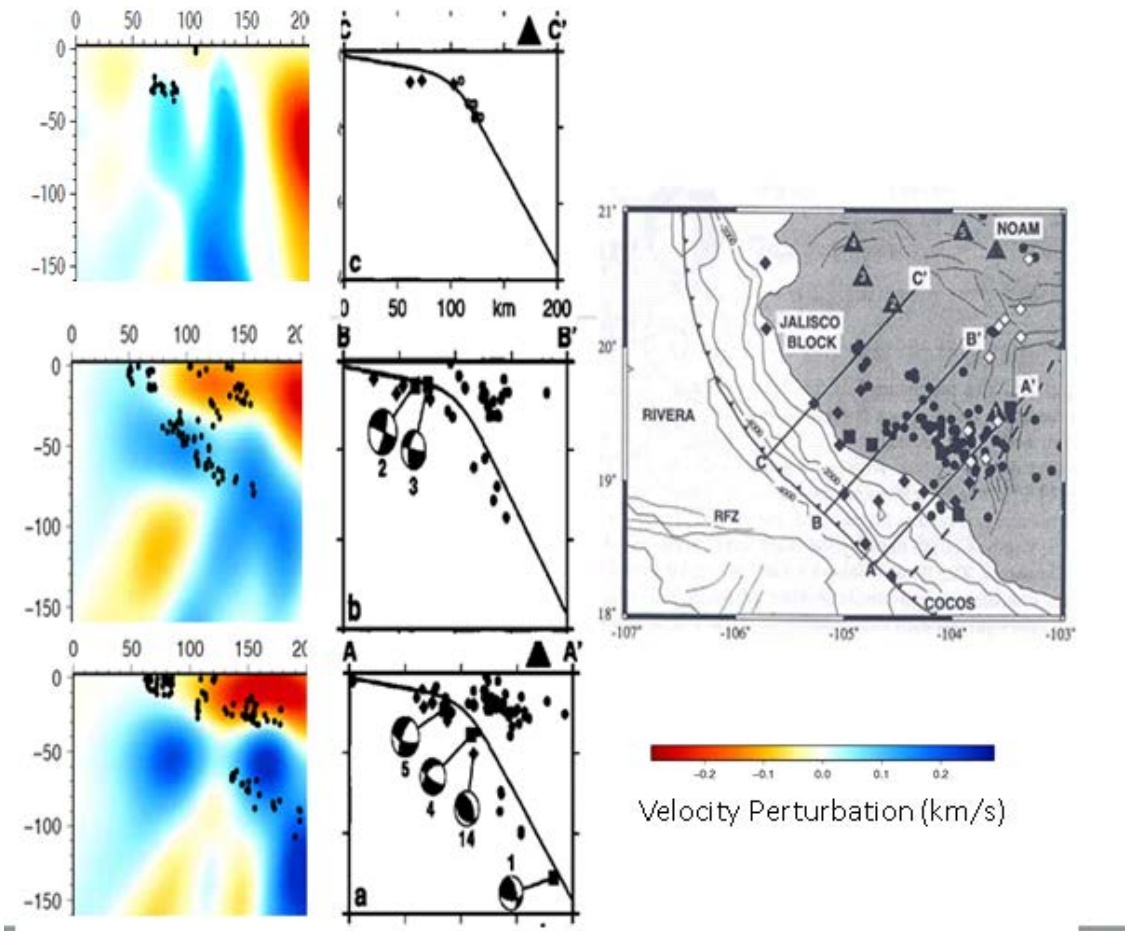

Figure 5.22 Comparison between Pardo and Suarez (1995) results with the joint inversion hypocenter locations from this study. The hypocenters from Pardo and Suarez were largely micro earthquakes shown as black circles located by a small temporary array with most events largely outside the aperture of the array and thus poorly located. Solid diamonds are teleseismic events that occurred from 1964 to 1983 and were relocated using the Joint Hypocenter Determination method (Dewey, 1971) and solid squares are teleseismic events constrained by the long period body wave inversion scheme of Nabelek (1984). Black triangles are volcanoes above the subducting plate.

km depth above the Benioff zone (marked with a polygon on Figure 5.22). Cross section profile A-A' represents the eastern most side of the Rivera plate. The new seismicity maps show a cluster of events at shallow depth then a gap in events in the fast velocity structure followed by dipping seismicity to a depth of 100 km. The tomography model also suggests a change in dip at a depth of 100 km of the fast velocity structure into a steeper dipping structure. Pardo and Suarez interpret their seismicity results to show a shallow dipping slab to about 30 km depth with a sharp bend in the slab to more steeply dipping below. My results show a more complicated scenario where the slab dip gradually changes to a steeper dip to 100 km depth at which point there is a sharp bend to a very steeply dipping slab at greater depths.

Magmatism in Southwestern Mexico

Southwestern Mexico magmatism shows a complex age and composition distribution. One of the complexities is the recent magmatism trending in the northwest direction located above the Rivera plate trenchward of the Trans Mexican Volcanic Belt. Bandy et al. (2001) has called these young (<3 Ma) volcanoes the Central Jalisco Volcanic Lineament (CJVL) with ages from 3 Ma to the southeast reaching .05 to .06 Ma to the northwest in the Mascota graben. Associated with the volcanic lineament are extensional basins. The mafic magmatism has been explained as due to slab roll back and consequent progressive asthenosphere upwelling trenchward (Ferrari et al. 2001) or as due to extensional stresses within the Jalisco block due to the progressive increasing

obliquity of Rivera plate subduction to the northwest (Luhr et al., 1985; Kostoglodov and Bandy, 1995). Compared to the abundant events on the Cocos plate, new relocated seismicity shows few events in this region. However, I observed two clusters of shallow events reaching depths near 30 km (shown as X and V in Figures 5.23 and 5.24) within the Jalisco block close to the Talpa De Allende and Mascota volcanic fields in the west and the Ayutla volcanic field further east. These volcanic fields are part of the CJVL. My receiver function study showed high Vp/Vs ratios over 1.8 for stations along a band located close to these event clusters (shown as letter H's on Figure 5.24). Joint tomography models show that the location of these events are close to the boundary between fast seismic velocity to the south and slow velocity to the north at a depth of 30 km (the boundary is shown as a brown dashed line in Figure 5.24). Finally, Figures 5.25 and 5.26 show joint inversion tomography results along lines through the seismicity clusters. A slow continuous seismic anomaly is detected beneath Mascota and Talpa de Allende extending from near 150 km depth to the surface (Figure 5.25). The slow anomaly is just to the north of a vertical fast anomaly that I interpret as the subducting Rivera plate. Figure 5.26 shows a similar slow mantle anomaly just to the north of Ayutla volcano again at the edge of the subducting Rivera plate near 100 km depth. These observations support the idea that the CJVL is an incipient volcanic arc. In both regions, however, the mid to lower crustal seismicity is located to the southwest of the volcanoes as well as southwest of the slow mantle anomalies (Figures 5.25 and 5.26) and thus these seismicity clusters are unlikely related to magma ascent beneath the volcanoes. The seismicity is, however, located within seismically slow crust.

I interpret the slow mantle anomaly to be upwelling hydrated mantle that is causing crustal melting beneath these volcanoes. Perhaps in the future, mantle melting may produce arc volcanoes in the region. These results support the idea of slab steepening as a cause of at least the western CJVL as proposed by Ferrari (2001). Before slab roll-back, the Rivera slab may have had a shallower dip generating a volcanic arc further inland. On the other hand, the seismicity does not seem to be directly related to the volcanic activity. We do not have focal mechanisms for these small events but it is possible they are normal faulting as the result of the extensional stresses proposed by Kostoglodov and Bandy (1995). Perhaps warming of the crust adjacent to the magmatic zone is allowing for the extensional deformation to occur.

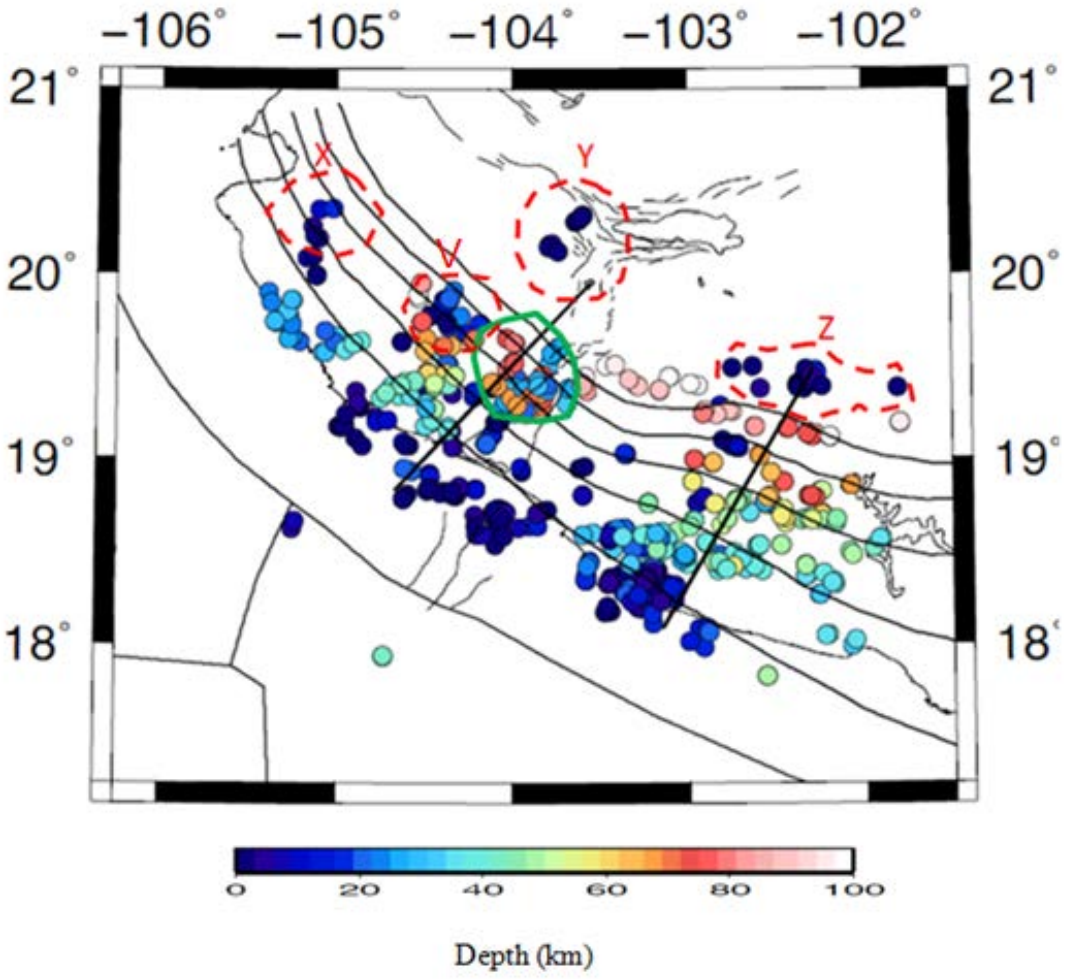

Figure 5.23 Seismicity map for Southwestern Mexico. The red dashed lines show clusters of intra-plate shallow events. Most of these events are less than 10km deep and are still located within the station network. The green circle shows a cluster of intermediate depth events (20-40 km deep) close to Colima Volcano. X and V are the location of in-land seismicity close to the Central Jalisco Volcanic Lineament. Y is the in-land seismicity close to the rifting and Z is the in-land seismicity cluster inside the MGVF close to Tancitaro and Paricutin volcano.

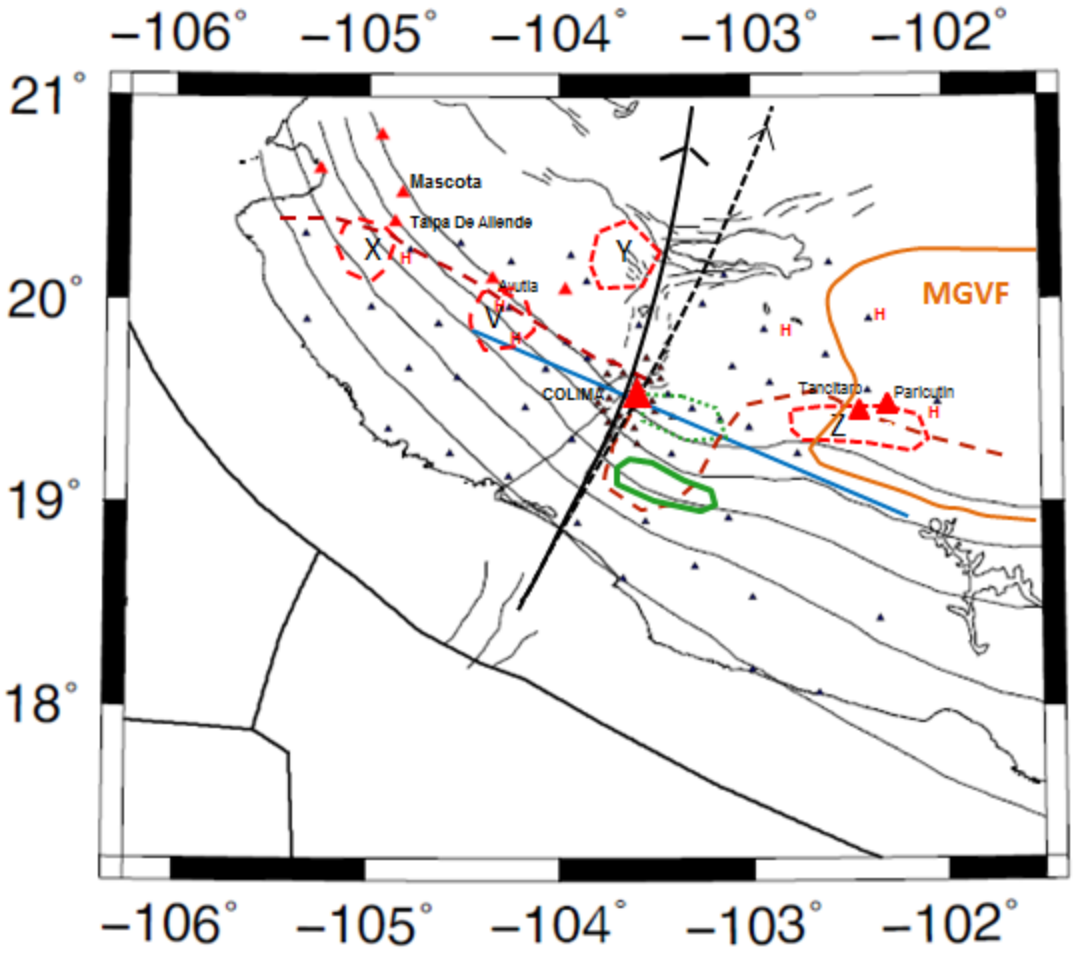

Figure 5.24 Simplified geophysical structures in southwestern Mexico. The dashed brown line is the boundary between slow velocity and fast velocity at a depth of 30km from the joint inversion velocity model. Areas located to the north of this line are dominated by slow velocities. X, Y and Z inside the red circles are relocated in-land clusters of shallow earthquakes. The blue line is where Bandy (1995) did a gravity survey and the dashed green circle is the location of his low gravity anomaly that he interpreted as the Cocos – Rivera plate boundary. The green polygon is the location of a slab tear that detected at a depth of 40km. To the east, red triangles show young volcanoes known as the Central Jalisco Volcanic Lineament and to the west, red triangles show the Tancitaro and Paricutin volcanoes inside the MGVF volcanic field (orange color). Red H's are MARS stations that show high Vp/Vs crustal ratios. The black line is the projection of the Rivera plate motion relative to the North American plate using the poles of rotation from DeMets and Wilson (1997) with the plate boundary from Yang et al. (2009). The dashed black line is the projection of the Cocos plate motion.

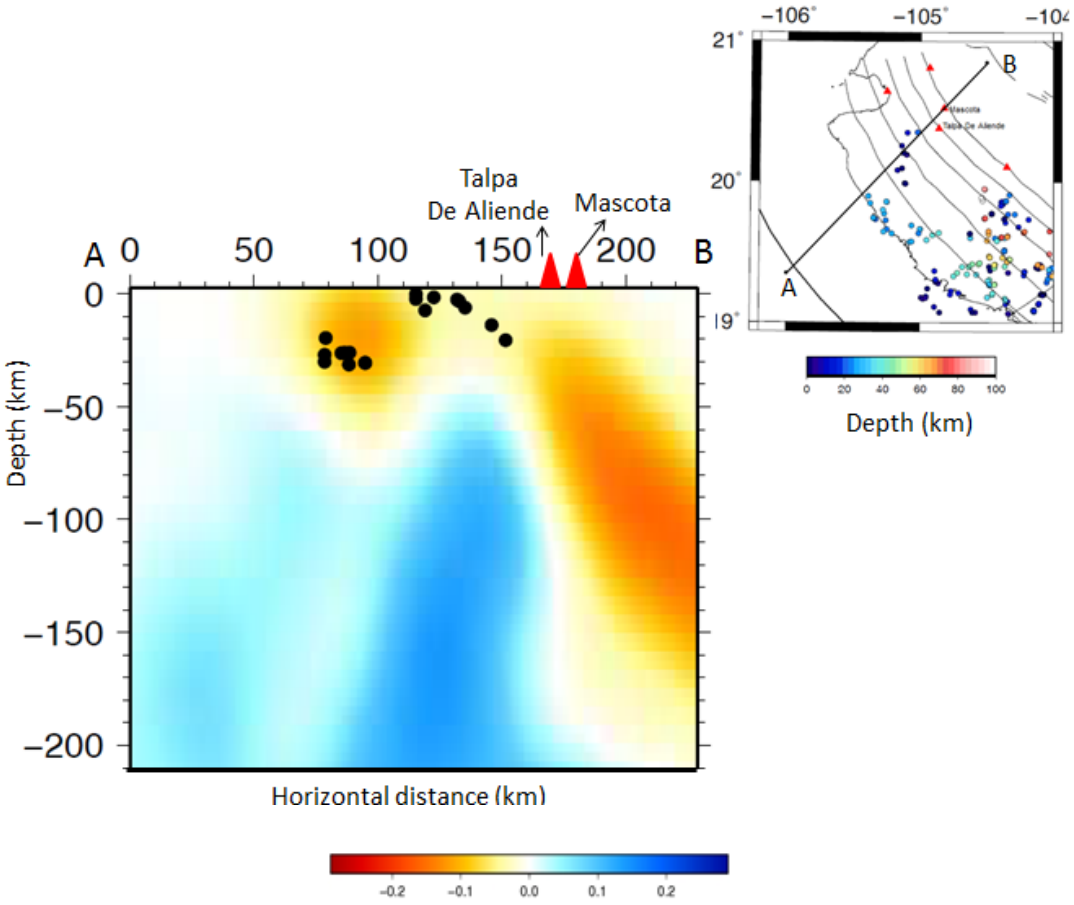

Figure 5.25. Joint inversion tomography model with seismicity near the CJVL. Red triangles show the young volcanoes Talpa De Allende and Mascota and black dots show relocated seismicity.

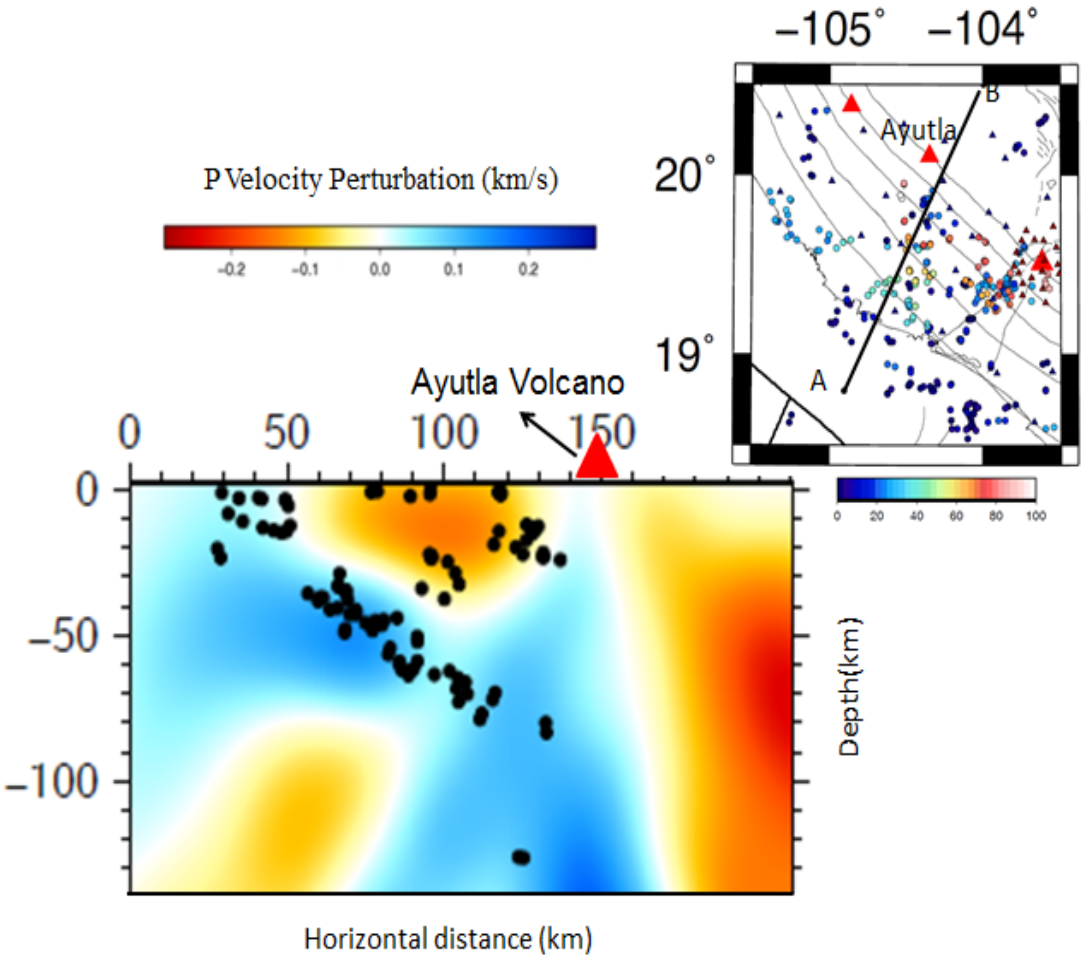

Figure 5.26. Joint inversion tomography model with seismicity along a line close to the Ayutla volcano. Black dots are relocated earthquakes.

The largest, most active volcano in Southwestern Mexico is Colima Volcano. It is clearly an arc volcano but is located closer to the trench than the trend of the TMVB. Yang et al. (2009) and our joint inversion results show a clear gap between the Rivera and Cocos slabs at a depth of about 150 km that increases in size with depth (Figure 5.16). The gap is explained by the different Euler rotation poles for the Rivera and Cocos plates relative to North America that gives diverging trajectories in the subsurface as shown in Figure 5.24. The gap allows hot hydrated asthenosphere to rise between the plates resulting in Colima volcano at the boundary between the two plates. Figure 5.27 shows a cross section of the joint inversion tomography model with seismicity through Colima volcano. Unlike the cross sections through recent volcanic centers in the Jalisco block, I do not detect slow mantle velocities directly beneath the volcano but rather see the slow velocities about 100 km north of the volcano. It is not clear if there is largely shallow southward mantle flow feeding Colima or if we do not have the resolution to detect a very narrow upwelling between the Cocos and Rivera plates directly beneath the volcano. Interestingly, if one examines Figures 5.19 and 5.20, the slow velocity mantle to the north of Colima is more prominent to the west than to the east. Soto et al. (2009) examined shear wave splitting of MARS stations and proposed a clockwise toroidal mantle follow field around the edge of the Rivera plate at depth. Thus Colima may ultimately be due to return flow asthenospheric mantle from beneath the Rivera plate flowing southward and upward within the opening gap between the Rivera and Cocos plates.

In the vicinity of Colima Volcano, I observed a region of deep crustal seismicity above the Benioff zone. The seismicity is shown within a green polygon in Figure 5.23

and circled in the cross section shown in Figure 5.27. The seismicity is 20-30 km deep and is within slow velocity crust. A similar pattern of seismicity was found by Pardo and Suarez (1995). The northern events in this cluster may be related to magma movements as the events are directly beneath Colima volcano, however, most of the seismicity is to the south of the volcano, similar to what we found for seismicity associated with the CJVL. The seismicity is probably related to extension within the rift.

Magmatism above the Cocos plate is confined to the Michoacan-Guanajuato Volcanic Field (MGVF), a wide region of volcanic activity that began about 2.8 Ma and continues today (Gomez-Tuena et al., 2007). The volcanic field is located in the northeast corner of our seismic array (Figure 5.24). Hasenaka and Carmichael (1985) studied the cinder cones that are dominant in the volcanic field and concluded that the total magma supply in this region is low compared to the typical magma supply within the Trans Mexican Volcanic Belt. The cross sections through the tomography model shown in Figure 5.19 show that the Cocos slab is roughly 150 km depth beneath the MGVF (cross section A6B6) but the slow velocities above the slab are not as strong as the slow velocities above the slab to the west. To the west the slabs (both the Rivera and the Cocos) have steeper dips than the Cocos plate along profile A6B6 and perhaps this has resulted in a more focused upwelling there. On the other hand, the mantle wedge along profile A6B6 is located at the northern edge of our array and it is likely the image is degraded somewhat in this location. In any case, the MGVF seems to be located above slab at depths commonly associated with arc volcanism and, as with the CJVL in the Jalisco block, our results support the idea that the MGVF is an incipient arc which is moving trenchward as the Cocos plate steepens and rolls back.

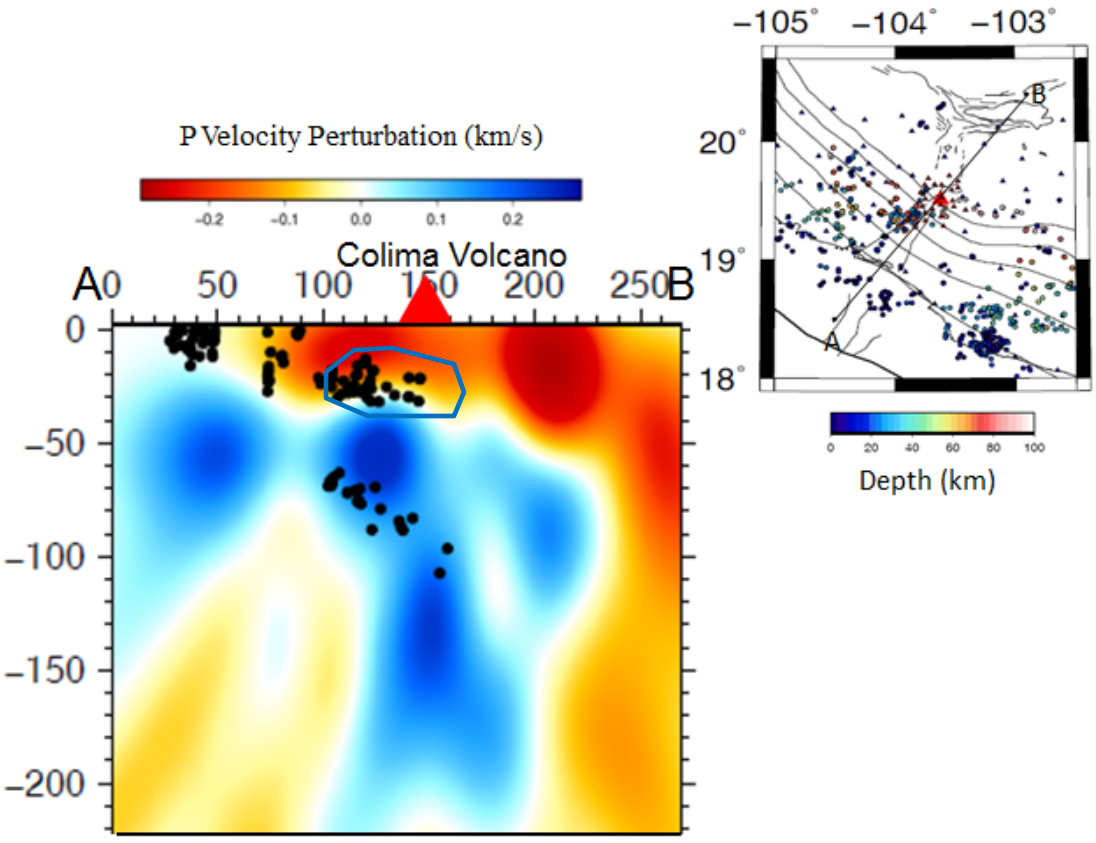

Figure 5.27. Cross section tomography model and seismicity around Colima volcano.

Shallow seismicity above the Cocos plate is mostly limited to the MGVF (region Z in Figure 5.23). Unlike the shallow seismicity in the Jalisco block, I find the seismicity in region Z to be very shallow with most events less than 10 km depth. Cross section A4B4 (Figure 5.19) shows that these events are in slow crust but near a transition to faster crust to the south. In figure 5.28 we show a map view of the seismicity and it appears that most of the shallow events are associated with the Tancitaro and Paricutin volcanoes. Pacheco et al (1999) reported an earthquake swarm in the same region. Paricutin was born in 1943 and Tancitaro is an andesitic-dacitic young stratovolcano in a field that has been active from 1 Ma to present (Maciel et al., 2009). It seems likely that the shallow seismicity we locate here is related to mid to upper crustal magma migration.

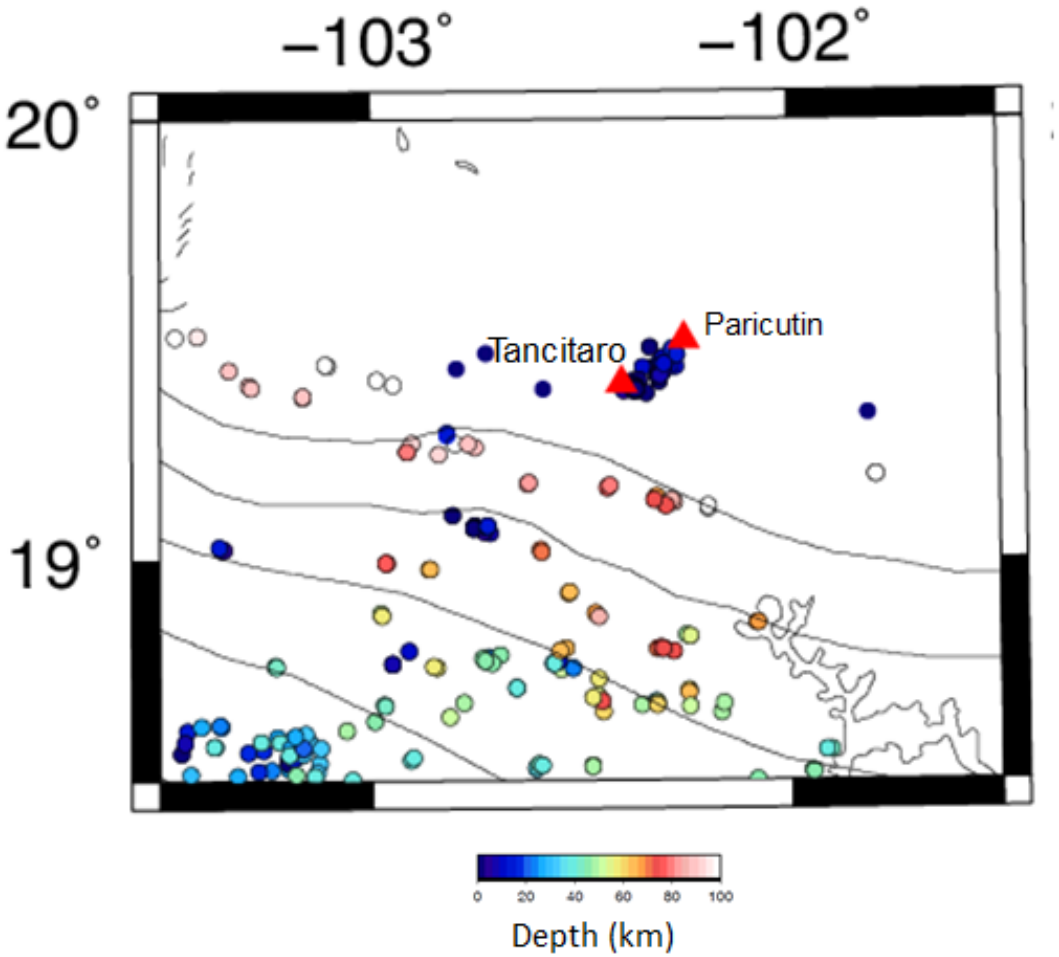

Figure 5.28. Close up of shallow in-land seismicity from figure 5.22 showing events located between Tancitaro and Paricutin volcanoes.

The western edge of the Cocos plate

The western boundary of the Cocos plate is shown in Figure 5.24 as a dashed line. The location is based on the results of tomography (Yang et al., 2009) as well as projecting the surface location to the subsurface using the pole of rotation for the Cocos plate relative to North America. As can be seen in Figure 5.24, the slab depth contours from Pardo and Suarez (1994) show a steeper dip for the Cocos plate along its western edge. Figure 5.29 shows a new seismicity contour map based on our joint inversion results. The new contour map is similar to Pardo and Suarez (1995) for the Cocos plate but has a much steeper dipping Rivera plate. However, the new contour map still shows a steeper dip for the Cocos plate along its western edge. Bandy (1995) measured gravity along a profile through Colima and perpendicular to the rift. He found a zone of lower gravity to the east of Colima (shown as a dashed green line in Figure 5.24) that he proposed to be a gap between the Cocos and Rivera plates. The seismic tomography model for the plate boundary, however, is located to the west of this low gravity zone. Finally, Leon Soto et al. (2009) showed a change in shear wave splitting fast direction from a plate motion direction to a more eastward direction near the gravity low. The edge of the Cocos plate may be steepening as a result of the gap in slab to the east such that asthenospheric flow in to the mantle wedge becomes easier resulting in a smaller mantle wedge “suction force”. Based on the shear wave anisotropy results, it appears the asthenosphere that flows laterally to accommodate the steepening deep comes from the deep mantle rising between the two plates. This injection of warmer mantle may explain the lower gravity zone seen by Bandy (1995) as well as the hot springs seen in the region.

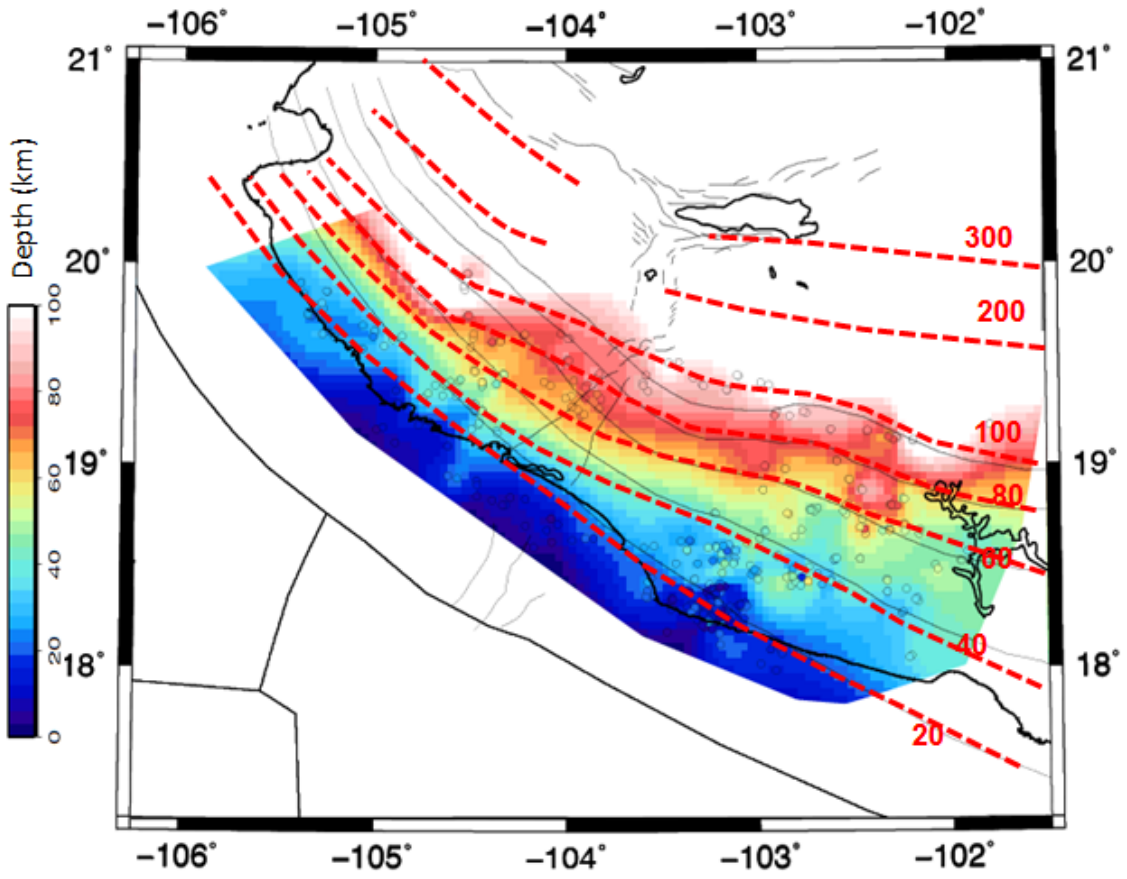

Figure 5.29. Subducted slab contours from the joint inversion relocated seismicity (20 km to 100 km) and the joint inversion seismic model (200 km and 300 km contour lines). The black lines in the background are contour lines from Pardo and Suarez, 1995. The gridded color image is interpolated data from the seismicity study after removing shallow in-land data.

In another sign of instability of the Cocos slab along its western edge, I find a possible tear in the plate at about 50 km depth. Cross section profiles along the eastern side of the Colima rift show a gap in high velocity at a depth of about 50 km. The gap is best seen in cross sections A4B4 and A5B5 in Figure 5.19 and is circled with a red dashed line. The region seems to be well sampled by both regional and teleseismic raypaths so that the break in high velocity is likely real. The zone is shown in map view in Figure 5.24 within a green circle. It is also interesting that there is a distinct lack of seismicity within the gap in high velocity shown in Figures 5.19 and 5.20.

The gap in high velocity at 50 km depth within the Cocos plate is interpreted to be a tear in the plate that extends 50-60 km from the western edge of the plate to its interior. A schematic diagram interpretation is shown in Figure 5.30. Such shallow tearing of slabs has been proposed by Keskin (2003) to have occurred in East Anatolia and by Liu and Stegman (2012) to have occurred in the western United States in the past. It should be noted that the location of the tear just to the east of Colima rift is where the youngest oceanic plate is subducting (Figure 1.2) and thus where the plate is likely the weakest. If the downdip section of the Cocos plate is steepening and perhaps twisting to the northeast, tensional stresses can increase within the updip portion of the plate and thus result in the tear we observe.

If a tear is present at depth an interesting question is what affect it has on large earthquakes updip of the tear. Two large earthquakes that occurred in 1995 and 2003 caused significant damage in Colima, but both ruptured to the west of the slab tear (Schmitt et al. 2007). In 1973 a magnitude 7.5 earthquake occurred in the state of

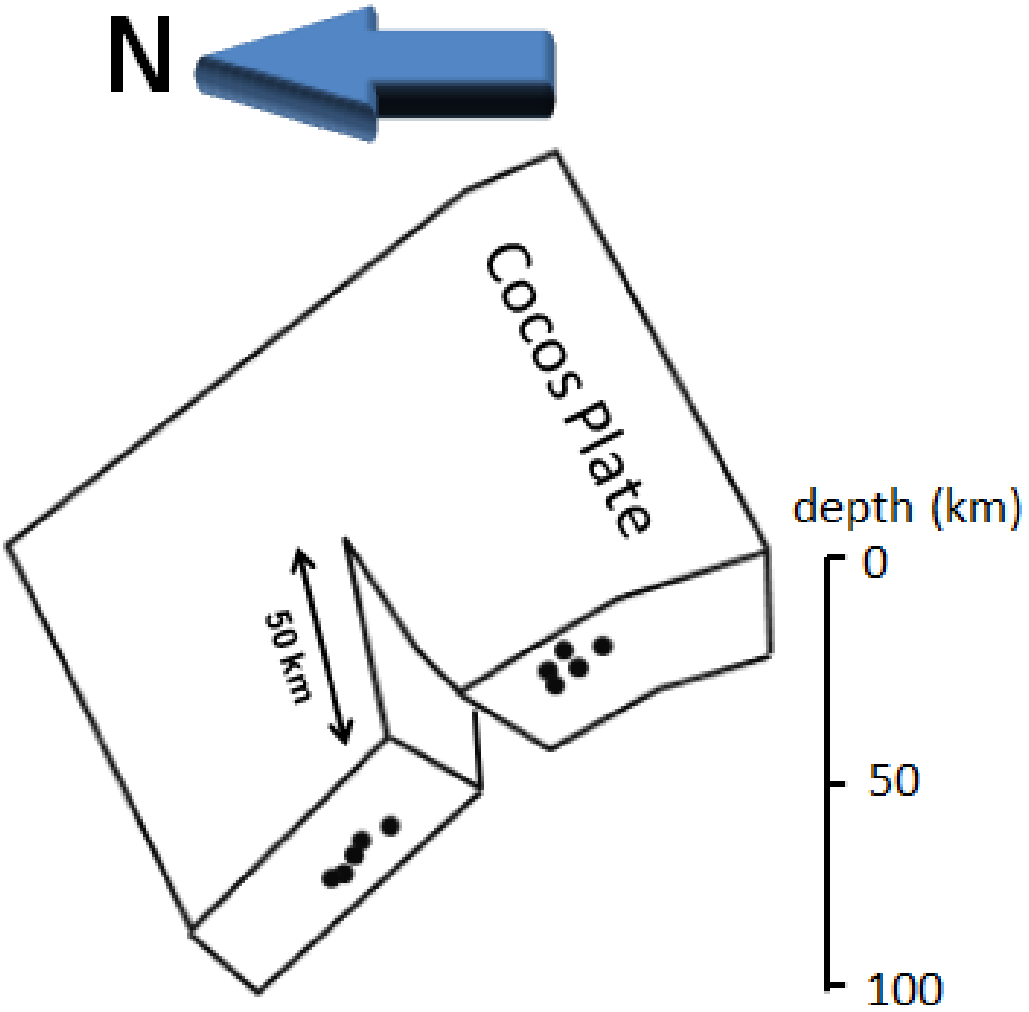

Figure 5.30 Cartoon illustration of a possible slab tear along the western side of the Cocos plate. The tear in the slab is located at a depth of 50 km. and extends 50-60 km to the east. The black circles represent relocated seismicity.

Michoacan but its epicenter was to the east of the slab tear (Reyes et al., 1979). According to Schmitt et al. (2007) this event ruptured to the northwest to fill in the gap between the epicenter of the 1973 event and the slip modeled for the 2003 event. Currently, it is unclear what affect a tear like we propose would have on the earthquake potential updip from the tear although it is likely to perturb the stress state there.

Summary

The upper mantle and lithosphere seismic structure beneath southwestern Mexico was determined by a combined tomographic inversion of teleseismic and regional P wave arrivals recorded by the MARS and CODEX seismic experiments. The model was constructed using 3-D ray tracing and a joint inversion technique that includes local event locations as unknowns. The inclusion of regional data over just teleseismic data improves both the resulting seismic model as well as the locations of regional seismicity.

The image of the shallow structure of the western Jalisco block is not improved over the teleseismic inversion due to the lack of local events. However, the images of the subducting and overriding plates are significantly improved over a pure teleseismic data inversion through most of our study area. Similarly, the event locations through double difference and joint inversion of local seismicity located by the MARS and Codex arrays are improved over the previous locations determined with a one dimensional velocity model. The seismicity I relocated shows that the interplate locked zone extends to 30 to 35 km depth with only intraplate deeper events. Deeper seismicity appears to show an abrupt change in dip of the Rivera plate near 100 km where the subducting plate becomes

nearly vertical. Very slow mantle velocities associated with the mantle wedge above the Rivera plate seem to be associated with the CJVL volcanic activity in the Jalisco block supporting the idea that the CJVL may be an incipient arc. Mid to lower crustal seismicity to the south of the CJVZ, however, supports a model for active crustal extension. Determining earthquake mechanisms for some of this seismicity would help clarify their significance.

The Cocos plate appears to descend with a shallower and more uniform dip than the Rivera plate. The MGVF volcanic field is above where the Cocos plate reaches 150 km depth or so and thus this is consistent with the MGVF as an incipient arc. However, the mantle wedge velocities are not as slow here as above the Rivera plate. The wedge is at the edge of our array so that it is possible the true velocity anomaly associated with it is under estimated and it would require a future deployment of instruments further inland to confirm the difference in shallow mantle velocities between the mantle wedge above the Rivera and Cocos plates.

Another interesting finding from the joint inversion relates to the western edge of the Cocos plate. The edge seems to dip more steeply than to the east and there appears to be a tear in the edge of the Cocos slab at about 50 km depth extending just 50 km or so into the slab. To understand the dynamical cause and consequences of this feature is left to future work.

Chapter 6: Summary, model and future works

In this chapter, I review all geophysical studies done in this study. A receiver function study has been done to estimate the crustal depth of the dipping oceanic crust and the in-land continental crust. By using crustal multiples, a receiver function study can estimate not only a crustal depth underneath a receiver, but also the Vp/Vs ratio of the crust. Overall, the main conclusions of the crustal study are summarized as follows:

1. In total, I obtained 24 reliable Vp/Vs ratio measurements and 47 reliable crustal thickness measurements for receiver function study. The contour plots using the H-K method show strong peaks and good resolution for most inland stations. The mean value of continental crust thickness is 39 km and crustal depth measurement ranges from 20 km on the coast to 43 km in land, the Vp/vs ratio has 1.81 mean ranging from 1.72to 1.87.
2. Crustal thickness and topography do not correlate well. Higher topography inland with thinner crust may be related to buoyant mantle that agrees with the slab steepening model previous proposed by Ferrari (2004) and Yang et al (2008).
3. The crustal thickness map shows less than 1 km thinning of crust in the Colima Rift that may be interpreted that there has been very little extension in the Rift. This agrees with the conclusion of Rosas-Elguera (1996) that the southern Colima Rift is actually a broad slowly extending (< 1 mm/yr) zone that has been active only since the late Pliocene.
4. Three regions show unusual high Vp/Vs ratio. The first region is located in the central part of the Jalisco block, close to a series of young volcanoes known as the

Central Jalisco Volcanic Lineament. Four stations located at the southwestern edge of the region show Vp/Vs ratios of 1.85 or greater. A possible interpretation is that the crust is being broadly heated with possible partial melt developing trenchward of the recent volcanism The second region, located to the northeast of Colima Volcano, shows a band of high Vp/Vs ratios ranging from 1.85 to 1.87. I conclude that the high Vp/Vs ratios are related to partial melt or high fluid content within the crust although some mafic underplating of the crust could also contribute. The last region is located within the Michoacan-Guanajuato Volcanic Field (MGVF), a wide region of volcanic activity that began about 2.8 Ma and continues today (Gomez-Tuena et al., 2007). I interpret this as an area of widely distributed partial melt that may be related with partial slab steepening and roll back of the Cocos plate.

5. Plots of stacked receiver function with respect to the depth of slab taken from Pardo and Suarex (1993, 1995) shows dipping signals that are associated with the geometry of the slab down to a depth of 60 km. Waveform modeling of negative signals above a positive signal suggests a 3 km slow velocity layer with high 2.5 Vp/Vs ratio. My findings support the idea of Audet (2009) and Kim et al (2010) that the top of the oceanic crust formed of sediments, pillow basalts and sheeted dikes of gabbro, contains significant water as well as hydrated minerals. As the plate subducts, some of the rocks compact and minerals dehydrate creating high pore fluid pressures that cause the dramatic drop in observed shear velocity. At deeper depths, the slab receiver function signals seem to disappear. This likely marks the basalt to eclogite phase transition.

6. The receiver function image also displays a weak Moho in certain regions. The region is from where the slab reaches 50 km depth and extend 30-50 km inland. Following Bostock (2002), I interpret the zone with a weak Moho to have a serpentenized mantle wedge. Serpentine has shear velocity close to crustal value that does not have velocity contrast across the moho.

In the fourth chapter, I performed a teleseismic tomography inversion of delay times for all teleseismic events recorded at our stations. I used a sophisticated 3-D fast marching ray tracing and subspace inversion in the inversion. I compared the results with a previous teleseismic inversion that use finite frequency seismic tomography (Yang et al, 2009). Teleseismic inversion has the ability to image the structure at deeper depths but suffers in resolution at shallow depths due to near vertical ray paths near the stations. Overall, the main conclusions from this chapter are summarized as follows:

1. The finite frequency tomography model and 3-D ray tracing model show similar results with a few possibly important differences. Both models show a northwest-southeast band of high velocities that dips to the northeast. My seismic models support the interpretation of Yang et al (2009) and Ferrari (2004) that slab steepening is occurring in South Western Mexico that leads to a coastward migration of volcanism and mixed geochemical signatures observed in the western TMVB. Both tomography models also show a gap between the Rivera and Cocos slab that increases in size with depth. The main difference is that the 3-D ray tracing model shows a clear fast velocity band down to a depth of 400 km

beneath Jalisco that does not indicate a slab tear of the Rivera plate above 400 km depth. If there is a tear in the slab as proposed by Ferrari (2004), the slab end is deeper. Unfortunately, the resolving power of both our tomography inversions becomes weak below a depth of 400 km , especially to the north.

2. The comparison between finite frequency tomography and 3-D ray tracing tomography shows that the finite frequency models have up to 50% higher amplitude recovery in slow velocity structure. However, the 3-D raytracing model produced sharper images of fast velocity structures in the mantle. In our example, the deeper slabs are more coherent and show less broadening with depth than inversions using 1D finite frequency kernels

In the fifth chapter, I measured local events by visual observation and automatic picking. The seismicity is then relocated using the double difference method before finally added to a joint inversion combined with teleseismic data. Teleseismic inversion suffers from poor resolution at shallow depth and adding local events can solve this problem. The output from this study is not only a seismic model that has resolution at shallow and deeper depth, but also better seismicity location. I summarize the results of the joint inversion as follows:

1. The Joint inversion models show clear and continuous fast velocity anomaly at shallow depth compared to the teleseismic inversion. Although the western part of the Rivera slab does not show an improved velocity image due to a lack of local events in this region, the eastern part of the Rivera and the Cocos plate show

better resolution in fast velocity structure. The slow velocity structure at the northern part of southwestern Mexico displays a stronger slow velocity amplitude compared to the model from teleseismic inversion.

2. Relocated seismicity from January 2006 to June 2007 after the double difference relocation and joint inversion clearly shows the Benioff zones associated with the subduction of the Rivera and Cocos plates. The western side of the Rivera plate is largely aseismic but the eastern side, close to the Colima Rift to the east, shows an abundance of seismicity.
3. Further seismicity analysis combined with the tomography and receiver function analyses show that the interplate earthquakes occur to a depth of about 30 km (possibly a few kms deeper in some regions), but below that depth events are occurring within the top part of the descending plate.
4. A cluster of shallow events were detected in-land with estimated magnitude range between 2.5 and 3.3. The first cluster is located above the Rivera slab inside a slow velocity region close to the Central Jalisco Volcanic Lineament volcanoes. Crustal structure studies in Chapter 3 also found stations that have high Vp/Vs ratios close to these events. My interpretation suggests that warming of the crust adjacent to the magmatic zone is allowing for extensional deformation to occur. The second cluster is located close to Colima Volcano inside a slow velocity region. I interpret these northern events may be related to magma movement as the events are directly beneath Colima, however, most of the seismicity is to the south of Colima volcano, similar to what we found for seismicity associated with the CJVL. The seismicity may be related to extension within the rift. The third

cluster is located to the north close to the Zacoalca rift where previous studies suggest they are events related to extension.. The fourth cluster is located inside the Michoacan Guajanato volcano field close to the Pacutin and Tancitaro volcano. It seems likely that the shallow seismicity I located here is related to mid to upper crustal magma migration.

5. The joint inversion models show interesting feature related to the western edge of the Cocos plate. The edge seems to dip more steeply than to the east and there appears to be a tear in the edge of the Cocos slab at about 50 km depth extending 60 km or so into the slab. Note that the region of the tear also shows a lack of seismicity for 1.5 years station deployment.

A simple geological model to explain the steep Rivera slab is proposed that supports a slab steepening model previously proposed by Ferrari (2001). Roughly at 10 Ma, the Rivera-Cocos slab likely had a shallow dip reaching 150 km depth or so beneath the Trans-Mexican Volcanic Belt. Since that time, the Rivera plate and to a lesser extent the western Cocos plate have steepened in dip and rolled-back. The possible reason for the slab roll-back may be associated with a decrease in slab convergence. The roll-back and steepening of the Rivera plate has resulted in migration of magmatism closer to the trench in the fore arc resulting in a series of young active magmatism known as the Central Jalisco Volcanic Lineament (Figure 6.1).

A slow velocity region located between fast velocity bands in the Colima rift suggests a break between the plates that occurs beneath the Colima Rift and may be responsible for the location of Colima Volcano. A simple diagram that shows the

relation of asthenosphere mantle flow from the break to the surface and the steep Rivera slab is presented in Figure 6.2. The opening between the plates creates a window to allow a toroidal-type flow to bring enriched deep mantle into the mantle wedge. Ferrari et al (2001) suggest that the termination of subduction at the northeast may allow flow around the northwestern edge of the Rivera plate.

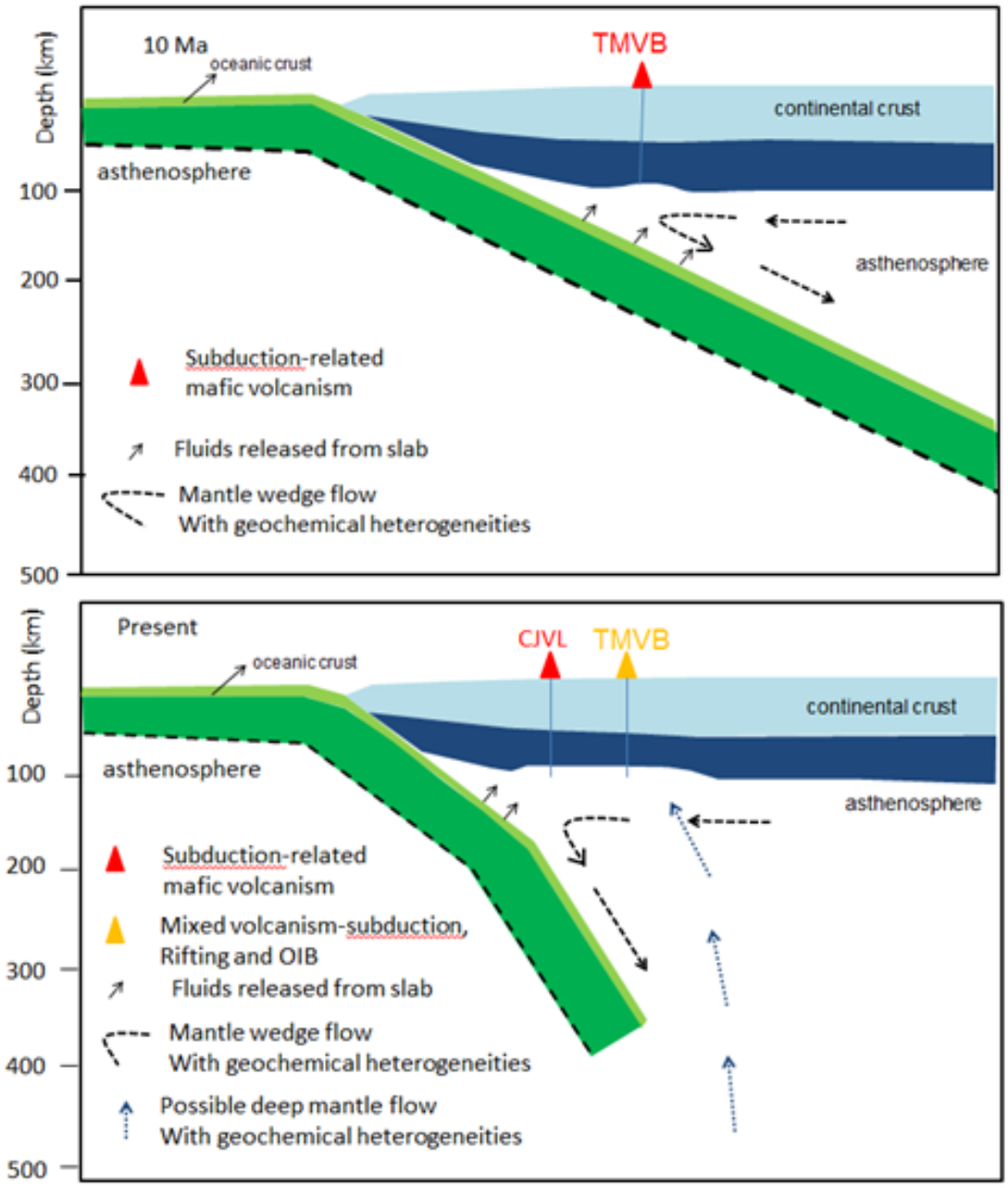

Figure 6.1 Schematic illustrations of the geometry of the Rivera slab beneath the Jalisco Block (a) 10 Ma and (b) at present. CJVL stands for central Jalisco Volcanic Lineament and TMVB is Trans Mexican Volcanic Belt.

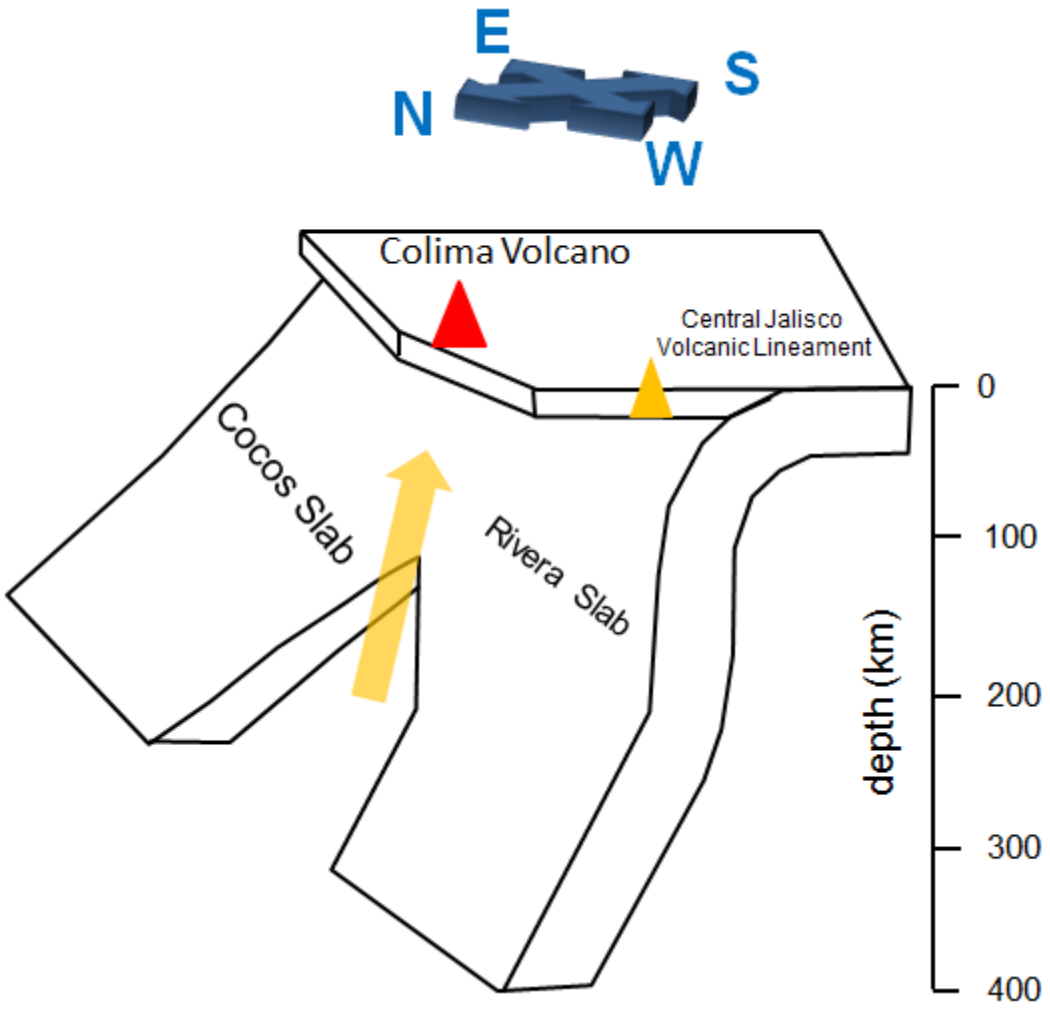

Figure 6.2 A cartoon that shows a break between Cocos and Rivera slab creates a window for asthenosphere mantle flow as a source of magmatism for Colima Volcano. The Rivera slab may be steepening due to a toroidal flow that goes to northern west at the Rivera slab.

Future works

Several future projects can be done to improve our understanding of this complex region as summarized below:

1. Ferrari (2004) proposed a tear model that propagated from the Gulf of California to the Gulf of Mexico during the late Miocene (Figure 6.3). The projected tear in the surface is roughly located beneath the northern part of the Trans Mexican Volcanic Belt. My tomography model shows good resolution down to a depth of 400 km with decreasing resolution at deeper depth. To investigate deeper slab structure, a new station network needs to be installed in the northern part of the Rivera and Cocos study. A global tomography model may also be used to get a better resolution at deeper depths.
2. Neither teleseismic nor joint inversion of S wave time has not been done in this region. Shear waves are more sensitive to changes in fluid content and may provide better information to explain the sources of magmatism in the region.
3. The double difference hypocenter calculations in this study only employed delay time information. Better precision can be achieved by using waveform correlation for local events and using them for hypocenter estimation.
4. Better velocity and hypocenter locations can also be improved by doing a joint inversion that includes both P and S wave.
5. Using a variable grid size in tomography could also upgrade the images of the complex structure at shallow depths.
6. A focal mechanism study can be done to better understand the origin of shallow in-land events.

Appendices

Appendix A

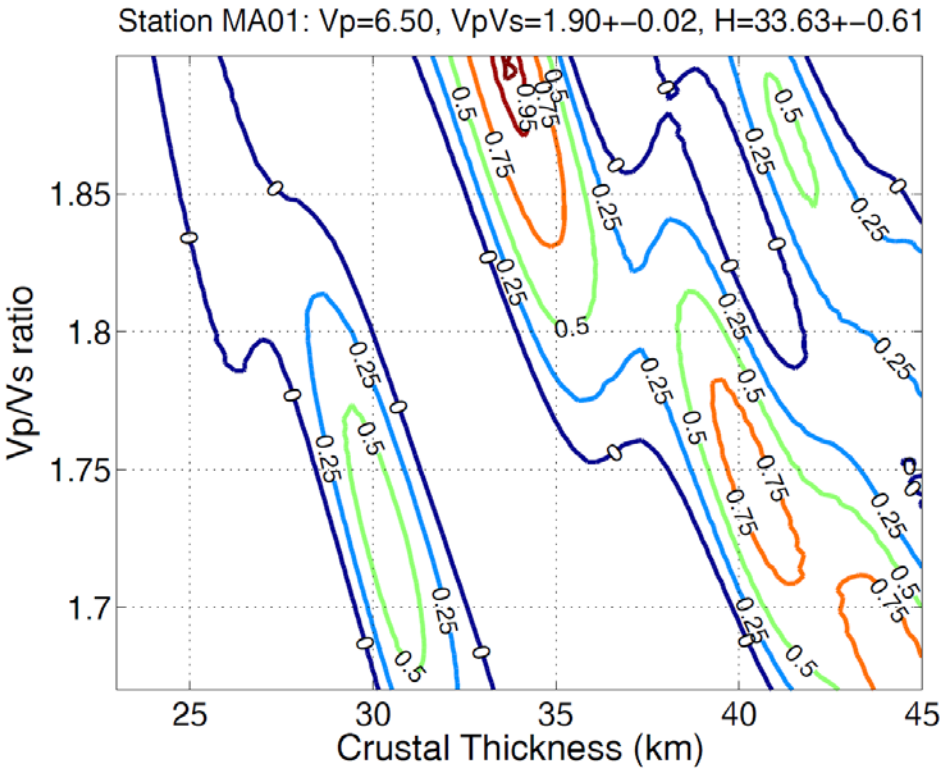
Station MA01: Vp=6.50, VpVs=1.90+−0.02, H=33.63+−0.61
Vp/Vs ratio
1.85
1.8
1.75
1.7
25
30
35
40
45
Crustal Thickness (km)

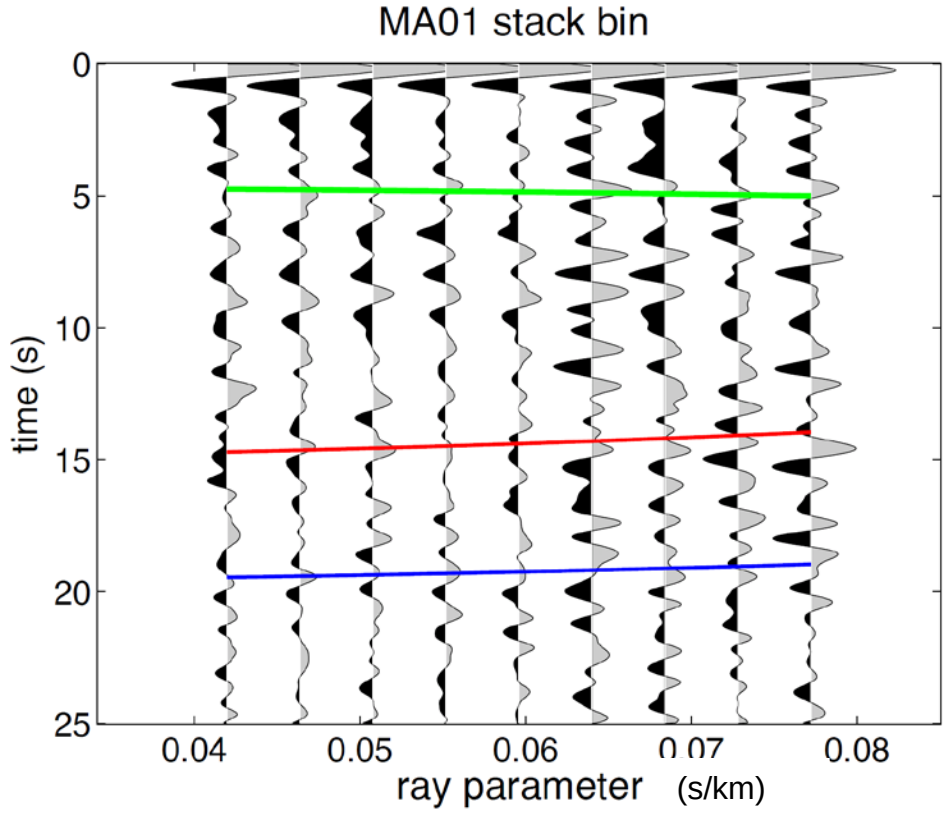
MA01 stack bin
time (s)
0
5
10
15
20
25
0.04
0.05
0.06
0.07
0.08
ray parameter (s/km)

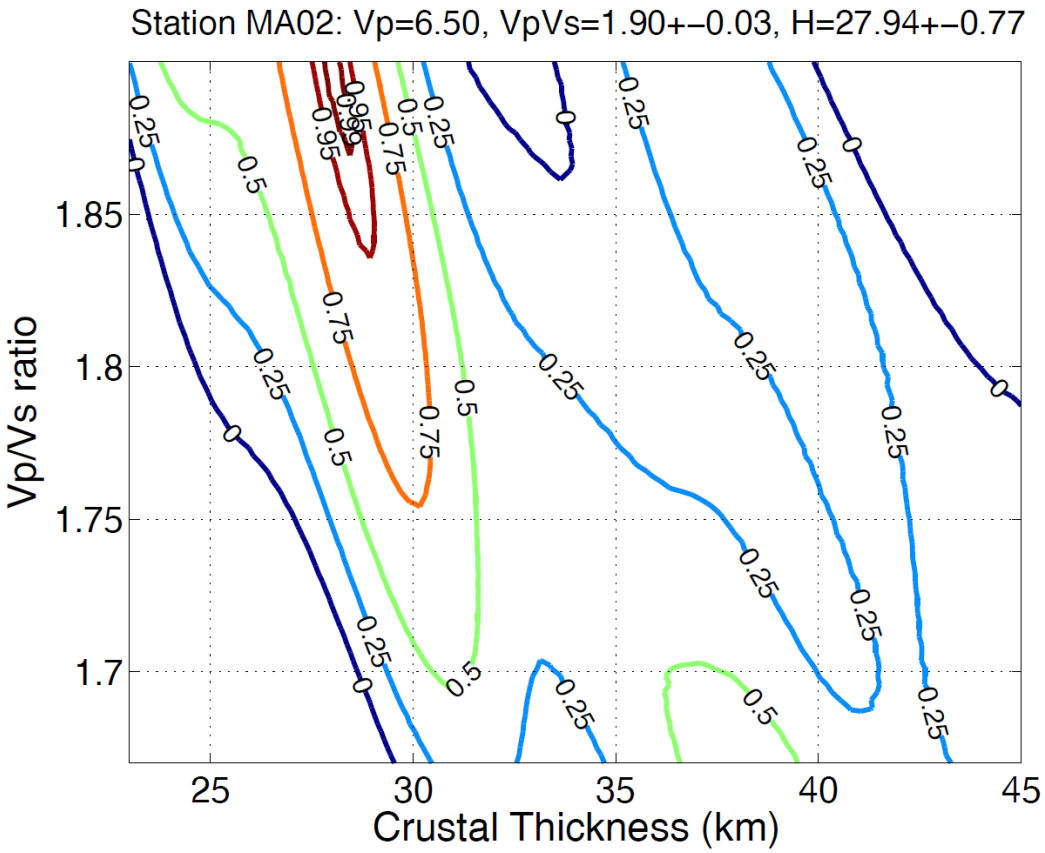
Station MA02: Vp=6.50, VpVs=1.90+−0.03, H=27.94+−0.77
Vp/Vs ratio
1.85
1.8
1.75
1.7
25
30
35
40
45
Crustal Thickness (km)

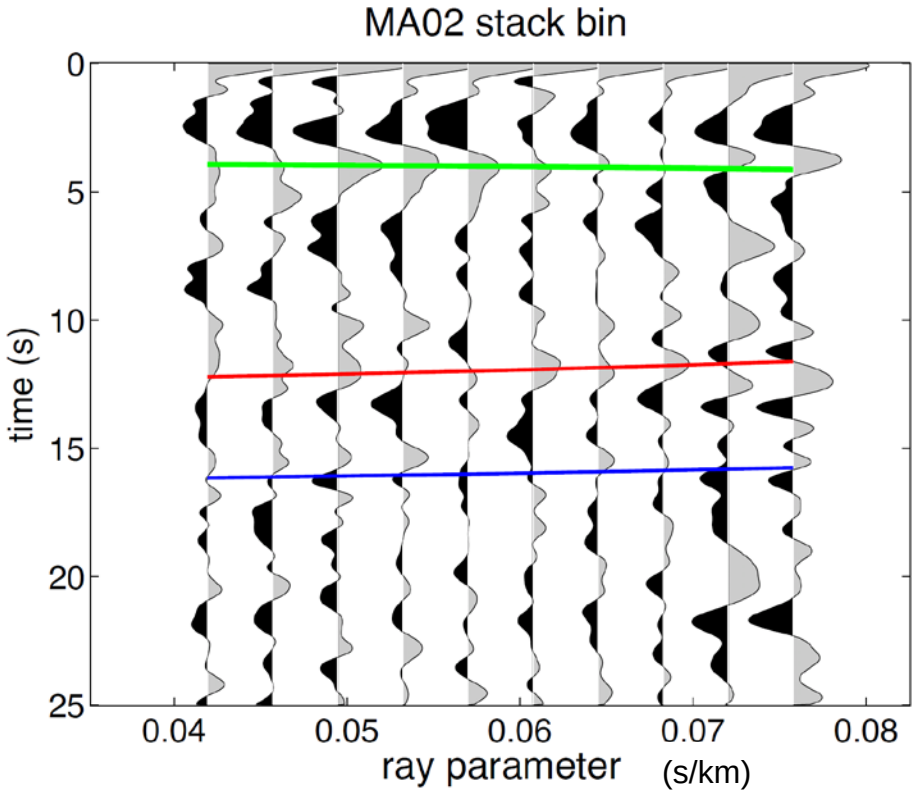
MA02 stack bin
time (s)
0
5
10
15
20
25
0.04
0.05
0.06
0.07
0.08
ray parameter (s/km)

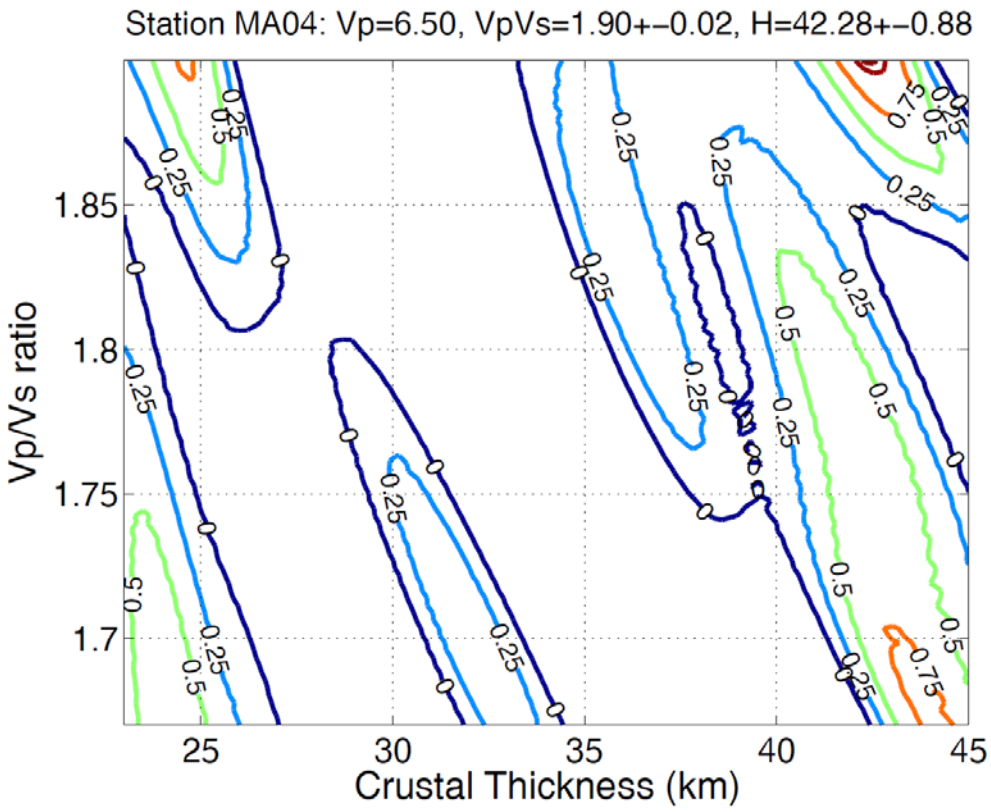
Station MA04: Vp=6.50, VpVs=1.90+−0.02, H=42.28+−0.88
Vp/Vs ratio
1.85
1.8
1.75
1.7
25
30
35
40
45
Crustal Thickness (km)

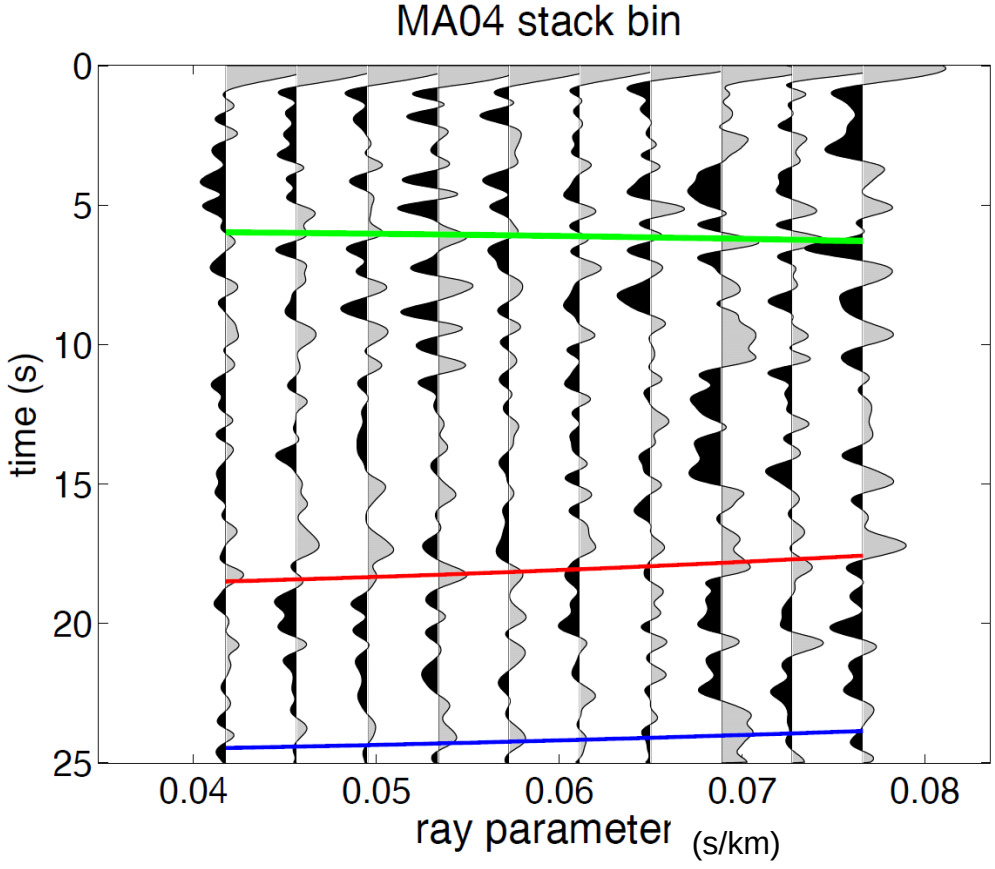
MA04 stack bin
time (s)
0
5
10
15
20
25
0.04
0.05
0.06
0.07
0.08
ray parameter (s/km)

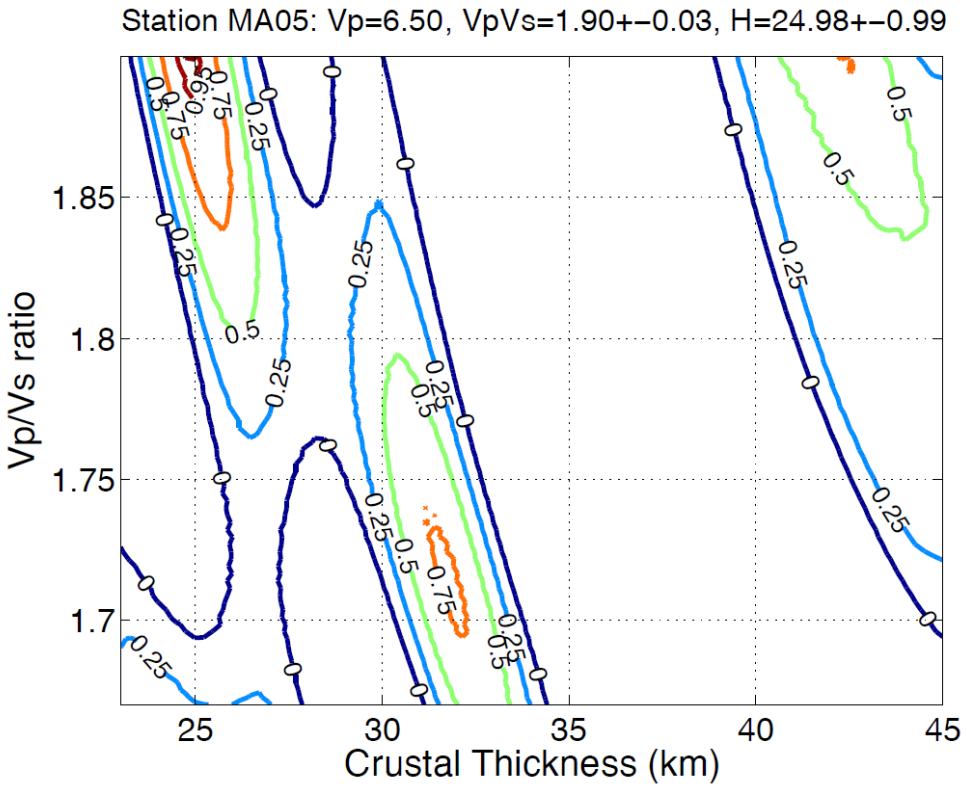
Station MA05: Vp=6.50, VpVs=1.90+−0.03, H=24.98+−0.99
Vp/Vs ratio
1.85
1.8
1.75
1.7
25
30
35
40
45
Crustal Thickness (km)

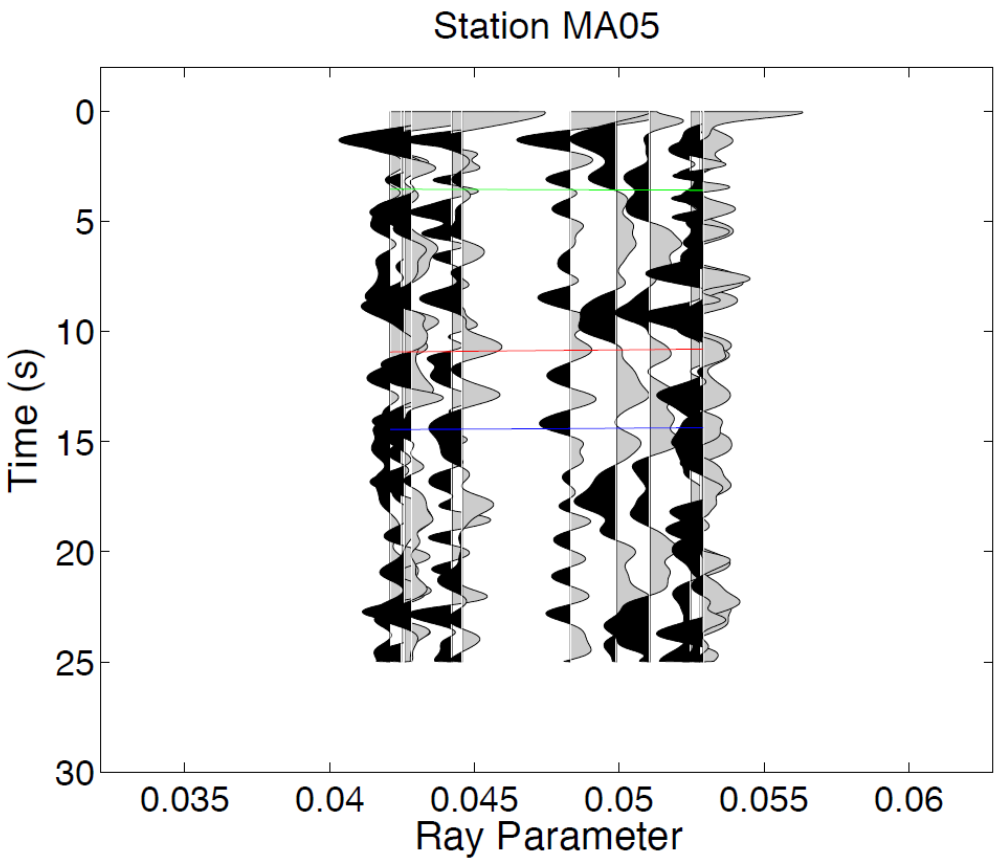
Station MA05
Time (s)
0
5
10
15
20
25
30
0.035
0.04
0.045
0.05
0.055
0.06
Ray Parameter

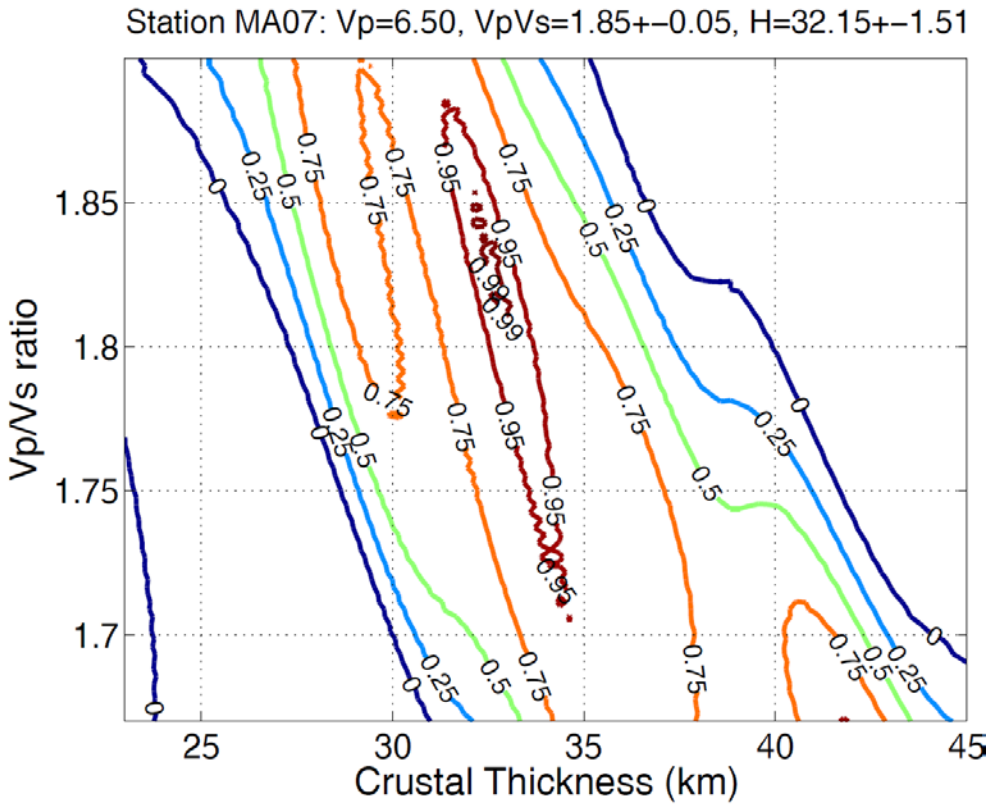
Station MA07: Vp=6.50, VpVs=1.85+−0.05, H=32.15+−1.51
Vp/Vs ratio
1.85
1.8
1.75
1.7
25
30
35
40
45
Crustal Thickness (km)

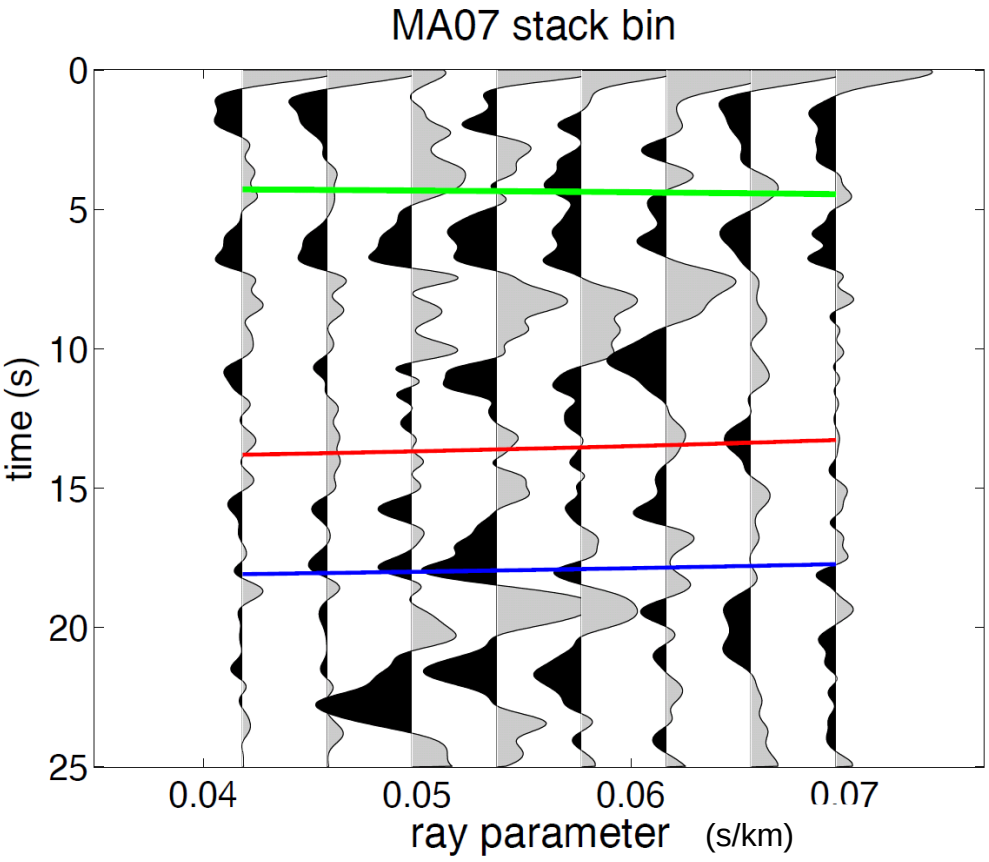
MA07 stack bin
time (s)
0
5
10
15
20
25
0.04
0.05
0.06
0.07
ray parameter (s/km)

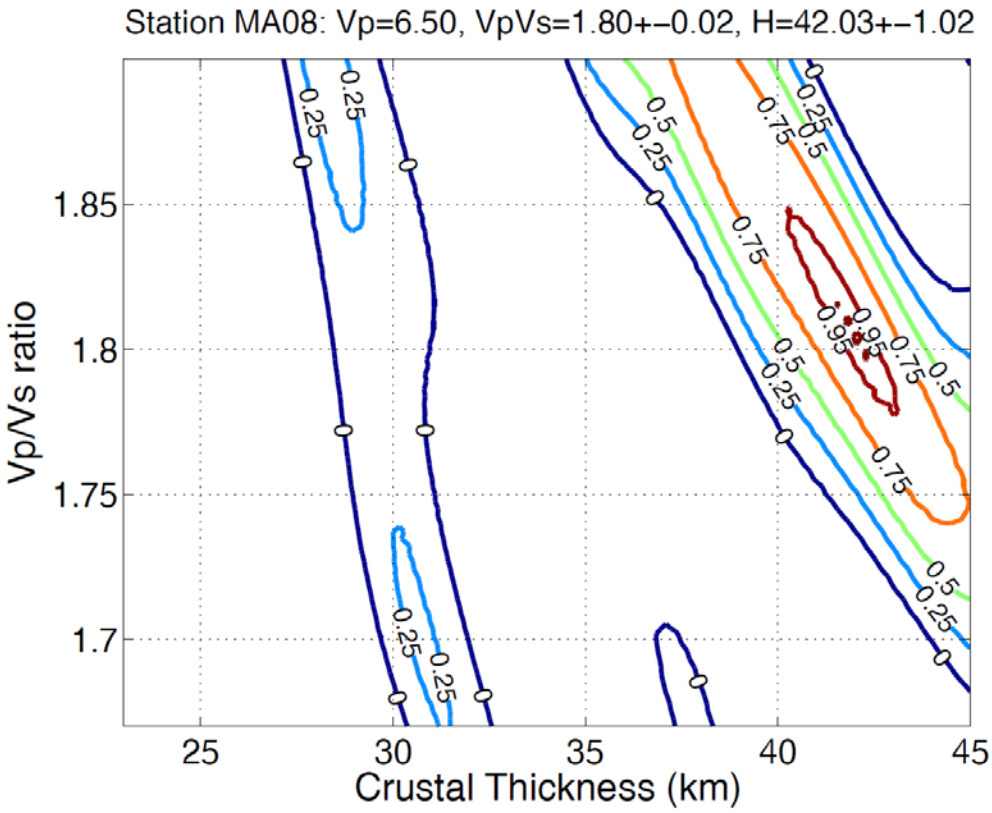
Station MA08: Vp=6.50, VpVs=1.80+−0.02, H=42.03+−1.02
Vp/Vs ratio
1.85
1.8
1.75
1.7
25
30
35
40
45
Crustal Thickness (km)

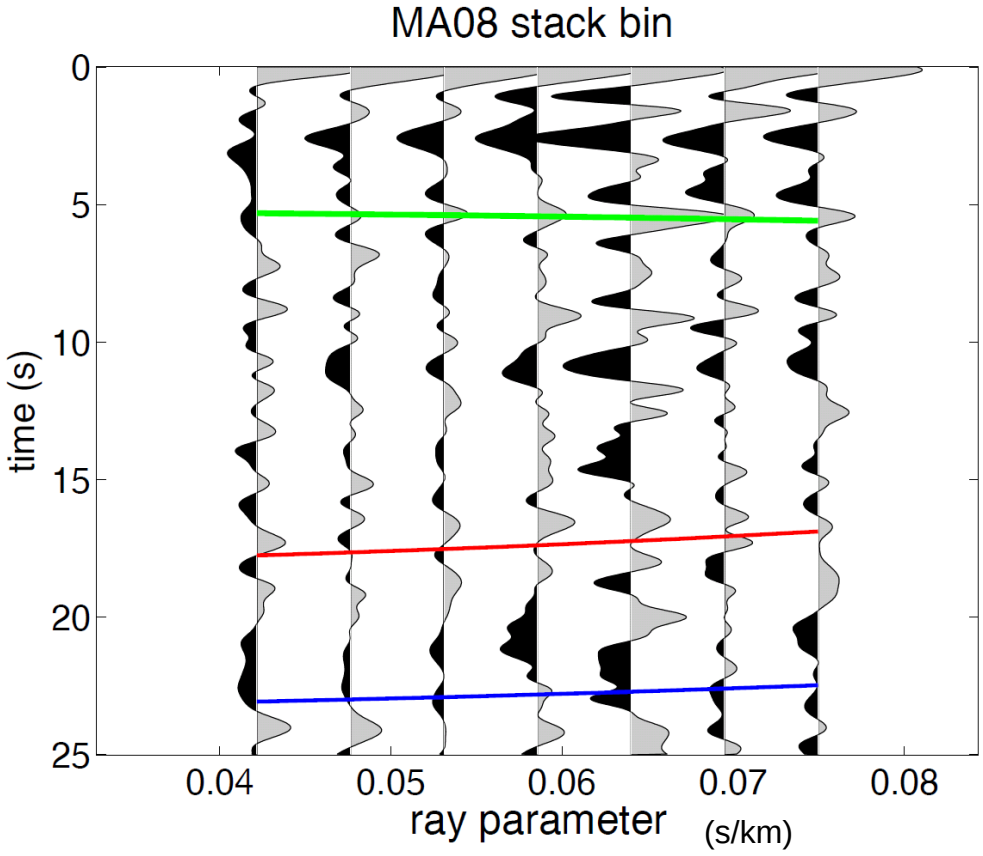
MA08 stack bin
time (s)
0
5
10
15
20
25
0.04
0.05
0.06
0.07
0.08
ray parameter
(s/km)

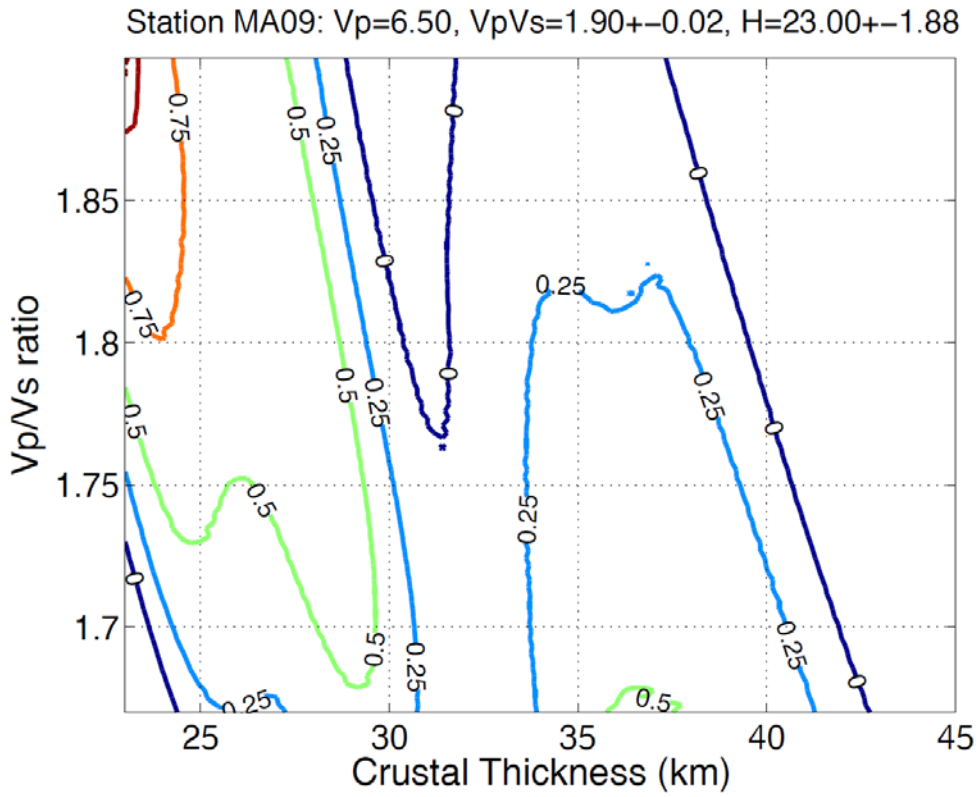
Station MA09: Vp=6.50, VpVs=1.90+−0.02, H=23.00+−1.88
Vp/Vs ratio
1.85
1.8
1.75
1.7
25
30
35
40
45
Crustal Thickness (km)

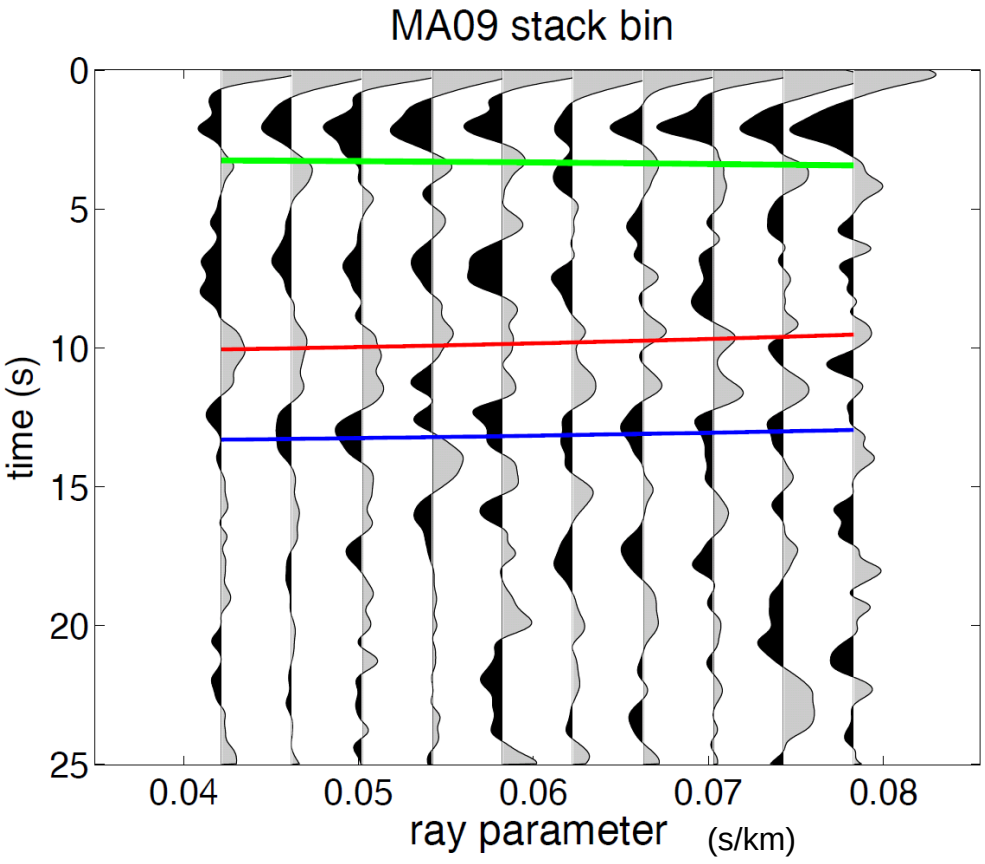
MA09 stack bin
time (s)
0
5
10
15
20
25
0.04
0.05
0.06
0.07
0.08
ray parameter (s/km)

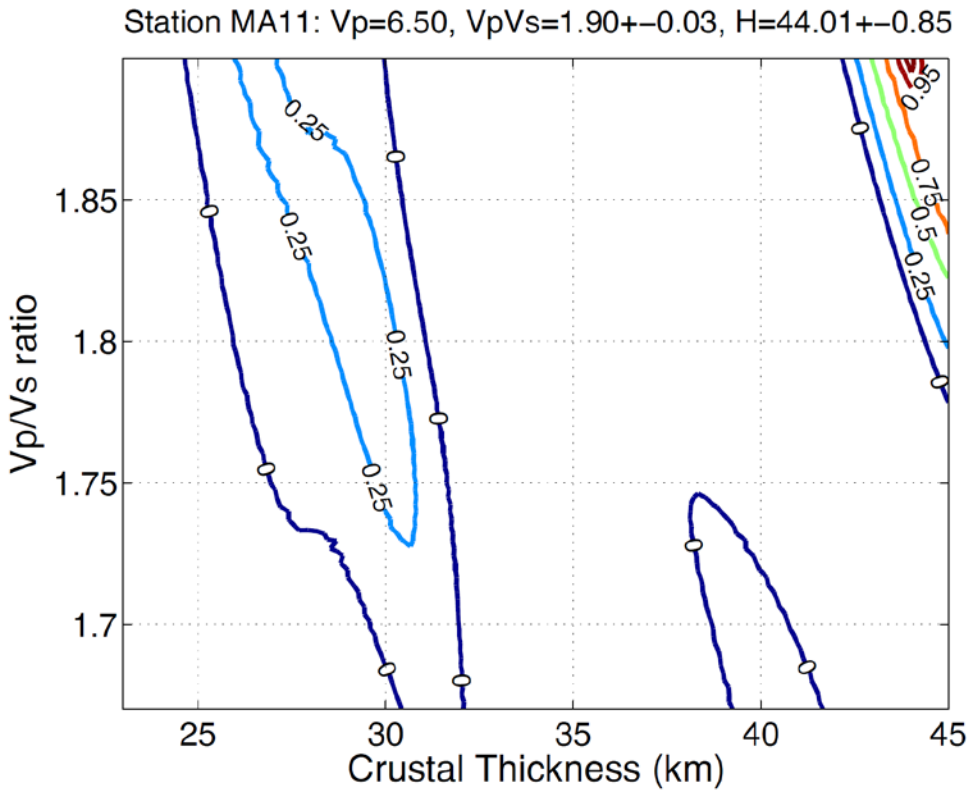
Station MA11: Vp=6.50, VpVs=1.90+−0.03, H=44.01+−0.85
Vp/Vs ratio
1.85
1.8
1.75
1.7
25
30
35
40
45
Crustal Thickness (km)
0.25
0.5
0.75
1.0

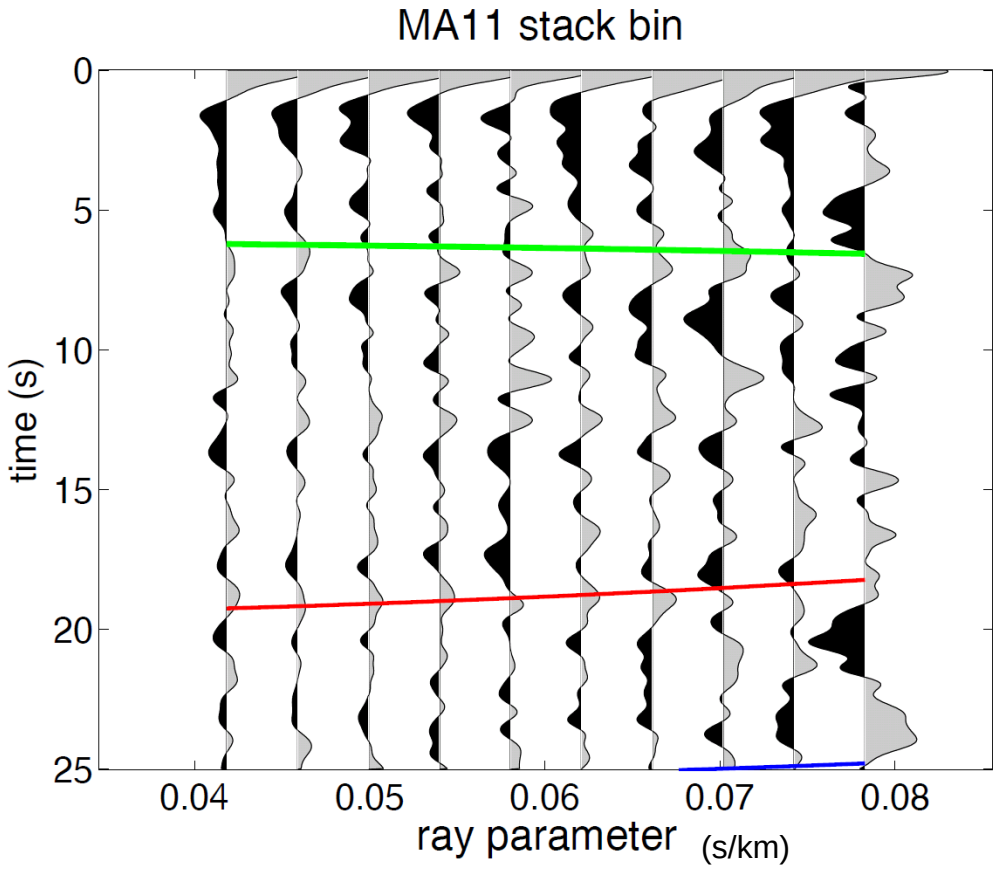
MA11 stack bin
time (s)
0
5
10
15
20
25
0.04
0.05
0.06
0.07
0.08
ray parameter (s/km)

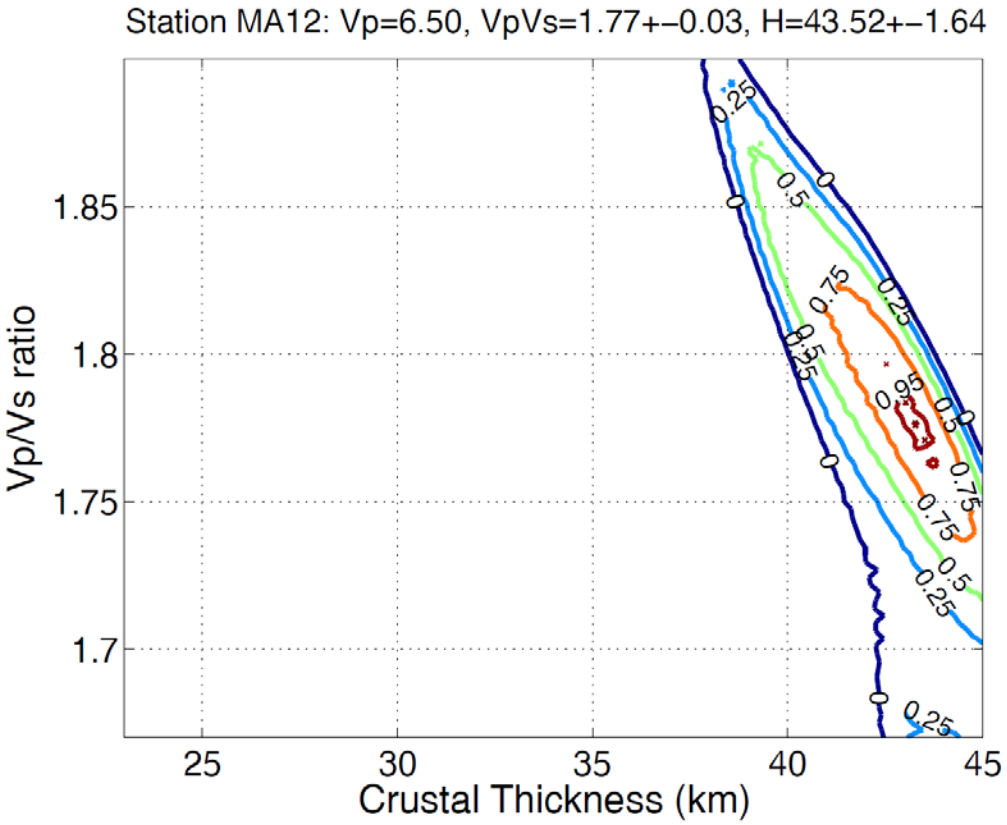
Station MA12: Vp=6.50, VpVs=1.77+−0.03, H=43.52+−1.64
Vp/Vs ratio
1.85
1.8
1.75
1.7
25
30
35
40
45
Crustal Thickness (km)

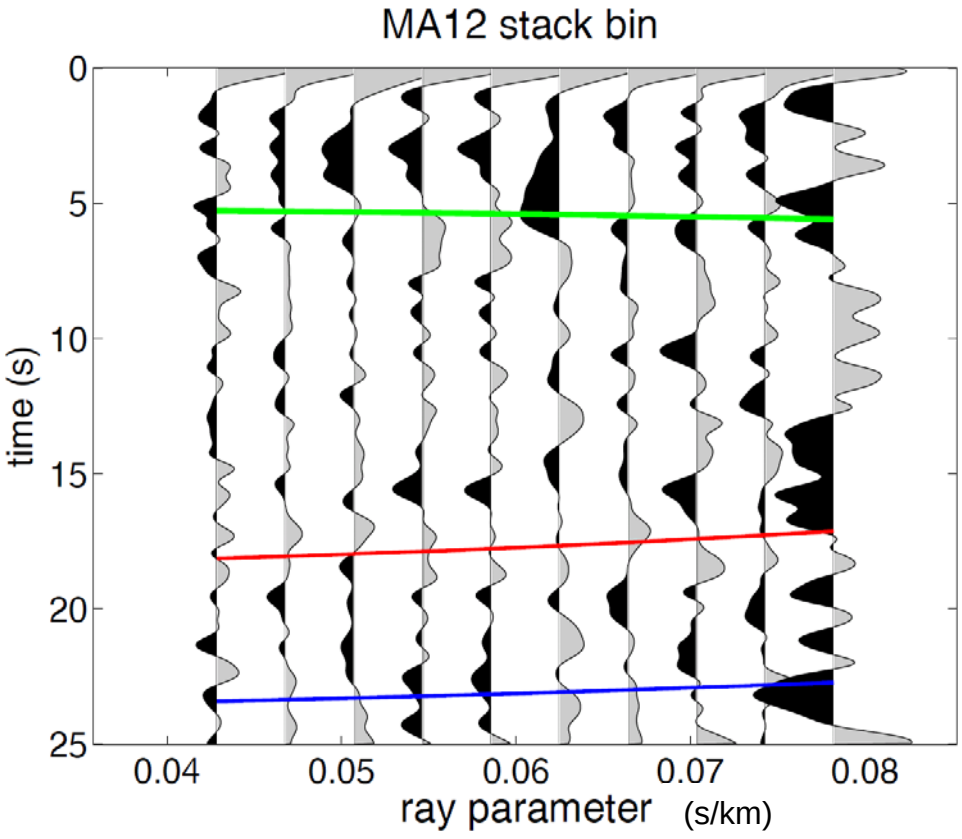
MA12 stack bin
time (s)
0
5
10
15
20
25
0.04
0.05
0.06
0.07
0.08
ray parameter (s/km)

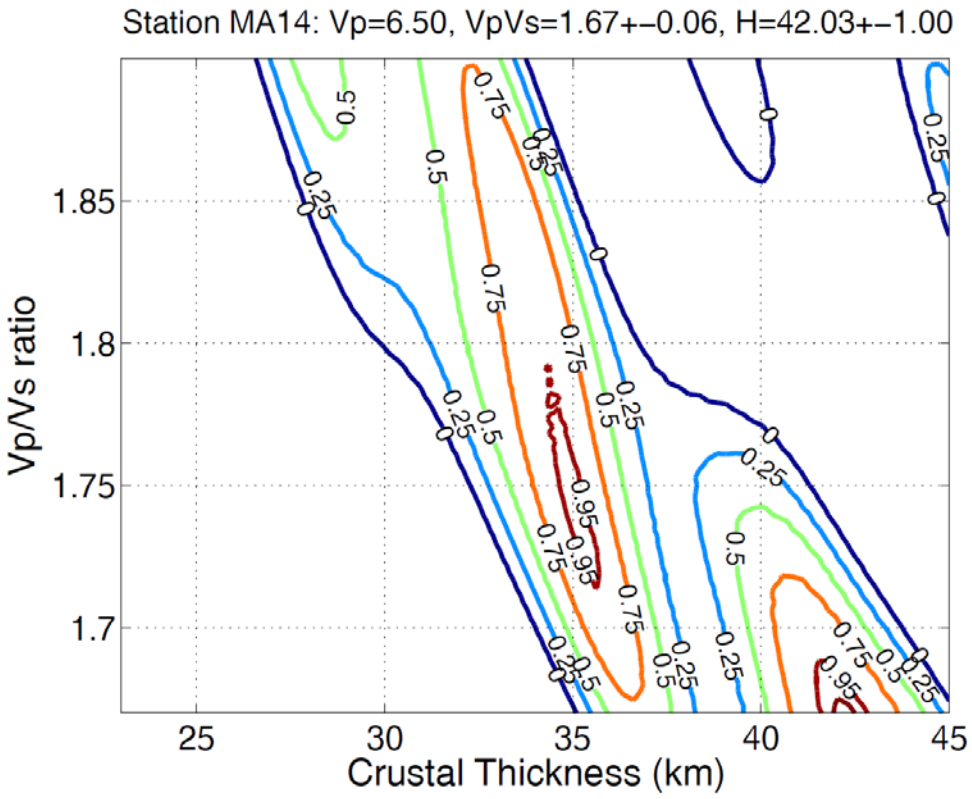
Station MA14: Vp=6.50, VpVs=1.67+−0.06, H=42.03+−1.00
Vp/Vs ratio
1.85
1.8
1.75
1.7
25
30
35
40
45
Crustal Thickness (km)

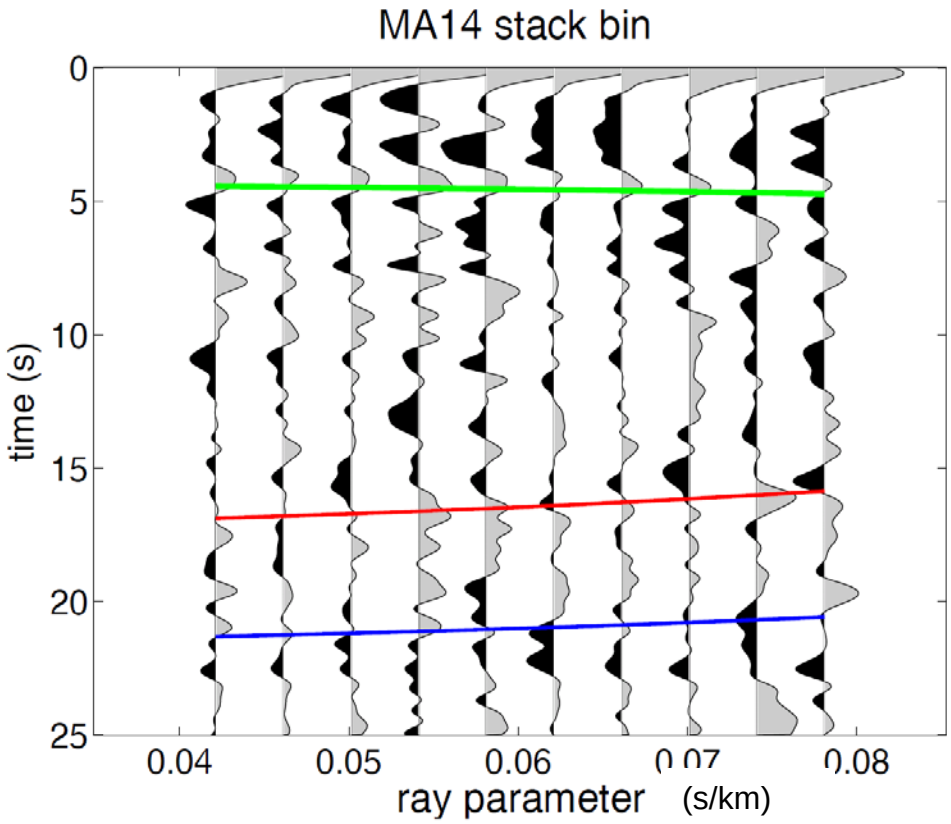
MA14 stack bin
time (s)
0
5
10
15
20
25
0.04
0.05
0.06
0.07
0.08
ray parameter (s/km)

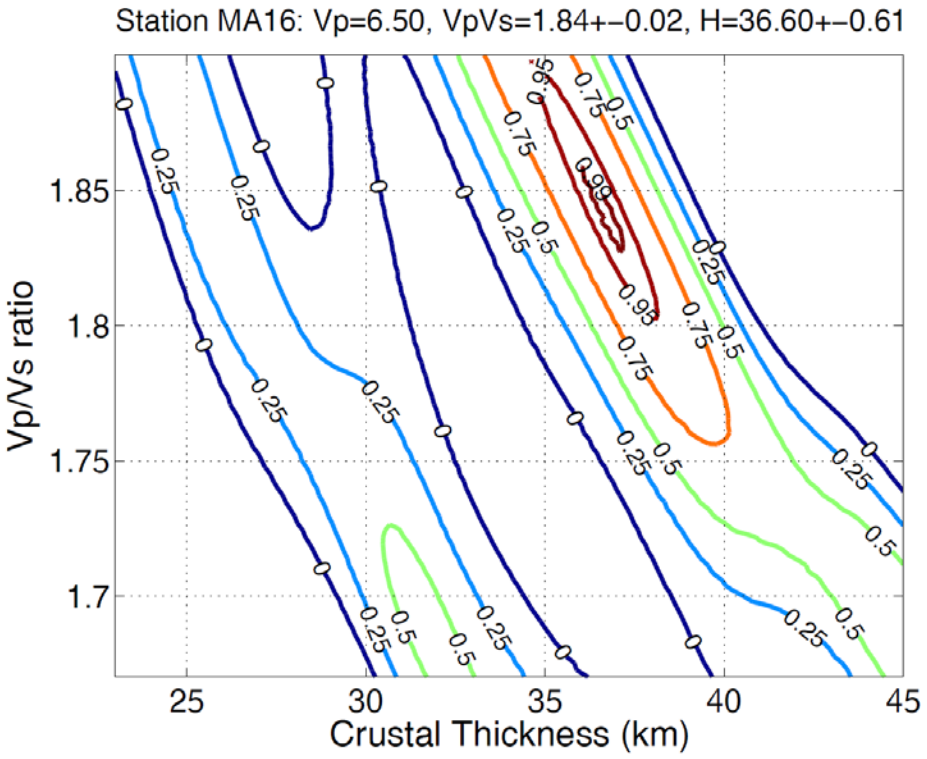
Station MA16: Vp=6.50, VpVs=1.84+−0.02, H=36.60+−0.61
Vp/Vs ratio
1.85
1.8
1.75
1.7
25
30
35
40
45
Crustal Thickness (km)

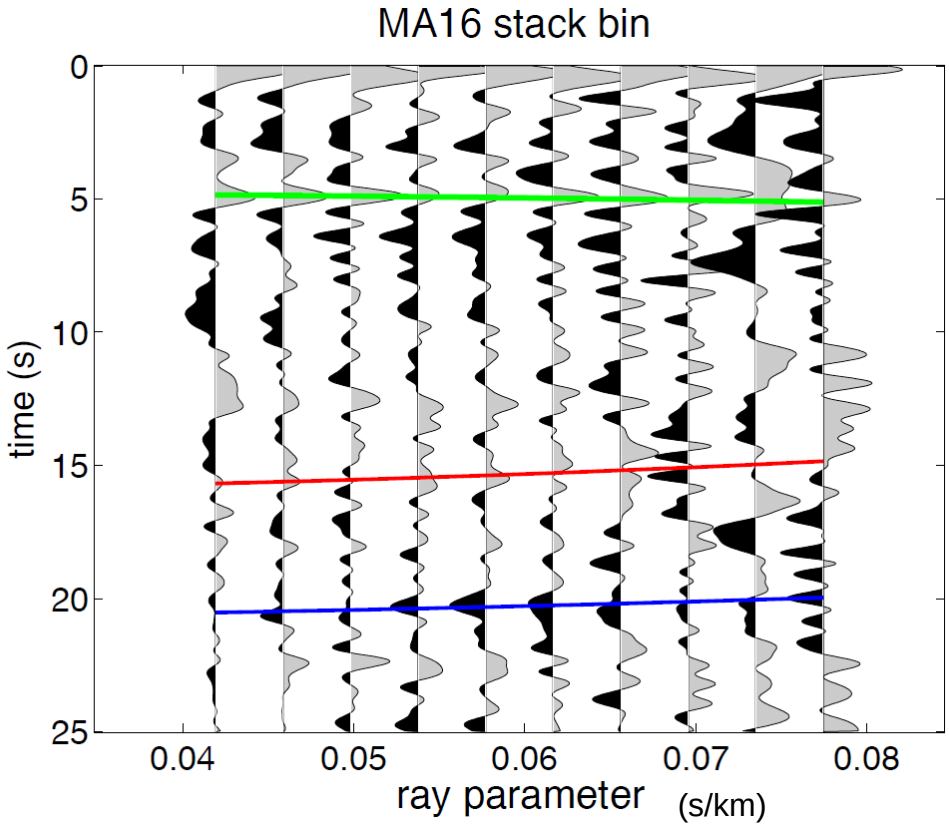
MA16 stack bin
time (s)
0
5
10
15
20
25
0.04
0.05
0.06
0.07
0.08
ray parameter (s/km)

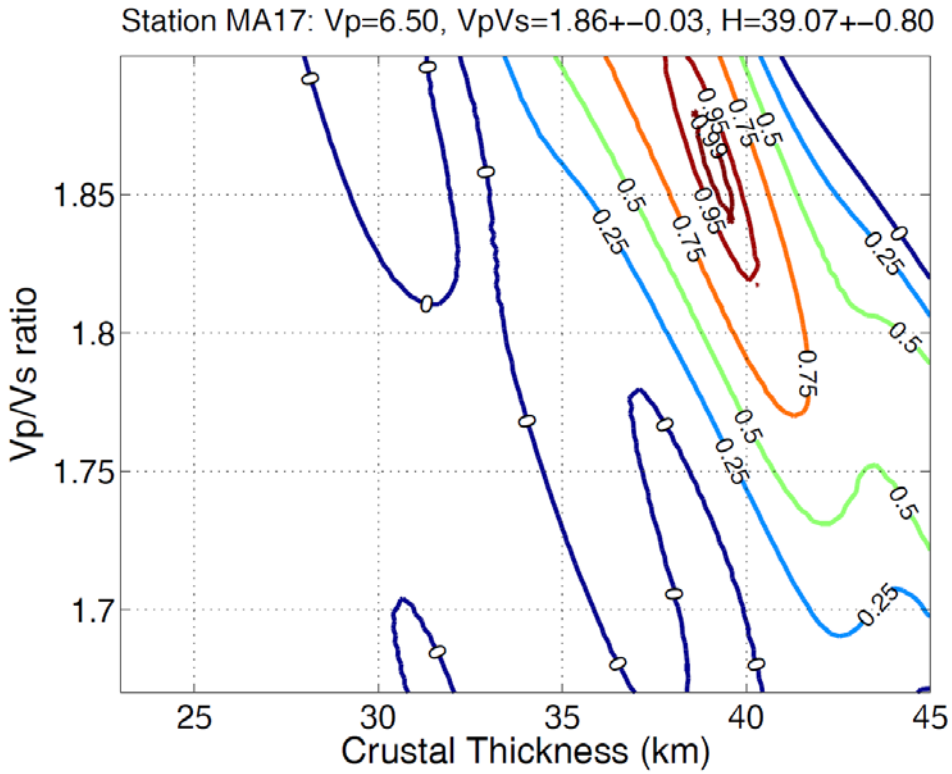
Station MA17: Vp=6.50, VpVs=1.86+−0.03, H=39.07+−0.80
Vp/Vs ratio
1.85
1.8
1.75
1.7
25
30
35
40
45
Crustal Thickness (km)

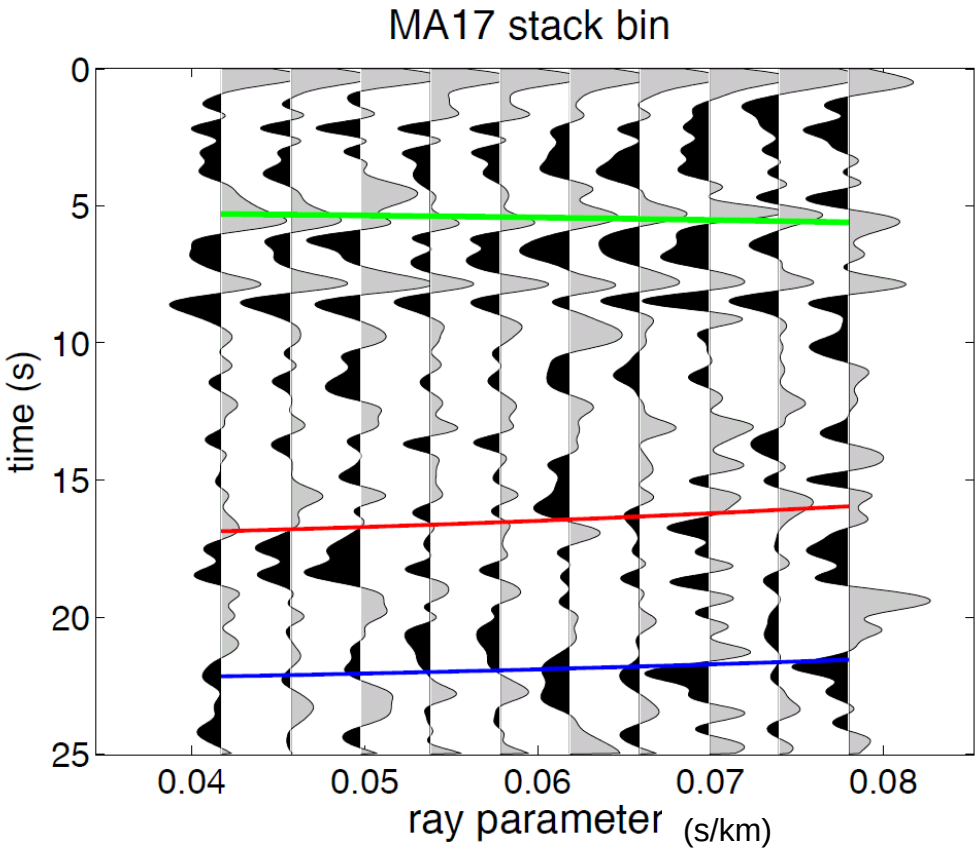
MA17 stack bin
time (s)
0
5
10
15
20
25
0.04
0.05
0.06
0.07
0.08
ray parameter (s/km)

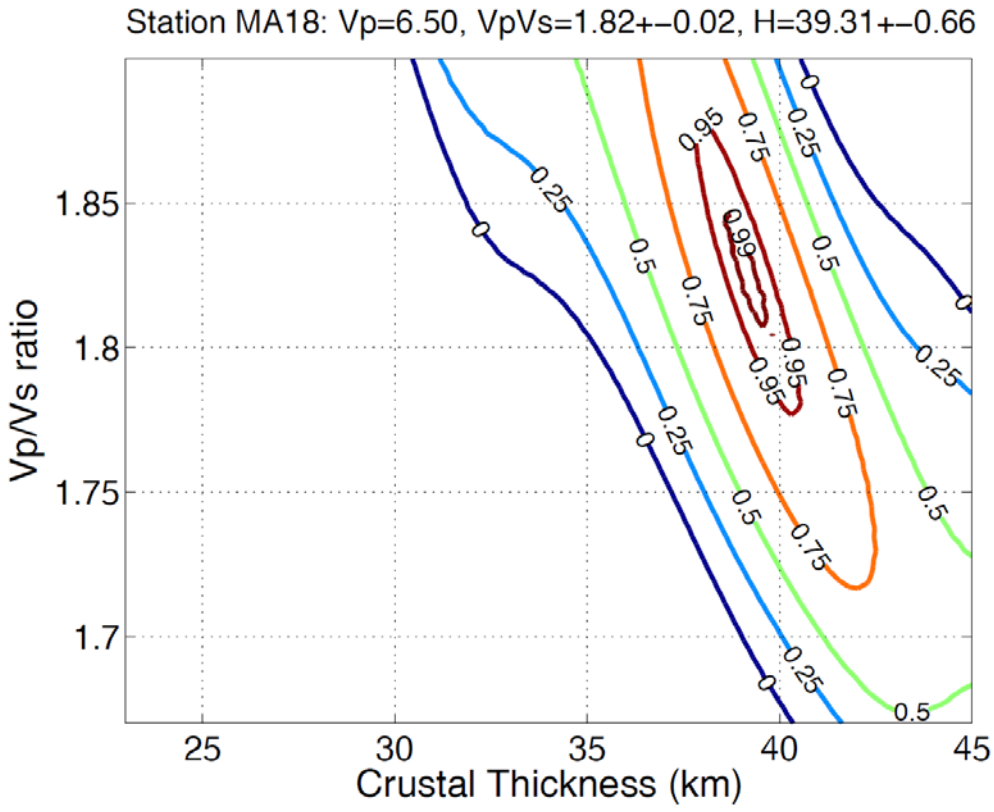
Station MA18: Vp=6.50, VpVs=1.82+−0.02, H=39.31+−0.66
Vp/Vs ratio
1.85
1.8
1.75
1.7
25
30
35
40
45
Crustal Thickness (km)
0
0.25
0.5
0.75
0.95
0.99

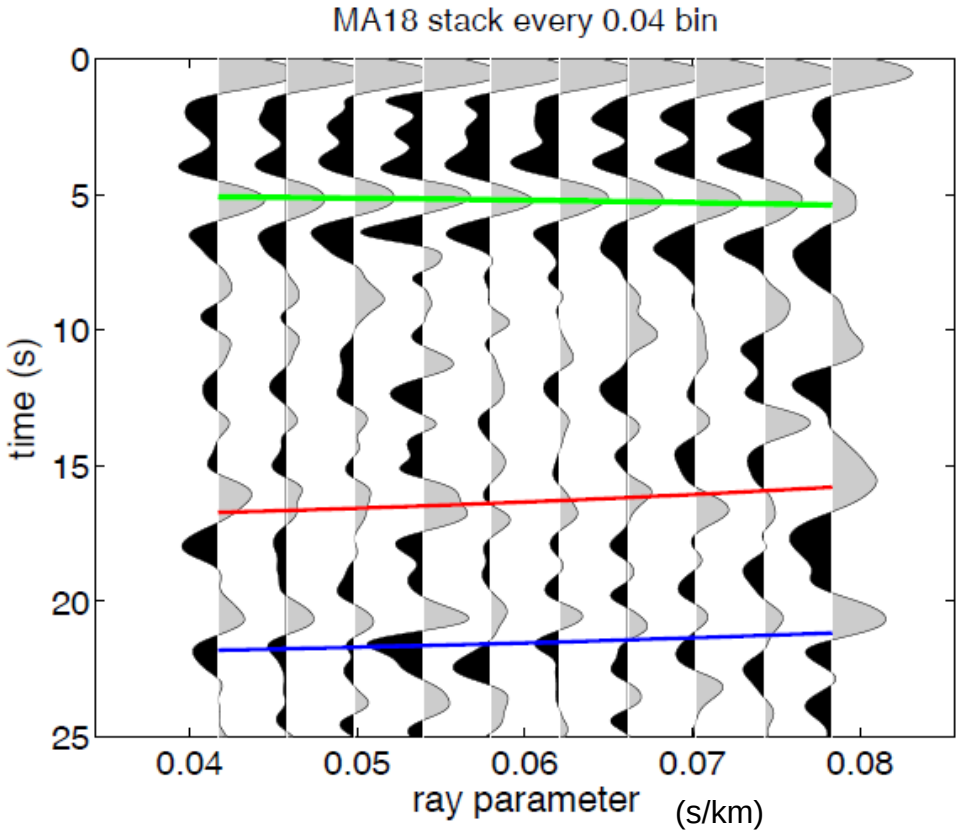
MA18 stack every 0.04 bin
time (s)
0
5
10
15
20
25
0.04
0.05
0.06
0.07
0.08
ray parameter (s/km)

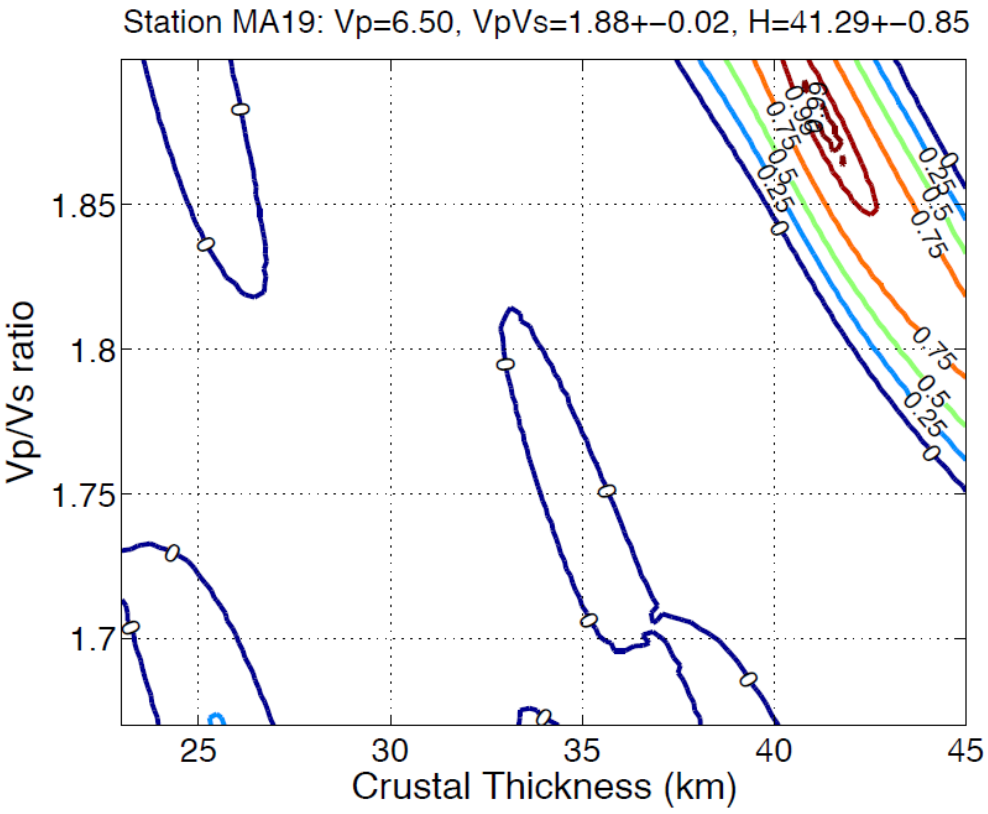
Station MA19: Vp=6.50, VpVs=1.88+−0.02, H=41.29+−0.85
Vp/Vs ratio
1.85
1.8
1.75
1.7
25
30
35
40
45
Crustal Thickness (km)

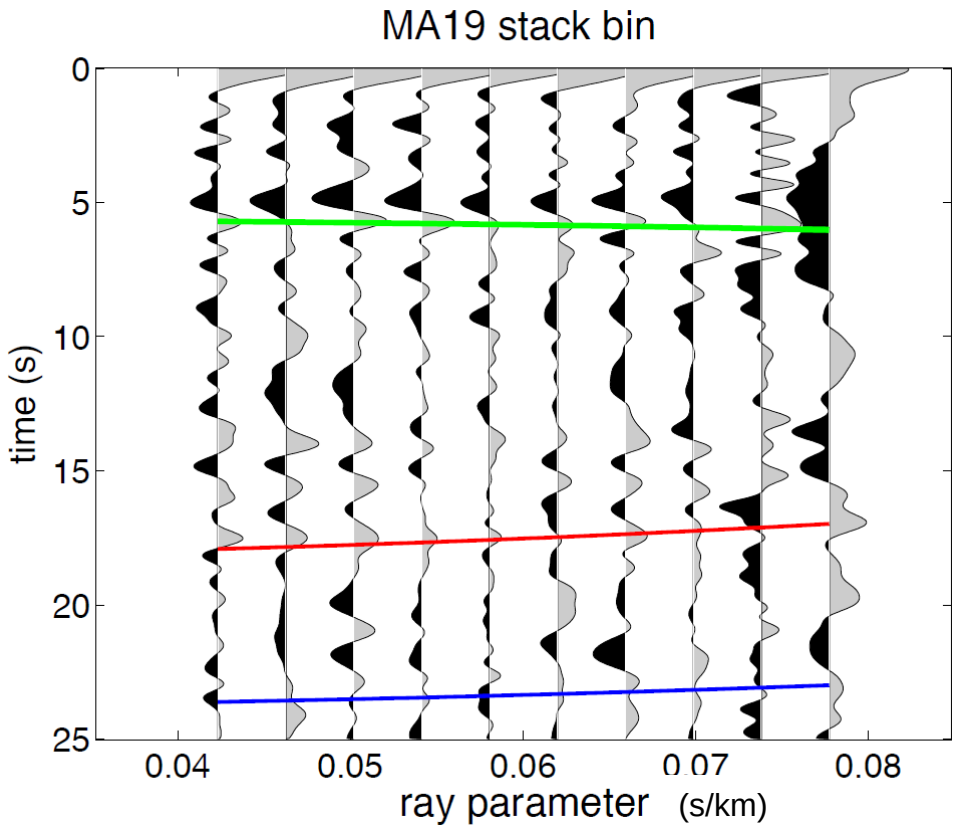
MA19 stack bin
time (s)
0
5
10
15
20
25
0.04
0.05
0.06
0.07
0.08
ray parameter (s/km)

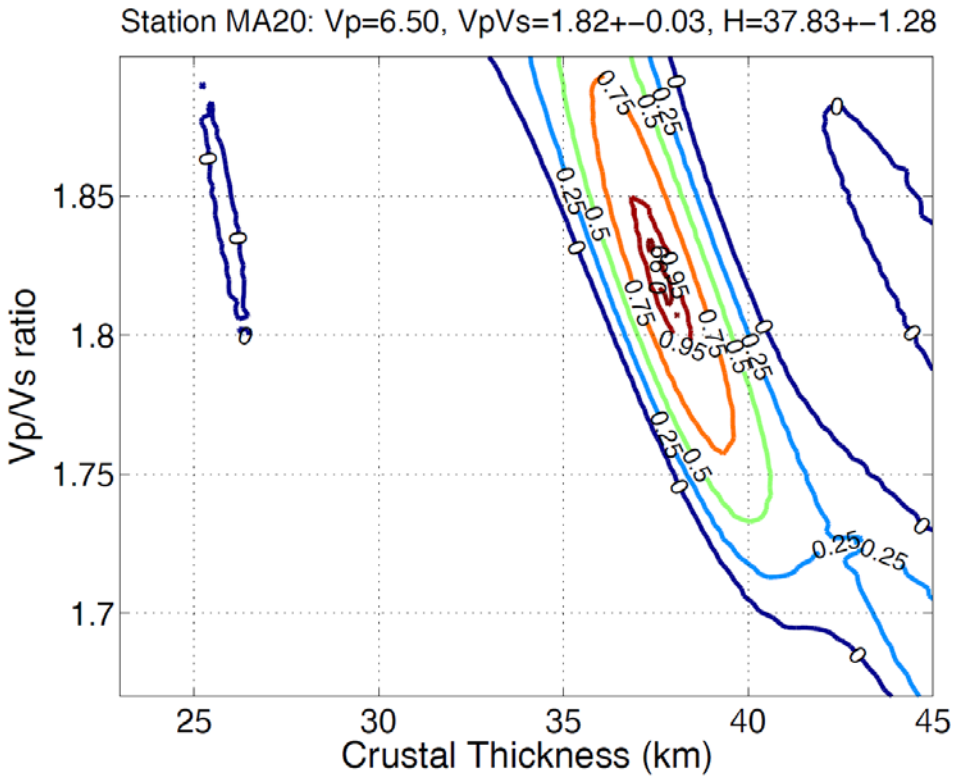
Station MA20: Vp=6.50, VpVs=1.82+−0.03, H=37.83+−1.28
Vp/Vs ratio
1.85
1.8
1.75
1.7
25
30
35
40
45
Crustal Thickness (km)

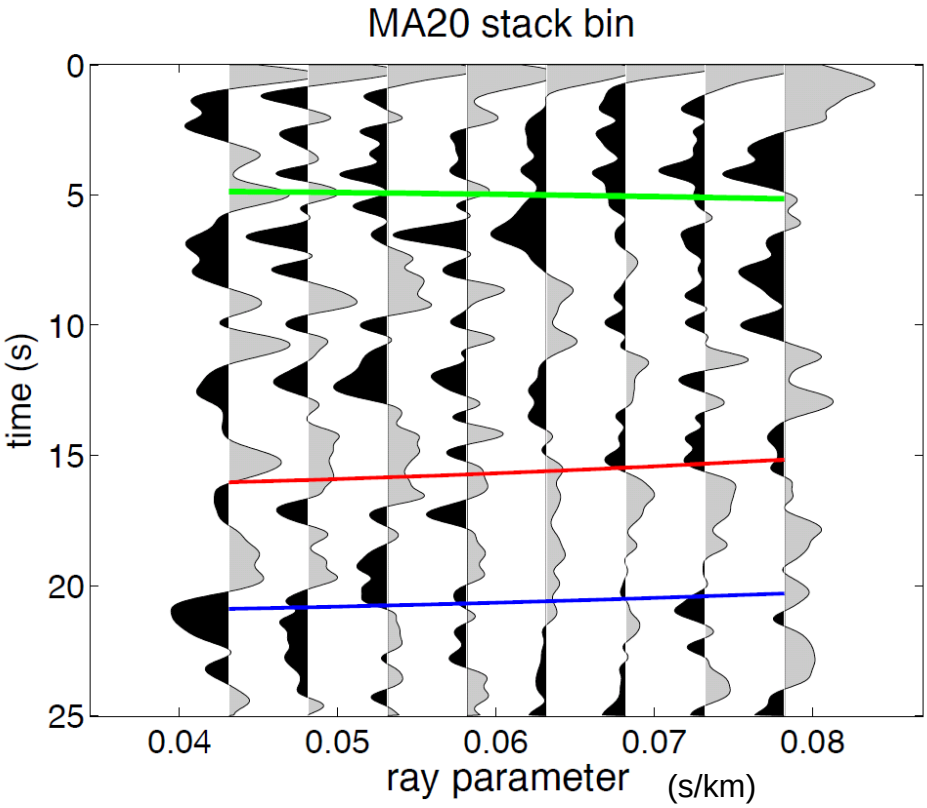
MA20 stack bin
time (s)
0
5
10
15
20
25
0.04
0.05
0.06
0.07
0.08
ray parameter (s/km)

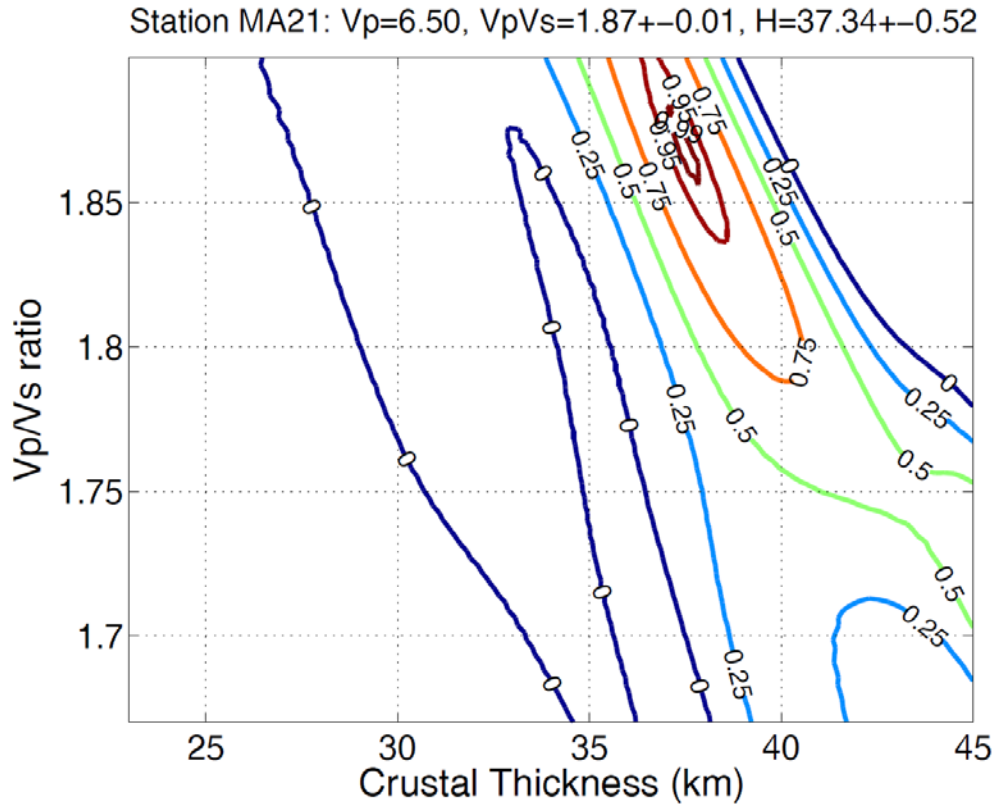
Station MA21: Vp=6.50, VpVs=1.87+−0.01, H=37.34+−0.52
Vp/Vs ratio
1.85
1.8
1.75
1.7
25
30
35
40
45
Crustal Thickness (km)
97.0

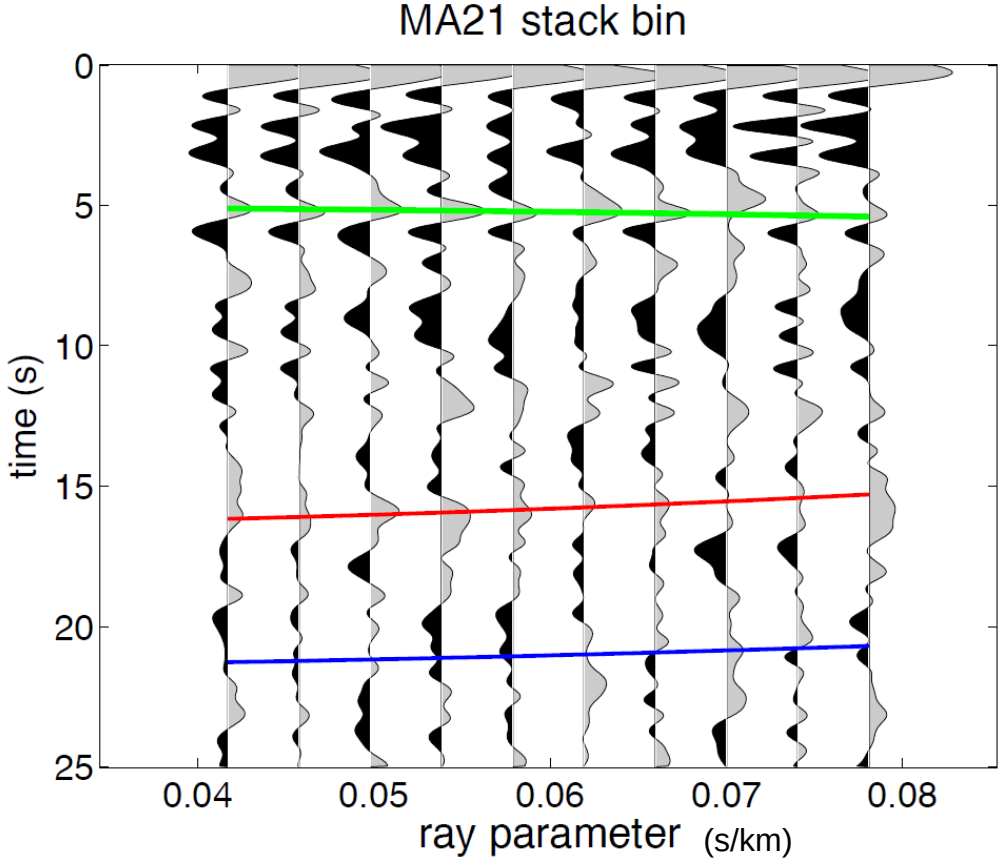
MA21 stack bin
time (s)
0
5
10
15
20
25
0.04
0.05
0.06
0.07
0.08
ray parameter (s/km)

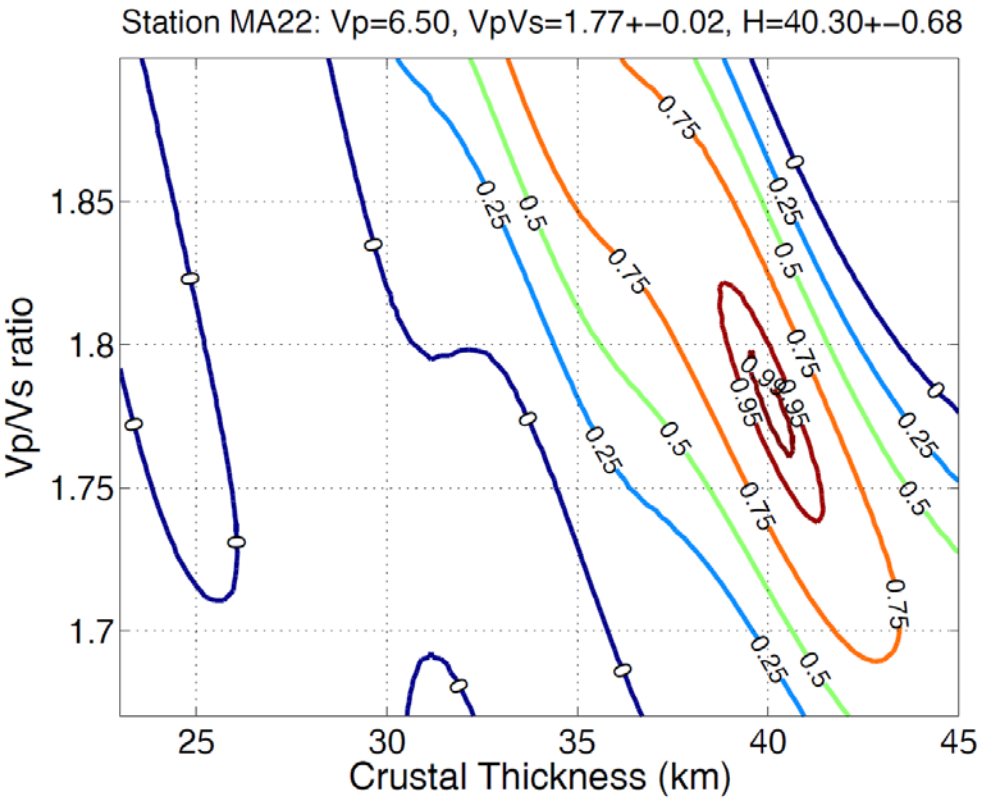
Station MA22: Vp=6.50, VpVs=1.77+−0.02, H=40.30+−0.68
Vp/Vs ratio
1.85
1.8
1.75
1.7
25
30
35
40
45
Crustal Thickness (km)
0
0.25
0.5
0.75
0.95

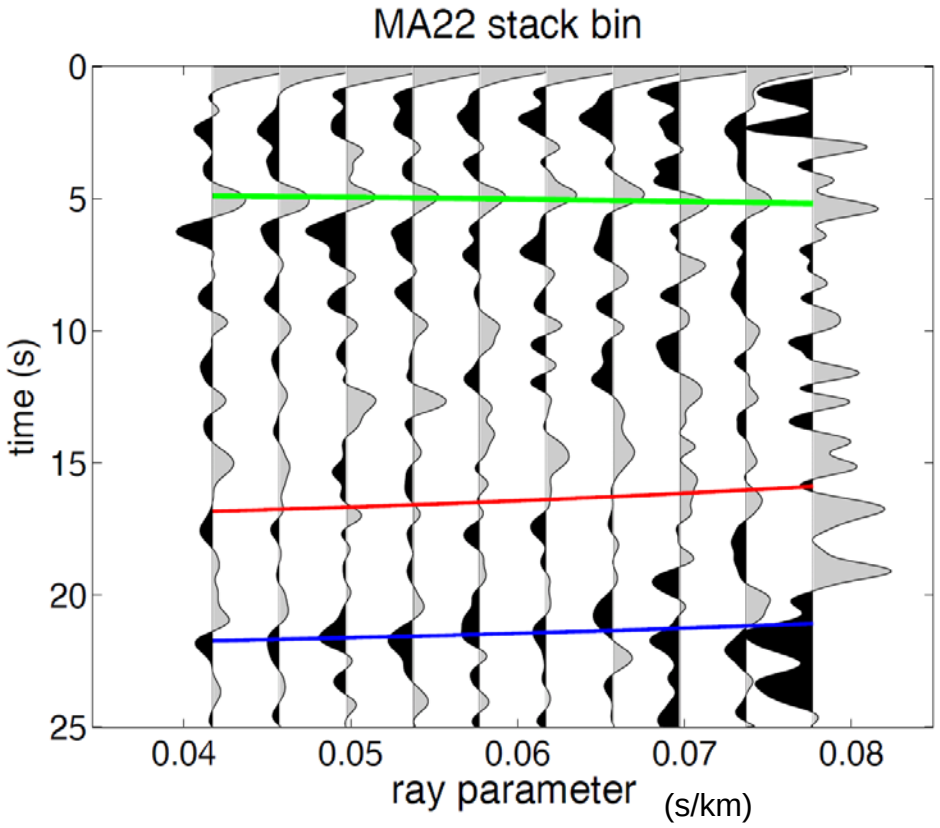
MA22 stack bin
time (s)
0
5
10
15
20
25
0.04
0.05
0.06
0.07
0.08
ray parameter (s/km)

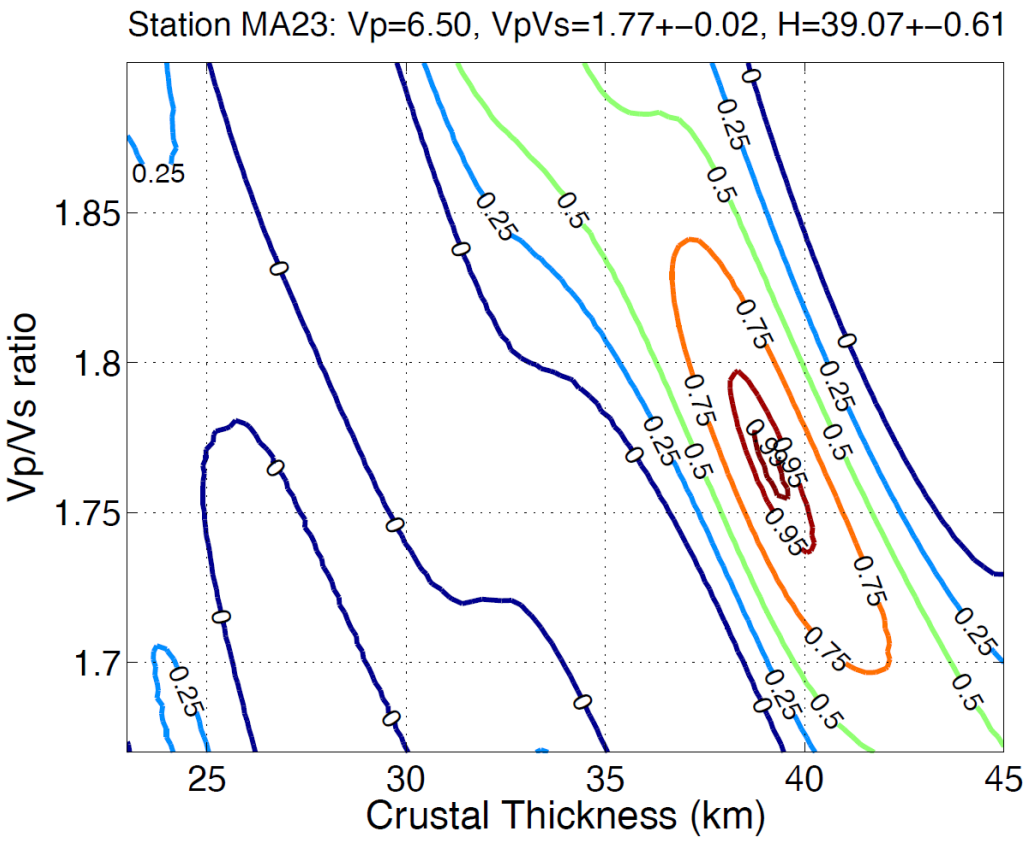
Station MA23: Vp=6.50, VpVs=1.77+−0.02, H=39.07+−0.61
Vp/Vs ratio
1.85
1.8
1.75
1.7
25
30
35
40
45
Crustal Thickness (km)
0.25
0
0.5
0.75
0.95
0.93

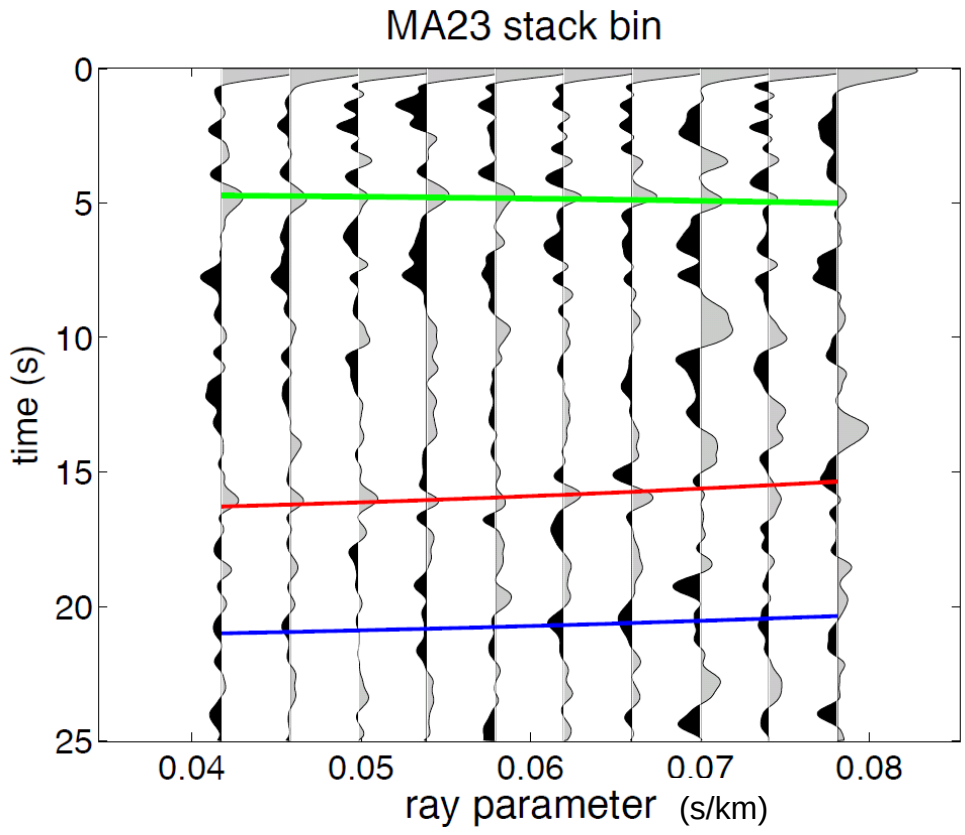
MA23 stack bin
time (s)
0
5
10
15
20
25
0.04
0.05
0.06
0.07
0.08
ray parameter (s/km)

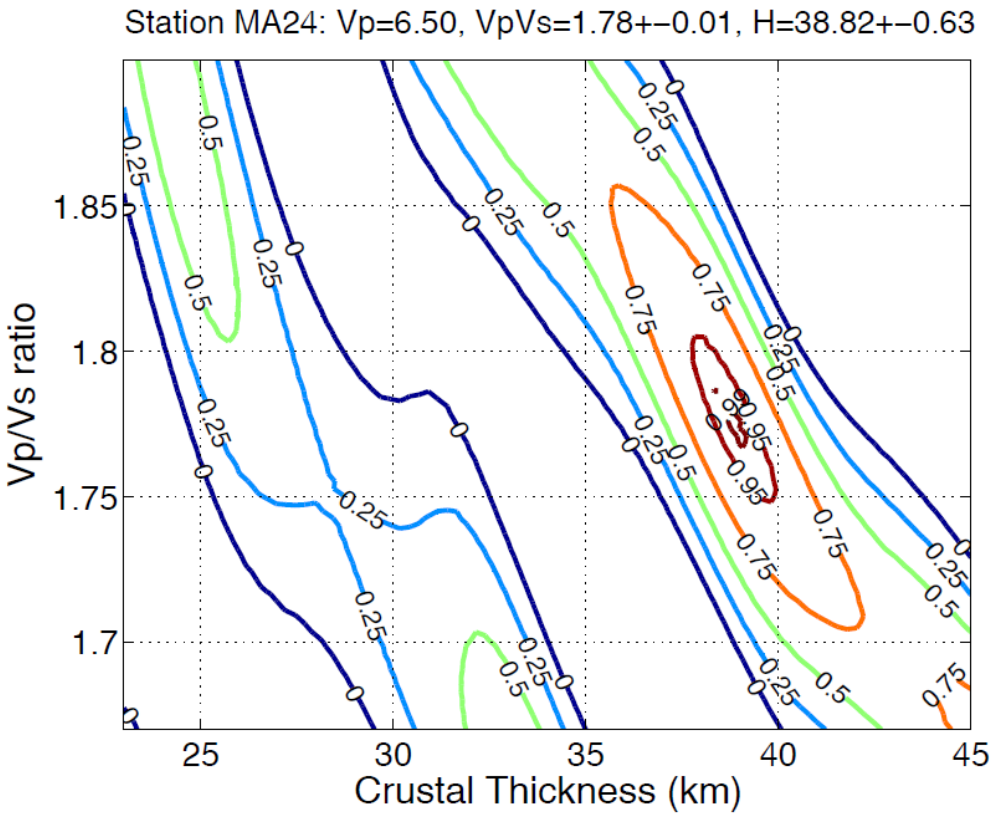
Station MA24: Vp=6.50, VpVs=1.78+−0.01, H=38.82+−0.63
Vp/Vs ratio
1.85
1.8
1.75
1.7
25
30
35
40
45
Crustal Thickness (km)

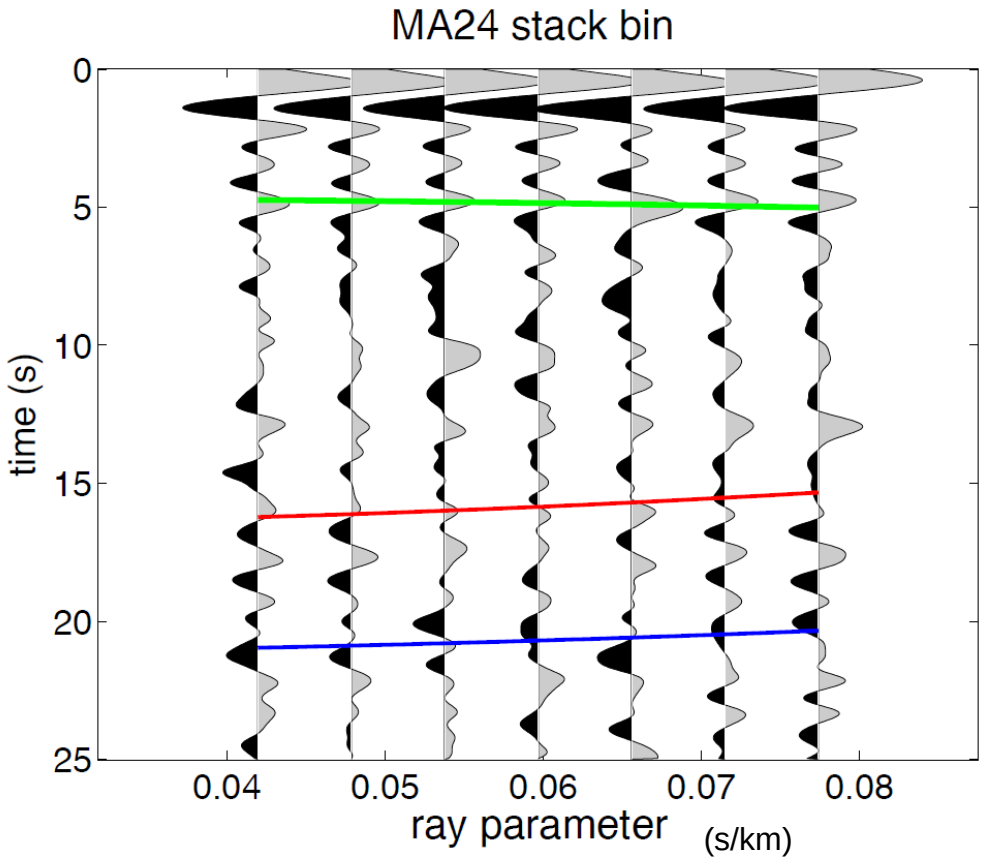
MA24 stack bin
time (s)
0
5
10
15
20
25
0.04
0.05
0.06
0.07
0.08
ray parameter
(s/km)

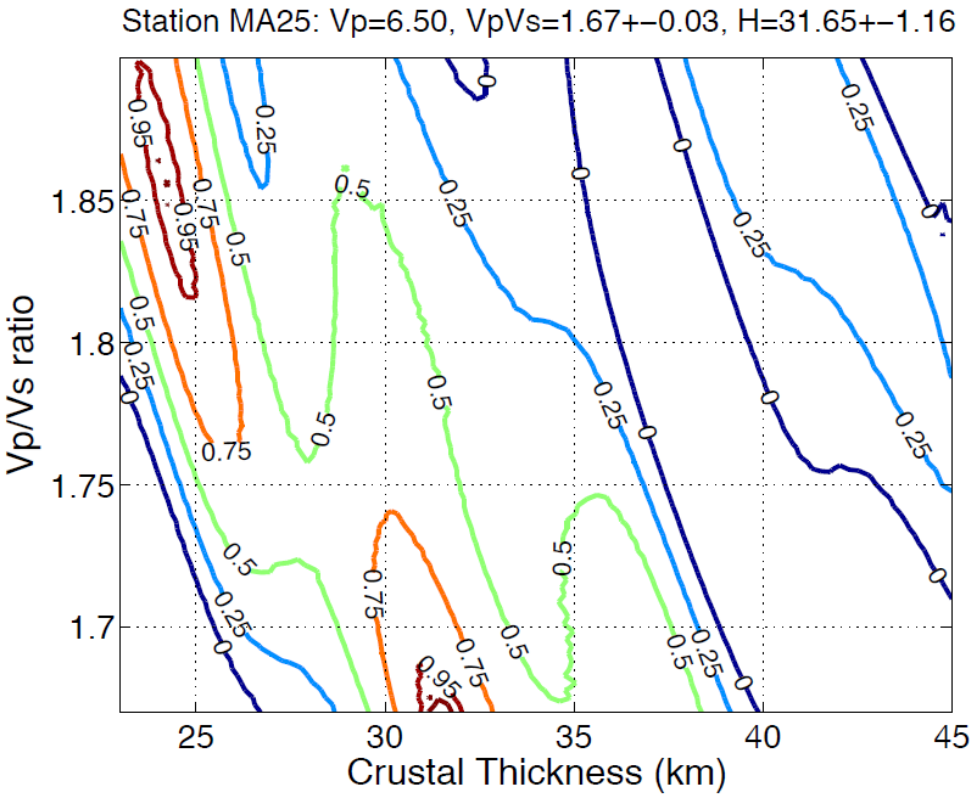
Station MA25: Vp=6.50, VpVs=1.67+−0.03, H=31.65+−1.16
Vp/Vs ratio
1.85
1.8
1.75
1.7
25
30
35
40
45
Crustal Thickness (km)

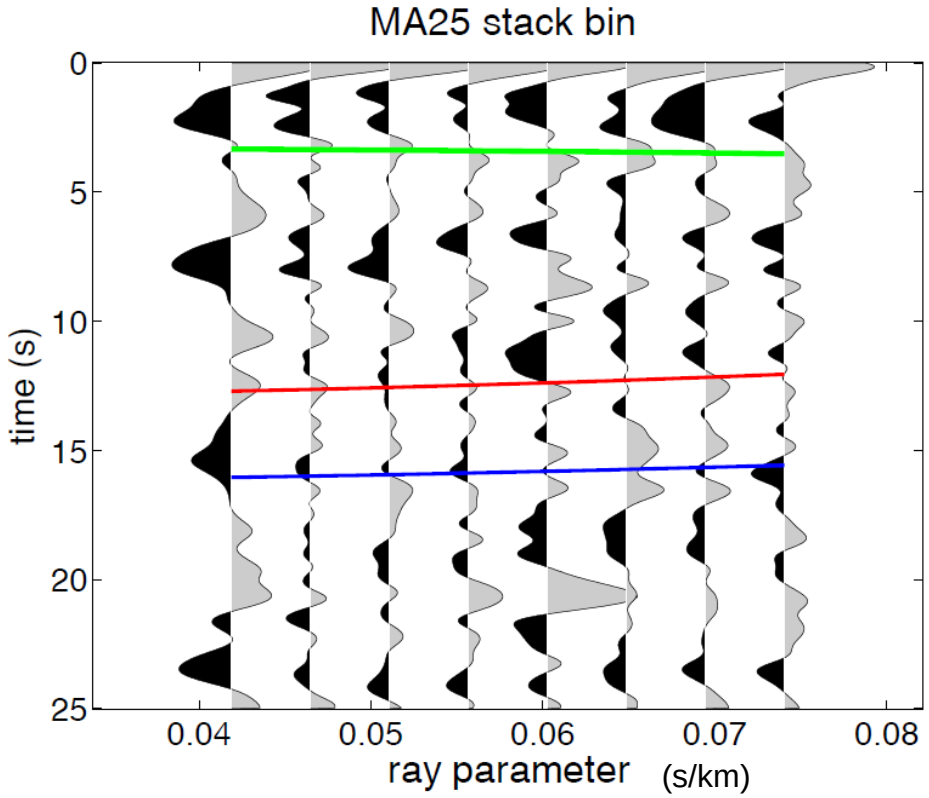
MA25 stack bin
time (s)
0
5
10
15
20
25
0.04
0.05
0.06
0.07
0.08
ray parameter (s/km)

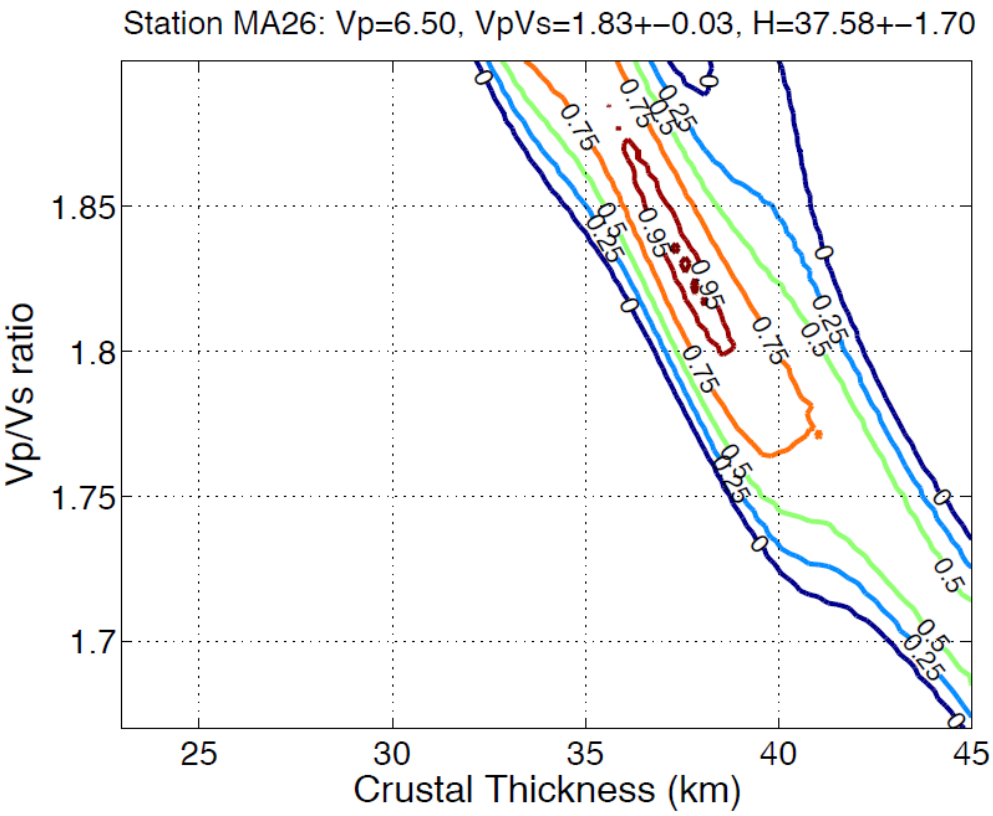
Station MA26: Vp=6.50, VpVs=1.83+−0.03, H=37.58+−1.70
Vp/Vs ratio
1.85
1.8
1.75
1.7
25
30
35
40
45
Crustal Thickness (km)

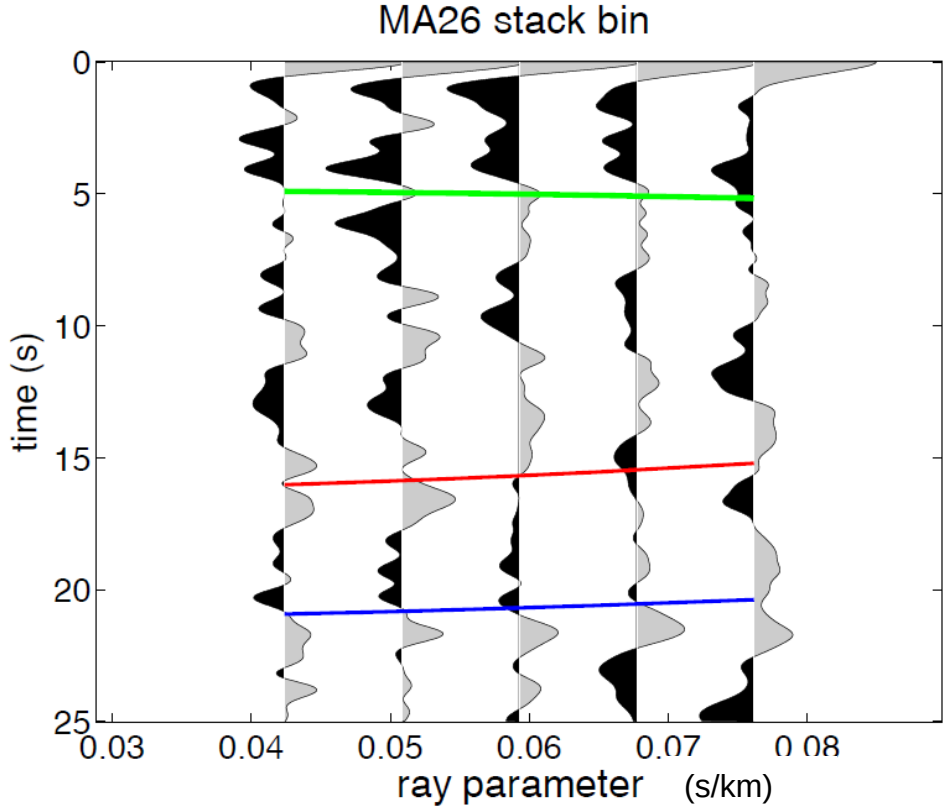
MA26 stack bin
time (s)
0
5
10
15
20
25
0.03
0.04
0.05
0.06
0.07
0.08
ray parameter (s/km)

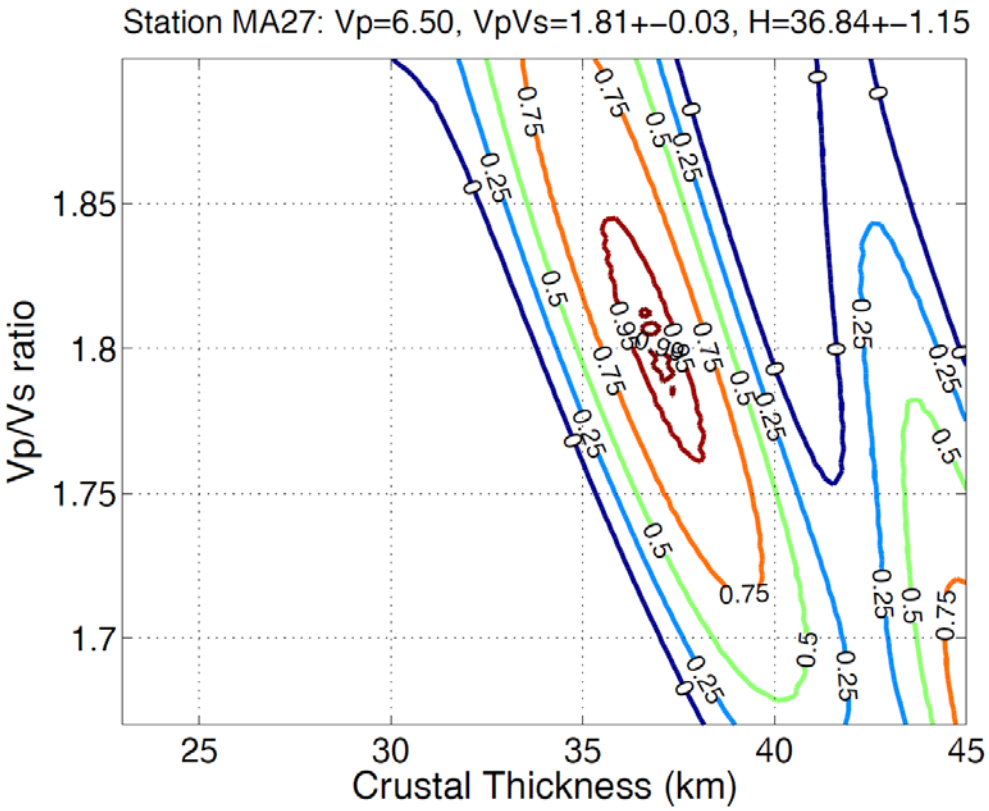
Station MA27: Vp=6.50, VpVs=1.81+−0.03, H=36.84+−1.15
Vp/Vs ratio
1.85
1.8
1.75
1.7
25
30
35
40
45
Crustal Thickness (km)

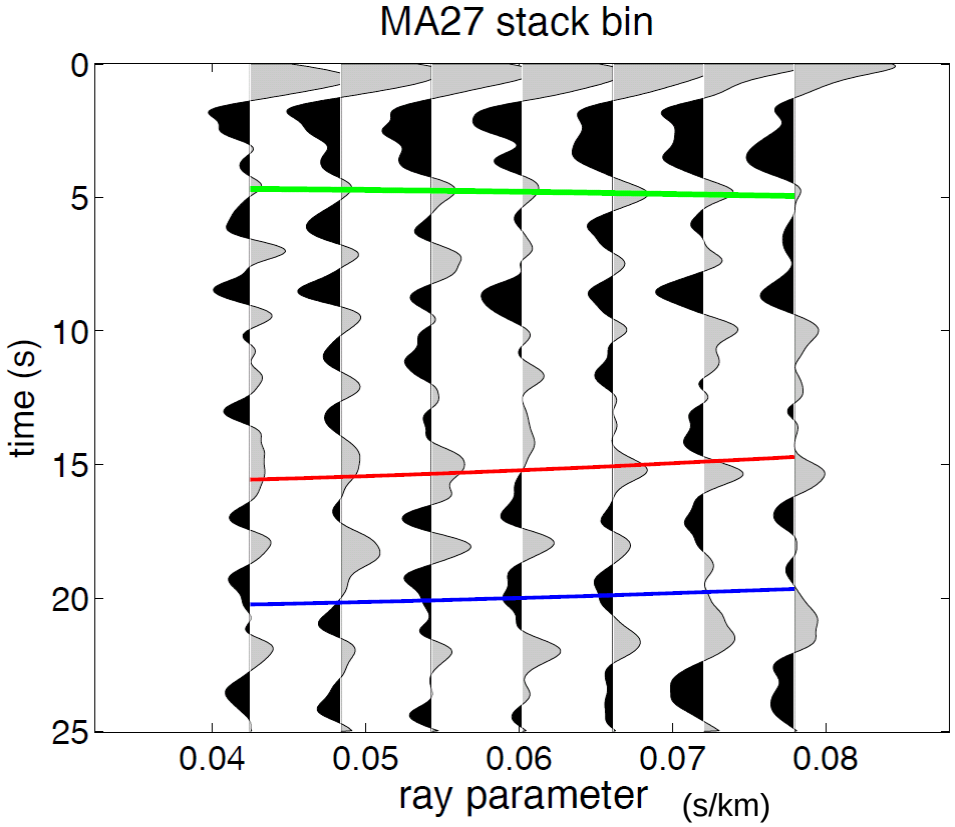
MA27 stack bin
time (s)
0
5
10
15
20
25
0.04
0.05
0.06
0.07
0.08
ray parameter (s/km)

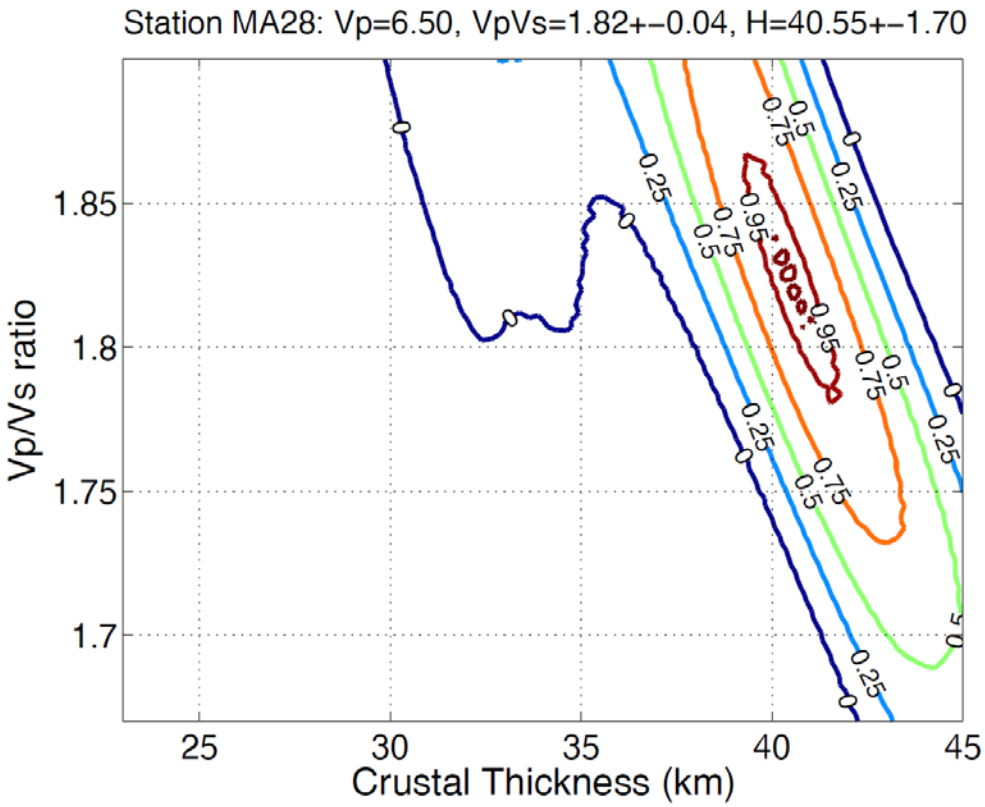
Station MA28: Vp=6.50, VpVs=1.82+−0.04, H=40.55+−1.70
Vp/Vs ratio
1.85
1.8
1.75
1.7
25
30
35
40
45
Crustal Thickness (km)

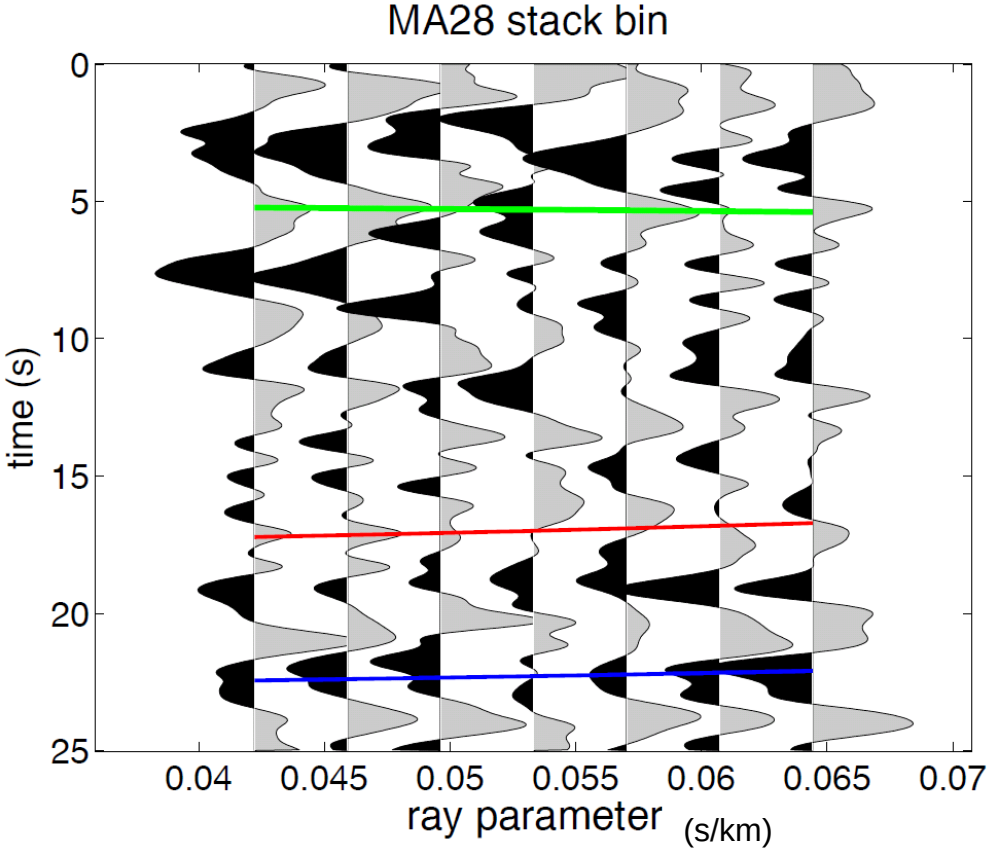
MA28 stack bin
time (s)
0
5
10
15
20
25
0.04
0.045
0.05
0.055
0.06
0.065
0.07
ray parameter (s/km)

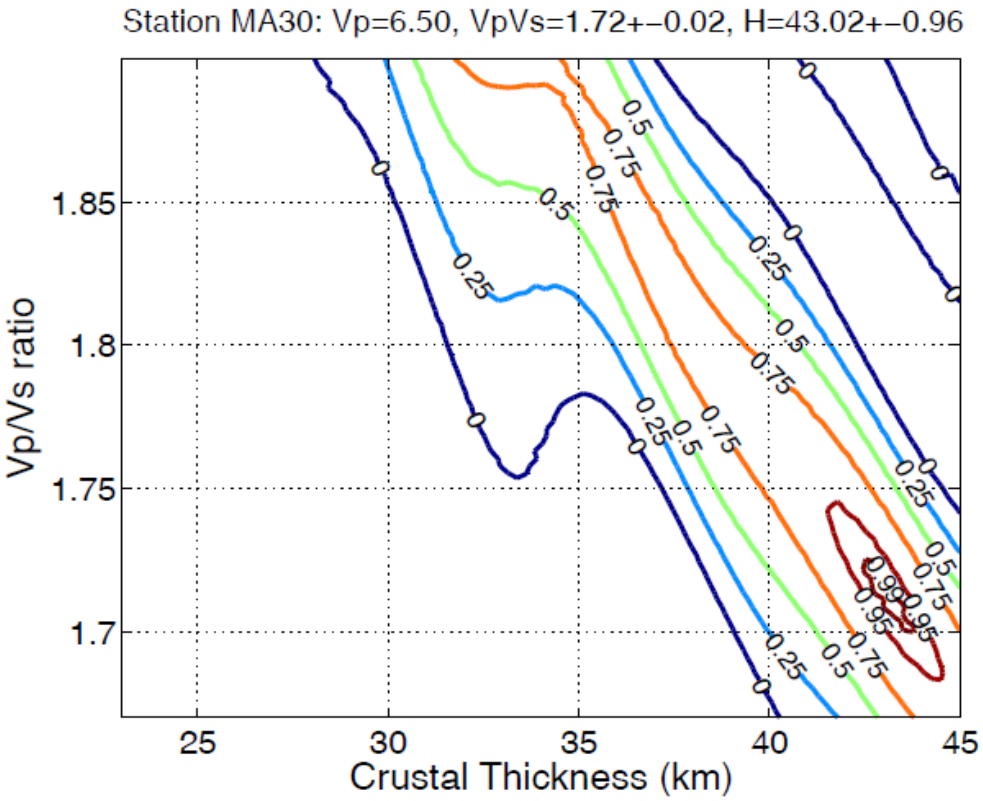
Station MA30: Vp=6.50, VpVs=1.72+−0.02, H=43.02+−0.96
Vp/Vs ratio
1.85
1.8
1.75
1.7
25
30
35
40
45
Crustal Thickness (km)

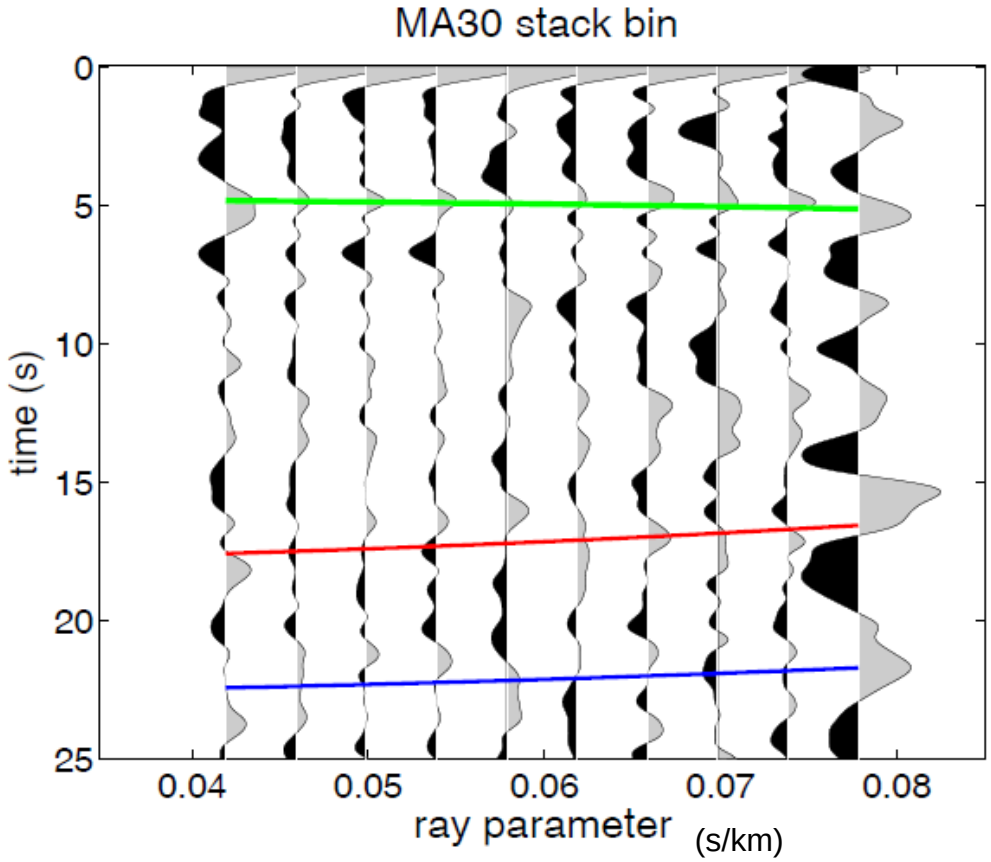
MA30 stack bin
time (s)
0
5
10
15
20
25
0.04
0.05
0.06
0.07
0.08
ray parameter (s/km)

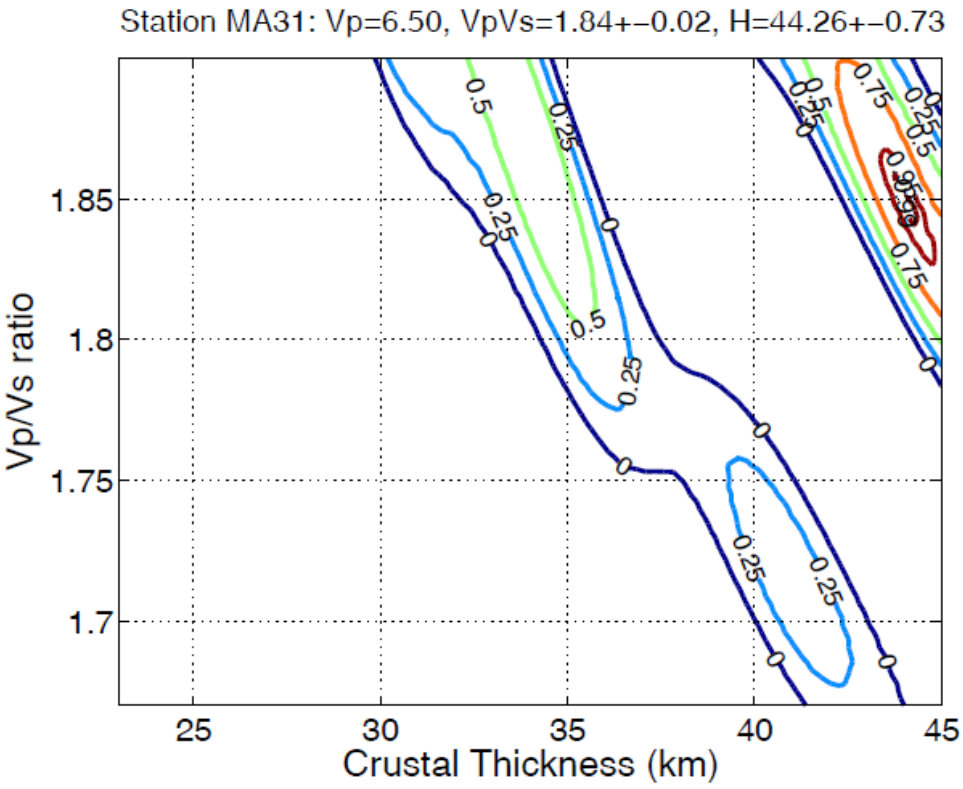
Station MA31: Vp=6.50, VpVs=1.84+−0.02, H=44.26+−0.73
Vp/Vs ratio
1.85
1.8
1.75
1.7
25
30
35
40
45
Crustal Thickness (km)

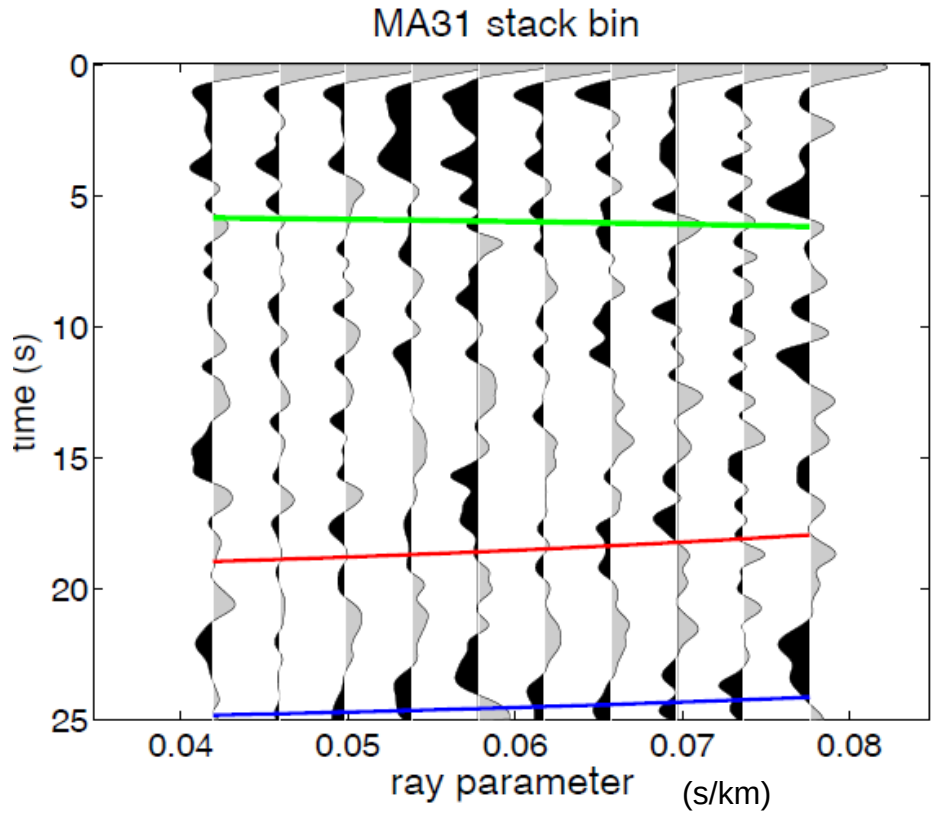
MA31 stack bin
time (s)
0
5
10
15
20
25
0.04
0.05
0.06
0.07
0.08
ray parameter
(s/km)

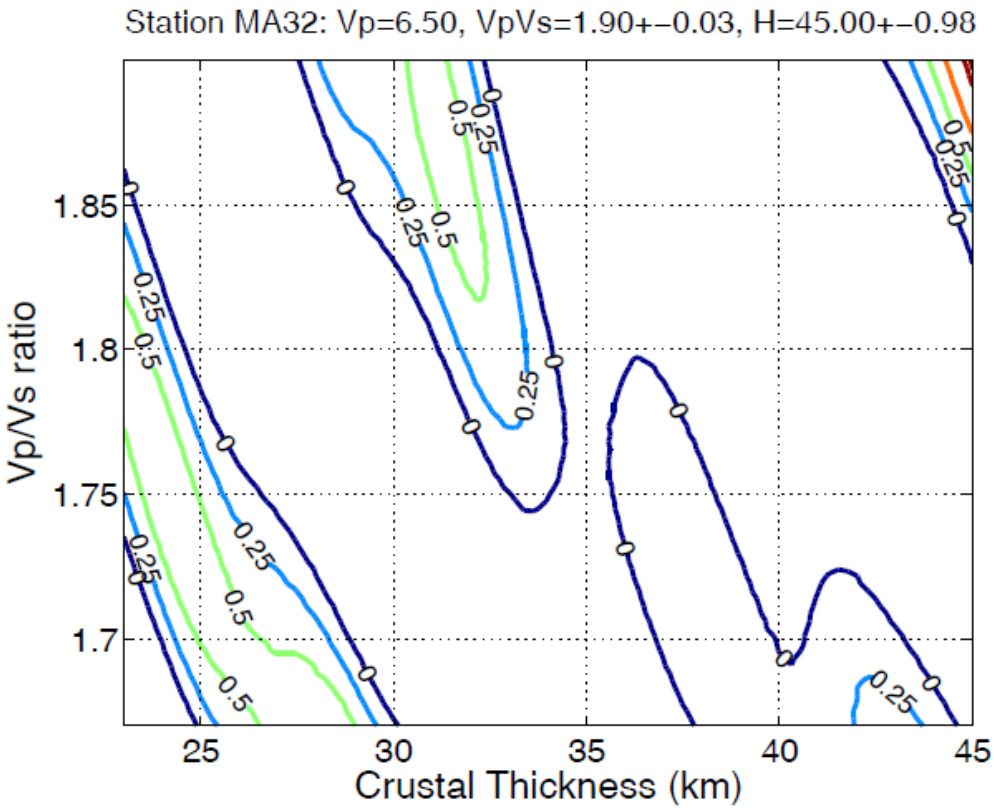
Station MA32: Vp=6.50, VpVs=1.90+−0.03, H=45.00+−0.98
Vp/Vs ratio
1.85
1.8
1.75
1.7
25
30
35
40
45
Crustal Thickness (km)

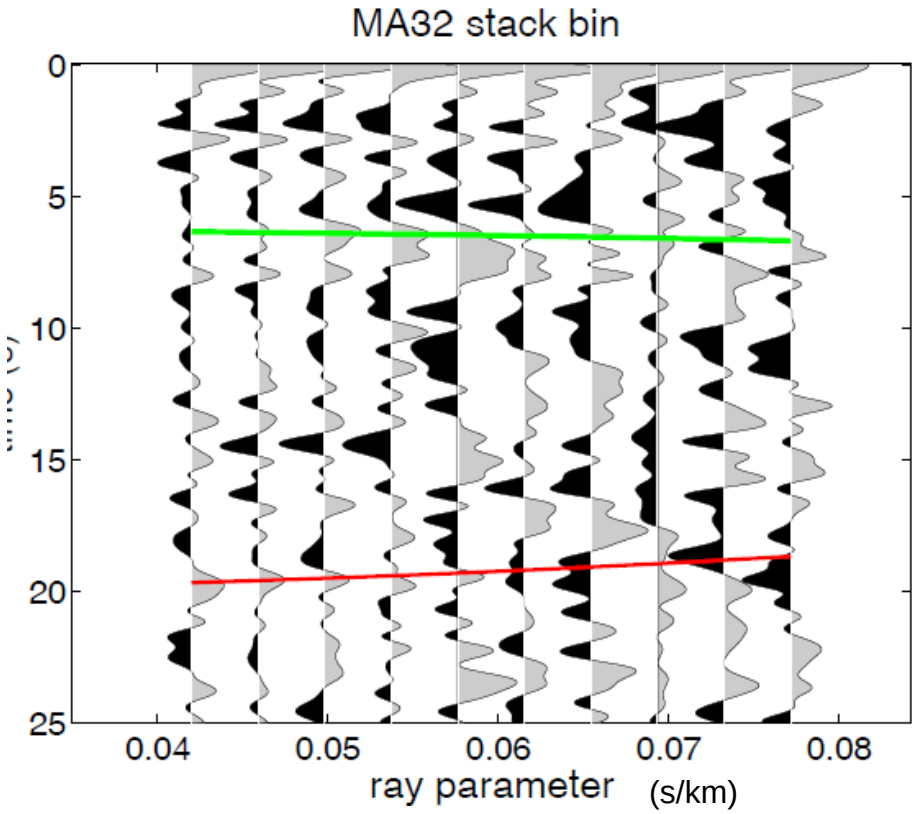
MA32 stack bin
0
5
10
15
20
25
0.04
0.05
0.06
0.07
0.08
ray parameter (s/km)

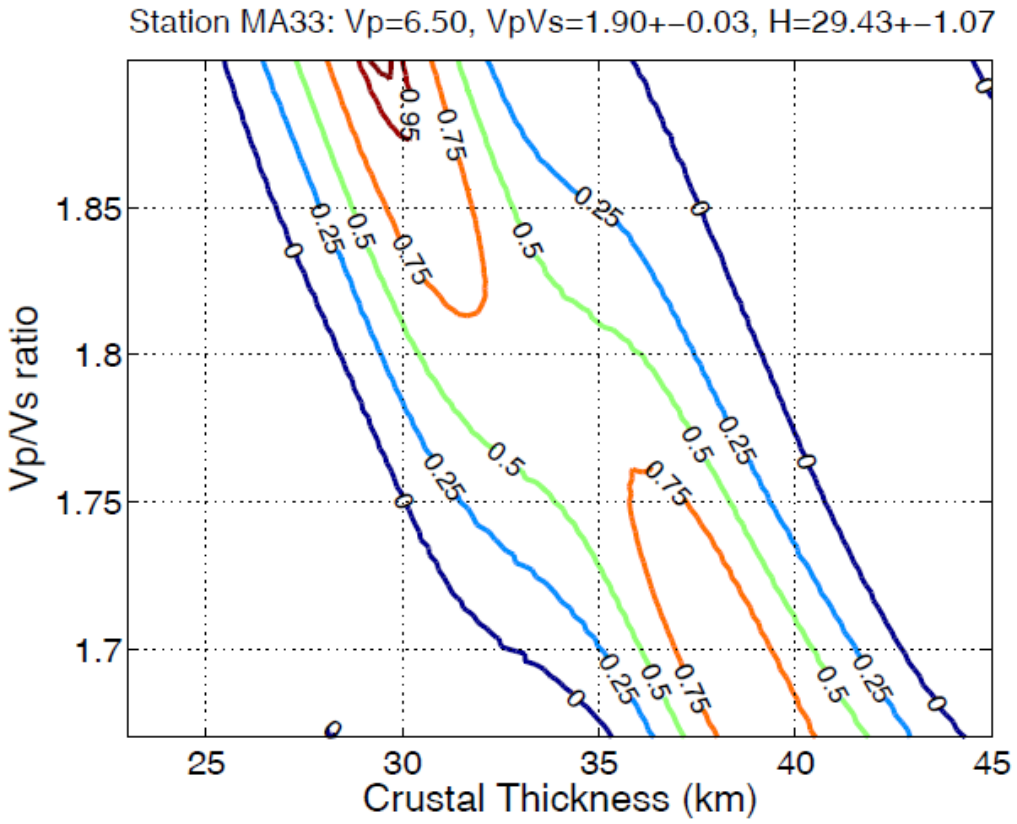
Station MA33: Vp=6.50, VpVs=1.90+−0.03, H=29.43+−1.07
Vp/Vs ratio
1.85
1.8
1.75
1.7
25
30
35
40
45
Crustal Thickness (km)
0.95
0.75
0.5
0.25
0

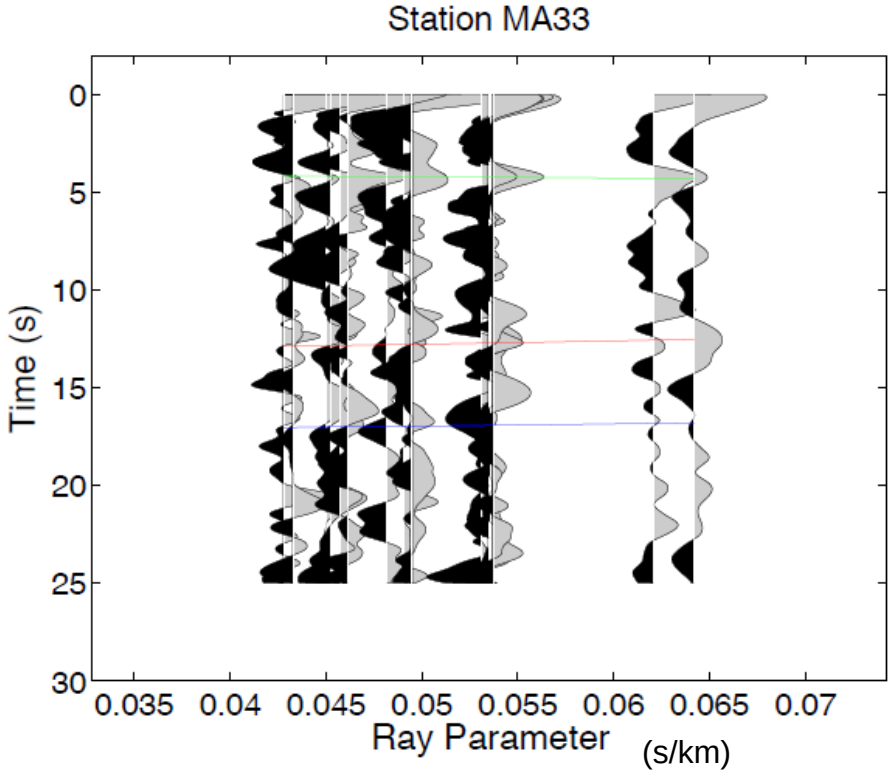
Station MA33
Time (s)
0
5
10
15
20
25
30
0.035
0.04
0.045
0.05
0.055
0.06
0.065
0.07
Ray Parameter (s/km)

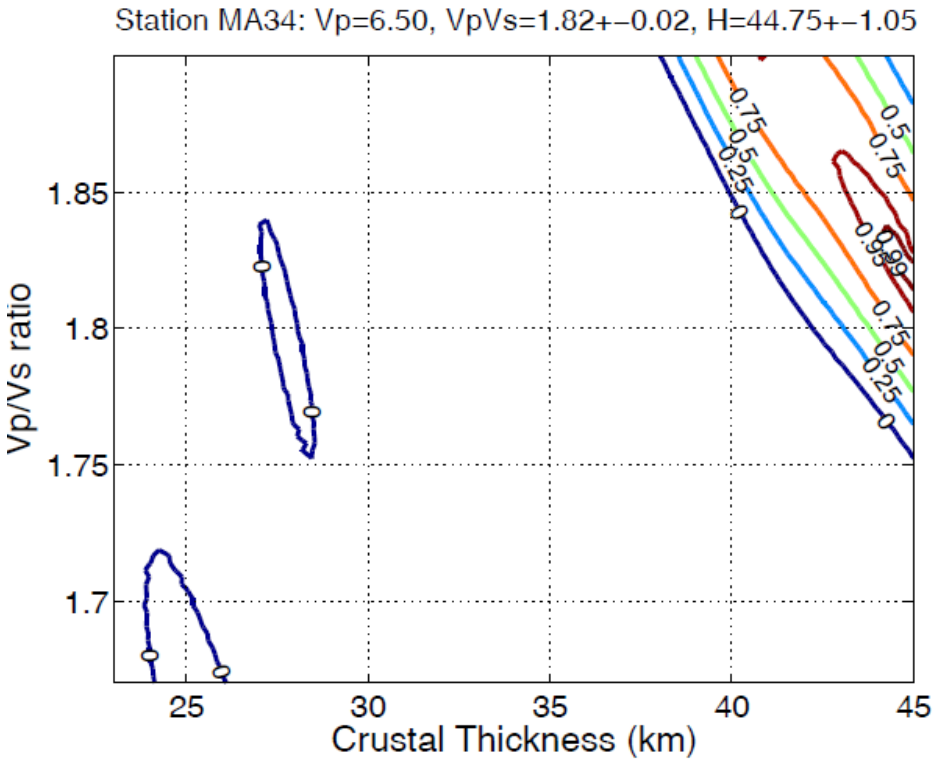
Station MA34: Vp=6.50, VpVs=1.82+−0.02, H=44.75+−1.05
Vp/Vs ratio
1.85
1.8
1.75
1.7
25
30
35
40
45
Crustal Thickness (km)

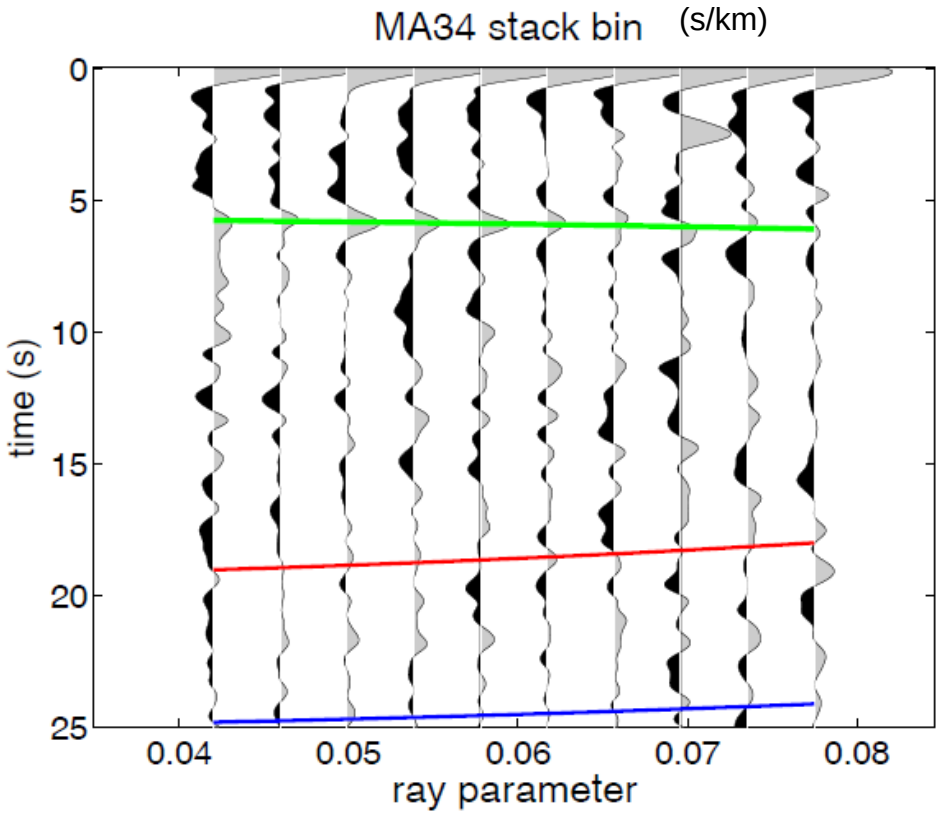
MA34 stack bin (s/km)
time (s)
0
5
10
15
20
25
0.04
0.05
0.06
0.07
0.08
ray parameter

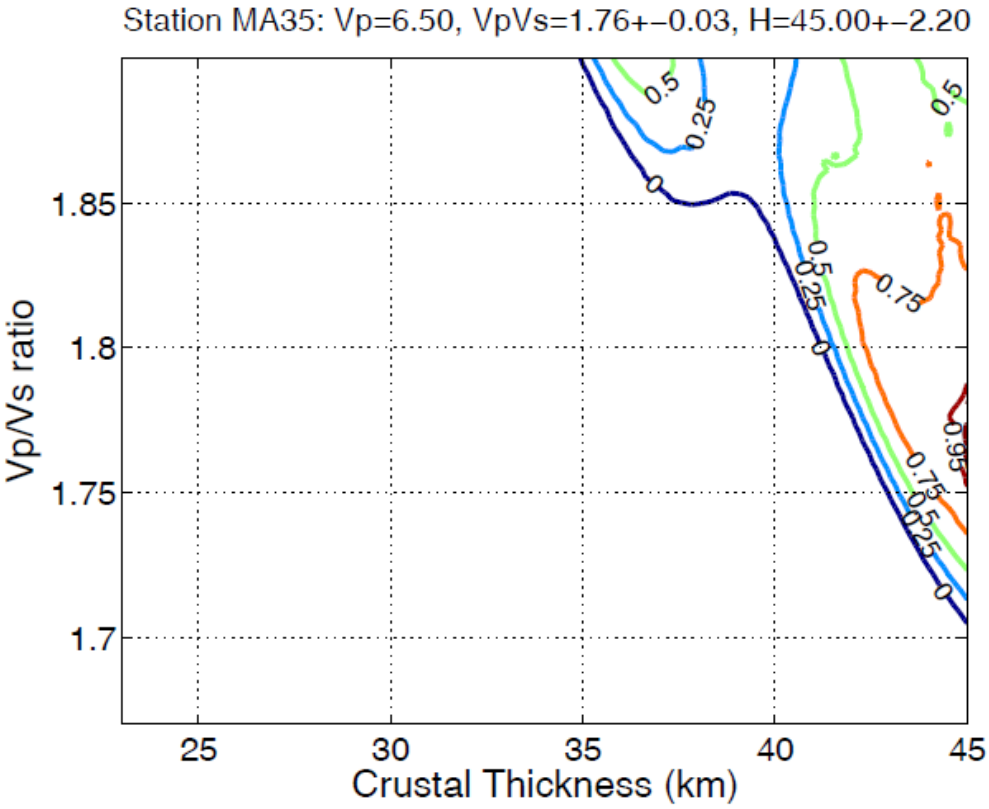
Station MA35: Vp=6.50, VpVs=1.76+−0.03, H=45.00+−2.20
Vp/Vs ratio
1.85
1.8
1.75
1.7
25
30
35
40
45
Crustal Thickness (km)
0.5
0.25
0
0.75
0.95

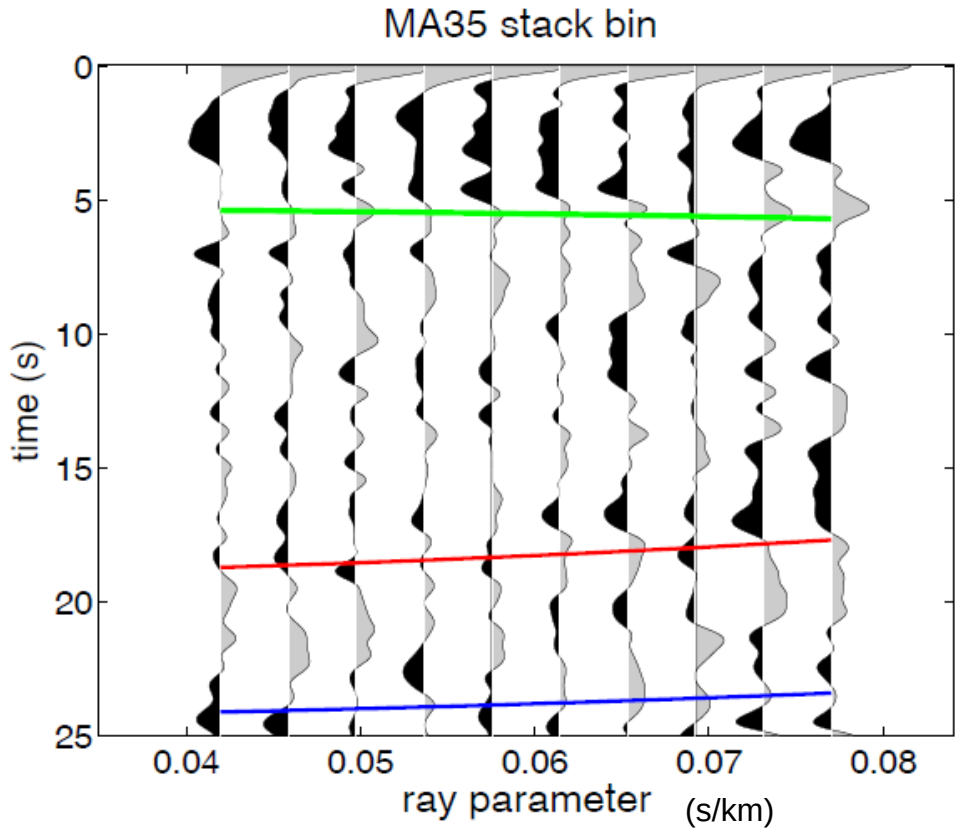
MA35 stack bin
time (s)
0
5
10
15
20
25
0.04
0.05
0.06
0.07
0.08
ray parameter (s/km)

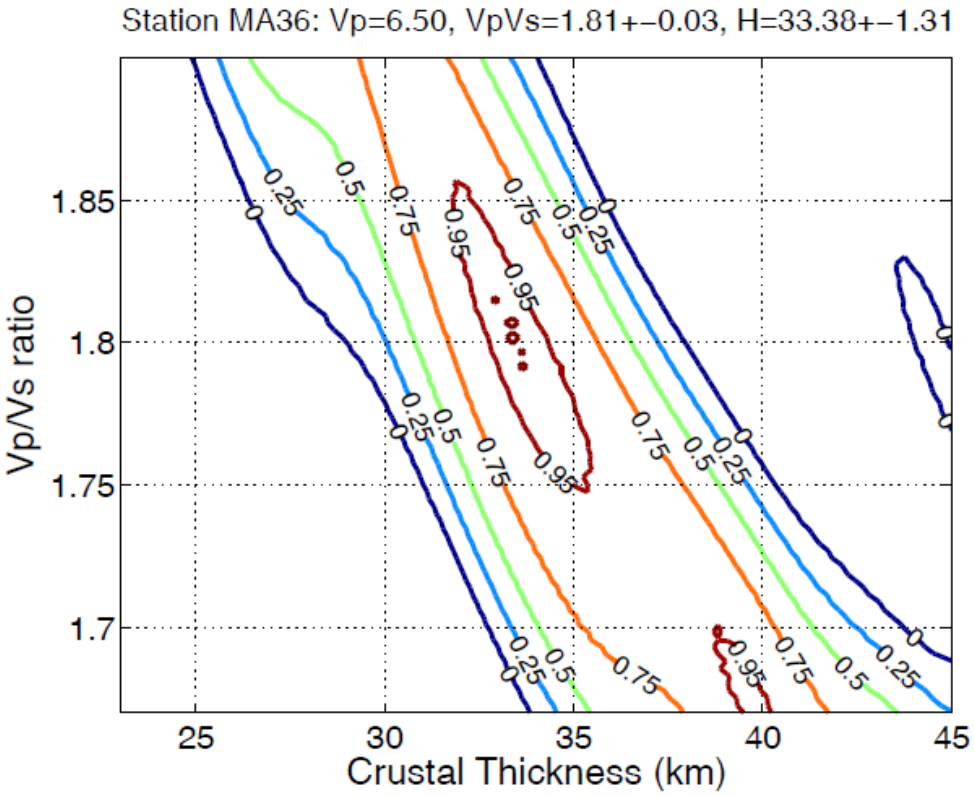
Station MA36: Vp=6.50, VpVs=1.81+−0.03, H=33.38+−1.31
Vp/Vs ratio
1.85
1.8
1.75
1.7
25
30
35
40
45
Crustal Thickness (km)
0
0.25
0.5
0.75
0.95

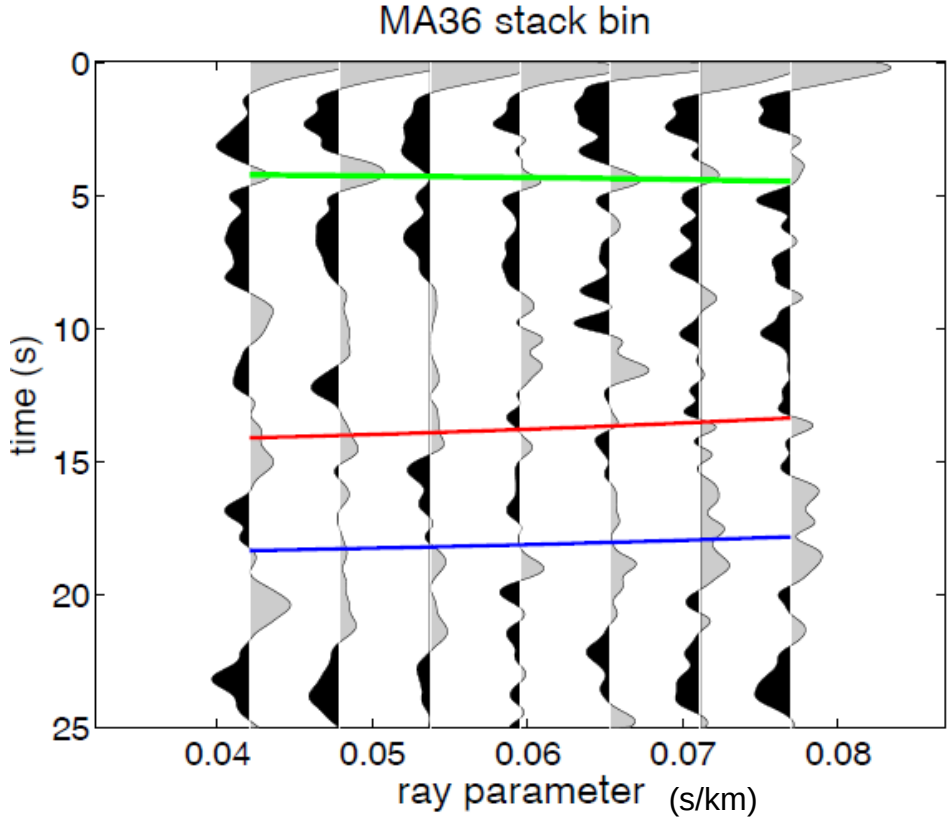
MA36 stack bin
time (s)
0
5
10
15
20
25
0.04
0.05
0.06
0.07
0.08
ray parameter (s/km)

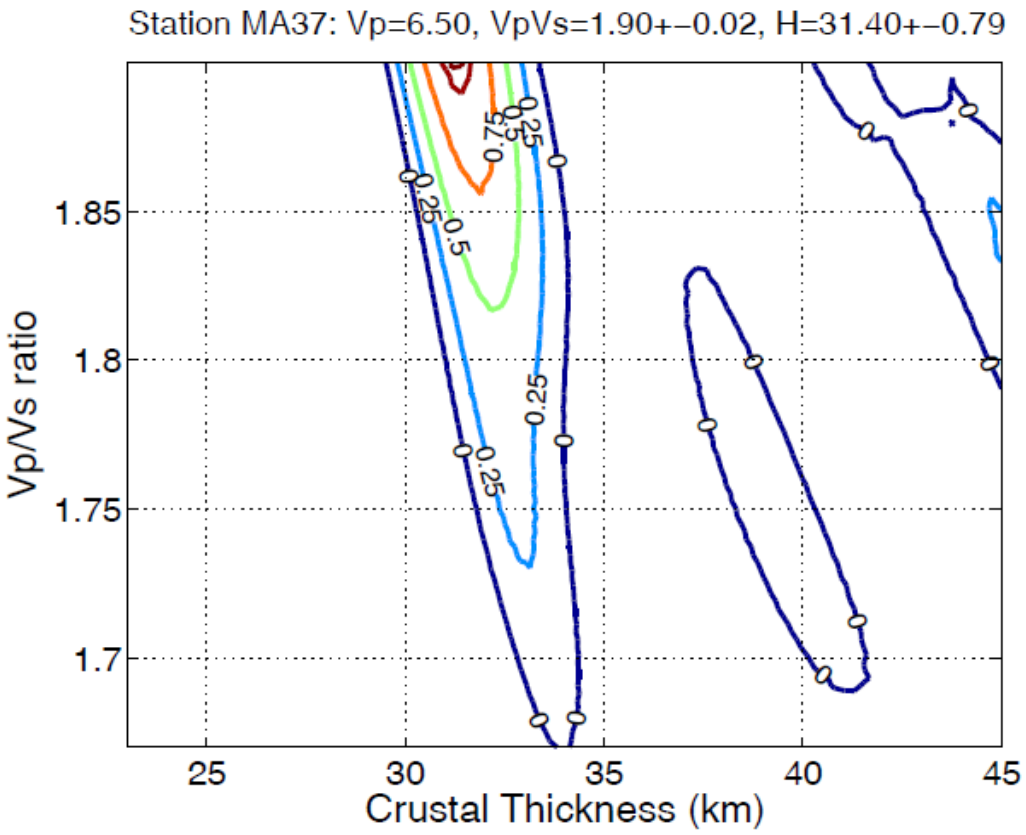
Station MA37: Vp=6.50, VpVs=1.90+−0.02, H=31.40+−0.79
Vp/Vs ratio
1.85
1.8
1.75
1.7
25
30
35
40
45
Crustal Thickness (km)
0.25
0.5
0.75
0

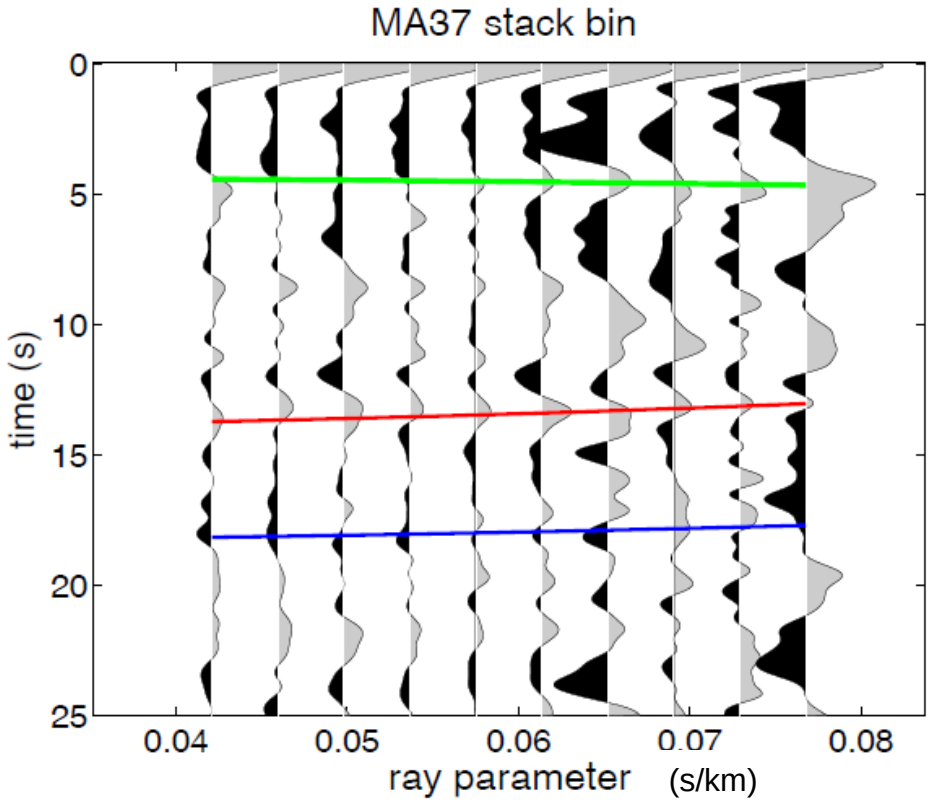
MA37 stack bin
time (s)
0
5
10
15
20
25
0.04
0.05
0.06
0.07
0.08
ray parameter (s/km)

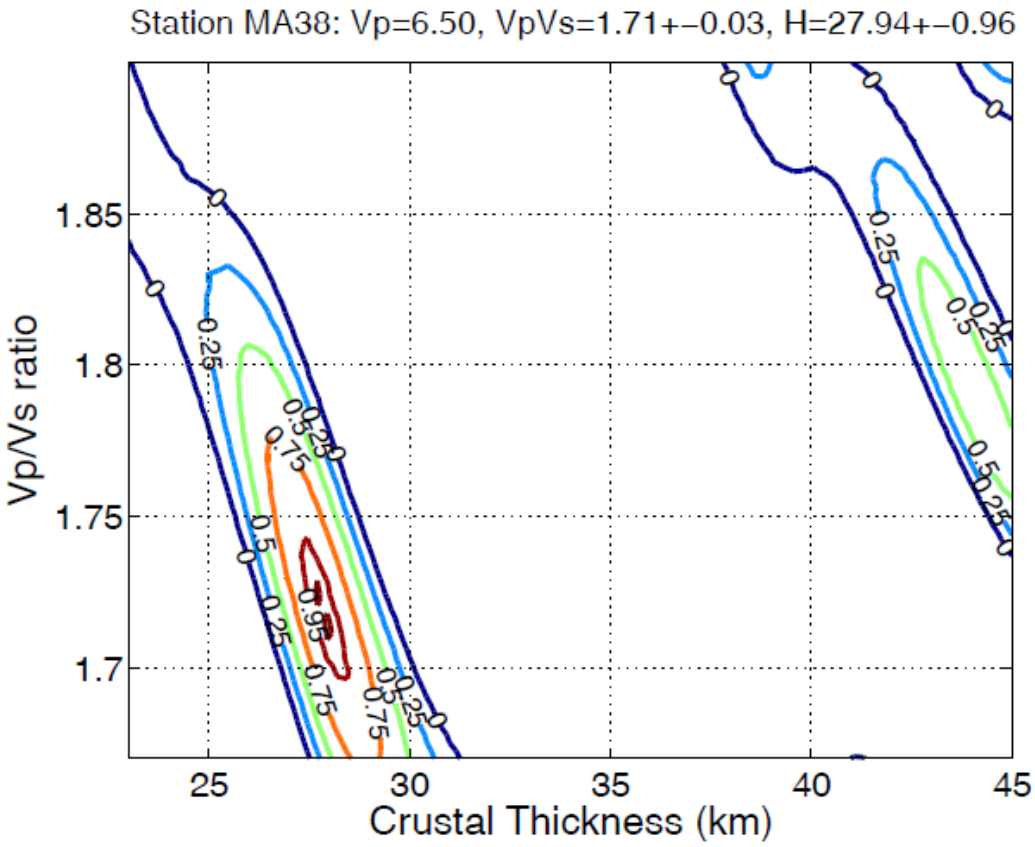
Station MA38: Vp=6.50, VpVs=1.71+−0.03, H=27.94+−0.96
Vp/Vs ratio
1.85
1.8
1.75
1.7
25
30
35
40
45
Crustal Thickness (km)

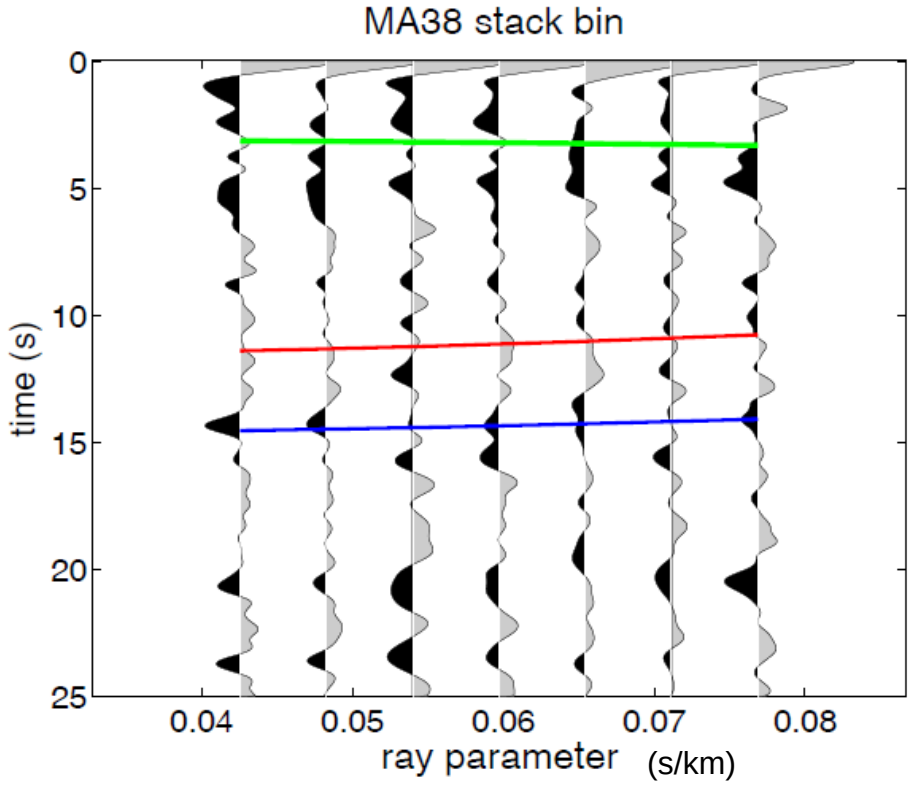
MA38 stack bin
time (s)
0
5
10
15
20
25
0.04
0.05
0.06
0.07
0.08
ray parameter (s/km)

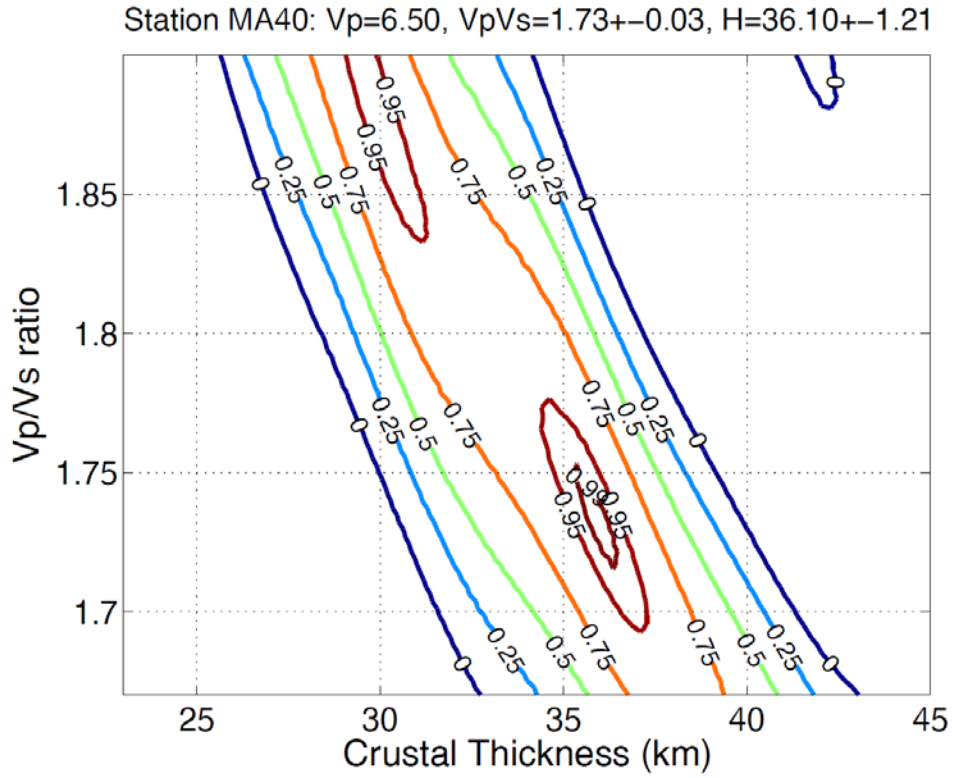
Station MA40: Vp=6.50, VpVs=1.73+−0.03, H=36.10+−1.21
Vp/Vs ratio
1.85
1.8
1.75
1.7
25
30
35
40
45
Crustal Thickness (km)
0
0.25
0.5
0.75
0.95

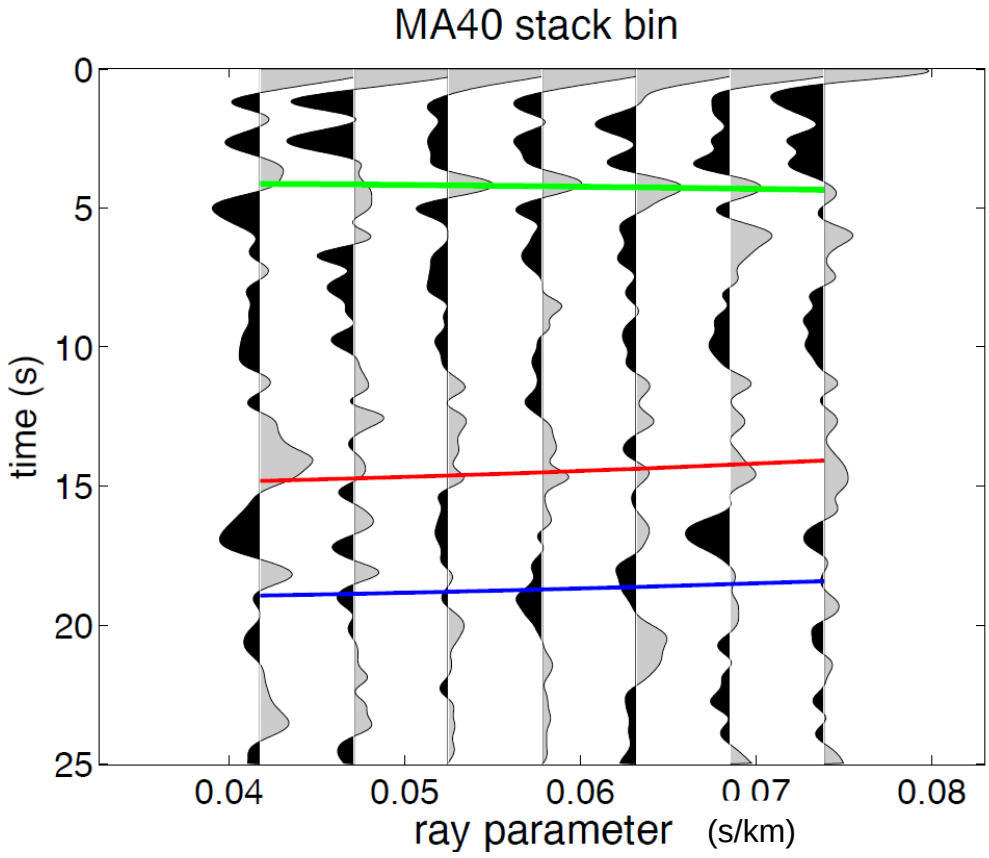
MA40 stack bin
time (s)
0
5
10
15
20
25
0.04
0.05
0.06
0.07
0.08
ray parameter (s/km)

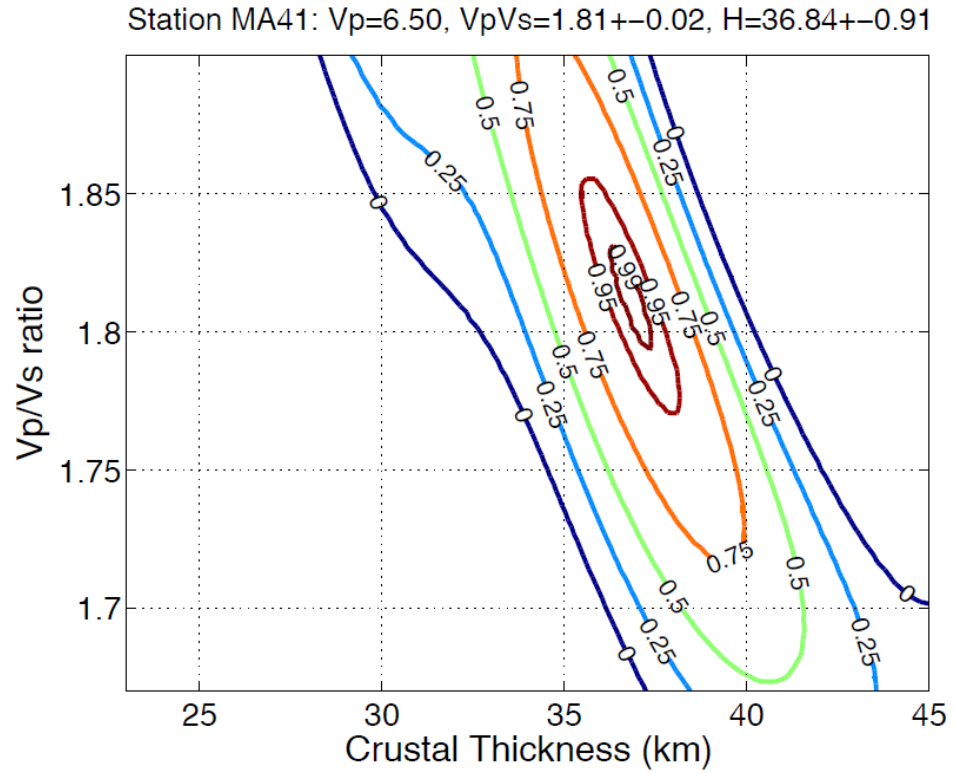
Station MA41: Vp=6.50, VpVs=1.81+−0.02, H=36.84+−0.91
Vp/Vs ratio
1.85
1.8
1.75
1.7
25
30
35
40
45
Crustal Thickness (km)

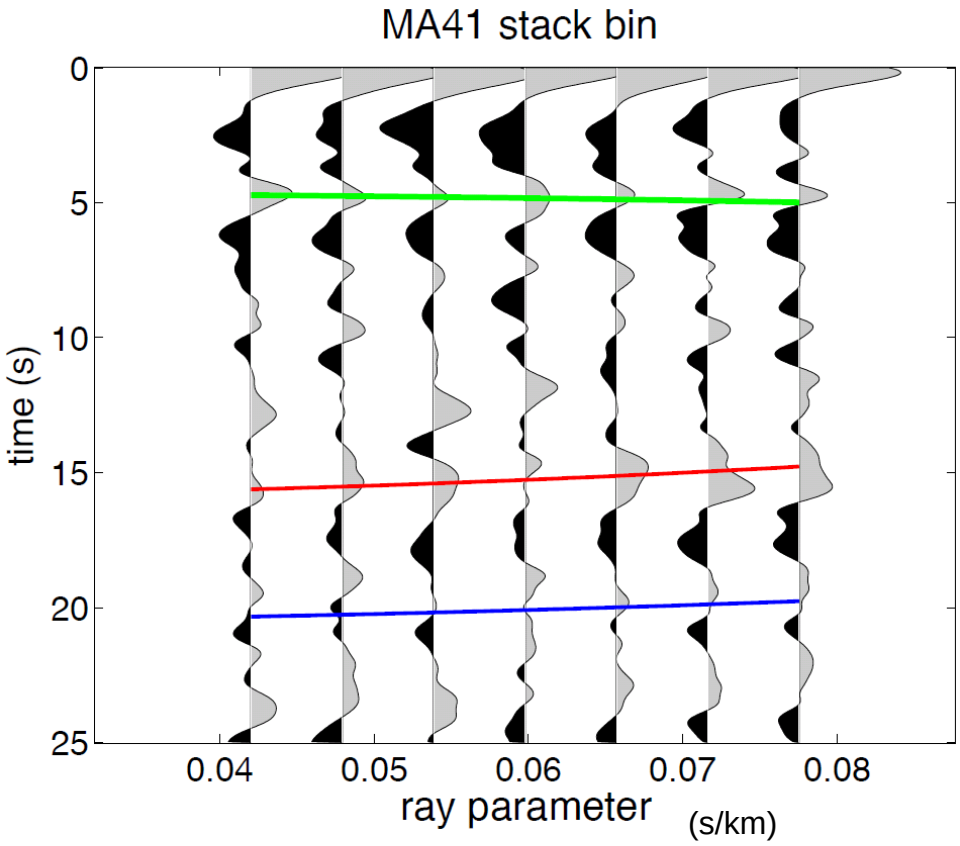
MA41 stack bin
time (s)
0
5
10
15
20
25
0.04
0.05
0.06
0.07
0.08
ray parameter
(s/km)

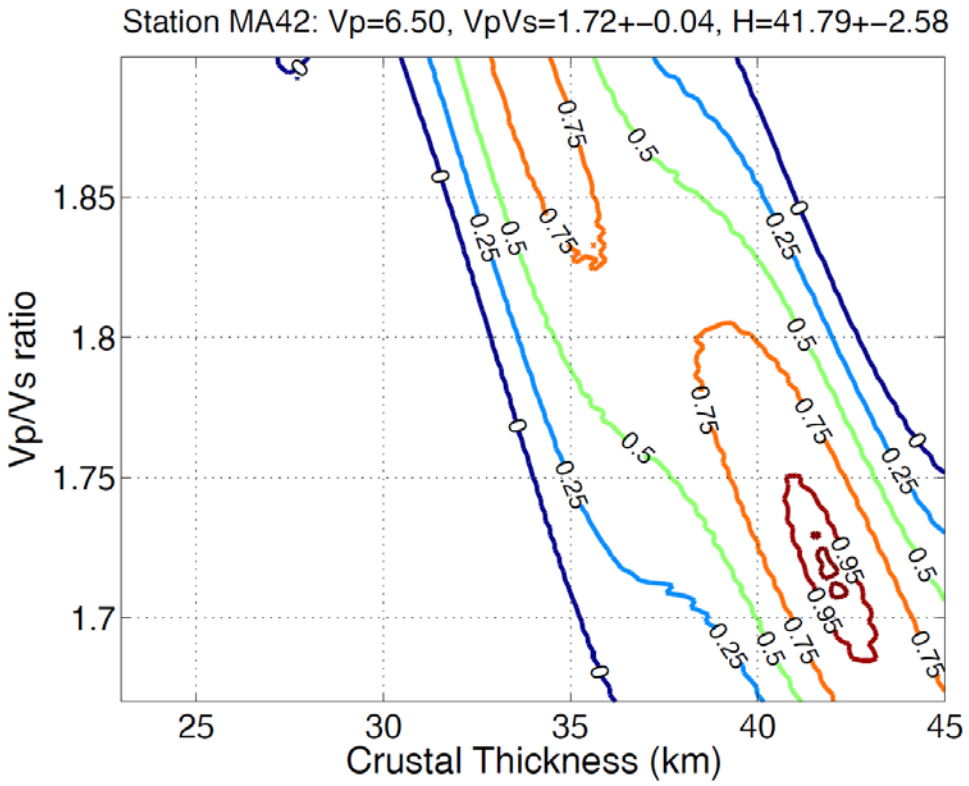
Station MA42: Vp=6.50, VpVs=1.72+−0.04, H=41.79+−2.58
Vp/Vs ratio
1.85
1.8
1.75
1.7
25
30
35
40
45
Crustal Thickness (km)
0
0.25
0.5
0.75
0.95

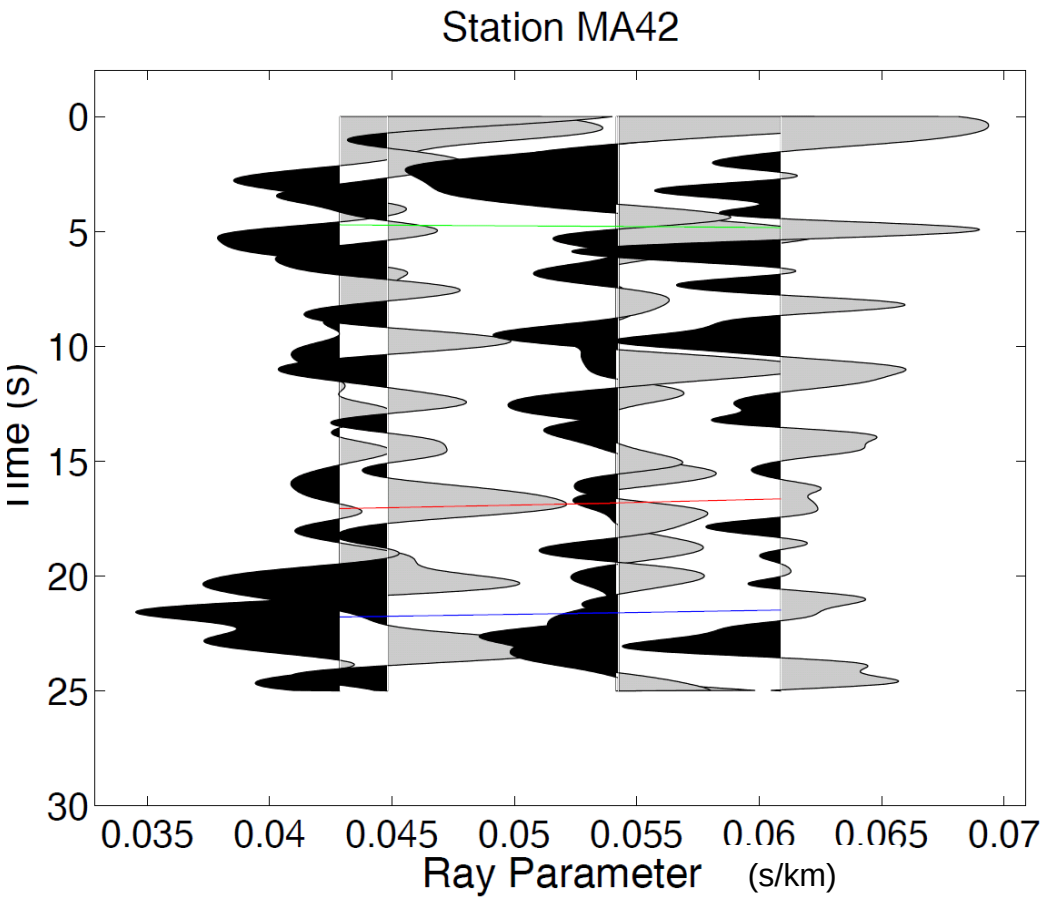
Station MA42
Time (s)
0
5
10
15
20
25
30
0.035
0.04
0.045
0.05
0.055
0.06
0.065
0.07
Ray Parameter (s/km)

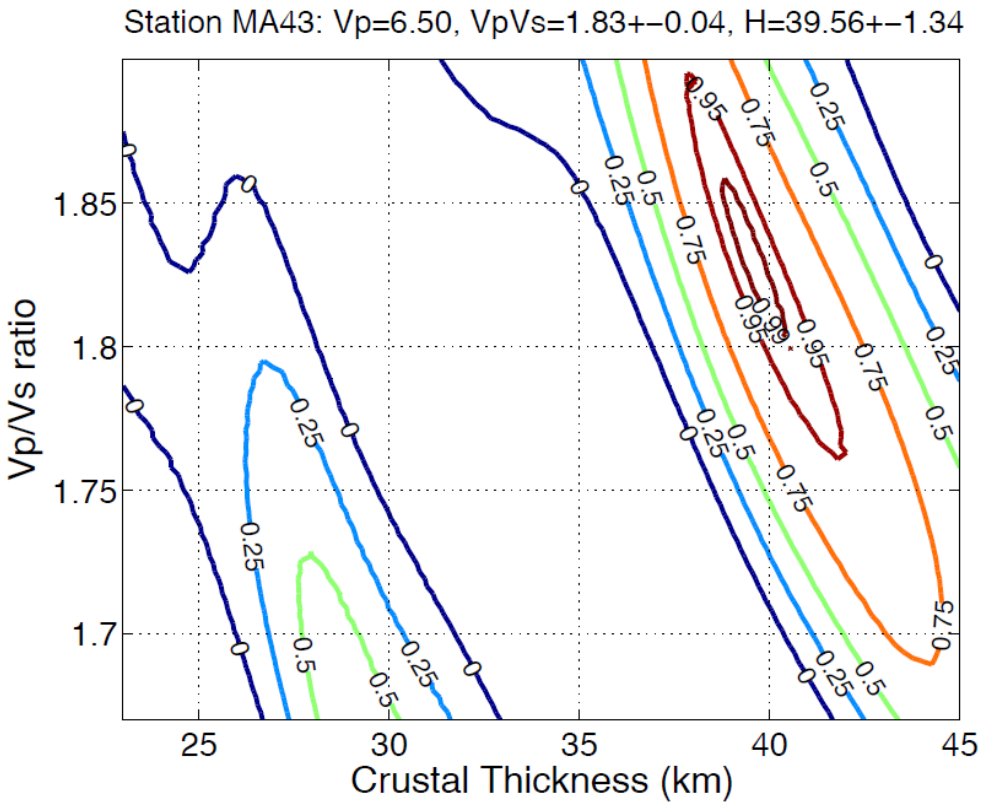
Station MA43: Vp=6.50, VpVs=1.83+−0.04, H=39.56+−1.34
Vp/Vs ratio
1.85
1.8
1.75
1.7
25
30
35
40
45
Crustal Thickness (km)

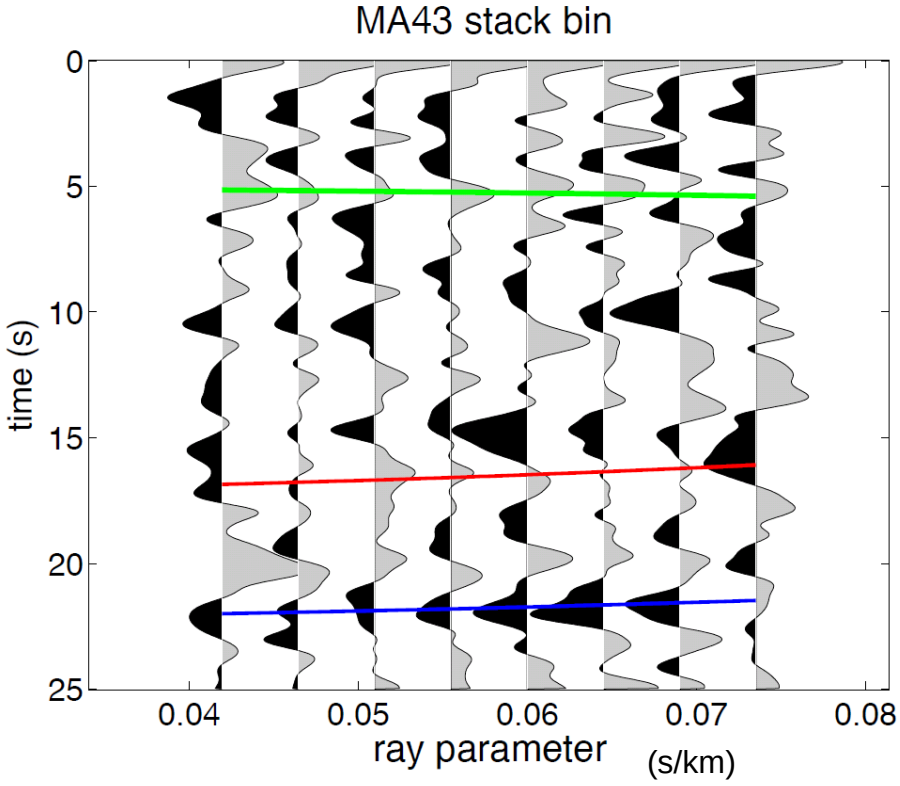
MA43 stack bin
time (s)
0
5
10
15
20
25
0.04
0.05
0.06
0.07
0.08
ray parameter
(s/km)

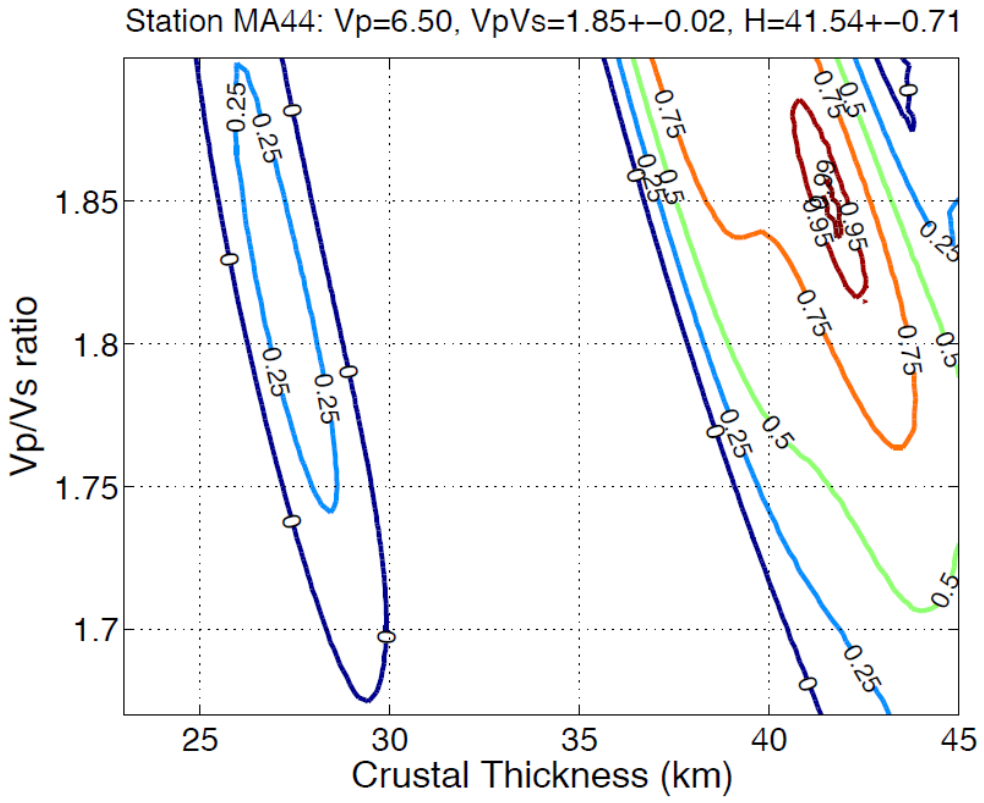
Station MA44: Vp=6.50, VpVs=1.85+−0.02, H=41.54+−0.71
Vp/Vs ratio
1.85
1.8
1.75
1.7
25
30
35
40
45
Crustal Thickness (km)

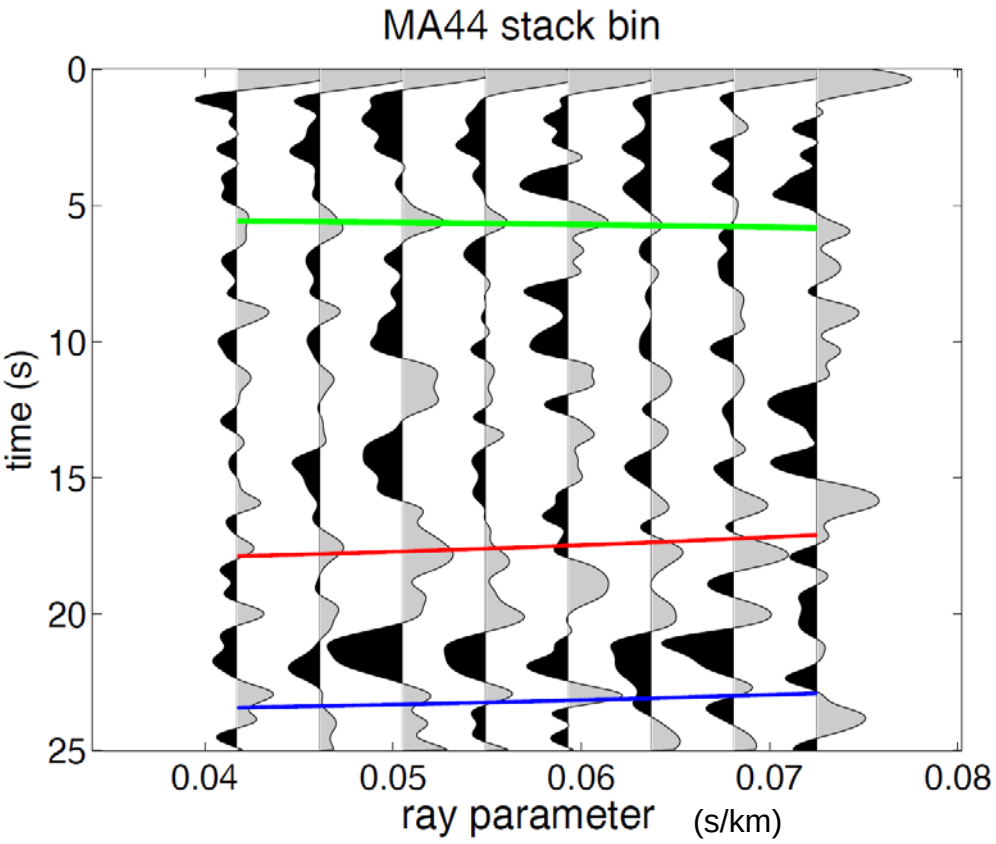
MA44 stack bin
time (s)
0
5
10
15
20
25
0.04
0.05
0.06
0.07
0.08
ray parameter (s/km)

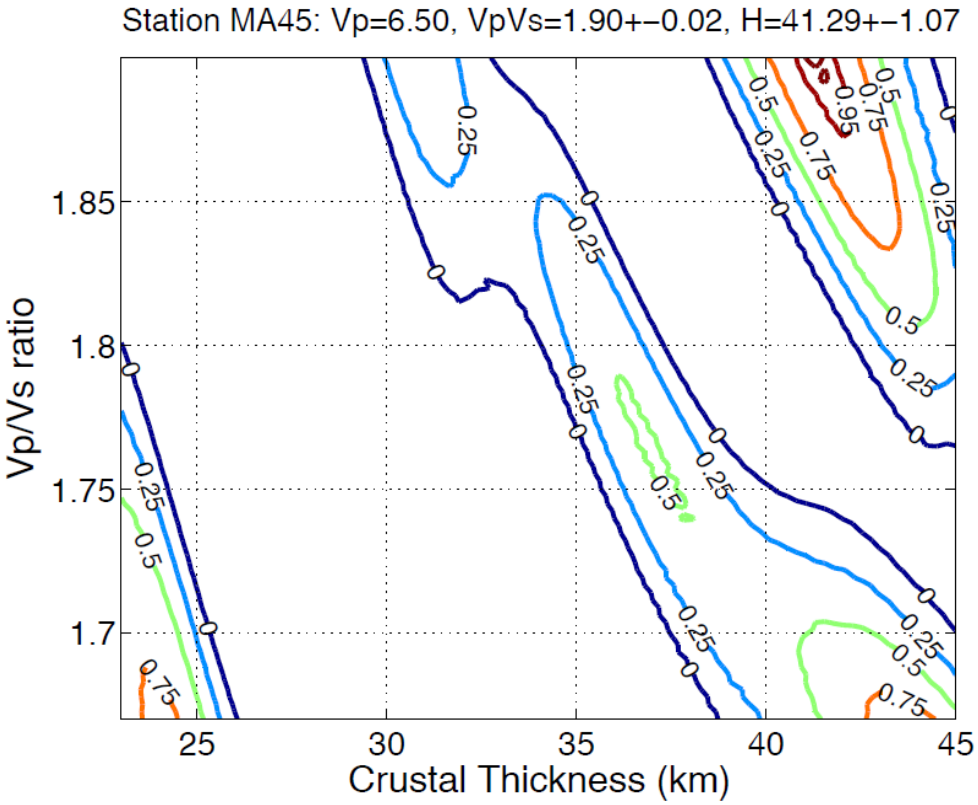
Station MA45: Vp=6.50, VpVs=1.90+−0.02, H=41.29+−1.07
Vp/Vs ratio
1.85
1.8
1.75
1.7
25
30
35
40
45
Crustal Thickness (km)

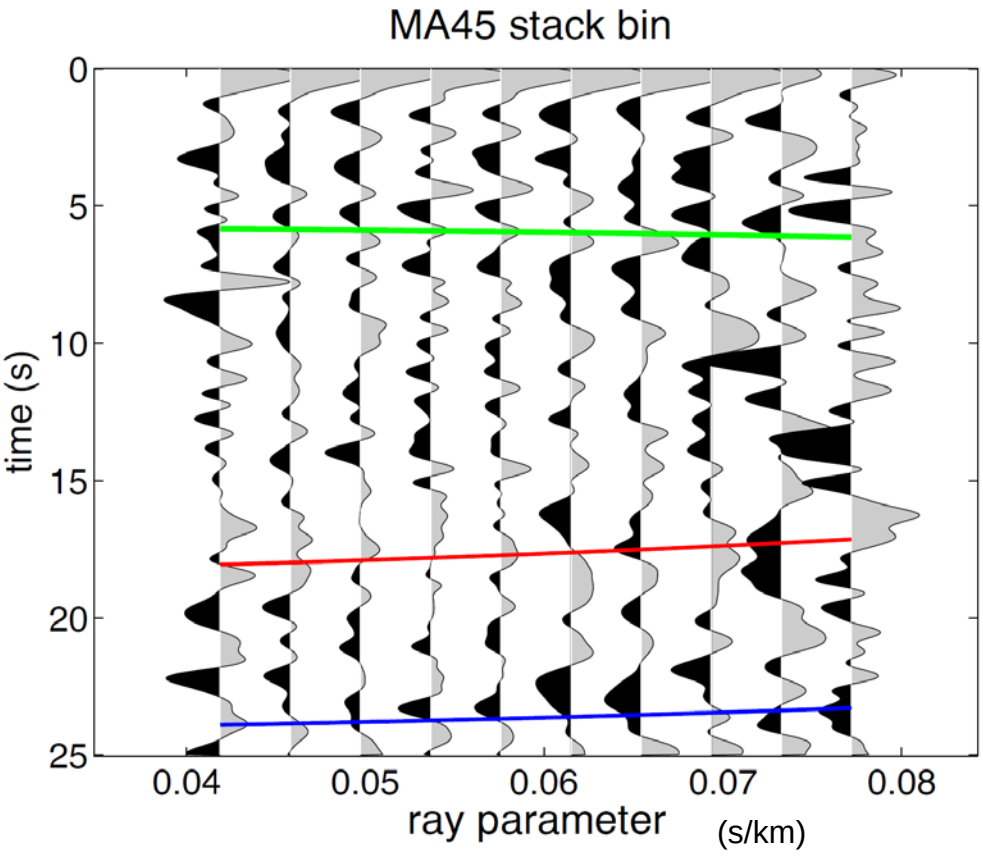
MA45 stack bin
time (s)
0
5
10
15
20
25
0.04
0.05
0.06
0.07
0.08
ray parameter
(s/km)

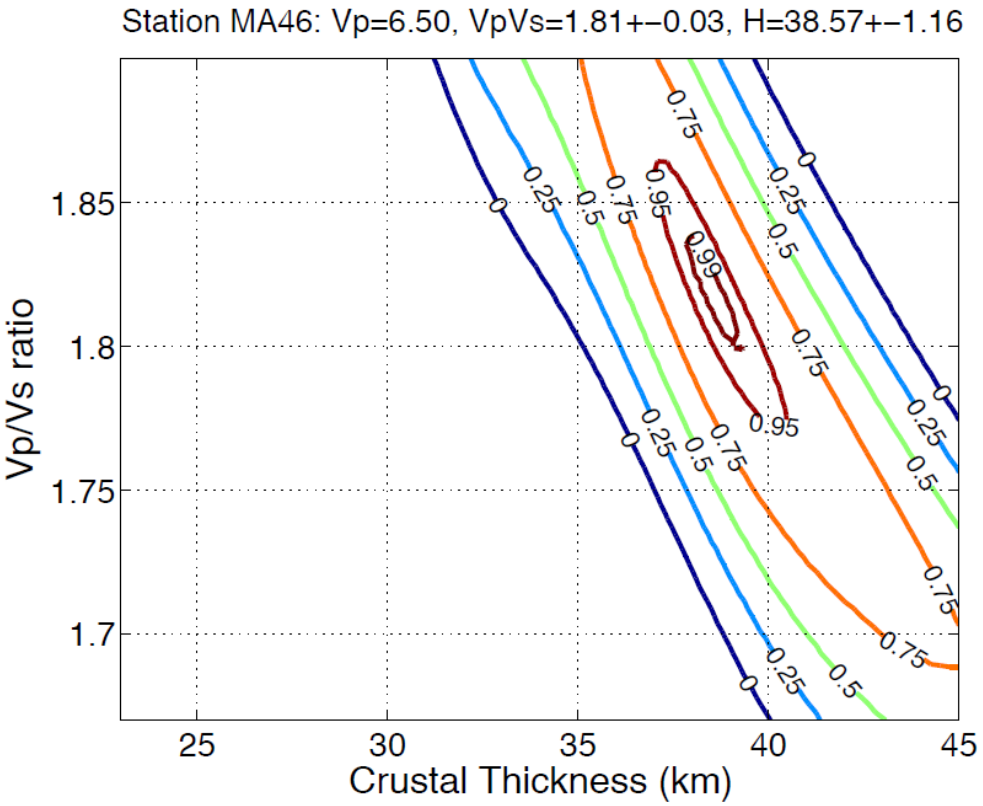
Station MA46: Vp=6.50, VpVs=1.81+−0.03, H=38.57+−1.16
Vp/Vs ratio
1.85
1.8
1.75
1.7
25
30
35
40
45
Crustal Thickness (km)
0
0.25
0.5
0.75
0.95
0.99

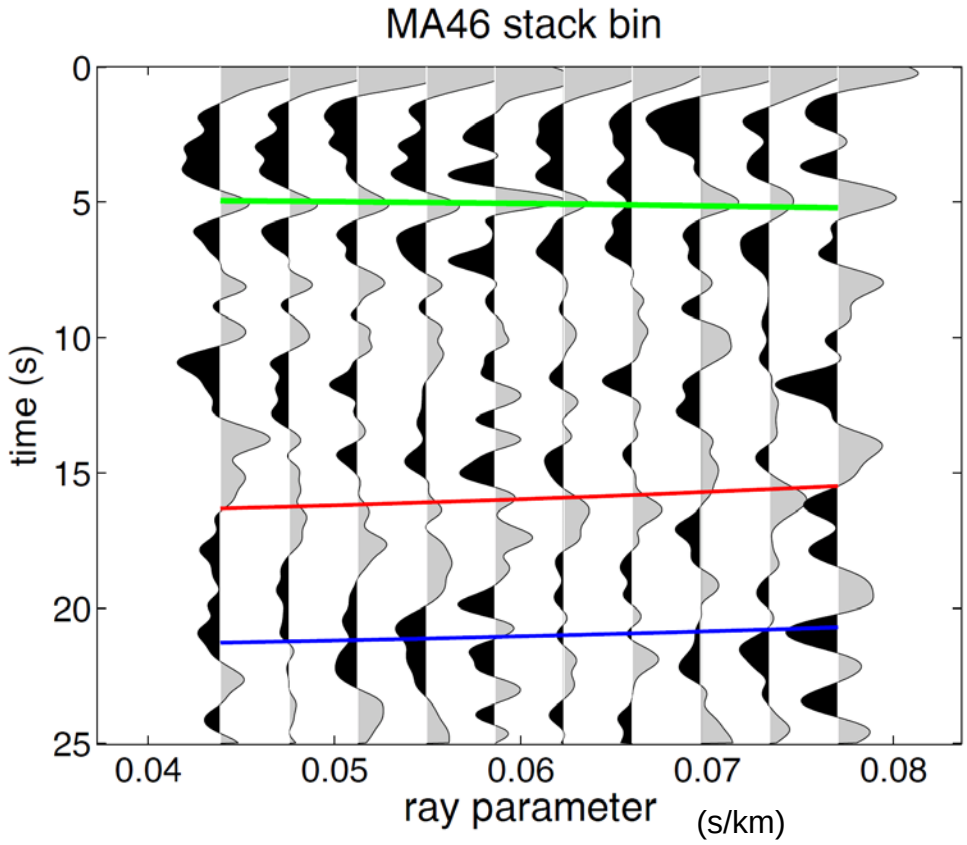
MA46 stack bin
time (s)
0
5
10
15
20
25
0.04
0.05
0.06
0.07
0.08
ray parameter
(s/km)

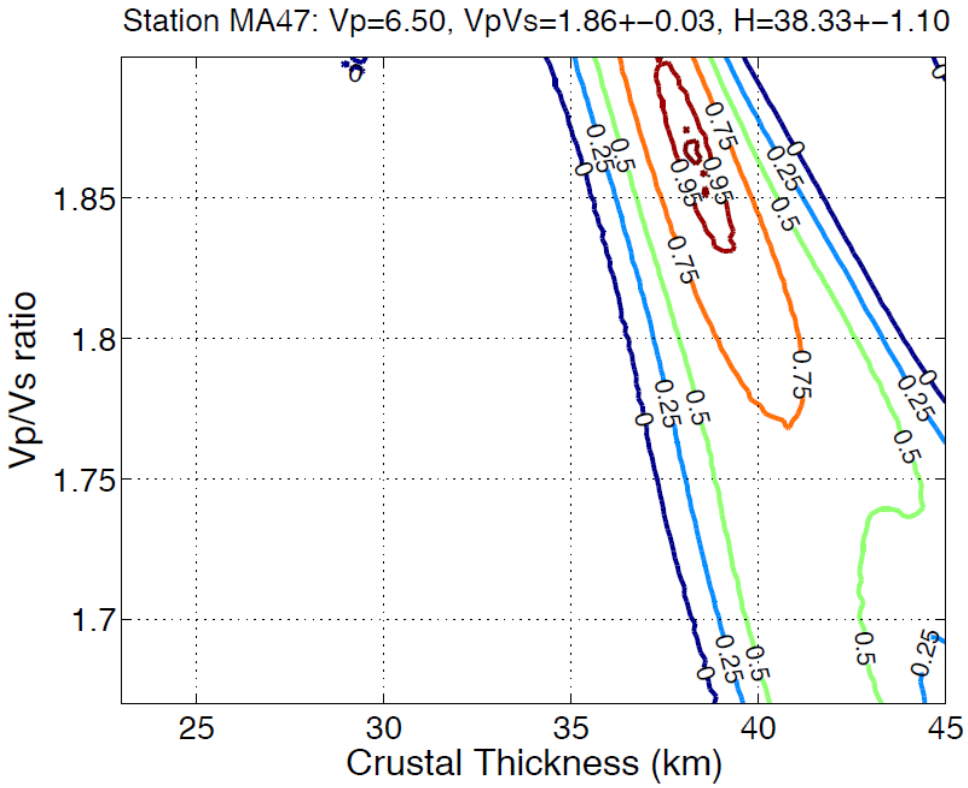
Station MA47: Vp=6.50, VpVs=1.86+−0.03, H=38.33+−1.10
Vp/Vs ratio
1.85
1.8
1.75
1.7
25
30
35
40
45
Crustal Thickness (km)

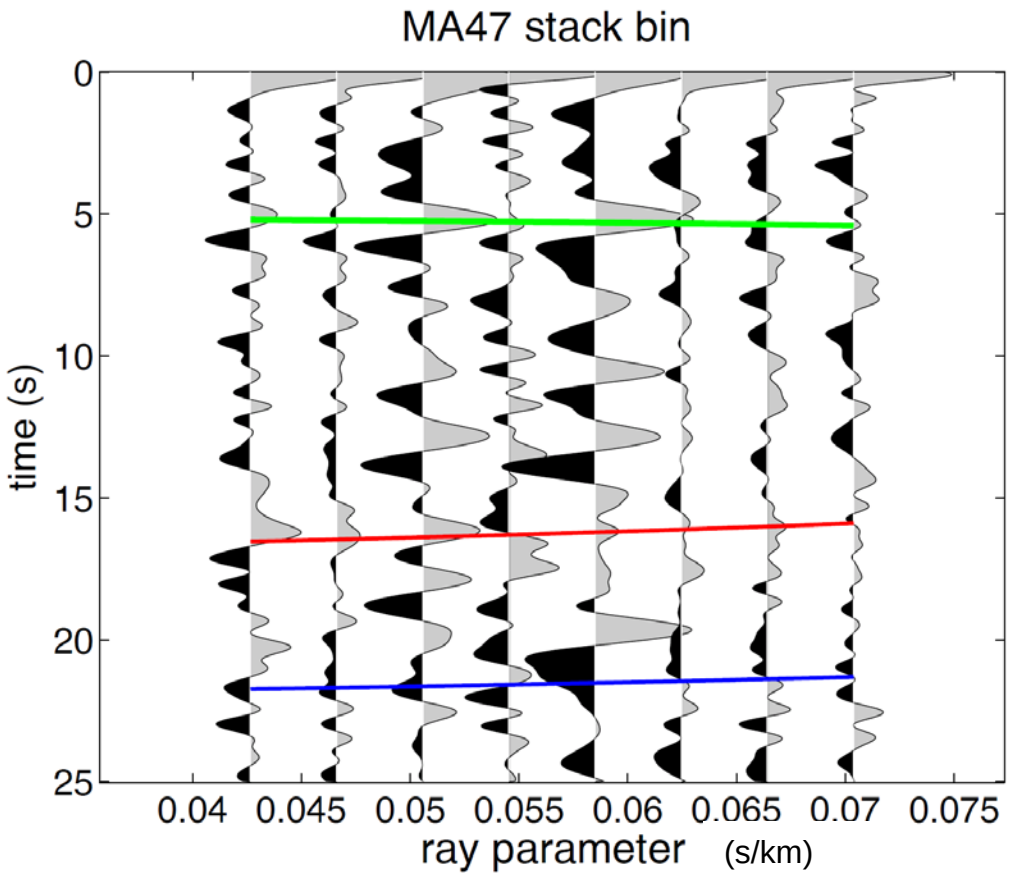
MA47 stack bin
time (s)
0
5
10
15
20
25
0.04
0.045
0.05
0.055
0.06
0.065
0.07
0.075
ray parameter (s/km)

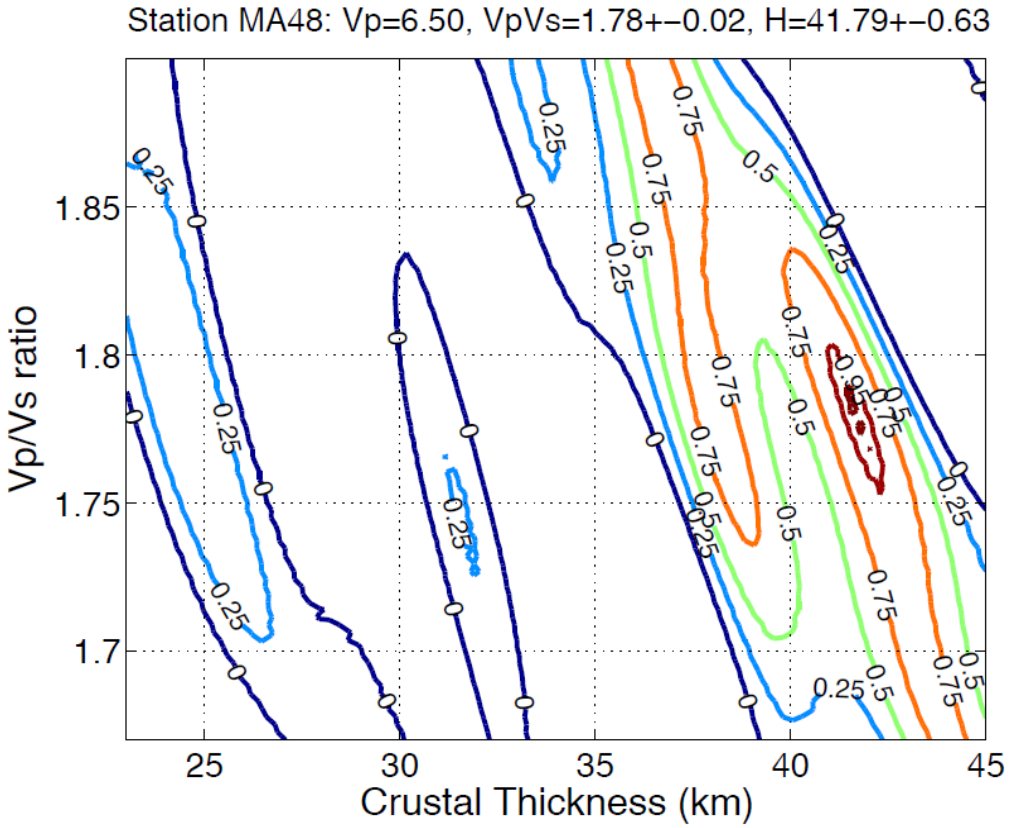
Station MA48: Vp=6.50, VpVs=1.78+−0.02, H=41.79+−0.63
Vp/Vs ratio
1.85
1.8
1.75
1.7
25
30
35
40
45
Crustal Thickness (km)

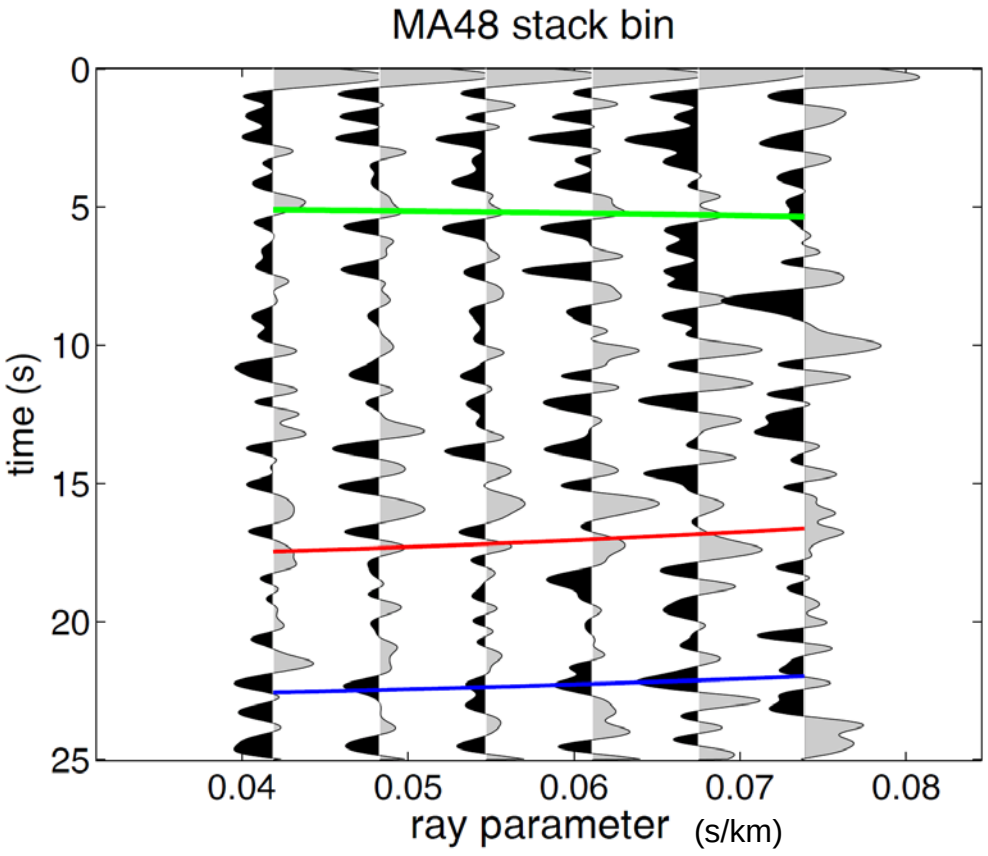
MA48 stack bin
time (s)
0
5
10
15
20
25
0.04
0.05
0.06
0.07
0.08
ray parameter (s/km)

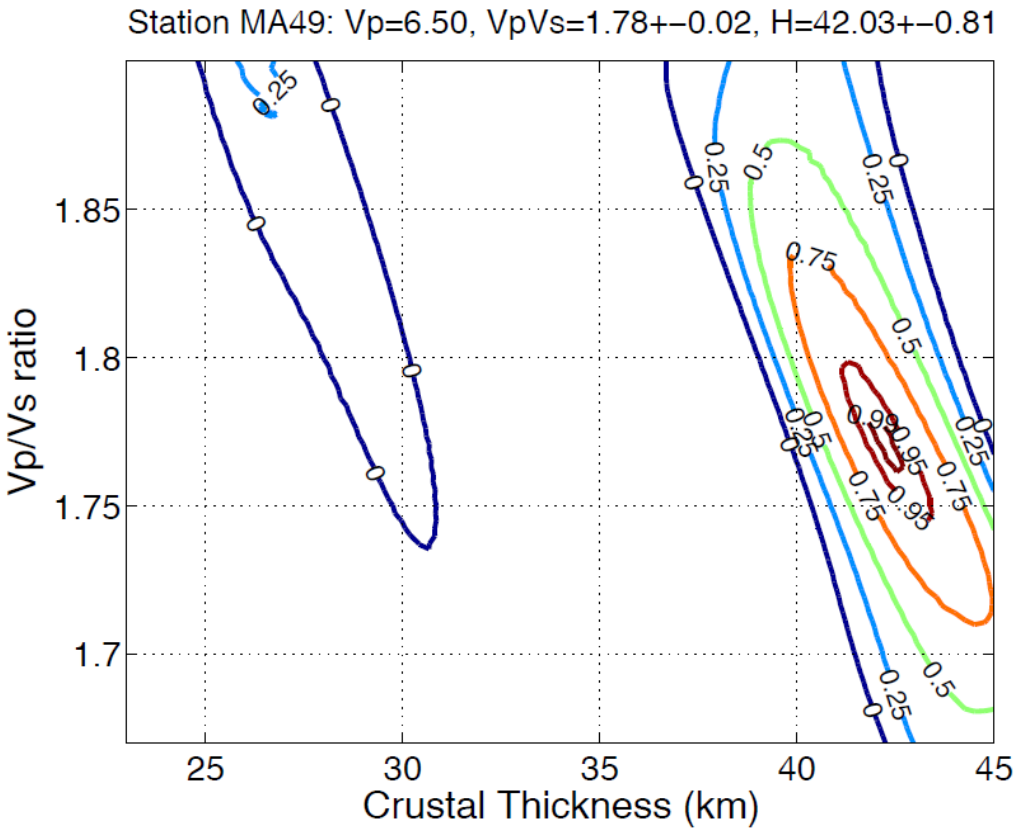
Station MA49: Vp=6.50, VpVs=1.78+−0.02, H=42.03+−0.81
Vp/Vs ratio
1.85
1.8
1.75
1.7
25
30
35
40
45
Crustal Thickness (km)

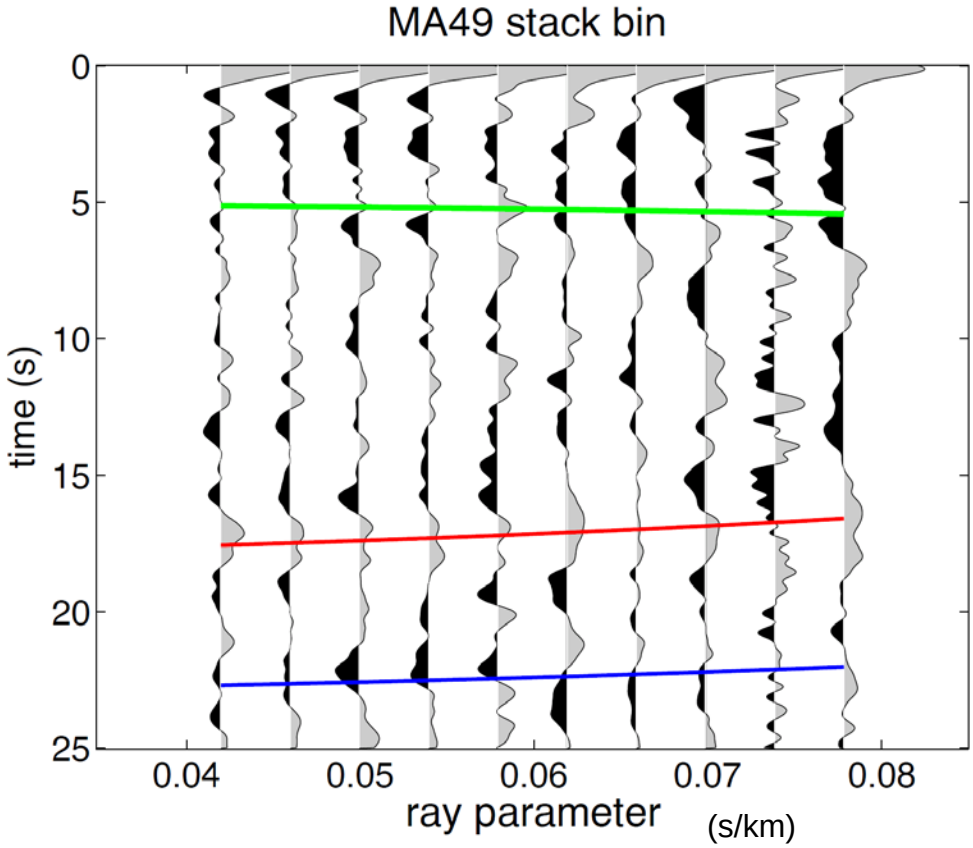
MA49 stack bin
time (s)
0
5
10
15
20
25
0.04
0.05
0.06
0.07
0.08
ray parameter
(s/km)

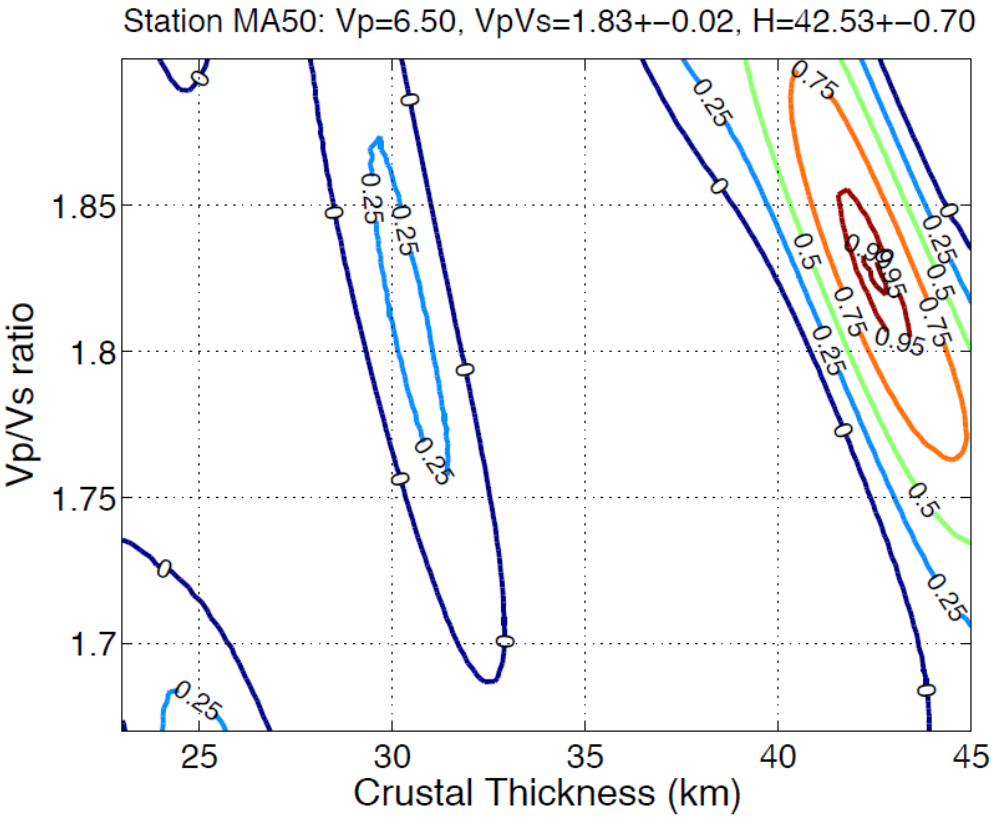
Station MA50: Vp=6.50, VpVs=1.83+−0.02, H=42.53+−0.70
Vp/Vs ratio
1.85
1.8
1.75
1.7
25
30
35
40
45
Crustal Thickness (km)

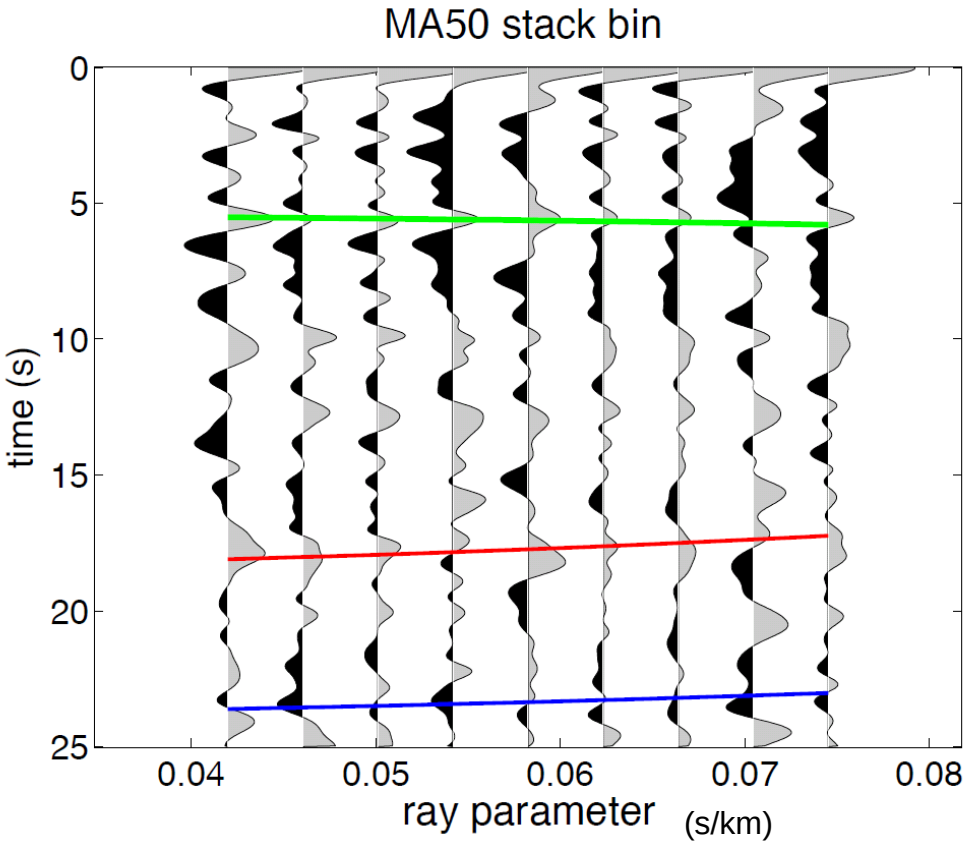
MA50 stack bin
time (s)
0
5
10
15
20
25
0.04
0.05
0.06
0.07
0.08
ray parameter (s/km)

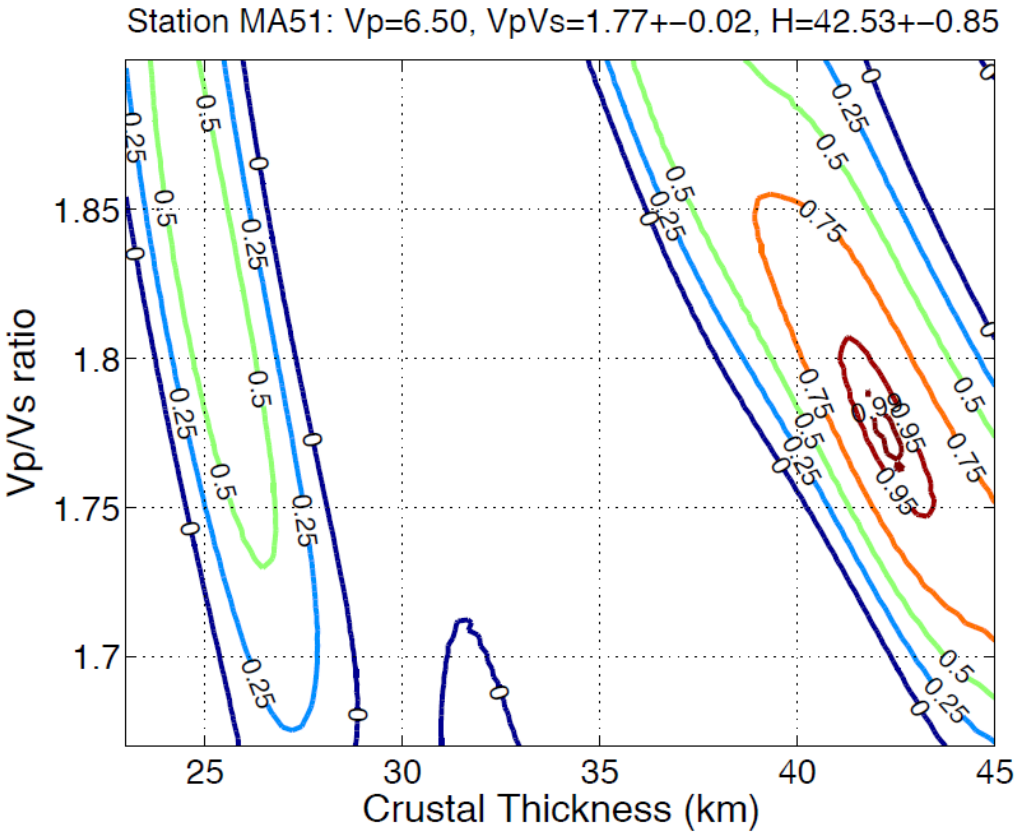
Station MA51: Vp=6.50, VpVs=1.77+−0.02, H=42.53+−0.85
Vp/Vs ratio
1.85
1.8
1.75
1.7
25
30
35
40
45
Crustal Thickness (km)

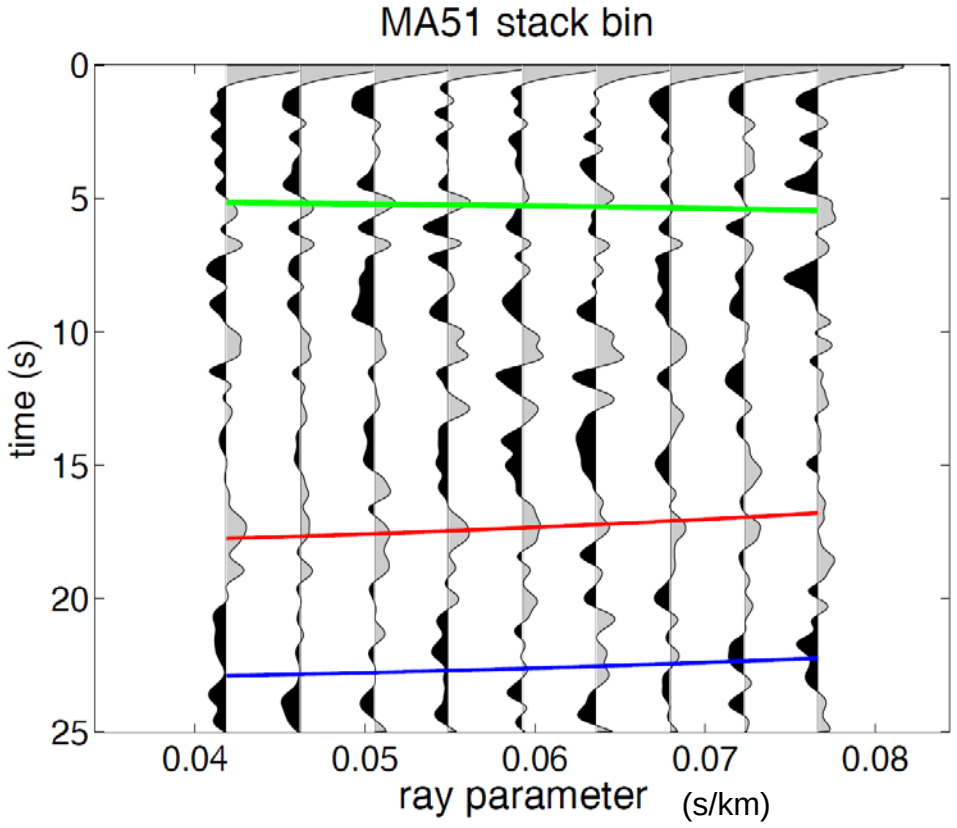
MA51 stack bin
time (s)
0
5
10
15
20
25
0.04
0.05
0.06
0.07
0.08
ray parameter (s/km)

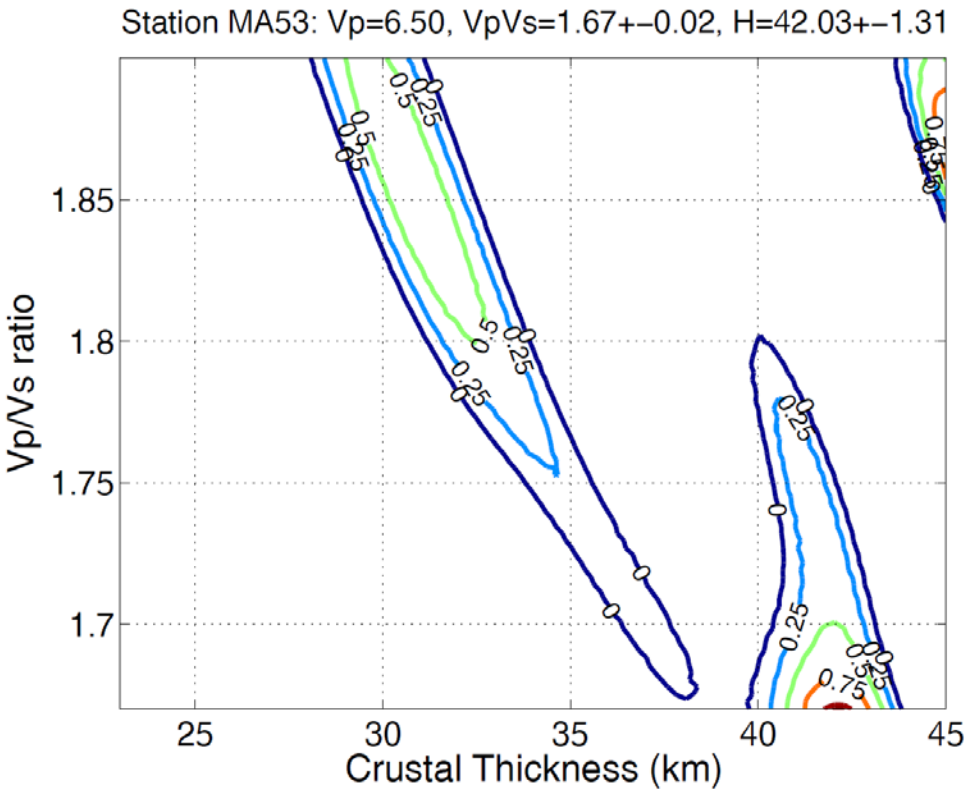
Station MA53: Vp=6.50, VpVs=1.67+−0.02, H=42.03+−1.31
Vp/Vs ratio
1.85
1.8
1.75
1.7
25
30
35
40
45
Crustal Thickness (km)

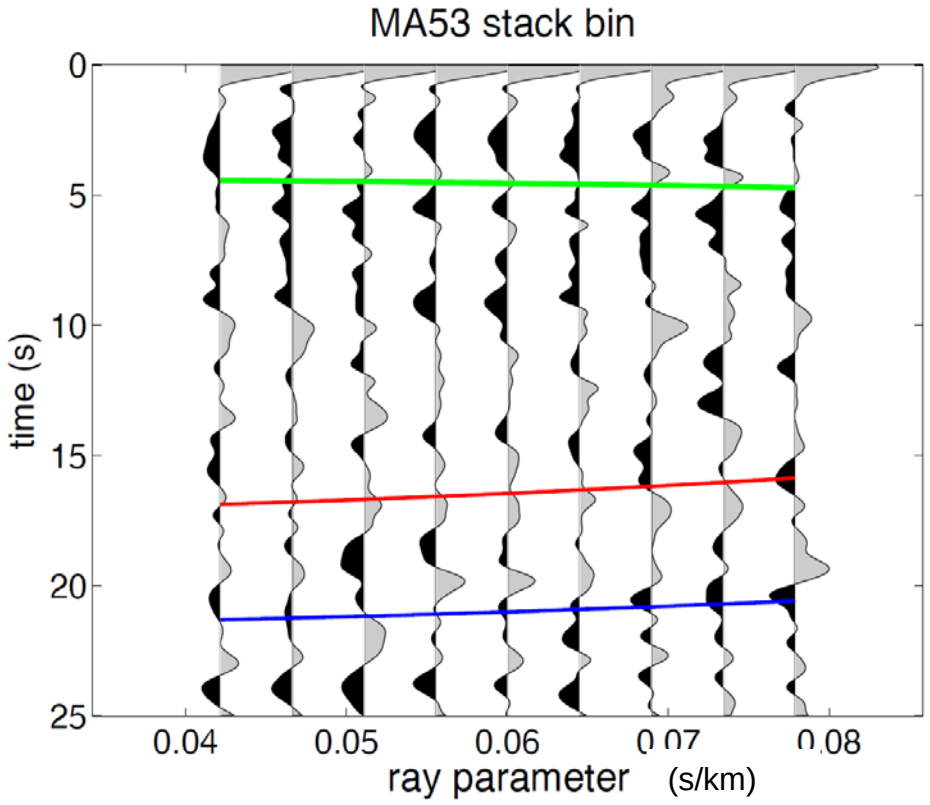
MA53 stack bin
time (s)
0
5
10
15
20
25
0.04
0.05
0.06
0.07
0.08
ray parameter (s/km)

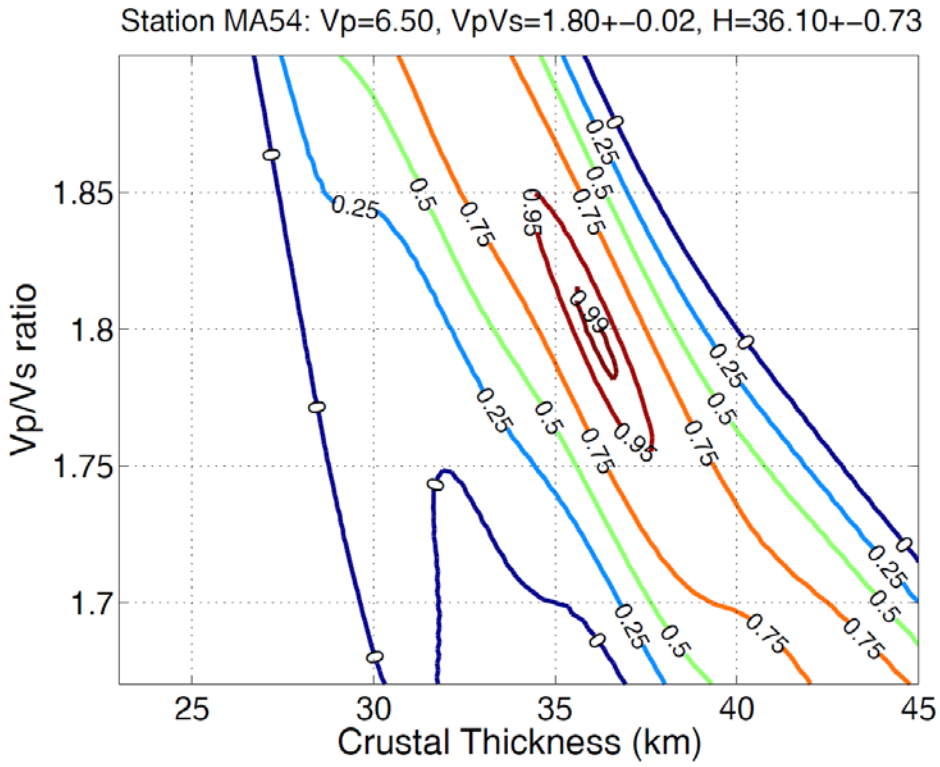
Station MA54: Vp=6.50, VpVs=1.80+−0.02, H=36.10+−0.73
Vp/Vs ratio
1.85
1.8
1.75
1.7
25
30
35
40
45
Crustal Thickness (km)
0
0.25
0.5
0.75
0.95
0.99

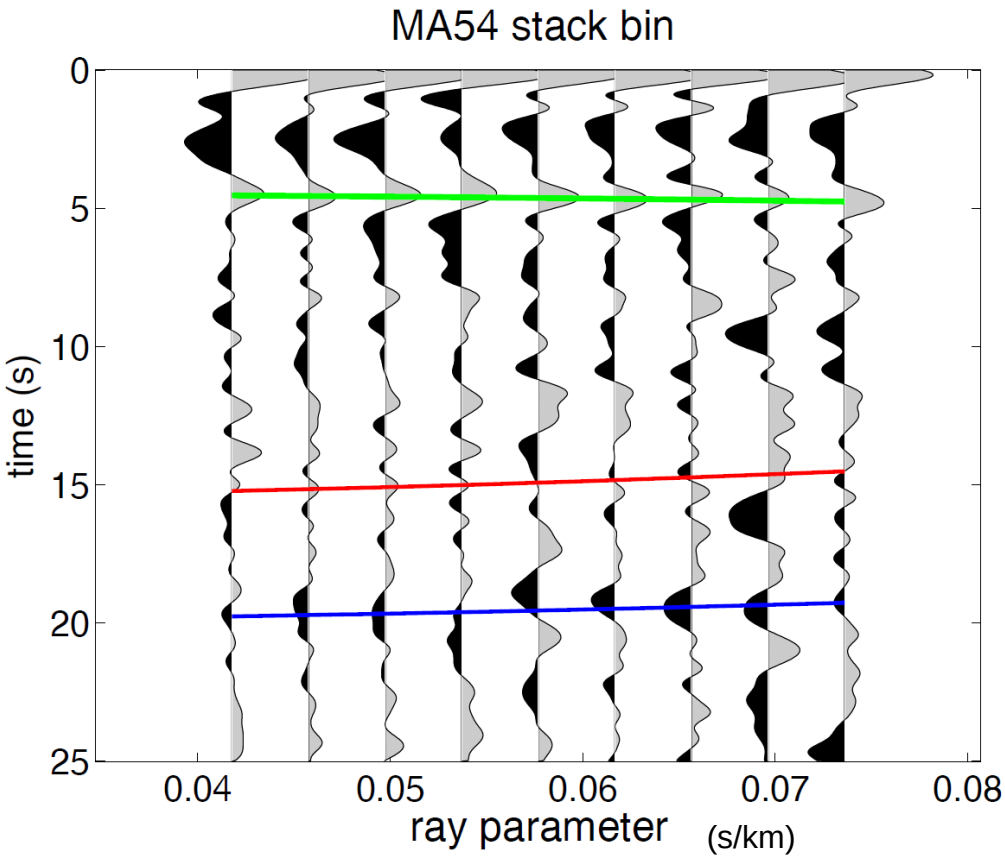
MA54 stack bin
time (s)
0
5
10
15
20
25
0.04
0.05
0.06
0.07
0.08
ray parameter
(s/km)

Appendix B

A reliable estimation of travel time and ray path between two points within a laterally heterogeneous 2D or 3D medium is necessary to solve many challenges in seismology such as accurate hypocenter estimation and robust subsurface velocity imaging. Early tomography imaging studies have employed geometric ray tracing based on a shooting or bending method. In the shooting method, (e.g., Julian and Gubbins, 1977; Sambridge and Kennett, 1990) the ray equation is treated as an initial value problem that allows a complete ray to be traced if the trajectory from the source is specified. The final raypath is determined by trying different directions from the source. The boundary value problem of locating the required two-point path is then solved using an iterative update procedure. In the bending method, the ray tracing is done (e.g., Um and Thurber, 1987) by iteratively adjusting the geometry of an initial arbitrary path that connects the source and the receiver until Fermat's principle is satisfied. However these two methods have some disadvantages such as they are time consuming during and there is a possibility that the method fails to converge in complex velocity structures.

A more recently developed method becoming popular in the exploration industry for predicting travel times in complex media is to use finite-differences of the eikonal equation throughout a gridded velocity field. (eg., Vidale, 1988, 1900; van Trier and Symes, 1991; Hole and Zelt, 1995; Buske and Kästner, 2004). A recently developed grid based numerical algorithm to do this is called the fast marching method (FMM) that computes a finite difference solution of the eikonial equation by tracking an evolving interface/wavefront along a narrow band (Sethian, J.A., 1996)

Numerically, the FMM systematically constructs travel times, T, in a downwind fashion from known upwind results by using a narrow band approach. Starting at a point, new travel times at adjacent points are calculated using equation 4.9

$$\left[\begin{array}{l}\max(D_a^{-r}T,-D_b^{+r}T,0)^2 \\ +\max(D_c^{-\theta}T,-D_d^{+\theta}T,0)^2 \\ +\max(D_e^{-\phi}T,-D_f^{+\phi}T,0)^2\end{array}\right]_{i,j,k}^{1/2} = s_{i,j,k} \qquad \text{……eq 4.9}$$

where,

$$D_{+x}T = \frac{T(x+\delta x)-T(x)}{\delta x}$$

$$D^{-x}T = \frac{T(x)-T(x-\delta x)}{\delta x} \qquad \text{……..eq. 4.10}$$

(i,j,k) are spherical grid increment variables in (r,θ,ϕ), and the integer variables a,b,c,d,e,f define the order of accuracy of the upwind finite difference operator used in each of the six cases. Next, all new travel times at its adjacent point will be sorted from the minimum to maximum to dictate the direction of flow..

Figure 4.14 displays an illustration of the Fast marching method. All grid points are labeled as either *Alive*, *Close* or *Far*. *Alive* points shown as black circles lie upwind of the narrow band and have correct travel time values already calculated; *Close* points shown as white circles lie within the narrow band and have trial values that are calculated using equation 4.8 from *Alive* points only; *Far* points lie downwind of the narrow band and have no travel time values calculated. The narrow band is updated by identifying the *Close* point with minimum travel time, then tagging it as *Alive,* (the new alive point is shown as blue circle in the figure) and then tagging all neighboring *Far* points as the new

Close point. Finally, all *Close* points adjacent to the new *Alive* point have their travel times updated using equation 4.8. The shape of the narrow band approximates the shape of the first arrival wave front, and the idea is to propagate the band through the grid until all points become *Alive*. Once all points become Alive and has information, a ray path can be constructed by following the time gradient or minimum travel time from a point in receiver until it reaches to source.

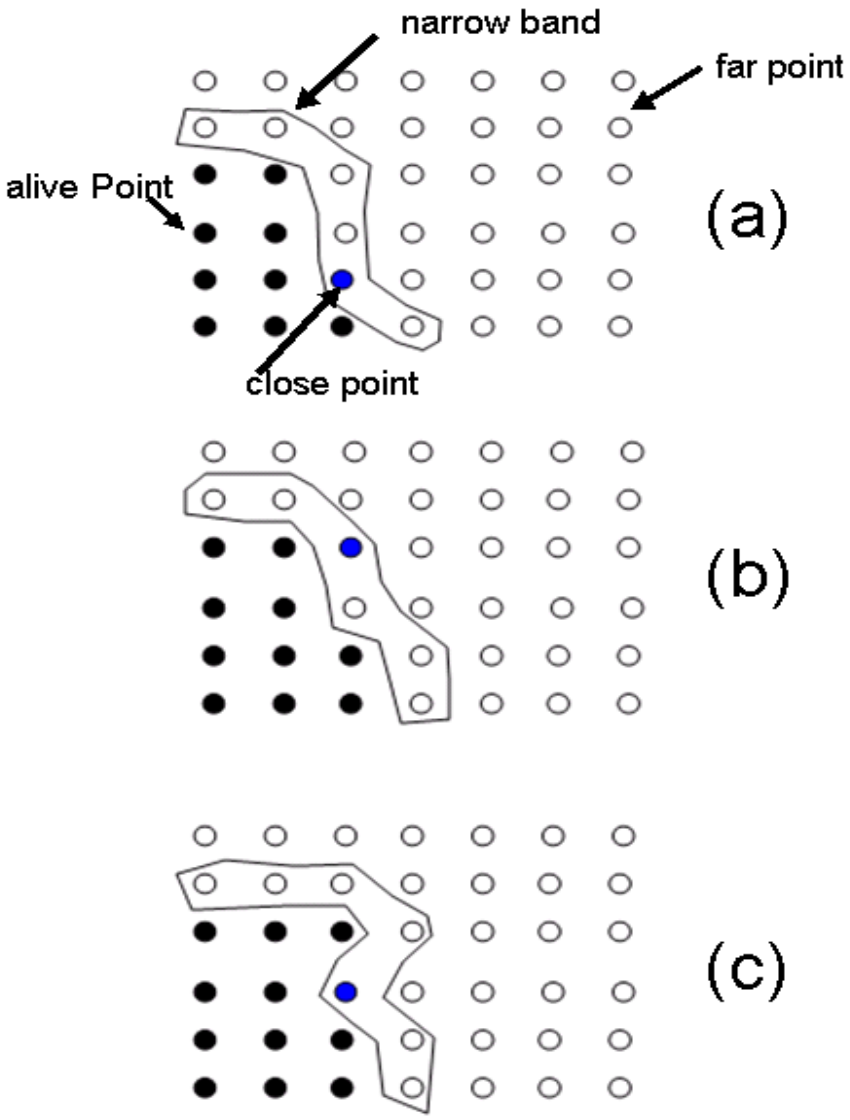

Figure B.1. An illustration of Fast marching method on a grid velocity. Narrow band is evolving from (a) to (c) act as a propagating wavefront. The initial condition (a) has alive point marked as black circles. Close points are all the neighbor points from alive points that have not been calculated and grouped as narrow band. The next step will sort all the value calculated inside the narrow band and the minimum value will be selected as the new alive points. That new alive point will take new neighbor point and put inside the narrow band to replace the old one. The process will repeat until all new points become alive.

Appendix C

* ph2dt.inp - input control file for program ph2dt

* Input station file:

station1.dat

* Input phase file:

neworigins

*MINWGHT: min. pick weight allowed

*MAXDIST: max. distance in km between event pair and stations

*MAXSEP: max. hypocentral separation in km

*MAXNGH: max. number of neighbors per event

*MINLNK: min. number of links required to define a neighbor

*MINOBS: min. number of links per pair saved

*MAXOBS: max. number of links per pair saved

*MINWGHT MAXDIST MAXSEP MAXNGH MINLNK MINOBS MAXOBS

0 250 20 8 4 4 40

Output log for identifying process :

> P-phase pairs total = 51250

> S-phase pairs total = 13839

> outliers = 1653 (2%)

> phases at stations not in station list = 0

> phases at distances larger than MAXDIST = 391

> P-phase pairs selected = 48263 (94%)

> S-phase pairs selected = 13584 (98%)

> weakly linked events = 126 (8%)

> linked event pairs = 7739

> average links per pair = 7

> average offset (km) betw. linked events = 11.6202974

> avg. offset (km) betw. strongly linked events = 13.6202974

> max. offset (km) betw. strongly linked events = 29.7753258

Appendix D

* RELOC.INP:

*--- input file selection

* cross correlation diff times:

dt.cc

*

*catalog P diff times:

dt.ct

*

* event file:

event.dat

*

* station file:

station1.dat

*

*--- output file selection

* original locations:

hypoDD.loc

* relocations:

hypoDD.reloc

* station information:

hypoDD.sta

* residual information:

hypoDD.res

* source paramater information:

*hypoDD.src

```
*
*--- data type selection:
* IDAT:  0 = synthetics; 1= cross corr; 2= catalog; 3= cross & cat
* IPHA: 1= P; 2= S; 3= P&S
* DIST:max dist [km] between cluster centroid and station
* IDAT   IPHA   DIST
   2     3     300
*
*--- event clustering:
* OBSCC:    min # of obs/pair for crosstime data (0= no clustering)
* OBSCT:    min # of obs/pair for network data (0= no clustering)
* OBSCC  OBSCT
    0     0
*
*--- solution control:
* ISTART:       1 = from single source; 2 = from network sources
* ISOLV:        1 = SVD, 2=lsqr
* NSET:         number of sets of iteration with specifications following
*  ISTART  ISOLV  NSET
   2       2      2
*
*--- data weighting and re-weighting:
* NITER:              last iteration to used the following weights
* WTCCP, WTCCS:        weight cross P, S
* WTCTP, WTCTS:        weight catalog P, S
* WRCC, WRCT:          residual threshold in sec for cross, catalog data
* WDCC, WDCT:          max dist [km] between cross, catalog linked pairs
* DAMP:                damping (for lsqr only)
```

```
*       ---  CROSS DATA ----- ----CATALOG DATA ----
* NITER WTCCP WTCCS WRCC WDCC WTCTP WTCTS WRCT WDCT DAMP
  4    1      0.5   29  13   1.01   1.0   -9    10   50
  4    1      0.5    5   13   1.01   1.0    5    10    50
*
*--- 1D model:
* NLAY:         number of model layers
* RATIO:        vp/vs ratio
* TOP:          depths of top of layer (km)
* VEL:          layer velocities (km/s)
* NLAY  RATIO
   6     1.73
* TOP
0.0 1.0 3.0 6.0 24.0 38.0
* VEL
3.77   4.64   5.34   5.75   6.22  7.98
*
*--- event selection:
* CID:  cluster to be relocated (0 = all)
* ID:   cuspids of event to be relocated (8 per line)
* CID
    1
* ID
```

Appendix E

IT	EV	CT	RMSCT	RMSST	DX	DY	DZ	DT	OS	AQ	CND
	%	%	ms	%	ms	m	m	m	ms	m		
1	100	97	191	-55.2	0	1266	1293	4460	192	0	52	234
2	91	81	193	1.2	0	1192	1218	4366	175	0	22	205
3	88	78	193	-0.1	0	1179	1193	4403	170	0	7	201
4	88	77	193	-0.1	0	1178	1182	4404	169	0	1	201
5	88	77	193	0.1	0	1177	1179	4402	169	0	1	198
6	1 87	77	192	-0.3	481	1177	1179	4398	169	2908	0	198
7	79	62	119	-38.0	481	331	299	1440	46	2908	17	165
8	2 77	59	108	-9.7	247	312	269	1004	40	1103	0	161
9	75	54	85	-21.1	247	147	148	323	22	1103	6	149
10	3 75	52	80	-5.9	206	143	143	256	20	603	0	145
11	74	50	68	-15.4	206	93	94	161	13	603	3	137
12	4 74	49	65	-3.7	190	92	93	148	13	638	0	139
13	73	48	57	-12.5	190	68	67	105	10	638	1	134
14	5 73	47	55	-3.0	143	68	67	103	9	628	0	133
15	73	46	50	-9.8	143	54	50	196	7	628	9	128

The first two columns (IT) in Table 2 indicate the iteration number. The first column numbers each iteration, while the second column numbers only the sucessful iterations (i.e. the ones without airquakes).

The third column (EV) indicates the percentage of events used in each iteration. Events get deleted if they lose connection to other events (due to outlier removal or distance cutoff), or if they locate above the surface (air quakes).

The forth (CT) and fifth column (CC) give the percentage of catalog data and cross-correlation data, respectively, used in each iteration. These values indicate how much of the data is removed by reweighting and can guide on the choice of the weighting parameters.

The sixth (RMSCT) and seventh (RMSCC) double-columns indicate the RMS residual (in ms) and its percent change from the last iteration for each of the two data types.

The eighth column (RMSST) indicates the largest RMS residual observed at a station.

The ninth to twelve columns (DX, DY, DZ, DT) indicate the average absolute value of the change in hypocenter location and origin time during each iteration.

The thirteenth (OS) indicates the absolute shift in cluster origin, i.e. the shift between the cluster centroid of the initial locations and the cluster centroid of the relocations

The fourteenth column (AQ) indicates the number of air earthquakes detected and discarded.

The last column (CND) indicates the condition number for the system of double-difference equations. A low value may indicate overdamping of the solution, a high value underdamping. Generally, a condition number between 40 and 80 has been shown to be appropriate.

References

Aki, K. and Lee, W., (1976), Determination of three-dimensional velocity anomalies under a seismic array using first P arrival times from local earthquakes, a homogeneous initial model, Journal of Geophysical Research 81, 4381 - 4399

Allan, J. F., Nellon, A. S., Luhr, F. J., Carmichael, E. S. I., Wopat, M. and Wallace, J. P., (1991), Pliocene-Holocene rifting and associated volcanism in southwest Mexico: an exotic terrane in the making. The Gulf and Peninsular Province of the California's, edited by Dauphin, P. J. and Simmoneit, T. R. B., pp. 425-445, American Association of Petroleum Geologists Memoir, 47, AAPG, Tulsa, OK.

Anderson, D. L., (1989), Theory of the Earth.Blackwell Scientific Publications, Boston, p. 366

Ankeny, L. A., Braile, L. W., & Olsen, K. H., (1986), Upper crustal structure beneath the Jemez Mountains volcanic field, New Mexico, determined by three-dimensional simultaneous inversion of seismic refraction and earthquake data, Journal of Geophysical Research, 91, 6188–6198.

Atwater, T., (1970), Implications of plate tectonics for the Cenozoic tectonic evolutions of western North America, Geological Society of America Bulletin, 81, 3513-3536.

Audet, P., M. G. Bostock, N. I. Christensen, and S. M. Peacock, (2009), Seismic evidence for overpressured subducted oceanic crust and megathrust fault sealing, Nature, 457, 76–78.

Baig, A., F. A. Dahlen, and S.-H. Hung, (2003), Traveltimes of waves in random media, Geophysical Journal International, 153, 467–482.

Bandy, W., Mortera-Gutierrez, C., Urrutia-Fucugauchi, J. and Hilde., C. W. T., (1995), The subducted Rivera-Cocos plate boundary: Where is it, what is its relationship to the Colima rift ?, Geophysical Research Letter, 22, 3075-3078.

Bandy, W., Kostoglodov, V., Hurtado, Díaz, A., Mena,M., (1999). Structure of the southern Jalisco subduction zone, Mexico, as inferred from gravity and seismicity. Geofísica Internacional, july-september, 127-136.

Bandy, W., Urrutia-Fucugauchi, J., McDowell, W. J., and Morton-Bermea, O., (2001), K-Ar ages of four mafic lavas from the Central Jalisco Volcanic Lineament: Supporting evidence for a NW migration of volcanism within the Jalisco block, western Mexico, Geofisica Internacional, v. 40, 259-269.

Blatter, D.L., Carmichael, E. S. I., Deino, L. A. and Renne, R. P., (2001), Neogene volcanism at the front of the central Mexican volcanic belt: Basaltic andesites to dacites, with contemporaneous shoshonites and high-TiO2 lava, Geological Society of America Bulletin, 113, 1324-1342.

Bostock, M. G., Hyndman, D. R., Rondenay, S and Peacock M. S., (2002), An inverted continental Moho and serpentinization of the forearcmantle, Nature, 417, 536–539

Buske, S., and Kästner, U., (2004), Efficient and accurate computation of seismic travel times and amplitudes. Geophysical Prospecting, 52, 313–322.

Campillo, M., Singh, S., Shapiro, N., Pacheco, J., and Herrmann, R., (1996), Crustal structure south of the Mexican volcanic belt, based on group velocity dispersion: Geofísica Internacional, v. 35, no. 4, p. 361–370.

Campos-Enríquez, J., Arroyo-Esquivel, M., and Urrutia-Fucugauchi, J., (1990), Basement, curie isotherm and shallow-crustal structure of the Trans-Mexican Volcanic Belt, from aeromagnetic data: Tectonophysics, v. 172, 77–90

Campos-Enríquez, J., and Sánchez-Zamora, O., (2000), Crustal structure across southern Mexico inferred from gravity data. Journal of South American Earth Sciences, v. 13, 479–489

Cande, S. C., and Kent, D. V., (1995), Revised calibration of the geomagnetic polarity timescale for the Late Cretaceous and Cenozoic, Journal of Geophysical Research - Solid Earth, 100(B4): 6093-6095.

Chevrot, S., and Van der Hilst, R.D., (2000), The Poisson's ratio of the Australian crust: geological and geophysical implications, Earth and Planetary Science Letters, v. 183/1-2, p. 121-132.

Christensen, N. I., (1996), Poisson's ratio and crustal seismology, Journal of Geophysical Research, 101(B2), 3139–3156.

Constable, S.C., Parker, R.L., and Constable, C.G., (1987), Occam's inversion: a practical algorithm for generating smooth models from electromagnetic sounding data, Geophysics, 52, 289–300

Crosson, R. S. and Owens J. T., (1987), Slab geometry of the Cascadia subduction zone beneath Washington from earthquake hypocenters and teleseismic converted waves, Geophysical Research Letter, 14, 824-827.

Dahlen, F. A., Hung, H. S. and Nolet, G., (2000), Frechet kernels for finite frequency traveltimes, I: Theory, Geophysical Journal International, 141, 157–174.

Demant, A., (1978), Características del Eje Neovolcánico Transmexicano y sus

problemas de interpretación, Revista Instituto de Geología, v. 2, p. 172–187.

DeMets, C. and Stein, S., (1990), Present day kinematics of the Rivera plate and implications for tectonics in southwestern Mexico, Journal of Geophysical Research, 95, 21, 931-21, 948.

DeMets, C. and Traylen, S., (2000), Motion of the Rivera plate since 10Ma relatives to the Pacific and North American plates and the mantle, Tectophysics, 318,119-159.

Dueker, K. G. and Sheehan, F. A., (1997), Mantle discontinuity structure from midpoint stacks of converted P to S waves across the Yellowstone hotspot track, Journal of Geophysical Research, 102, 8313-8327.

Eagar, K. C., Fouch, M. J., James, E. D., (2010), Receiver Function imaging of upper mantle complexity beneath the Pacific Northwest, United States, Earth and Planetary Science Letters v. 297, Issues 1-2, 141-153.

Eissler, H. K.and McNally, C. K., (1984), Seismicity and tectonics of the Rivera plate and implications for the 1932 Jalisco, Mexico, earthquake, Journal of Geophysical Reseacrh, 89, 4520-4530.

Ferrari, L., Pasquaré, G., Venegas, S., and Romero, F., (2000), Geology of the western Mexican volcanic belt and adjacent Sierra Madre Occidental and Jalisco block, in Delgado, G.H., et al., eds., Cenozoic tectonics and volcanism of Mexico: Geological Society of America Special Paper, 334, 65–84.

Ferrari, L., (1995), Miocene shearing along the northern boundary of the Jalisco block and the opening of the southern Gulf of California, Geology, v. 23, no. 8, p. 751–754

Ferrari, L., Petrone, C. and Francalanci, L., (2001), Generation of oceanic-island basalt-type volcanism in the western Trans-Mexican volcanic belt by slab rollback, asthenosphere infiltration, and variable flux melting, Geology, 29, 507-510.

Ferrari, L., Petrone, C., Francalanci, L., Tagami, T., Eguchi, M., Conticelli, S.,Manetti, P., and Venegas-Salgado, S., (2003), Geology of the San Pedro-Ceboruco graben, western Trans-Mexican Volcanic Belt: Revista Mexicana de Ciencias Geológicas, v. 20, p. 165–181.

Ferrari, L., (2004). Slab detachment control on mafic volcanic pulse and mantle heterogeneity in central Mexico, Geology, 32(1): 77 – 80.

Flores-Ruiz, J., (1997), Estructura cortical de la Faja Volcánica Transmexicana [Ph.D. thesis]: Mexico, D.F., Universidad Nacional Autónoma de México.

Forsyth, D. W., Webb, S., Dorman, L. and Shen, Y., (1998), Phase velocities of Rayleigh waves in the MELT experiment on the East Pacific Rise, Science, 280, 1235-1238.

García-Perez, F., and Urrutia-Fucugauchi, J.,(1997), Crustal structure of the Arteaga Complex, Michoacán, southern Mexico, from gravity and magnetics, Geofísica Internacional, v. 36, 235–244.

Gardine, M., Dominguez, T., West, M., Grand, S., Suhardja, S., (2007), The Deep Seismic Structure of Volcan de Colima, Mexico Eos Trans. AGU, 88(23), Fall Meeting Supplementary, Abstract T51A-02.

Geolimex-Group, (1994), Reflections of the subducting plate?, First results of a Mexican geotraverse, in Miller, H., Rosenfeld, U., and Weber-Diefenbach ,K., eds., 13th Symposium on Latin-America Geosciences: Teil, Zentralblattfür Geologie und Paläontologie, 541–553.

Gómez-Tuena, A., Orozco-Esquivel, Ma.T., and Ferrari, L., (2007), Igneous petrogenesis of the Trans-Mexican Volcanic Belt, Geological Society of America Special Paper, 422.

Hasegawa, A., Zhao, D., Hori, S., Yamamoto, A. and Horiuchi, (1991), Deep structure of the northeastern Japan arc and its relationship to seismic and volcanic activity, Nature, 352, 683-689.

Hasenaka, T. and Carmichael, I.S.E., (1985), The cinder cones at Michoacan-Guanajuato, Central Mexico: their age, volume, and distribiution, and magma discharge rate: Journal of Volcanology and Geothermal Research, v. 25, p. 105-124.

Heaton, T. H. and S. H. Hartzell., (1987), Earthquake hazards on the Cascadia subduction zone, Science, 236, 162-168.

Hole, J. A., and Zelt, B. C., (1995), 3-D finite-difference reflection travel times, Geophysical Journal International, 121, 427–434.

Hung, S.H., Dahlen, A. F. and Nolet G., (2001), Wavefront healing: A banana-doughnut perspective, Geophysical Journal International, 146, 289–312.

Hung, S.H., Shen, Y. and Chiao, Y. L., (2004), Imaging seismic velocity structure beneath the Iceland hot spot: A finite frequency approach, Journal of Geophysical Research, 109, B08305, doi: 10.1029/2003JB002889.

Hutton W., DeMets, C., Sanchez, O., Suarez, G. and Stock J., (2001), Slip kinematics and dynamics during and after the 1995 Colima-Jalisco earthquake, Mexico, from GPS geodetic constrains, Geophysical Journal Internacional, 146, 637-658.

Jording, A., Ferrari, L., Arzate, J., and Jodicke, H., (2000), Crustal variations and terrane boundaries in southern Mexico as imaged by magnetotelluric transfer functions: Tectonophysics, v. 327, 1–13.

Julian, B. R., and Gubbins, D., (1977), Three-dimensional seismic ray tracing: Journal of Geophysics, 43, 95–113.

Katsura, T. and Ito, E., (1989).The system Mg_2SiO_4–Fe_2SiO_4 at high pressures and temperatures: Precise determination of stabilities of olivine, modified spinel and spinel, Journal of Geophysical Research, 94, 15663-15670.

Kennett, B. L. N., Sambridge, M. S. and Williamson, P. R., (1988), Subspace methods for large scale inverse problems involving multiple parameter classes, Geophys. J., 94, 237 – 247.

Kennett, B. L. N., and Engdahl, E. R., (1991), Traveltimes for global earthquake location and phase identification, Geophysical Journal International, 122, 429–465.

Kennett, B. L. N., Engdahl, E. R. and Buland, R., (1995), Constraints on seismic velocities in the Earth from travel times, Geophysical Journal International, 122, 108 – 124

Keskin, M. (2003), Magma generation by slab steepening and breakoff beneath a subduction-accretion complex: An alternative model for collision-related volcanism in Eastern Anatolia, Turkey, Geophysical Research Letter., 30, 8046.

Kim, Y., Clayton, R. W. and Jackson, J. M., (2010), Geometry and seismicproperties of the subducting Cocos Plate in central Mexico, Journal of Geophysical Research., 115, B06310.

Kirby, S.H., Engdahl, E. R. and Denlinger, R., (1996), Intraslab earthquakes and arc volcanism: dual physical expressions of crustal and uppermost mantle metamorphism in subducting slabs in Subduction: Top to Bottom, Geophysical Monograph, p. 194–214.

Kirby, S.H., (2000), Taking the temperature of slabs. Nature 403,31–34.

Kostoglodov, V., and Bandy, W., (1995), Seismotectonic constraints on the convergence rates between the Rivera and North American plates, Journal of Geophysical Research, v. 100, no. B9, 17.977–17.989.

Langston, C. A., (1977), Corvallis, Oregon, Crustal and upper mantle structure from teleseismic P and S waves, Bull. Seismol. Soc. Am., 67, 713–724.

Lawver, L. A., Dalziel, I. W. D., Norton, I. O., Gahagan, L. M., and Davis, J., (2013),

The Plates 2013 Atlas of Plate Reconstructions (500 Ma to Present Day), Plates Progress Report No. 359-0413, University of Texas Technical Report No. 199.

Lee, K. D. and Grand, P. S., (1996), Upper mantle shear structure beneath the Colorado Rocky Mountain front, Journal of Geophysical Research, 101, 22.233-22.244.

Leon Soto, G., Ni, F. J., Grand, P. S., Sandvol, E., Valenzuela, W. R., Guzman Speziale, M., Gomez Gonzalez, M. J., and T. Dominguez Reyes, (2009), Mantle flow in the Rivera-Cocos subduction zone, *Geophys. J. Int.*, 179, 1004–1012.

Liu, L. and Stegman, R. D., (2012), Origin of Columbia River flood basalt controlled by propagating rupture of the Farallon slab, Nature, 482, 386-389.

Londsdale, P., (1991), Structural patterns of the Pacific floor offshore Peninsular California, in Dauphin, J., and Simoneit, B., eds., The Gulf and the Peninsular Province of the Californias: Tulsa, Oklahoma, American Association of Petroleum Geologists Memoir 47, 87–125.

Lyle, M., and Ness, G., (1991), The opening of the Southern Gulf of California, in Dauphin, J. P., and Simoneit, B. R. T., eds., The Gulf and Peninsular Provinces of the Californias, American Association of Petroleum Geologists Memoir, 47, 403–423.

Luhr, J. F., Allan, F. J., Carmichael, E. S. I., Nelson, A. S. and Hasenaka T., (1985), Active rifting in southwestern Mexico: Manifestation of an incipient eastward spreading ridge jump, Geology, 13, 54-57.

Manea, M., Manea, V., and Kostoglodov, V., (2003), Sediment fill in the Middle America Trench inferred from gravity anomalies, Geofísica Internacional, v. 42, no. 4, 603–612.

Maillol, J. M., Bandy L. W. and Ortega-Ramirez J., (1997), Paleomagnetism of Plio-Quaternary basalts in the Jalisco block, western Mexico, Geofisica Internacional, 36,21-35.

Mammerickx, J. and Klitgord, K.D., (1982), Northern East Pacific Rise; evolution from 25 m.y B.P to the present, Journal of Geophysical Research, v. 87, 6751-6759.

Marquering, H., F. A. Dahlen, and G. Nolet., (1999), Three-dimensional sensitivity kernels for finite-frequency travel times: The banana-doughnut paradox, Geophysical Journal Internacional, 137, 805– 815.

Marquez, A., Oyarzun, R., Doblas, M., and Verma, P. S., (1999), Alkalic (ocean-island basalt type) and calc-alkaline volcanism in the Mexican volcanic belt: A case for pluma-related magmatism and propagating rifting at an active margin?, Geology,

27, 51-54.

McCaffrey, R., Qamar, I. A., King, W. R., Wells, R., Khazaradze, G., Williams, A. C., Stevens, W. C., Vollick, J. J. and Zwick, C. P., (2007), Fault locking, block rotation and crustal deformation in the Pacific Northwest, Geophysical Journal Internacional, 169, 1315 – 1340.

Menard, H., (1978), Fragmentation of the Farallon plate by pivoting subduction: The Journal of Geology, v. 86, 181–201.

Molina-Garza, R., and Urrutia-Fucugauchi, J., (1993), Deep crustal structure of central Mexico derived from interpretation of Bouger gravity anomaly data: Journal of Geodynamics, v. 17, 181–201.

Montelli, R., Nolet, G., Masters, G., Dahlen, F. A. and Hung, S.-H., (2004), Global P and PP travel time tomography: rays versus waves. Geophysical Journal International, 158, 637–654.

Moore, G., Marone, C., Carmichael, E. S. I. and Renne, P., (1994), Basaltic volcanism and extension near the intersection of the Sierra Madre volcanic province and the Mexican belt, Geological Society of America Bulletin, 106, 383-394.

Moser, T. J., VanEck, T. and Nolet, G., (1992), Hypocenter determination in strongly heterogeneous earth model using the shortest path method, Journal of Geophysical Research, 97, 6563-6572.

Muirhead, K.J., (1968), Eliminating false alarms when detecting seismic events automatically, Nature, 217, 533-534.

Nabelek, J., Li, Q. X., Azevedo, S., Braunmiller, J., Fabritius, A., Leitner, B., Trehu, A. M. and Zandt, G., (1993), A high-resolution image of the Cascadia subduction zone from teleseismic converted phases recorded by a broadband array, EOS Trans. AGU, 74, Fall Meeting Supplementary, 431.

Nava, A., Núñez-Cornu, F., Córdoba, D., Mena, M., Ansorge, J., González, J., Rodríguez, M., Banda, E., Müller, S., Udias, A., García-García, M., and Calderón, G. (1988), Structure of the Middle America trench in Oaxaca, México: Tectonophysics, v. 154, 241–251.

Nixon, G., (1982), The relationship between Quaternary volcanism in central Mexico and the seismicity and structure of subducted ocean lithosphere: Geological Society of America Bulletin, v. 93, 514–523.

Nolet, G., (1993), Solving large linearized tomographic problems in Seismic Tomography, Theory and Practice, edited by Iyer M. H. and Hirahara, K., Chapman & Hall, London, 227-247.

Nyblade, A. A., Owens, J. T., Gurrola, H., Ritsema, J.and Langston, C. A., (2000), Seismic evidence for a deep upper mantle thermal anomaly beneath East Africa , Geology, 28, 599-602.

Owens, T. J., Zandt, G. and Taylor, R. S., (1984), Seismic evidence from an ancient rift beneath Cumberland plateau, Tennesse, Journal of Geophysical Research, 89, 7783-7795.

Pacheco, J. F., Valdés-González, C., Delgado, H., Singh, S. K., Zúñiga,R., Mortera-Gutiérrez, C. A., Santoyo, M. A., Domínguez, J.,Barrón, R., (1999), Tectonic implications of the earthquake swarmof 1997 in the Michoacán Triangle, Mexico. Journal of South American Earth Sciences, 12, 567–577.

Paige, C. C, and Saunders, M. A., (1982), Algorithm 583; LSQR: Sparse linear equations and least-squares problems, TOMS 8(2), 195-209.

Pardo, M., and Suárez, G., (1993), Steep subduction geometry of the Rivera platebeneath the Jalisco Block in western Mexico, Geophysical Research Letters, v. 20, p. 2391–2394.

Pardo, M. and Suarez, G., (1995), Shape of the subducted Rivera and Cocos plate in the southern Mexico: Seismic and tectonic implications, Journal of Geophysical Research, 100, 12. 357-12.373.

Parsons, T. and Zoback, M. L., (1997), Three-dimensional upper crustal velocity structure beneath San Francisco Peninsula, California, Journal of Geophysical Research, 102, 5473–5490.

Perarnau, M., Gilbert, H., Alvarado, P., Martino, R., Anderson, M., (2012), Crustal structure of the Eastern Sierras Pampeanas of Argentina using high frequency local receiver functions,. Tectonophysics v. 580, 208-217.

Rasmussen, J. and Humphreys, E., (1988), Tomographic image of the Juan de Fuca plate beneath Washington and western Oregon using teleseismic P-wave travel times, Geophysical Research Letter, 15, 1417-1420.

Rawlinson, N. and Sambridge, M., (2003), Seismic traveltime tomography of the crust and lithosphere, Advances in Geophysics, 46**,** 81-198.

Rawlinson, N. and Sambridge M., (2005), The fast marching method: An effective tool for tomographic imaging and tracking multiple phases in complex layered media, Explor. Geophys., 36, 341-350.

Rea, D.K., and L.J. Ruff, (1996), Composition and mass flux of sediment entering the world's subduction zones: Implications for global sediment budgets, great

earthquakes, and volcanism, Earth and Planetary Science Letters, 140 , 1-12.

Reyes, A., Brune, J. and Lomnitz, C., (1979), Source mechanism and aftershock study of the Colima, Mexico earthquake of January 30, 1973, Bull. Seismok Soc. Am., 69, 1819-1840.

Righter, K. and Carmichael, E. S. I., (1992), Hawaiites and related lavas in the Atenguillograben, western Mexican volcanic belt, Geological Society of America Bulletin, 104, 1592-1607.

Righter, K., Carmichael, E. S. I., and Becker, T., (1995), Pliocene-Quaternary faulting and volcanism at the intersection of the Gulf of California and the Mexican Volcanic Belt: Geological Society of America Bulletin, v. 107, 612–627.

Rondenay, S., Abers, G.A., van Keken, P.E., (2008), Seismic imaging of subduction zone metamorphism, Geology, 36, 275–278.

Rosas-Elguera, Ferrari, L. J., Garduno-Monroy H. V. and Urrutia-Fucugauchi, J., (1996), Continental boundaries of the Jalisco block and their influence in the Pliocene Quaternary kinematics of western Mexico, Geology, 24, 921-924.

Thurber C. H., (1983), Earthquake locations and three-dimensional crustal structure in the Coyote Lake area, central California, Journal of Geophysical Research, 88, 8226–8236.

Sambridge, M. S., and Kennett, B. L. N., (1990), Boundary value ray tracing in a heterogeneous medium: A simple and versatile algorithm: Geophysical Journal International, 101, 157–168.

Sato, T., Kosuga, M., & Tanaka, K., (1996), Tomographic inversion for P wave velocity structure beneath the northeastern Japan arc using local and teleseismic data, Journal of Geophysical Research, 101, 17.597–17.615.

Schaaf, P., Heinrich, W. and Besch, T., (1994), Composition and Sm-Nd isotopic data of the lower crust beneath San Luis Potosí, central Mexico: Evidence from a granulite-facies xenolith suit,: Chemical Geology, v. 118, p. 63–84

Schaaf, P., Moran-Zenteno, D., Hernandez-Bernal, M., Solis-Pichardo, G., Tolson, G., (1995), Paleogene continental margin truncation in southwest Mexico: Geochronological evidence, Tectonics, 14, 1339-1350.

Schmitt, S., C. DeMets, J. Stock, O. Sánchez, B. Márquez-Azúa, and G. Reyes, A geodetic study of the 22 January 2003 Tecomán, Colima, Mexico Earthquake, (2007), Geophysical Journal International,.169, doi: 10.1111/j.1365-246X.2006.03322.x.

Schulte-Pelkum, V., Monsalve, G., Sheehan, A., Pandey, M. R., Sapkota, S., Bilham, R., Wu, F. (2005), Imaging the Indian subcontinent beneath the Himalayan. Nature 435, 1222-1225

Sedlock , R.L., (1993), Mesozoic geology and tectonics of blueschist and associated oceanic terranes in the Cedros–Vizcaino–San Benito and Magdalena–Santa Margarite regions, Baja California. In: Dunne, G.C. and McDougall, K.A., Editors, 1993. Mesozoic Paleogeography of the Western United States – II Book71, Pacific Section, Society of Economic Paleontologists and Mineralogists, 113–125.

Sheth, H., Torres-Alvarado, I., and Verma, S., (2000), Beyond subduction and plumes: A unified tectonic-petrogenetic model for the Mexican volcanic belt: International Geology Review, v. 42, no. 12, 1116–1132.

Song, T. H., Helmberger, V. M., Brudzinski, R. M., Clayton, W. R., Davis, P., Perez-Campos, X. and Singh K. S., (2009), Subducting slab ultra-slow velocity layer coincident with silent earthquakes in southern Mexico, Science, 324, 502-506.

Stock J. M. and Lee, J.,(1994). Do microplates in subduction zones leave a geological record? Tectonics, 13, 6, 1472-1487.

Urn, J. and Thurber, H. C., (1987), A fast algorithm for two-point seismic ray tracing, Bull. Seismic Society of America, 77, 972-986.

Urrutia-Fucugauchi, J., and Del Castillo, L., (1977), Un modelo del EjeVolcánico Mexicano: Boletín de la Sociedad Geológica Mexicana, v. 38, 18–28.

Urrutia-Fucugauchi, J., (1986), Crustal thickness, heat flow, arc magmatism, and tectonics of Mexico—Preliminary report, Geofísica Internacional, v. 25, no. 4, 559–573.

Urrutia-Fucugauchi, J., and Böhnel, H., (1987), Tectonic interpretation of the Trans-Mexican Volcanic Belt: Tectonophysics, v. 138, 319–323.

Urrutia-Fucugauchi, J. and Molina-Garza, R., (1992), Gravity modeling of regional crustal and upper mantle structure of the Guerrero terrrane- 1. Colima graben and southern Sierra Madre Occidental, western Mexico, Geofísica Internacional, 31, 493-507.

Van Andel TH., (1975), Mesozoic/Cenozoic calcite compensation depth and the global distribution of calcareous sediments, Earth and Planetary Science Letter, 26,187–194.

Van Decar, J. C. and Crosson, S. R., (1990), Determination of teleseismic relative phase

arrival times using multi-channel cross-correlation and least squares, Bull. Seismol. Soc. Am., 80, 150– 169.

Van Trier, J., and Symes, W. W., (1991), Upwind finite-difference calculation of travel times, Geophysics, 56, 812–821.

Valdés, C., Mooney, W., Singh, S., Meyer, R., Lomnitz, C., Luetgert, J., Helsley, C., Lewis, B. and Mena, M., (1986), Crustal structure of Oaxaca, Mexico, from seismic refraction measurements: Bulletin of the Seismological Society of America, v. 76, 547–563.

Verma, S., (1999), Geochemistry of evolved magmas and their relationship to subduction-unrelated mafic volcanism at the volcanic front of the central Mexican Volcanic Belt: Journal of Volcanology and Geothermal Research, v. 93, p. 151–171.

Verma, S., (2000a), Geochemistry of the subducting Cocos plate and the origin of subduction-unrelated mafic volcanism at the front of the central Mexican Volcanic Belt, in Delgado-Granados, H., Aguirre-Díaz, G., and Stock, J., eds., Cenozoic Tectonics and Volcanism of Mexico: Geological Society of America Special Paper 334, 1–28.

Verma, S., (2002), Absence of Cocos plate subduction-related basic volcanism in southern Mexico: A unique case on Earth?: Geology, v. 30, no. 12, 1095–1098,

Vidale, J. E., (1988), Finite difference calculations of traveltimes: Bulletin of the Seismological Society of America, 78, 2062–2076.

Wagner, L.S., Beck, L. S. and Zandt, G., (2005), Upper mantle structure in the south central Chilean subduction zone (30 to 36S), Journal of Geophysical Research, 110, B01308, doi:10.1029/2004JB003238.

Wallace, P. & Carmichael, E. S. I., (1992), Alkaline and calc-alkaline lavas near Los Volcanes, Jalisco, Mexico: geochemical diversity and its significance in volcanic arcs. Contributions to Mineralogy and Petrology, 111, 423–439.

Waldhauser, F. and Ellsworth, L. W., (2000), Fault structure and mechanics of the Hayward Fault, California, from double-difference earthquake locations Journal of Geophysical Research., 107(B3), 2054.

West, M., Ni, J., Baldridge, S., Wilson, D., Aster, R., Gao, W. and Grand, S., (2004), Comparison of the uppermost mantle across the Colorado Plateau, Rio Grande rift and Great Plains from surface wave dispersion, Journal of Geophysical Research, doi:1029/2003/JB002575.

Wilson, D. S., (2002), The Juan de Fuca plate and slab—Isochron structure and Cenozoic

plate motions: U.S. Geological Survey Open-File Report 02-328, p. 9-12.

Yang, T., Shen, Y., van der Lee S., Solomon, C. S. and Hung, H. S., (2006), Upper mantle structure beneath the Azores hotspot from finite-frequency seismic tomography, Earth and Planetary Science Letter, 250, 11 –26.

Yang, T., Grand, P. S., Wilson, D., Guzman-Speziale, M., Gomez-Gonzalez, M. J., Dominguez-Reyes, T. and Ni. J., (2009), Seismic structure beneath the Rivera subduction zone from finite-frequency seismic tomography, Journal of Geophysical Research, 114, B01302.

Zhao, Z., Kubota, R., Fumio, S. and Iizuka, S., (1997), Crustal structure in the southern Kanto-Tokai region derived from tomographic method for seismic explosion survey, Journal of Geophysical Research, 45, 433– 453.

Zhao, L., Jordan, H. T. and Chapman, H. C., (2000), Three-dimensional Frechet differential kernels for seismic delay times, Geophysical Journal International, 141, 558– 576.

Zhu, L. and Kanamori, H., (2000), Moho depth variation in southern California from teleseismic receiver functions, Journal of Geophysical Research, 105(B2), 2969–2980.